DISSERTATION

STUDIES OF TUNING MAGNETIC PROPERTIES OF FERROMAGNETIC HETEROSTRUCTURES

Submitted by

Joshua Lauzier

Department of Physics

In partial fulfillment of the requirements

For the Degree of Doctor of Philosophy

Colorado State University

Fort Collins, Colorado

Spring 2020

Doctoral Committee:

Advisor: Jose de la Venta Granda

Kristen Buchanan
Martin Gelfand
Stuart Field
Carmen Menoni

ABSTRACT

STUDIES OF TUNING MAGNETIC PROPERTIES OF FERROMAGNETIC HETEROSTRUCTURES

The magnetic properties of hybrid systems have increasingly become an area of intense focus in both fundamental research and technological application due to the inherent flexibility in material properties by mixing and matching various constituent components. One particularly interesting choice is hybrid heterostructures that consist of ferromagnetic (FM) materials and materials that undergo phase transitions, coupled via structural, electronic, and/or magnetic coupling. Two canonical examples of phase transition materials are vanadium dioxide (VO_2) and iron rhodium ($Fe_{50}Rh_{50}$, abbreviated FeRh). Both materials undergo structural phase transitions (SPT). With increasing temperature, VO_2 transitions from a low temperature monoclinic to high temperature rutile structure at 340 K. The SPT is concurrent with a 4-5 orders of magnitude metal to insulator transition (MIT) from a low temperature insulating phase to a high temperature metallic phase. Similarly, FeRh undergoes an isotropic 1% volume expansion at 370 K with increasing temperature. Coincident with the SPT, FeRh also undergoes a magnetic transition from a low temperature antiferromagnetic (AF) to a high temperature ferromagnetic (FM) phase, which is unusual for magnetic materials. The delicate nature of these transitions makes them sensitive to parameters such as stoichiometry, growth conditions, and external stimuli, which allows for high tunability of their respective phase transitions.

In this thesis, we first show in Chapter 3 that the surface morphology and MIT properties of sputtered VO_2 thin films can be tuned via deposition conditions such as deposition

temperature and O_2 flow rate during the sputtering process while maintaining the quality of the VO_2 transition. Films grown at higher temperatures (> 525 ℃) and low O_2 flow rate show sub 2 nm surface roughness. Higher temperatures lead to a 'melted'-like surface morphology along with a 5 orders of magnitude MIT, comparable to single crystals. Choice of substrate allows another avenue to strongly tune both the morphology and the MIT characteristics while maintaining a strong VO_2 transition due to lattice mismatch.

In Chapter 4, we turn to a discussion of VO_2/Ni bilayer structures, where the temperature induced VO_2 SPT will impart a strain across the interface into the FM layer, which will then influence the magnetic properties via magnetoelastic coupling. Due to an inverse magnetostrictive effect the coercivity and magnetization of the FM layer can be strongly modified. Tuning the VO_2 SPT via growth conditions or substrate choice then allows for tuning the coupled magnetic properties of the FM. For sufficiently smooth films, there is a strong enhancement in the coercivity localized close to their respective SPT T_c due to phase coexistence in the SPT material. This chapter is largely based on work previously published as "Coercivity enhancement in VO_2/Ni bilayers due to interfacial stress" in Journal of Applied Physics.[1]

VO_2/FM hybrid films also show a dependence on the growth conditions during the FM deposition, which is explored in Chapter 5. Films with the FM deposited above the VO_2 phase transition critical temperature (T_c) show a high coercivity below T_c and a low coercivity above T_c, whereas films deposited below T_c show the opposite behavior. Films deposited below T_c also show an irreversibility in their magnetic properties the first time they are thermally cycled. A similar irreversibility is observed in the resistance vs. temperature (R vs. T) properties of bare VO_2 films, and cracking as the VO_2 crosses the SPT is proposed as a common mechanism. The plausibility of cracking as a mechanism is investigated via computational modeling of the R vs.

T properties in a random resistor network, as well as probed directly via Atomic Force Microscopy (AFM). The work shown in this chapter has been previously published under the title “Magnetic irreversibility in VO_2/Ni bilayers” in Journal of Physics: Condensed Matter.[2]

Sputtered FeRh/FM bilayer films show a similar sensitivity as the VO_2/FM system to the growth conditions, with the coercivity below T_c tunable whether the FM is initially deposited above or below T_c. Above T_c, the magnetic FeRh phase adds an additional complication, dominating the magnetic response via exchange coupling. This effect is explored in FeRh/Ni bilayer systems in Chapter 6. Polarized neutron reflectometry (PNR) allows for depth dependent structural and magnetic characterization with nanometer resolution. PNR measurements show that the bilayer’s magnetic behavior below T_c is likely driven by magnetoelastic effects due to the structural transition of the FeRh, rather than simple magnetic coupling or a pinned interfacial FM layer. The overall magnetic properties of the bilayers are therefore a product of both structural and magnetic coupling between the FeRh and the FM Ni layer. The results of this chapter have been previously published as “Using structural phase transitions to enhance the coercivity of ferromagnetic films” in Applied Physics Letters Materials.[3]

ACKNOWLEDGEMENTS

First, I would like to thank my advisor, Prof. Jose de la Venta Granda, for all his knowledge and guidance across the years. I was very lucky to have an advisor who not only had the technical knowledge, but also leadership, planning skills, and also passion for mentoring to pass that knowledge on while keeping everything moving forward smoothly. All the skills that are necessary in a modern-day lab, from the experimental to theory, to the more mundane scheduling, I learned from him.

I would also like to thank the members of my committee: Prof. Carmen Menoni, Prof. Martin Gelfand, Prof. Kristen Buchanan, and Prof. Stuart Field for agreeing to be on this committee, but also for valuable discussions, comments and suggestions that have all directly improved my work in some fashion in the course of these studies. Special thanks to Tao Liu and Peng Li for answering any questions, however trivial. And of course, a thank you to my lab partners Logan Sutton and Mathew Mehrian, the latter who took on a significant portion of the initial tuning, literature search, and studies in the thin films presented in Chapter 7. This work wouldn't be complete without the efforts of Ryan F. Need and Brian J. Kirby in designing, running and interpreting Polarized Neutron data in Chapter 7. As well, Brian Newell, for the training, maintenance and suggestions in most of the measurement techniques used throughout this dissertation. And last, I'd like to thank Siming Wang for useful discussions on theoretical concerns studying resistor network problems.

TABLE OF CONTENTS

LIST OF FIGURES

LIST OF ACRONYMS

AF	Antiferromagnet, Antiferromagnetic
AFM	Atomic Force Microscopy
ARPES	Angle Resolved Photoemission Spectroscopy
BTO	Barium Titanate, $BaTiO_3$
CPS	Counts Per Second
DC	Direct Current
DREAM	DiffeRential Evolution Adaptive Metropolis algorithm
E_F	Fermi Energy
FeRh	Iron Rhodium, $Fe_{50}Rh_{50}$ unless noted
FM	Ferromagnetic
FWHM	Full Width at Half Maximum
GGA	Generalized Gradient Approximation
GPU	Graphical Processing Unit
HAMR	Heat Assisted Magnetic Recording
H_C vs. T	Coercivity vs. temperature
HT	"High Temperature", indicating a deposition onto a phase transition material above that materials' critical temperature
J-A-S	Jiles-Atherton-Sablik
LDA	Local Density Approximation
LHS	Left Hand Side
M1	Monoclinic 1
MBE	Molecular Beam Epitaxy
MCMC	Markov Chain Monte Carlo
ME	Magnetoelectric
MgO	Magnesium Oxide
MIT	Metal to Insulator Transition

mM	Metallic Monoclinic
MOKE	Magneto-optical Kerr Effect
M_S	Saturation Magnetization
MSPT	Magnetostructural Phase Transition
M vs. H	Magnetization vs. applied Magnetic field
M vs. T	Magnetization vs. Temperature
NC	Nevot-Croce
NCNR	NIST’s Center for Neutron Research
NM	Nelder-Mead
NN	Nearest Neighbor
PBR	Polarized Beam Reflectometer
PCG	Preconditioned Conjugate Gradient
PE	Piezoelectric
PES	Photoemission Spectroscopy
PLD	Pulsed Laser Deposition
PM	Paramagnetic
PNR	Polarized Neutron Reflectometry
PPMS	Physical Properties Measurement System
Q	Momentum transfer vector
R	Rutile
RF	Radio Frequency
RHS	Right Hand Side
RT	“Room Temperature”, indicating a deposition onto a phase transition material below that materials’ critical temperature
R vs. T	Resistance vs. Temperature
SA	Spin Asymmetry
SLD	Scattering Length Density
SPT	Structural Phase Transition
SQUID	Superconducting Quantum Interference Device

sSNIM	Scattering Scanning Infrared Microscopy
T_c	Critical Temperature
V_2O_3	Vanadium Trioxide
VO_2	Vanadium Dioxide
VSM	Vibrating Sample Magnetometry
XMCD	X-ray Magnetic Circular Dichroism
XPEEM	X-ray Photoemission Electron Microscopy
XRD	X-ray Diffraction
XRR	X-ray Reflectivity

Chapter 1. Introduction

1.1 Magnetic heterostructures

The two materials at the focus of this work, vanadium dioxide (VO_2) and iron rhodium (FeRh) have both long attracted attention since their initial discovery due to their unique properties, as well as the elusiveness of a comprehensive understanding of those properties from first principles.[4–6] Both belong to larger families of functional materials that are interesting from a theoretical standpoint as well as useful in applications.

VO_2 is a member of the family of transition metal oxides, which have been the focus of intense study for decades. This family of compounds, which often have strong electron-electron correlations, exhibit a wide range of phenomena. The family of manganites exhibit the so-called colossal magnetoresistance effect, where the magnetoresistance can change by orders of magnitude.[7] The cuprates have played a significant role in high temperature superconductivity.[8] Transition metal oxides can display various forms of ferroic order, such as the traditional ferromagnetism or antiferromagnetism, but also more exotic types such as ferroelectricity, or ferroelasticity.[9–11] Many of transition metal oxides are multiferroics, in which various degrees of electronic order are coupled.[12] On top of these novel properties, the energetic landscape of these materials means that they have multiple states which are energetically quite similar, which can nevertheless lead to large changes in physical properties. They include materials that undergo structural phase transitions (SPT),[13] where the underlying crystal structure becomes distorted. These transitions are often accompanied by transitions in other properties such as abrupt changes in the resistivity via a metal to insulator transition (MIT) that can be several orders of magnitude.[13–15] The various forms of ferroic order often undergo a transition as well.[13] In the case of VO_2, it exhibits a SPT at 340 K from a low temperature monoclinic crystal structure to a high temperature rutile crystal structure. Simultaneous with this SPT is a 5 orders of magnitude MIT from a low temperature insulating state to a high temperature metallic state.

FeRh belongs to a similarly storied family of compounds in the magnetic intermetallics. Heusler alloy intermetallics display peculiar magnetic properties despite nonmagnetic constituent atoms. R_5T_4 rare earth intermetallics can show a giant magnetocaloric effect.[16] $MgCu_2$ type intermetallics display giant magnetostriction effects.[17] Many of these effects are driven by the strong coupling between the structural and magnetic properties of the systems. This can also lead to multiferroic behavior such as in magnetic shape memory alloys,[18] including magnetostructural phase transitions (MSPT) where both the structure and magnetic properties change due to the coupling between magnetic and structural degrees of freedom in the material. FeRh exhibits a MSPT at 370 K where it undergoes an isotropic 1% expansion of its cubic unit cell along with an unusual concurrent antiferromagnetic (AF) to ferromagnetic (FM) magnetic transition with increasing temperature.

Both classes of materials are often difficult to synthesize, and their unique properties are often highly sensitive to various parameters such as growth conditions and stoichiometry. The strong interest in these materials has thus led to refinement of techniques such as chemical vapor deposition,[19] sputtering,[20] molecular beam epitaxy,[21] and pulsed laser deposition (PLD).[22] Chemical methods are also being investigated as a means of cheaply scaling production while maintaining the high quality required to preserve the physical behavior of these materials.[23]

While the exact mechanisms behind many of the previously mentioned material properties aren’t completely understood, work has begun on integrating them as components into larger devices and structures. Thin film heterostructures allow for large coupling between multiple electronic properties, yielding a composite whose constituent parts can be mixed and matched for the desired properties. In addition, the thin film geometry may allow interfacial effects and symmetry breaking to dominate, which can lead to unique properties. Thus, the combination of two different materials in a heterostructure allows for a much wider range of functionality in tuning the magnetic properties of the thin film than can be realized in a single-phase material. While they often offer new challenges in synthesis, a number of these composite systems have been realized.[24–26] These heterostructures can display properties such as multiferroicity, giant magnetoresistance, exchange bias or electric field control of magnetism that are not seen in the constituent materials.[27–30]

One way to interact directly with a magnetic film is via the exchange interaction. This fundamentally quantum mechanical phenomenon is a powerful tool in magnetic heterostructures that can act as a very large local field. One of the more striking examples is exchange bias in (AF)/(FM) heterostructures.[25,30] AFs are relatively insensitive to applied fields, and exchange between the top layer of the AF and the ferromagnet acts as an internal biasing field, leading to horizontal shifts in the M vs. H loop of the system. Spin valves have taken this effect one step further, using exchange to create a ‘hard’ layer and adding further multilayers on top to take advantage of the giant magnetoresistance effect. Multilayer structures with many stacks of an FM and spacer layer can show oscillations in the exchange strength between FM layers by varying the spacer layer thickness, including antiferromagnetic coupling.[31]

A unique subset of magnetic heterostructures are those mediated via strain. Rather than utilizing direct electronic interactions, indirect coupling is mediated via strain fields with the magnetostrictive effect and its inverse in the ferromagnet providing the avenue for this strain to influence the magnetic properties. Despite the indirect nature and typically small magnetostrictive coefficients, magnetostrictive coupling can lead to large changes in magnetic properties in thin film heterostructures. Here we touch on four large areas: strain engineering via substrate, multiferroic heterostructures, piezoelectric/ferromagnetic heterostructures, and an SPT/FM heterostructure. For more comprehensive reviews, see [27,32–37].

Strain engineering in heterostructures has long shown promise as a way to tune various electronic properties, potentially over a wide range of parameters. Perhaps the simplest method is the choice of substrate, which can impart strain via lattice mismatch. Misfit strain has been used to tune the magnetic anisotropy in various ferromagnetic systems.[38–40] In addition to tuning T_c, substrate misfit strain can even stabilize ferroic phases in materials that are not intrinsically ferroic in bulk.[41,42]

Synthetic multiferroics can display magnetoelectric (ME) coupling orders of magnitude larger than known single-phase multiferroics. Investigations into this idea began with bulk composites and laminates.[27,43] Even the first bulk composites displayed ME coupling an order of magnitude larger than single-phase multiferroics. However, thin films offer advantages over both of these techniques for maximizing the magnetostrictive effect. Nanostructured films have relatively large surface area, allowing the interfacial effects to dominate. They also allow for epitaxial growth, which leads to excellent strain propagation as compared to other methods.[33,44] Strain in epitaxial films is both efficiently transferred and very uniform, allowing for better characterization.[33]

A piezoelectric (PE)/FM heterostructure is a popular choice in designing magnetic heterostructures, as it allows for finely tuned voltage control of the strain and thus the magnetic properties, which is desirable from an electronics application standpoint. Control of various magnetic properties, such as the magnetization,[45,46] magnetic anisotropy,[26,47] and magnetic domain formation have been shown. Piezoelectric strain can also be used to tune magnetic phase transitions,[48] even in materials which do not undergo corresponding SPTs. Strain in PE/FM heterostructures have been shown to be able to influence domain wall formation[49] and dynamics[50,51] as well as magnetic vortex states.[52,53]

However, a heterostructure between a material that undergoes an SPT with a ferromagnet offers an attractive avenue for exploration. Here, the SPT takes the place of the piezo effect, where the intrinsic strain of the SPT can be transmitted at the interface of the heterostructure and influences the magnetic properties of the ferromagnetic layer via inverse magnetostriction. One benefit of using an SPT material are the variety of stimuli that can be used to trigger the transition. SPTs have been induced using applied electromagnetic fields,[54,55] heat,[14,56,57] femtosecond laser pulses,[58,59] and strain.[60,61] This could be desirable for applications such as Heat Assisted Magnetic Recording (HAMR). The abrupt change in properties localized near T_c (or equivalent for alternative stimuli) also make them attractive in switching applications, as well as for a strongly nonlinear response. SPTs are also able to generate relatively large strains and are tunable via doping.

The canonical SPT material is the ferroelectric perovskite $BaTiO_3$ (BTO), which undergoes multiple structural phase transitions as a function of temperature.[57] BTO is also a suitable substrate for many interesting magnetic systems ($La_{1-x}Sr_xMO_3$,[45] $La_{1-x}Ca_xMO_3$,[62] Fe_3O_4,[63] Fe,[64] $CoFe_2O_4$,[65] among others). Above 130 °C it has a cubic lattice structure. As the temperature is decreased, it transitions to a tetragonal structure until 0 °C, then to an orthorhombic structure from 0 °C to -90 °C, and finally to a rhombohedral structure. BTO heterostructures utilizing its SPT have been shown to tune magnetization,[45,63,64] transport,[66,67] spin reorientation,[68] magnetic anisotropy,[62,69] coercivity,[63] magnetic transition temperature,[66] and colossal magnetoresistance.[45,70] It has even been used to modify the MSPT of FeRh films at −90 ℃ due to interfacial strain caused by the orthorhombic to rhombohedral SPT of the BTO substrate.[61,71,72]

1.2 Metal to insulator and structural phase transitions in vanadium dioxide

The first discovery of a MIT in the vanadium oxides was by Morin in 1959.[14] Ever since, this family of materials has offered a rich system of physics to explore. While the focus of this thesis is on VO_2, many of the others in the family of vanadium oxides show MITs as well. Figure 1 shows resistance vs. (inverse) temperature for various VO_x compounds belonging to the so-called Magnéli family of homologous phases. Inset are the various critical temperatures T_c for the MIT, and the magnitude of the resistivity change at T_c. VO_2 is unique in that its transition temperature (T_c) is both above and reasonably close to room temperature at ~340 K in bulk VO_2. It also shows a relatively large change in the resistivity at 5 orders of magnitude at T_c.

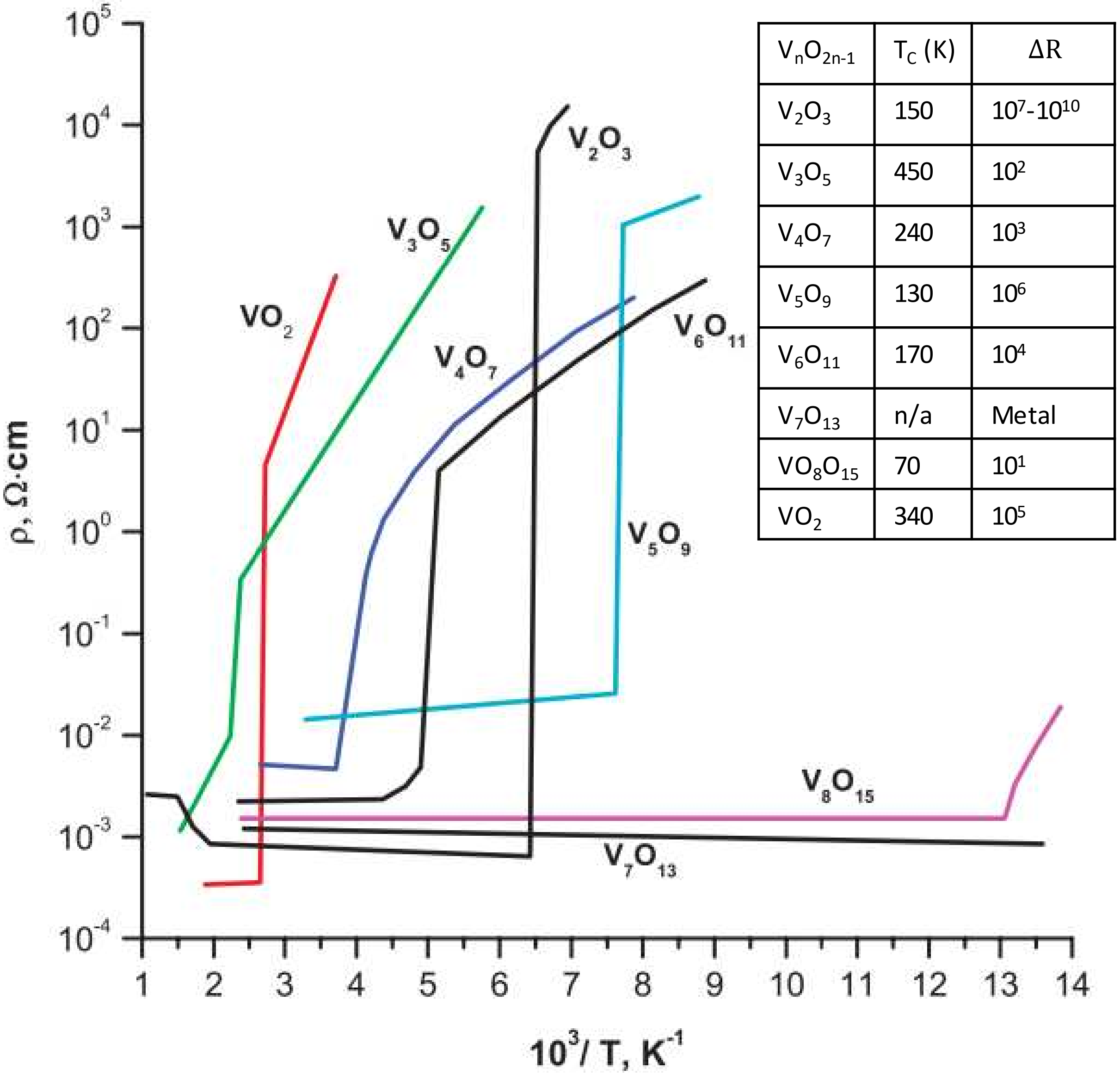

V_nO_{2n-1}	T_C (K)	ΔR
V_2O_3	150	10^7-10^{10}
V_3O_5	450	10^2
V_4O_7	240	10^3
V_5O_9	130	10^6
V_6O_{11}	170	10^4
V_7O_{13}	n/a	Metal
VO_8O_{15}	70	10^1
VO_2	340	10^5

Figure 1. Resistance vs. (inverse) Temperature for various vanadium oxides. (Inset) Summary of the critical temperature and magnitude of the resistance change in units of $\Omega \cdot$ cm across the MIT of the listed oxides. Figure and table reproduced from Ref.s [73,74], see reference for original data.

The Magnéli phases are characterized by a stoichiometric formula V_nO_{2n-1}, where n is an integer number from 2 to 9.[75,76] V_9O_{17} is only metastable, and integers above 9 have not been seen and are considered unlikely.[77] This corresponds to the series being bracketed by V_2O_3 for

$n = 2$, and VO_2 for $n > 9$ (formally, $n = \infty$). Oxygen deficient VO_2 films with reported stoichiometry $VO_{1.9319}$ are generally mixes of various Magnéli phases.[78,79] In addition to their chemical similarity and the presence of MITs, the materials in this series share a number of related properties. This includes crystal structures that can be formed from blocks of rutile and corundum structures of VO_2 and V_2O_3 respectively.[80] Increasing n corresponds to a change in valency states from 3 to 4, and the formal V 3d charge changes fractionally from 2 to 1. With the exceptions of VO_2 and V_7O_{13} the family also shows an anomaly in magnetic susceptibility across the MIT with decreasing temperature that resembles a paramagnetic to AF magnetic transition. Interestingly, in some cases the long-range order does not set in until a lower temperature than the MIT T_c.[78] V_7O_{13} has no transition as previously mentioned, whereas VO_2 does not show a magnetic transition unlike the other oxides in the family nor does it seem to show long-range ordering even at low temperatures. Instead, VO_2 is paramagnetic both above and below the transition,[81–83] although there is a noticeable change of roughly a factor of 8 in the magnetic susceptibility across the MIT from approximately $1 \times 10^{-6}\ \frac{\mathrm{Am^2}}{\mathrm{kg}}$ to $8 \times 10^{-6}\ \frac{\mathrm{Am^2}}{\mathrm{kg}}$. The magnetic susceptibility only shows a slight anisotropy and is relatively insensitive to temperature away from the MIT, with only slight decreases with increased temperature when above T_c.[83]

A similar but less well studied family, the Wadsley phases,[84] with formula V_nO_{2n+1} also exhibit MIT properties (not shown), with VO_2 as the lower end and an upper bracket of V_2O_5 ($n = \infty$). VO_2 is situated as the bridge in between these two series. Figure 2 shows an abridged phase diagram for the VO_x family, with VO_2 highlighted in red. The figure focuses on the rich phase space provided by the homologous series due to their interesting properties and stoichiometry close to VO_2. A more complete phase diagram including lower O concentrations and higher temperatures of the full V-O system can be found in Ref. [77]. The overall narrow region in the phase diagram corresponding to VO_2 means that synthesizing pure VO_2 is challenging. Small deviations in chemical composition can lead to impurities of phases which will degrade the quality of the VO_2 transition.

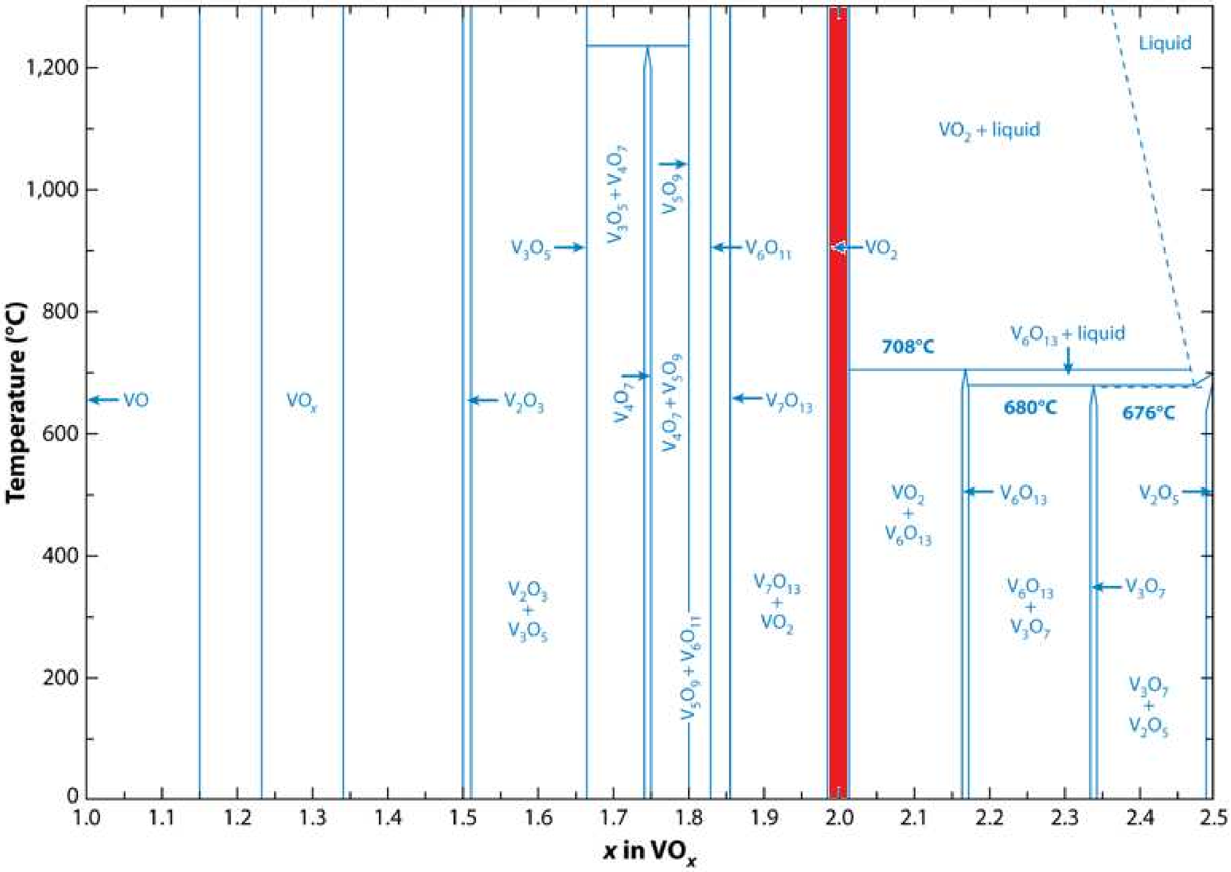

Figure 2. Phase diagram of vanadium oxides. The VO_2 region is highlighted in red. Graphic from Ref. [85], originally produced in Ref. [86].

Figure 3 shows many typical transition metal oxides that undergo MIT. VO_2 stands out, as the next closest candidates are at ~250 K or ~400 K, even outside the VO_x family. The combination of being both above yet close to room temperature is ideal for use in practical applications, particularly in electronics. VO_2 has been suggested as a strong candidate for field effect transistors,[87,88] oscillators,[89] and temperature[90] or chemical[91,92] sensing. A side effect of the MIT are changes in the optical properties of VO_2, which would be useful for metamaterial[93,94] or thermochromic[95] applications. VO_2 is also relatively stable although over time it will decay into the more energetically favorable V_2O_5 over the course of a few months if exposed to air.[96,97]

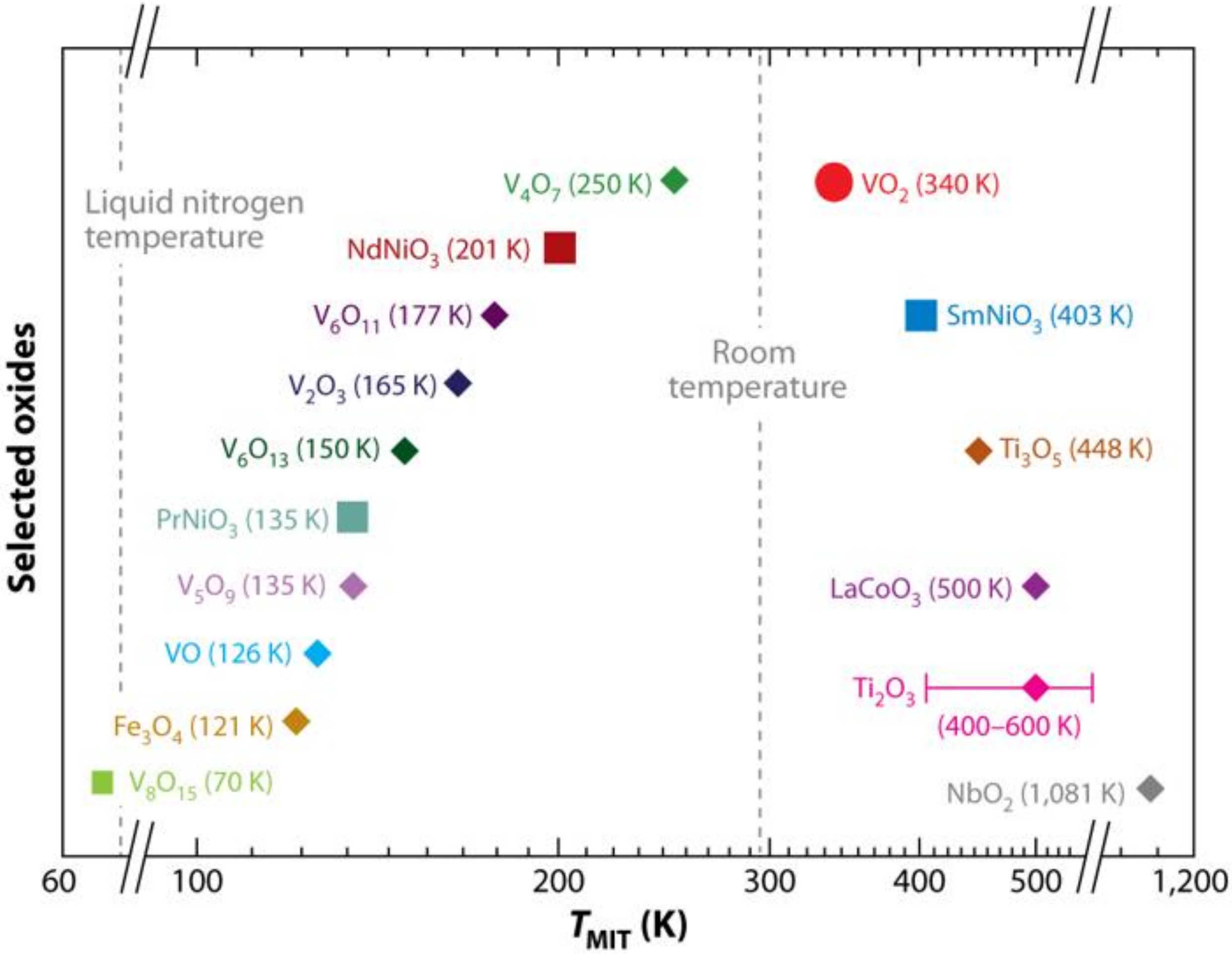

Figure 3. MIT critical temperatures for various oxides. Reprinted from Ref. [85].

The MIT is characterized by a 5 orders of magnitude change in the resistivity in high quality single crystal VO_2 with a thermal hysteresis of 0.5-1 K.[98,83] In thin film form, clamping effects from the substrate tend to reduce the magnitude of the transitions, but 4+ orders of magnitude is still achievable with an appropriate choice of substrate.[99] Even poor substrates such as Si or glass can still show a ~3 orders of magnitude transition.[100,101] A typical example of a resistivity measurement of a thin film VO_2 is given in Figure 4. Despite the MIT moniker, the resistivity of VO_2 is closer to a semiconductor below T_c and a poor metal above T_c. While the VO_2 transition is often induced thermally, it has been shown that a number of different external stimuli can induce the transition, including voltage/current,[54] femtosecond laser pulses[58], and applied pressure.[60,102]

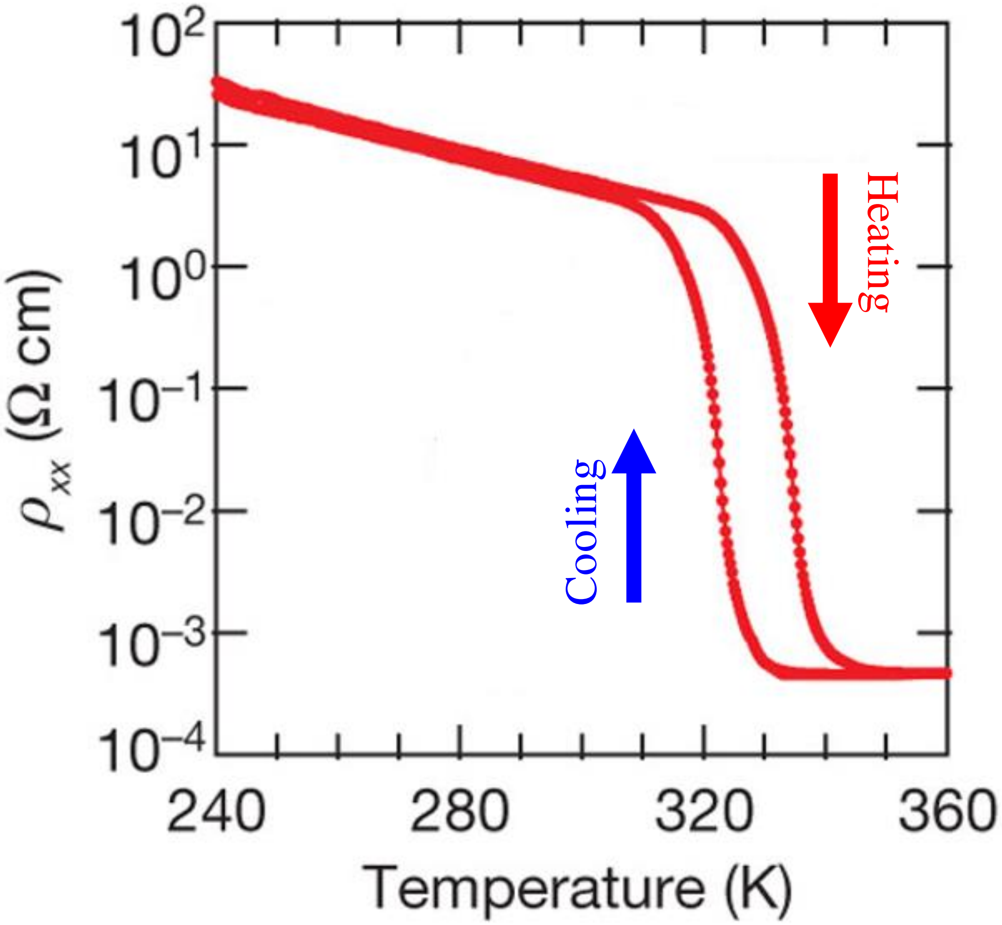

Figure 4. R vs. T for a typical 70 nm VO_2 film on TiO_2 substrate. Slightly modified from Ref. [103].

The intrinsic critical temperature (T_c) for the VO_2 transition occurs around 340 K. Both the onset of the transition as well as the width of the hysteresis are sensitive to the quality of the VO_2 as well as the underlying substrate. A hysteresis width of roughly 5 K is typical in the highest quality thin films, with the transition shifted to higher (lower) temperatures for increasing (decreasing) temperatures. This increased hysteresis is considerably larger than the intrinsic hysteresis seen in single crystals, ascribed to the martensitic nature of the structural transition that accompanies the MIT. The details of the structural transition will be discussed in the next paragraph. The thermal hysteresis of VO_2 thin films is known to be heavily tied to grain size, substrate, thickness of the film, deposition conditions, oxygen content, and twin boundaries.[104–109] The physical origin of thermal hysteresis in VO_2 thin films is still not completely understood but it is thought that the fact that several atoms must move simultaneously allows for substantial supercooling (superheating). This supercooling can be suppressed by defects which allows for easier nucleation of the VO_2 phase, and therefore smaller thermal hysteresis.

A comparison of the R vs. T for 7-20 nm VO_2 films grown by pulsed laser deposition on assorted orientations of Al_2O_3 and TiO_2 substrates is given in Figure 5. Note the roughly 70 K shift in T_c for the various samples, as well as significantly different hysteresis width. Substrates allow for a wide range of tuning of T_c and the thermal hysteresis without large degradation of the transition due to the lattice strain. For example VO_2 on (001) TiO_2 has a T_c of roughly 300 K, with a sharp transition due to the excellent epitaxial relationship.[110] Additional tunability can be achieved via doping, where atoms that are larger (smaller) than the V atom systematically cause a decrease (increase) in T_c. W or Cr are particularly popular.[111] W provides the largest decrease in T_c while maintaining a strong MIT, at $\Delta T_C = -22\ \frac{K}{at\%}$ due to both its larger size relative to a V atom and an extra electron.[112] Cr doping acts to increase T_c , but can stabilize various alternate

VO_2 crystal phases.[113] Control of oxygen nonstoichiometry using methods such as ionic liquid gating,[110] or growth conditions[86] can also influence T_c and thermal hysteresis width.

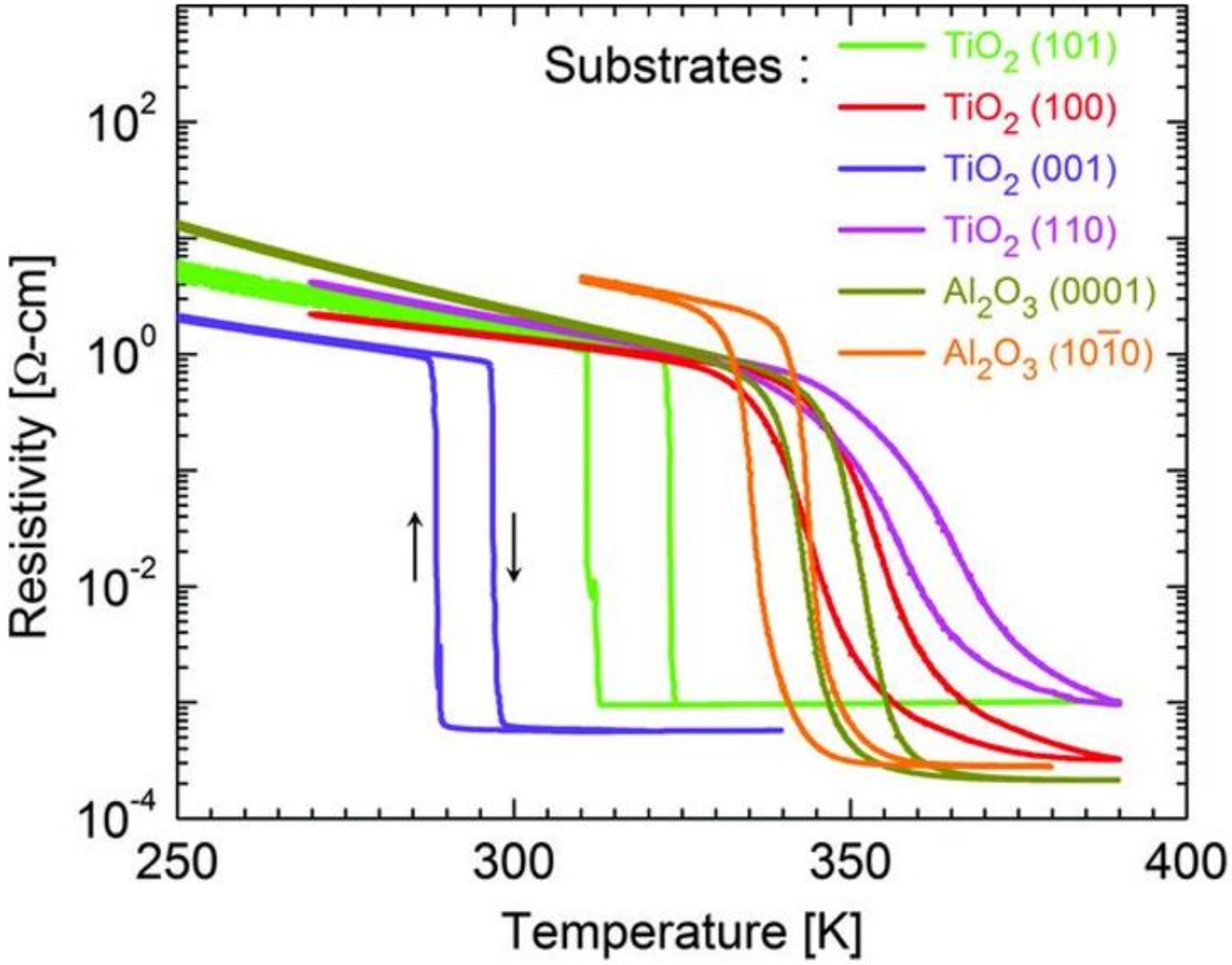

Figure 5. R vs. T for 7-20 nm VO_2 films on various orientation of Al_2O_3 and TiO_2 substrates. Reproduced from Ref. [110].

Concurrent with the MIT, VO_2 also undergoes a structural phase transition (SPT) from a low temperature monoclinic (M1) phase, to a high temperature rutile (R) phase. This occurs via a lattice distortion along the c-axis of the rutile structure with decreasing temperature. The vanadium atoms dimerize and cant slightly, while the overall length of the c-axis increases by ≅ 1%. The a and b axes also change length, leading to a net volume change of ≅ 0.044%.[114] The

M1 phase belongs to the $P2_1/c$ space group,[115] and the rutile to $P4_2/mnm$.[116] The two different crystal structures are shown in Figure 6. The reduction in symmetry leads to a doubling of the unit cell, as well as the opening of an optical bandgap of ~0.6-0.7 eV.[117,118]

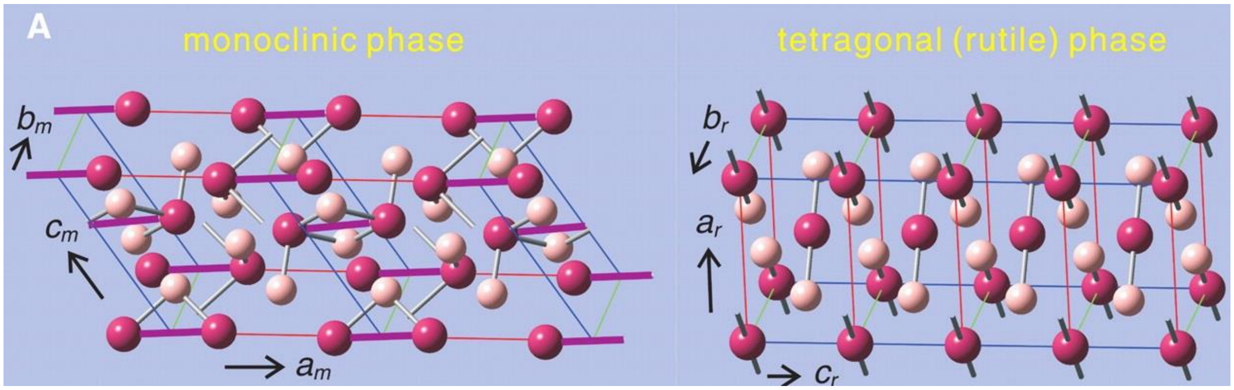

Figure 6. (left) Crystal structure of the low temperature monoclinic phase of VO_2. (right) High temperature rutile phase. Reprinted from Ref. [119].

The exact mechanism behind the VO_2 MIT is still under hot debate. A number of models have been proposed that are able to capture aspects of the MIT with varying success. To date, however, they all stumble in comprehensively capturing the broad range of features present across the transition. Historically, the leading candidates in the discussion have been whether it is a Mott-Hubbard phenomenon, Peierls, or spin-Peierls type. Fundamentally, this comes down to whether electron-electron interactions (Mott-Hubbard),[120,121] electron-phonon interactions (Peierls),[122,123] spin-phonon interactions (spin-Peierls)[124,125] or some combination[126] drive the transition. The search is complicated by the difficulty of modeling strongly correlated electron systems, as well as the lack of a clear empirical ‘smoking gun’.

A crystal field model proposed by Goodenough was able to qualitatively capture changes in the electronic band structure close to the Fermi energy (E_F).[127] In the rutile structure, the density of states at E_F is composed of partially filled $d_{||}$ orbitals as well as a π^* antibonding orbital, shown schematically in Figure 7 (right). This leads to the metallic state. In the monoclinic structure, there is a splitting of the $d_{||}$ orbitals due to the V-V dimerization. The pi* shifts to higher energy due to the canting of the V atoms away from c_r. The $d_{||}$ orbital becomes completely filled, while the $d_{||}^*$ and π^* shifts completely above E_F and are empty. These shifts leave the density of states empty at E_F, shown schematically in Figure 7 (left). The basic feasibility of this model was later confirmed by simulations.[128] This model is an example of the Peierls view, where the structural changes drive changes in the band structure and thus the MIT.

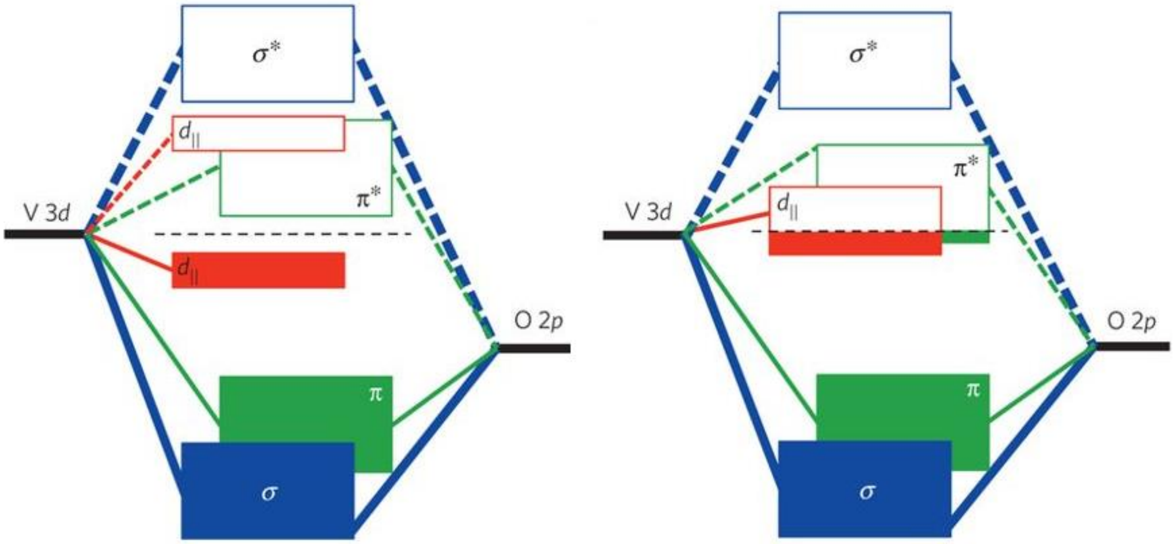

Figure 7. Schematic view of the band structure of (left) M1 VO_2 and (right) (R) VO_2. The dashed line represents the Fermi energy E_F. Reprinted from Ref. [129].

The Goodenough model received renewed interest and attention after a first principles molecular dynamics and resulting band structure study by Wentzcovitch et al. seemed to suggest that a Peierl's type transition was the dominant driving mechanism.[130] This study reignited the interest in the Mott-Hubbard or Peierls driving mechanism in the VO_2 transition, and debate has been vigorous ever since.

Despite the success of band theory to capture aspects of the VO_2 transition, it is not clear whether a single-electron-style model truly captures the physics behind the transition. Electronic structure calculations, particularly density functional theory using the local density approximation (LDA) or generalized gradient approximation (GGA) reinforce many of the parts of Goodenough's qualitative model. However, these models consistently fail to capture the optical band gap that should open up when using reasonable parameters. Experimentally, this gap has been confirmed to be ~0.6-0.7 eV in size. This failure is typical of LDA and is not unique to the VO_2 system. Zylbersztejn and Mott also pointed out that any gap that did open in this type of model would be quite small.[131]

Another complication to the Peierls viewpoint arises when considering other various phases of VO_2, particularly the M2 phase. The M2 phase of VO_2 is an insulating monoclinic phase, which can be stabilized by a small uniaxial stress or doping with very small amounts of Cr.[113,132] There is a continuous transition from the M2 to M1 phases via an intermediate triclinic phase with decreasing temperature. The low level of doping, strain, or temperature required to stabilize the phase implies that the M2 phase is likely an intrinsic phase of VO_2 at a local minimum. In the M2 phase, instead of all of V-V chains pairing and twisting, they become alternating chains. Half of the chains will pair but not twist, and the other half will twist but not pair. The unpaired chains contain a localized conduction d electron due to electron-electron correlations, a hallmark of a Mott-Hubbard insulator. These chains act as spin $\frac{1}{2}$ one dimensional Heisenberg chains making the M2 phase magnetic, in contrast to the paramagnetic M1 phase.[132,133] The M1 phase can be considered as a superposition of both M2 chains in each chain. The fact that the M2 phase is a Mott-Hubbard insulator therefore seems to strongly suggest that M1 may be as well.[121] This interpretation is further reinforced by the similarity of the band gap and electronic structure of the M1, M2 and triclinic phases despite the different structures.[134] Many theoretical studies, including Wentzcovitch et al. never considered this phase explicitly, which raised some questions regarding the validity of their model. Theoretical studies now often explicitly consider the M2 phase as a way to test the robustness of their models.[135]

Hybrid models which selectively include electronic correlations are overcoming the deficits in the pure DFT-LDA/DFT-GGA models. Calculations by Eyert are shown in Figure 8.[135,136] On the top left, the band structure of rutile VO_2 is shown, mapped to symmetry points shown in bottom left. The typical LDA manages to capture the essential features of the rutile phase and the augments required to model the other VO_2 phases do not significantly change the result. The top right figure shows the calculated band structure using the generalized gradient approximation (GGA), augmented by a Hartree-Fock exchange term. Again, the symmetry points are shown in the bottom right for the monoclinic structure. The improvement in agreement upon adding electron correlations is a compelling sign that electron correlations cannot be neglected in order to properly model the VO_2 MIT, although modified functionals might allow band theory to capture the essential features. However, while the results regarding the band gap are much improved, these hybrid models often still struggle to capture both the band gap as well as the proper magnetic state for monoclinic VO_2, often mistakenly predicting an AF regime. Investigations are still ongoing into models that can capture both features.[137]

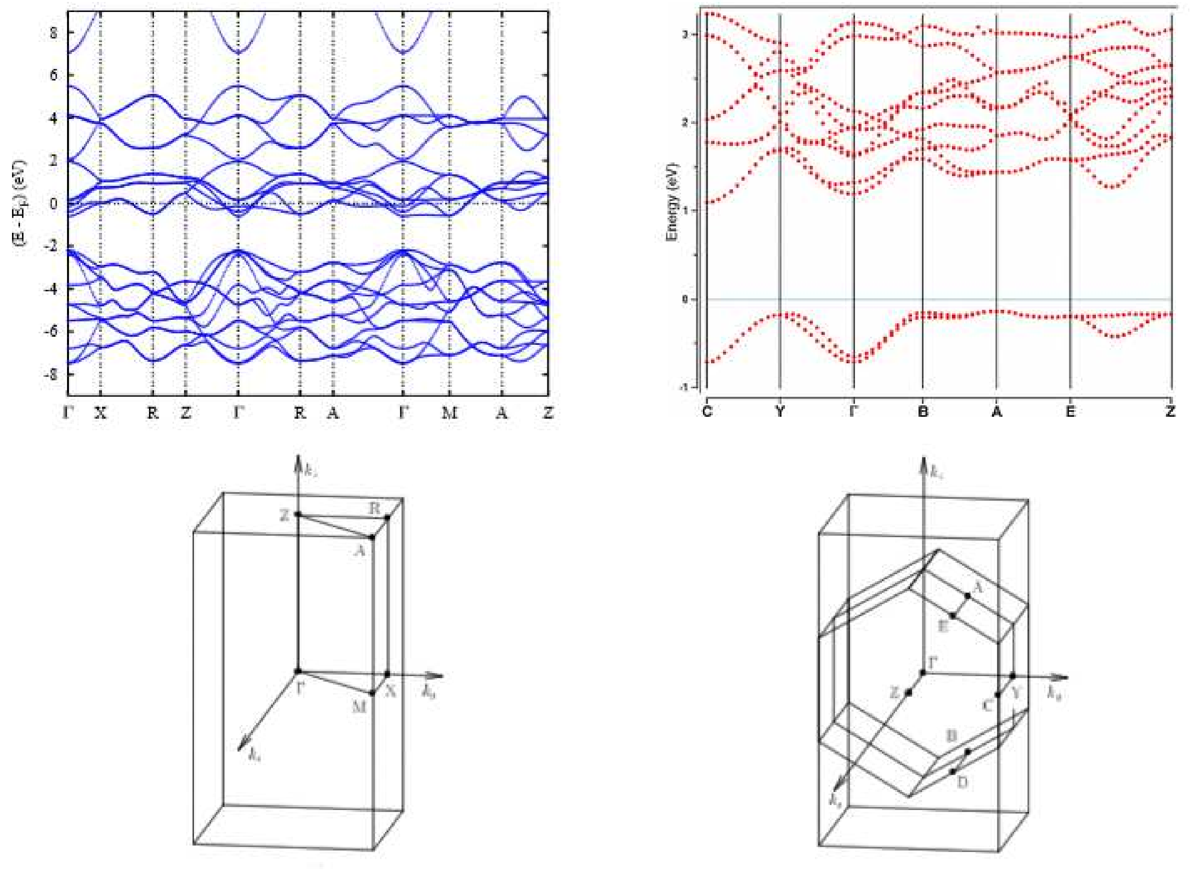

Figure 8. (Top left) band structure for rutile VO_2, using the LDA approximation in DFT. (Top right) band structure for monoclinic VO_2, which uses a hybrid GGA functional with corrections via Hartree-Fock exchange. (Bottom left) Schematic indicating symmetry points in the rutile unit cell. (Bottom right) Schematic indicating symmetry points in the monoclinic unit cell. Reproduced from Ref. [135,136].

The above discussion approaches the VO_2 MIT from a theoretical perspective, but experimental methods have been used to probe the MIT as well. Experimentally, photoemission spectroscopy (PES) and in particular angle resolved photoemission spectroscopy (ARPES) is a way to directly access the band structure of a material. PES techniques are an extremely common way of characterizing VO_2, and ARPES would seem to be a very powerful tool for clarifying the debate over the band structure of VO_2 in both phases. However, to date, ARPES spectra for VO_2 are relatively rare which has been attributed to the difficulty in obtaining chemically stable cleavage planes in VO_2 single crystals. Progress is being made in using thin films instead,[138–140] which are much more robust than their single crystal counterparts. VO_2 on TiO_2 (001) have an epitaxial relationship and can show the required smoothness. A full mapping hasn't been completed, but initial results show a rough agreement in overall features with calculations such as the ones by Eyert in Figure 8.

Another experimental approach is to image the VO_2 transition dynamically, using various pump-probe techniques. Optical pump-probe as well as optical pump- X-ray probe have been used to successfully characterize various ultrafast phenomena in solid state systems.[141] The VO_2 transition is ultrafast, on sub picosecond timescales to fully completely the transition.[58] A consequence of the sub-ps time scale is that fully characterizing the transition is difficult, even with modern ultrafast techniques.[142] Cavalleri et al. found transition happens in ~80 fs, with the MIT being bottlenecked by the SPT despite ultrafast hole injection. [143] These time scales for the SPT for the photo-induced transition must be from coherent phonon reactions, rather than thermalization.[58,144] More recently, a transient phase of VO_2 phase was identified, a metallic monoclinic (mM) phase.[144–146] This phase is a transient metallic, yet correlated, monoclinic phase that was inaccessible before femtosecond scale pump probe experiments. Rather than the direct M1 to R transition as originally assumed, the transition is a mixture of an initial fast hole driven Mott-Hubbard transition to the mM state and a slower but still sub-80 femtosecond structural transition to the R state. Alternative measurements such as ultrafast PES and electron diffraction studies have also confirmed this mM phase.[147–149] Other studies have also seen structural dynamics even after the transition to the rutile structure, that last on the order of ~100 ps.[119,150,151]

While there is not yet a consensus, the most recent literature seems to point towards both mechanisms being significant contributors.[152] What is clear is that there is still plenty of further research needed on both experimental and theoretical fronts to clarify the exact nature of the VO_2 transition.

1.3 Magnetostructural Phase Transition in FeRh

The initial discovery of intermetallic alloy FeRh and its unusual AF to FM phase transition was made in 1938 by Fallot,[56,153] who showed that bulk FeRh under certain conditions undergoes a phase transition near T_c= 350 K. Further studies revealed this transition to be a magnetostructural transition (MSPT), or metamagnetic transition. At T_c, the FeRh goes from a low temperature AF state to a higher temperature FM state with saturation magnetization change from 0 $\frac{\mathrm{Am^2}}{\mathrm{kg}}$ to 120 $\frac{\mathrm{Am^2}}{\mathrm{kg}}$ (H_{app} = 500 mT).[154] The transition to a FM state with increasing temperature is unusual, as typically FM order arises with decreasing temperature. Above T_c, the magnetic properties behave as a normal FM, with slowly decreasing magnetization as a function of increasing temperature and a Curie temperature of 670 K where it goes from FM to paramagnetic (PM) with a magnetization of 0 $\frac{\mathrm{Am^2}}{\mathrm{kg}}$ in a second order transition.[155] An M vs. T profile across both the MSPT and Curie temperatures is given in Figure 9. Concurrent with the magnetic phase transition is a SPT, the details of which will be given momentarily along with the crystallographic details.

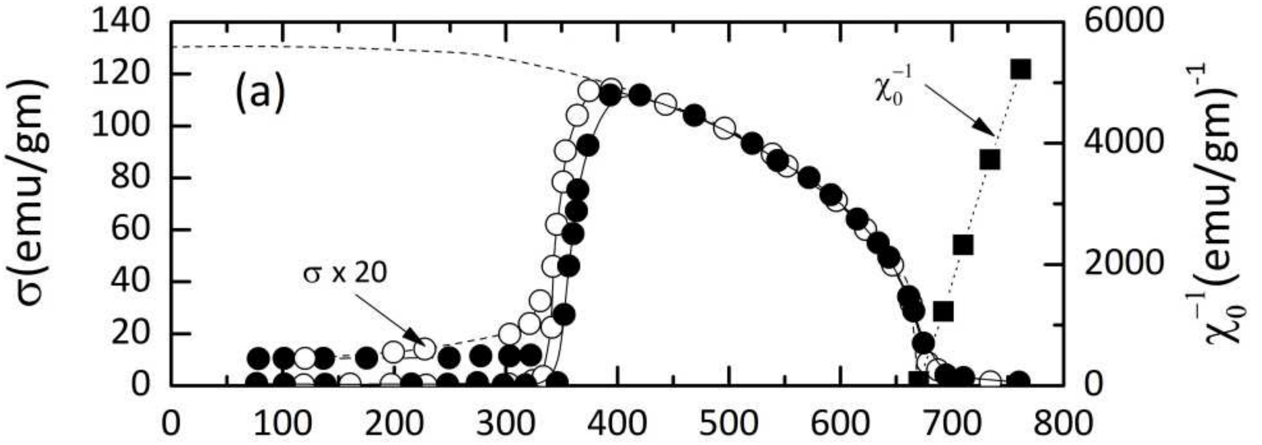

Figure 9. M vs. T of $Fe_{48}Rh_{52}$bulk from 77 K to 770 K. Reprinted from Ref. [6], original work done in Ref. [155].

Below T_c, AF FeRh has the CsCl (B2 ordered) crystal structure, with lattice parameter $a \approx 2.988$ Å.[56,153,156] The CsCl structure corresponds to two simple cubic structures for each atomic species being interleaved with each other, resulting in a net BCC type structure. As the temperature is increased, FeRh undergoes the MSPT, leading to an increase in the lattice parameter of 0.3% in each direction.[157] The change in lattice parameter, as measured by X-ray diffraction, is shown in Figure 10 (Bottom). The SPT involves the same expansion along each lattice vector, leading to an isotropic $\sim 1\%$ volume increase without a change in crystal symmetry or structure.[156] The crystal structure for both phases is shown in the top of Figure 10, with the addition of the magnetic moments in each phase. In the AF phase, the Fe atoms are arranged in a G-type configuration with a moment of $\sim 3.2\ \mu_B$ each, and the Rh has no moment due to cancellation of the exchange fields by the neighboring Fe atoms.[158] In the FM phase, all of the Fe atoms with moment $\sim 3.04\ \mu_B$ align, and the Rh gains an induced moment of $\sim 0.9 - 1\ \mu_B$ due to exchange interactions with the Fe.[154] These values are in rough agreement with first principle band structure calculations.[159]

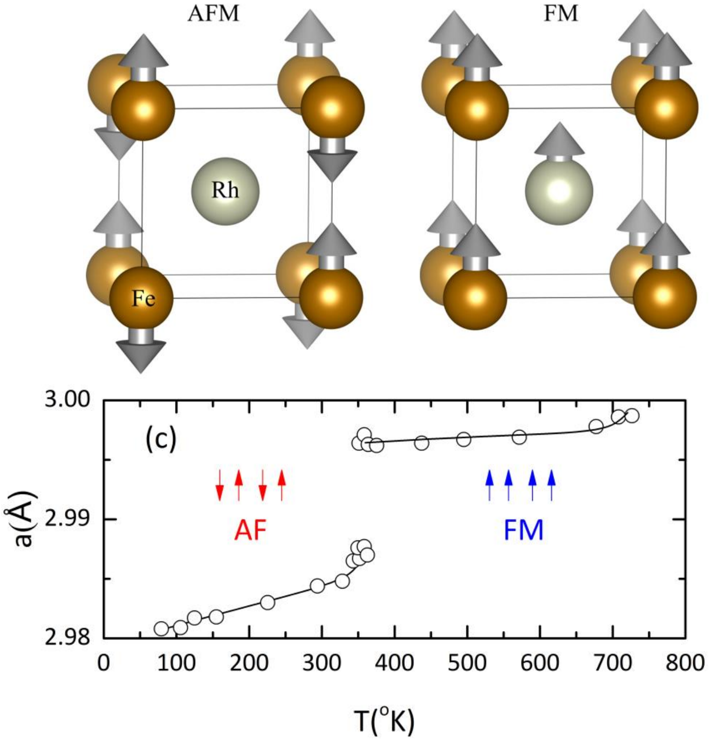

Figure 10. (Top left) CsCl crystal structure for αFeRh below T_c, with emphasis on the G-type AF order in the Fe atoms. (Top Right) CsCl crystal structure for αFeRh above T_c, with emphasis on the FM ordering.[160] (Bottom) Lattice parameter as a function of temperature across the FeRh transition. Reprinted from Ref. [6], original work done in Ref. [157].

FeRh alloys have 5 major stable equilibrium phases depending on the atomic percentages and temperature. An abbreviated phase diagram as a function of temperature and Fe concentration ($Fe_{1-x}Rh_x$, $0.20 < x < 0.80$) is given in Figure 11. Not shown is an additional δ phase that is BCC and PM as well as an α phase which is a low temperature FM BCC phase. Each phase is labeled with its magnetic state as well as associated crystal structure. The phase transition originally identified by Fallot is shown in the diagram as α″ to α′ phase. Notably, the transition is localized in a very narrow region to equiatomic FeRh, in the range $0.48 \leq x < 0.52$ for $Fe_{1-x}Rh_x$. With increasing Fe concentration, T_c monotonically decreases until eventually it is completely suppressed.

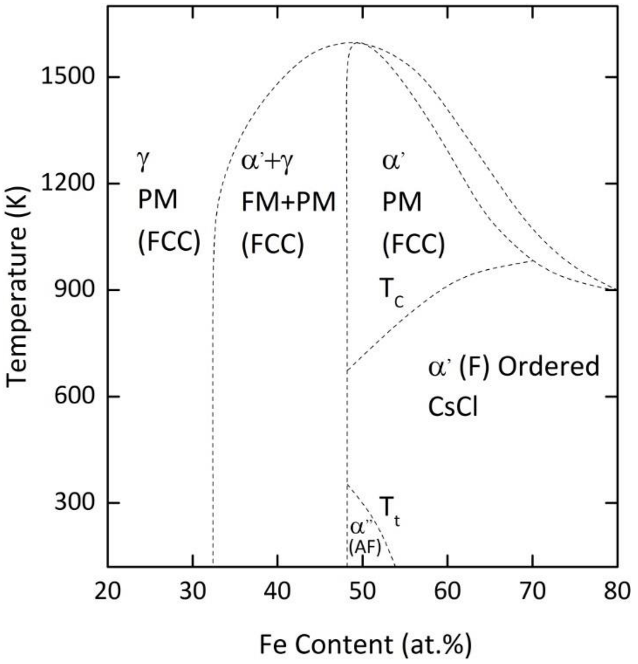

Figure 11. Phase diagram for the $\mathrm{Fe_xRh_{1-x}}$ system for $20 < x < 80$. Reprinted from Ref. [6], original work done in Ref. [161].

The FeRh MSPT is a first order transition with a latent heat of $2.2\ \frac{\mathrm{kJ}}{\mathrm{kg}}$.[162] The large latent heat is accompanied by a correspondingly large total entropy change $\Delta S = 138\ \frac{\mathrm{mJ}}{\mathrm{cm^3\ K}}$.[55] Specific heat measurements are able to decompose the magnetic, electronic and lattice contributions to the total entropy change. Cooke et al. obtained values $\Delta S_{\mathrm{tot}} = \Delta S_{\mathrm{magnetic}} + \Delta S_{\mathrm{electronic}} + \Delta S_{\mathrm{lattice}} = 17 \pm 3\ \frac{\mathrm{J}}{\mathrm{kgK}}$, with $\Delta S_{\mathrm{magnetic}} = 43 \pm 9\ \frac{\mathrm{J}}{\mathrm{kgK}}$, $\Delta S_{\mathrm{lattice}} = -33 \pm 9\ \frac{\mathrm{J}}{\mathrm{kgK}}$ and $\Delta S_{\mathrm{electronic}} = 8 \pm 1\ \frac{\mathrm{J}}{\mathrm{kgK}}$, respectively for FeRh thin films.[163] Not only is the magnetic contribution the largest, the signs indicate that the magnetic and electronic contributions drive the transition, whereas the lattice contribution stabilizes the AF phase, in agreement with free energy calculations.[164] Concurrent with the MSPT is a resistivity decrease of ≈ 30 % from the AF to FM state.[155]

Akin to VO_2, the exact mechanism and details behind the FeRh transition is something which is under hot debate. Several theoretical models have been proposed. One of the original proposed models was Kittel's exchange inversion,[165] where the exchange is a function of the lattice parameter in such a way as to switch signs at some distance. However, this model does not agree with experimental measurements of the entropy and elastic constants.[157,164,166] In addition, it does not account for the role of the Rh atom which goes from 0 moment to developing some nonzero moment above T_c. Another proposed model argues for a pseudogap opening at the Fermi level in the AF state due to Slater splitting of the d-band.[167] Ultraviolet PES experiments did not observe much change in electronic structure in 10 monolayer FeRh single crystals,[168] whereas X-ray PES with a penetration depth of 20 unit cells did register a clear difference that matched with DFT calculations.[169,170] More recent proposals usually focus on the Rh atom having a strong role in determining the overall magnetic state of the system.[171] One model by Gruner et al. has AF Fe-Fe interactions competing with FM Fe-Rh interactions to produce a transition driven by thermal instability of the competing $\sim 0\ \mu_B$ and $\sim 1\ \mu_B$ Rh states.[172] Work by Mryasov and then later refined by Barker and Chantrell takes a similar approach, but the change in Rh magnetic state is driven by interactions with the exchange fields of the Fe moments rather than thermal instabilities.[173,174] The Rh moment is not modeled directly, but instead is taken into account by mediating a higher order non-Heisenberg effective exchange term to the Fe-Fe Hamiltonian, which is able to reproduce a phase transition via competition between the Heisenberg and non-Heisenberg terms.

Ultrafast spectroscopy experiments have helped elucidate some of the details of the dynamics of the FeRh transition. An experimental study utilizing the magneto-optical Kerr effect (MOKE) in a pump-probe set up showed that the magnetic transition occurs on a ≈ 500 fs timescale.[59] The phonon driven lattice expansion begins at 1 ps, is largely complete at ≈ 10 ps, and stabilizes at ≈ 50 ps.[59,175] An additional MOKE study was able to clarify that the latter 2 timescales correspond to two different regimes by comparing to simulations solving Landau-Lifshitz-Gilbert equations.[176] The initial 10 ps corresponds to nucleation of various local FM domains in an AF matrix, as magnetic moments align.[177] Element sensitive XMCD shows that the ratio of Rh and Fe site magnetizations stays constant as they grow proportionately.[177,178] While there is a net average moment in the film, the Zeeman energy isn't strong enough to uniformly align all of the domains, and therefore they are not aligned with each other. A complementary MOKE and XRD study showed that these magnetic domains randomly align along 4 different directions, as expected for the cubic symmetry of the crystal, with a preference along the direction that coincides with the applied magnetic field.[179] In addition, the XRD results directly confirmed the timescale of the structural domains to be the same as the local magnetic domains.[179,180] The longer 50 ps timescale corresponds to these local magnetic domains eventually aligning with each other to form a single domain state due to exchange forces and domain wall motion when these domains come into contact with each other. Ultimately the dynamic behavior is the combination of local moment behavior, nonlocal domain growth and later alignment, with a precession caused by variable demagnetization fields during the transition. Further studies using a variety of ultrafast techniques found strong agreement with this nucleation model but disagree on the timescales involved. Some report the previously mentioned sub-ps dynamics,[59,175] while others report a process on a 30 ps[176] or even hundreds of ps scale.[177,179,180] To date it is not yet clear what the cause is for these discrepancies, and there is a heated debate on how to interpret these conflicting reports. Several potential confounding factors have been proposed, including varying beam size, fluence, transient optical artifacts in MOKE, varying heat sinks, and sample thickness.[179–181] In particular, these measurements are all bulk measurements, so a varying beam size or sample microstructure may determine whether the signal is averaged over a few domains or many.[179] This might make the signal more sensitive to the domain nucleation or alignment process rather than the initial local FM generation.

More recently the magnetic transition evolution was mapped out spatially using XMCD, albeit with only a 50 ps time resolution.[181] Preliminary results agree with the bulk averaged time scales for nucleation, as well aspects of the lateral magnetic nucleation spread being tied to the speed of sound of the material and therefore structural aspect of the transition.[179,180] However the poor temporal resolution and lack of structural sensitivity limit the information that can be extracted from these measurements. Improvements in these areas should allow for a better observation and understanding of the nucleation dynamics of the FeRh magnetostructural transition on ultrafast timescales.

In the mid 1960's, Lommel showed that FeRh could be produced in thin film form.[182] The material is extremely sensitive to growth conditions, but high quality FeRh on epitaxial substrates are able to almost entirely maintain the magnetic and structural properties of the MSPT. An example of an M vs. T curve for 110 nm FeRh on MgO substrate is given in Figure 12 (top left). Below T_c = 370 K, the FeRh is in the AF state. Typically, there is a small but measurable remanent FM moment on the order of $\sim 50\ \frac{\mathrm{A}}{\mathrm{m}}$, which is attributed to an interface stabilized FM state.[183–185] The shift in T_c from 350 K to 370 K is attributed to the in-plane compression (out-of-plane expansion) due to the epitaxial mismatch of 0.27% between MgO and FeRh. Substrate clamping effects also lead the transition to act more anisotropic, with the in-plane lattice expansion smaller as compared to out of plane. Above T_c, the FeRh maintains an

$M_{sat} = 1120\ \frac{A}{m}$, in good agreement with bulk values. Top right shows the same M vs. T in the heating branch for various applied magnetic field strengths. The applied field acts to stabilize the FM phase and therefore reduce T_c without otherwise distorting the M vs. T profile. A similar effect is seen in the cooling branch. The bottom left panel shows another M vs. T profile, this time with an Al_2O_3 substrate. Here, the substrate provides a tensile in-plane stress, which shifts T_c to lower than 350 K. The bottom right panel shows a typical hysteresis loop for the MgO sample during the transition. The distinctive wing shape of the loops corresponds to the applied field shifting T_c enough to transition portions of the film back to the high temperature FM phase. Accordingly, a smaller field is required at 380 K to do so than 360 K.

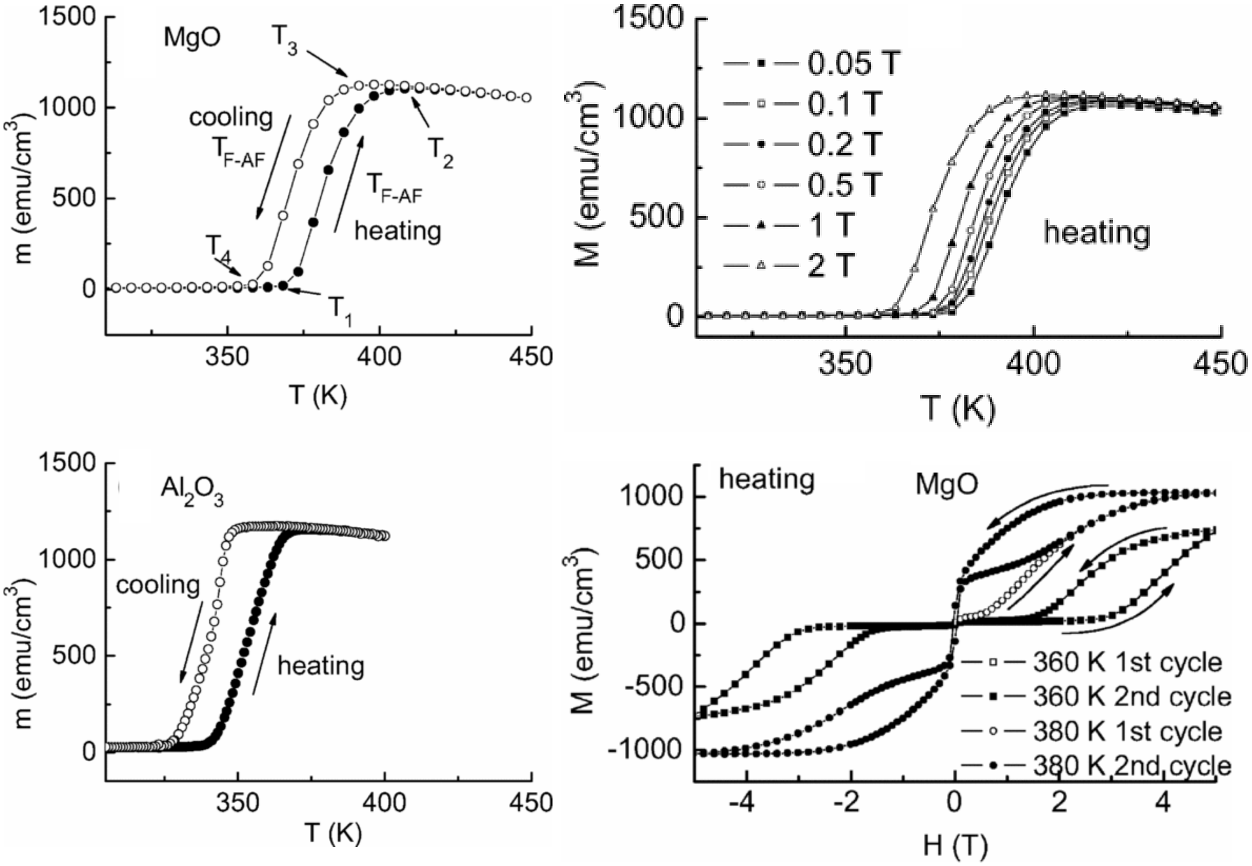

Figure 12. (Top left) M vs. T for a 110 nm $Fe_{49}Rh_{51}$thin film on MgO (001) substrate. (Top right) M vs. T of $Fe_{49}Rh_{51}$ on MgO for various applied magnetic fields. (Bottom left) M vs. T for a 110 nm $Fe_{49}Rh_{51}$thin film on Al_2O_3 (001) substrate. (Bottom right) Sample hysteresis loop for the $Fe_{49}Rh_{51}$ on MgO substrate. Reproduced from Ref. [186].

FeRh thin films show an interesting behavior for out of plane measurements, as shown in Figure 13 (left). In the in-plane configuration, the demagnetization field of an FM grain with strength $4\pi M_S$ acts to stabilize its neighbors. In the out-of-plane configuration, the demagnetization field acts to destabilize neighboring grains, as shown in Figure 13 (Right). The first order nature of the nucleation thus leads to a pronounced asymmetry in the M vs. T profile. A mean field correction term removes most of this asymmetry, with slight deviations where the mean field approximation is poor. This corresponds to temperatures of roughly 320 K in the cooling branch and 330 K in the heating branch, respectively. At these temperatures, the sample contains significant portions of both AF and FM phase, inhomogenously

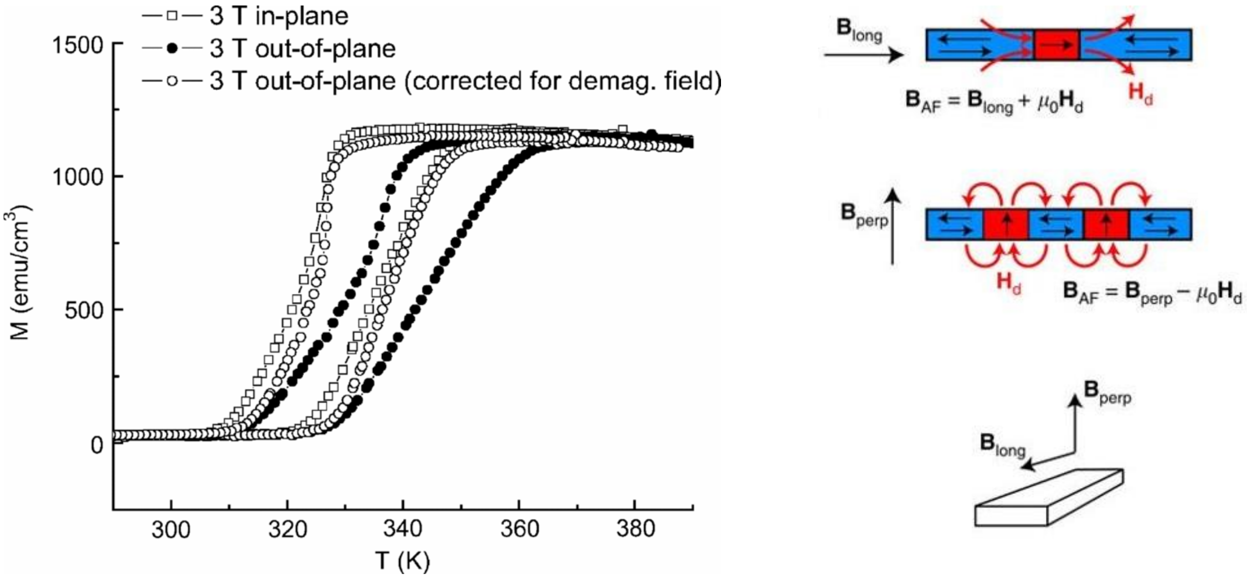

Figure 13. (Left) M vs. T for a 110 nm $Fe_{49}Rh_{51}$thin film on Al_2O_3 (001) substrate for both in plane and out of plane configurations. (Right) Schematic showing effect of demagnetization field by a FM grain. Reproduced from Ref. [186] and Ref. [187] respectively.

Due to the coupling between the lattice and magnetic states, MSPT can be triggered via a number different stimuli beyond temperature, including an applied magnetic field,[55] hydrostatic pressure,[157,188] strain,[71,186] and photoexcitation.[59] T_c has also proven to be highly tunable via Fe to Rh ratio,[189–191] doping by other metals,[55,188,192] growth conditions,[190,193,194] and choice of substrate in thin films.[186,195] In the case of an applied magnetic field, the critical temperature decreases by 8-9 K per Tesla and remains linear in the measured region, up to $\sim \pm 6$ T.[55,186] For an applied pressure the change is again linear, with a relation $\frac{dT_c}{dP} = 55\frac{K}{GPa}$ for pressures up to 2.5 GPa, with the sign depending on whether tensile or compressive pressure is applied.[188]

FeRh has been proposed as a candidate material for a variety of applications. A rather large entropy change is found when the material crosses it's MSPT. This also leads to a giant magnetocaloric effect, with a temperature change $\Delta T = 12.9$ K in adiabatic conditions under a 2T field.[196] This is competitive even with the best magnetocaloric materials for magnetic refrigeration applications. Indeed, it is the largest magnetocaloric effect known to date. The irreversible nature of the transition due to the large hysteresis and accompanying hysteretic losses has been a hurdle for adoption in devices.[71,197,198] More recently, it has been suggested that FePt/FeRh bilayers, where the FeRh can act as an exchange spring, may be useful for thermally assisted magnetic recording applications.[199] Memristor designs that take advantage of the anomalous magnetoresistance effect of AF FeRh have also been proposed,[200] and FeRh has relatively low intrinsic damping with a Gilbert damping constant $\alpha \cong 0.0013$, making it a potentially interesting material in spintronics.[201] However, a large hurdle to more widespread study and adoption into technology is the prohibitive cost and scarcity of Rh.

1.4 First Order Phase Transitions and Phase Coexistence

The phase transition of VO_2 is fundamentally a first order transition, using the Ehrenfest classification. It exhibits a latent heat of ~1020 cal/mol, and a corresponding entropy change of 3 cal/mol°C.[83,202] One important consequence is that both the monoclinic and rutile phases can then coexist at some specific temperature due to inhomogeneities in the sample. High quality single crystals switch abruptly, with a near discontinuous change in resistivity. But thin films will have inhomogeneities due to grain structure, slight variations in grain stoichiometry, point defects, etc. This leads to a slight smearing out of the transition over a range of temperatures as in Figure 4. The transition is still quite sharp but smoothed out in comparison to single crystal R vs. T measurements.

Qazilbash et al. showed this phase coexistence in VO_2 experimentally, shown here in Figure 14.[203] The top of Figure 14 shows nanoscale x-ray diffraction images of a 1.2 micron by 1.7 micron region, where the detector was sensitive to the slight change in the Bragg peak from 29.58 ° for the monoclinic (200) to 29.92 °, which correspond to the (101) rutile plane. By following this peak shift, they were sensitive to the structural phase transition with 15 nm resolution. The bottom of Figure 14 shows scattering scanning near field infrared microscopy (sSNIM) images. The sSNIM technique is sensitive to the dielectric function of a material, and thus sensitive to the different optical constants of the two phases.[204] It has a similar resolution of ~15nm. Both techniques show the same overall story as the temperature is varied. At low temperature (roughly 330 K in the figures), the sample is in the monoclinic insulating phase. As the temperature increases, portions of the sample transition and there is nucleation of regions of metallic rutile phase. Additional increases of the temperature transition larger portions of the sample, until it's fully in the metallic rutile phase at 360 K. This experiment thus demonstrates coexistence of both phases of VO_2 near T_c.

In addition, Qazilbash et al. show that the MIT and SPT may be decoupled in a very narrow region near T_c, adding further complication to understanding the VO_2 transition. Comparing the two measurements in Figure 14 shows a difference in how the phases spread through the transition. More surprising still, the nano-XRD imaging shows regions that nonmonotonically transition. That is, some regions which transition to the rutile phase transition back to the monoclinic phase, despite the elevated temperature. These regions only become rutile once the temperature is further increased. Their experimental setup has temperature stability of 0.05 K, and the authors argue this is not due to thermal instability. The sSNIM images show that metallic regions do not display this nonmonotonic behavior. Once a region becomes metallic at a given temperature, it stays metallic. The authors give further support by noting the resistivity, which should be sensitive to regional conductivity differences in their sample, is monotonic as well, in agreement with the sSNIM results. Further discussion of this behavior is beyond the scope of this thesis but is worth mentioning as it further complicates the discussion in the previous section of whether the VO_2 transition is Mott-Hubbard or Peierls type. However it may be consistent with a stabilized transient metallic monoclinic (mM) phase near T_c.[205] While it is not a direct analog, a decoupling between the MIT and SPT of the related V_2O_3 system, indicates it may be possible in other correlated systems such as VO_2.[206]

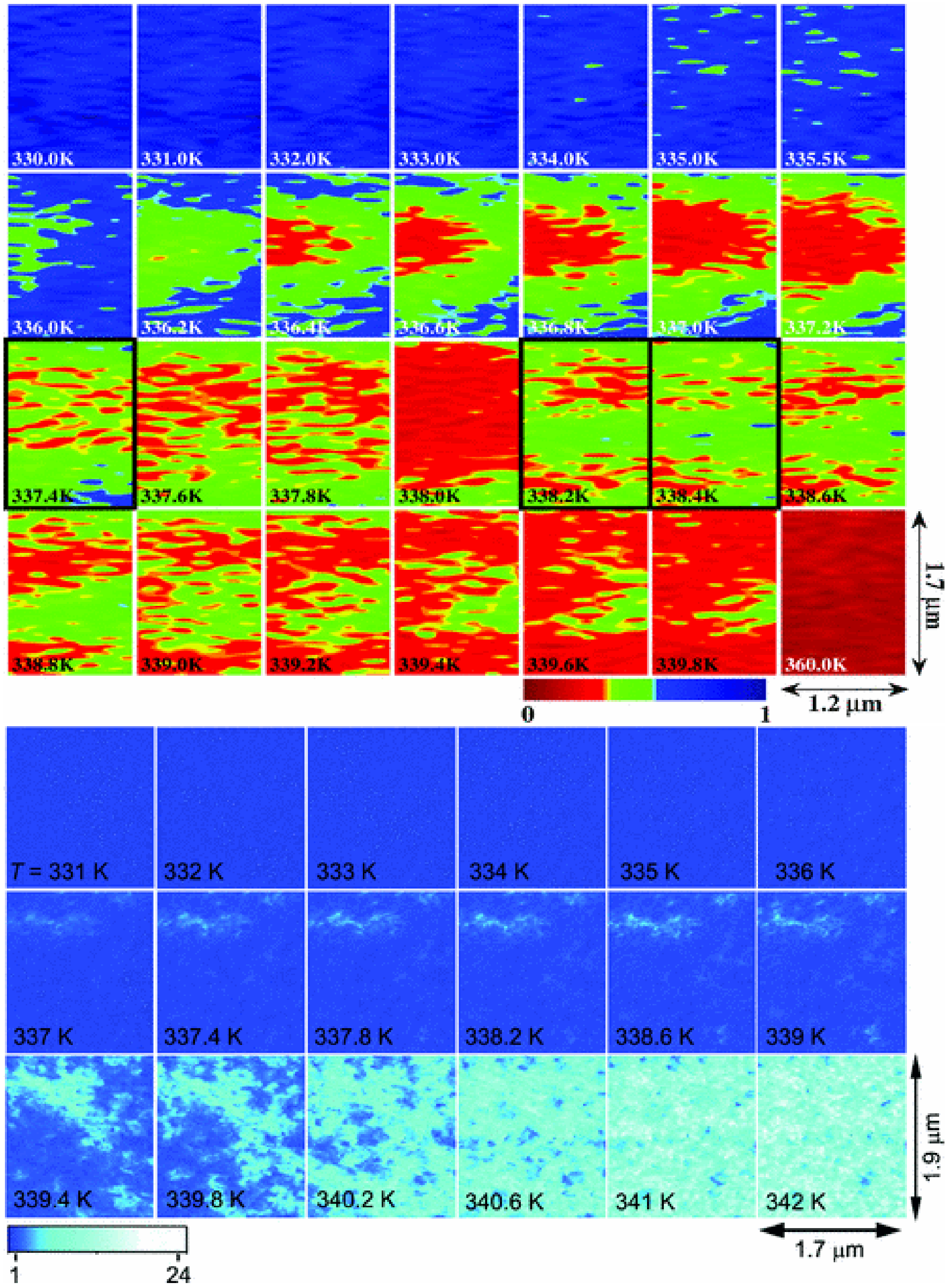

Figure 14. (Top) Nanoscale XRD of a VO_2 film, utilizing the shift from the 29.58 ° monoclinic to 29.92 ° rutile Bragg peak across the VO_2 SPT. The detector was set to 29.58 ° and therefore higher intensity (blue) indicates monoclinic phase. Low intensity (red) indicates rutile phase. Green indicates coexistence of both phases within the beam footprint. (Bottom) Nanoscale sSNIM using the third harmonic infrared scattering amplitude, which is sensitive to changes in the optical constants during the MIT. Low amplitude corresponding to the monoclinic (insulating) phase is shown in blue, and high amplitude corresponding to the rutile (metallic) phase is shown in white. Both images use the same sol-gel VO_2 film. Reproduced from Ref. [203].

Following similar arguments as above, FeRh thin films will also show phase coexistence. The technology to image magnetic domains was developed earlier than the methods needed to probe VO_2 , and the FeRh magnetic phase coexistence was first shown using magnetic force microscopy.[207,208] More recently, techniques such as X-ray Magnetic Circular Dichroism (XMCD) and X-ray photoemission electron microscopy (XPEEM) offer unprecedented spatial mapping of magnetic materials, down to nanometer scales. XMCD techniques take advantage of the fact that X-ray absorption depends on the helicity of the incoming radiation, in direct analogy to the well-known magneto-optical Faraday and Kerr effects. XMCD and XPEEM signals are sensitive to the portion of the magnetization along the direction parallel to the beam. The nucleation of the magnetic transition in FeRh has been mapped out in detail using these techniques.[209–211] Keavney et al. were able to combine XMCD/XPEEM measurements along with nanoscale XRD measurements to map both the structural and magnetic parts of the FeRh transition in the same sample. The top of Figure 15 shows results of the XPEEM measurement. Blue and red colors correspond to FM phase that is either parallel or anti-parallel to the incident beam, respectively. The AF phase, with no net moment, shows as a neutral white. At low temperature, the white AF phase is dominant, with some remanent FM phase even below Tc likely due to stabilization by the interface. As the temperature increases, the FM phase begins to nucleate into domains. The bottom of Figure 15 shows complementary nanoscale XRD measurements, done by tracking the roughly 0.3 ° shift in the (002) Bragg peak due to the lattice expansion across Tc. The AF phase is shown in blue, and the FM phase in red. It shows a similar picture to the XPEEM experiment. Below Tc, the film is primarily in the AF phase, with its smaller lattice constant. As the temperature is increased, portions of the film begin to nucleate by transitioning to the FM phase and its larger lattice constant. Both measurements show structural and magnetic phase coexistence very near Tc. Keavney et al. report that the structural transition seems to be consistent between thermal cycles, whereas the magnetic transition is less so. They interpret this to be due to the fact that the structural transition is driven due to local defects in the film, but these defects, while they may pin the initial FM formation, do not effective pin the magnetic structure after percolation is achieved. In addition, they were also able to perform XMCD simultaneously with the nanoscale XRD and show a strong match between the two (not shown, see Ref. [212]). They did not see depth dependence in the XMCD, which they interpret as a sign of the nucleation dynamics occurring in plane, and not strongly influenced by the interfaces.

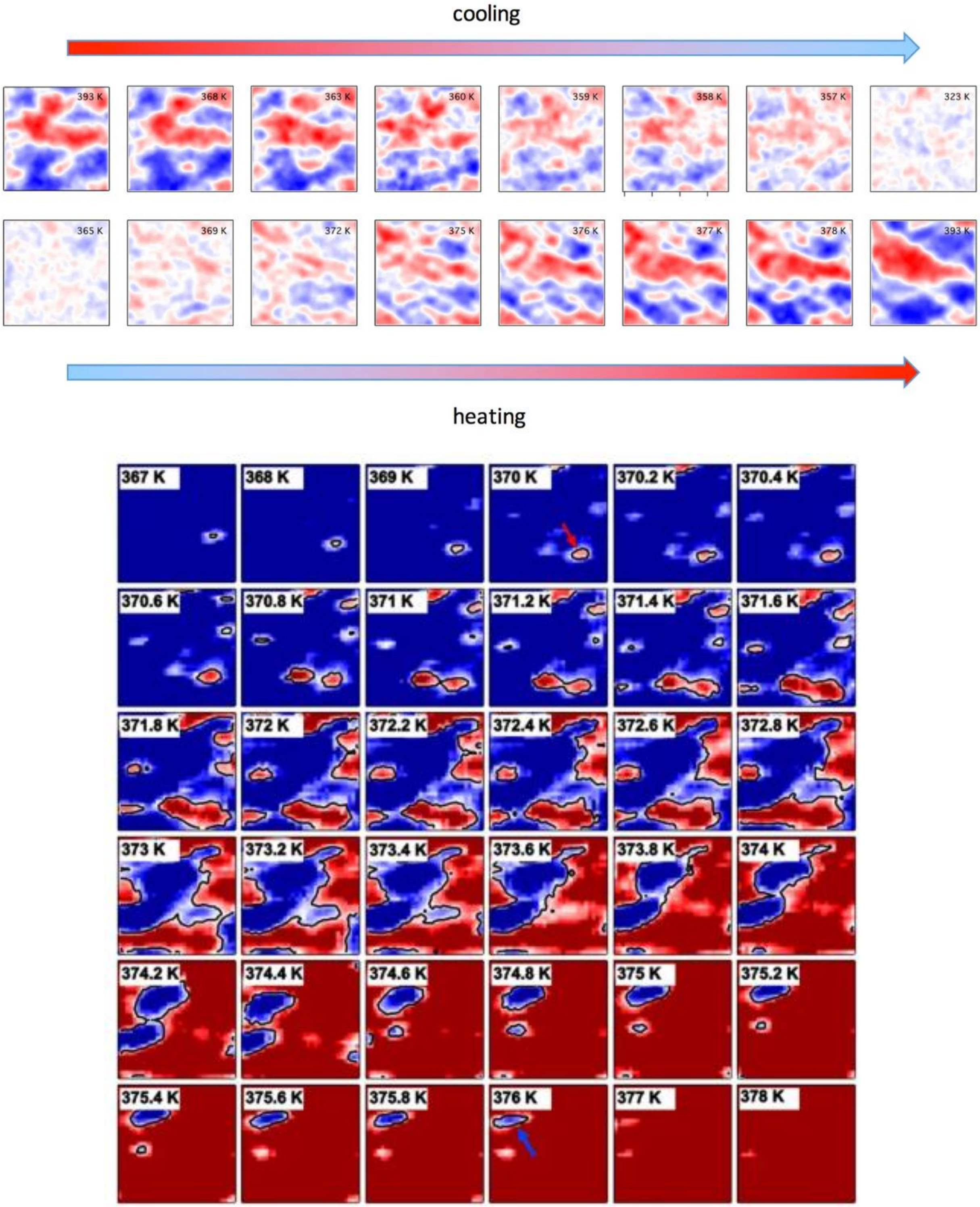

Figure 15. (Top) XPEEM image of 20 nm FeRh (001) on MgO (001) substrate, with resolution of 100 nm x 100 nm. No applied magnetic field. The image size is 4 microns x 4 microns. (Bottom) Nanoscale XRD, with 30nm x 30nm resolution of a 20nm (001) FeRh film on MgO (001) substrate. Blue (red) indicates the below-T_c (above-T_c) phase. No applied magnetic field. The image size is 4 microns x 4 microns. Reproduced from Ref. [212].

The nature of phase coexistence in first order phase transition materials also has implications for changes in various properties across the transition, such as the resistivity. This is issue is particularly acute for the MIT properties in VO_2 nanodevices. As portions of the VO_2 film transition to the metallic state, this leads to avalanches in the resistivity, in a process similar to Barkhausen noise in FMs.[213,214] In order to resolve these jumps, sufficient resolution of the measurement is required. In the case of resistivity, which is a bulk measurement, this implies devices on roughly similar length scales to the metallic and insulating phase domains. This would correspond to the microscale or nanoscale, so that an individual switching event in the sample has a large impact on the device resistivity. While larger devices will show the same behavior, the switching of an individual grain will have a negligible impact on the resistance of the sample and will be smeared out, potentially below the instrumental error. This avalanche type behavior has been seen for VO_2 devices with lateral dimensions 1 micron x 6 microns, shown in Figure 16(left). Eight consecutive R vs. Ts are shown. The overall process is inherently stochastic, due the fluctuations in the order parameter close to a first order phase transition. However, the process can be somewhat deterministic, with local defects that can cause a lower T_c in the nearby material. These defects then act as nucleation sites. In naturally highly textured films, the process can even be effectively deterministic.[215] In the VO_2 films, it was found that 1-3 jumps account for roughly 50% of the resistance change, and the size of these largest jumps scales linearly with inverse device length. The jumps exhibit a power law relationship between the likelihood of occurring and the jump size. V_2O_3 films also show avalanche behavior across their MIT, but with different characteristics, hinting that the driving mechanisms between the two materials' MITs may be fundamentally different.[216]

Avalanches have also been observed in the magnetoresistance of FeRh films patterned into mesoscale stripes, shown in Figure 16(right). Interestingly, the behavior is asymmetric as it was in the XPEEM and magnetization results, due to the differences in the interactions of AF and FM grains.[186,211,217] The stripe patterning serves to enhance this difference due to the fact that FM correlations are robust and long range, whereas AF interactions are much shorter range and sensitive to defects.[187] The cooling branch is characterized by supercooling due to stabilization by the FM interactions. In the heating branch, there are many small avalanche events, indicating a lack of superheating due to the sensitivity of the AF interactions as well as the ability of stabilized FM grains at the interface to act as nucleation sites.

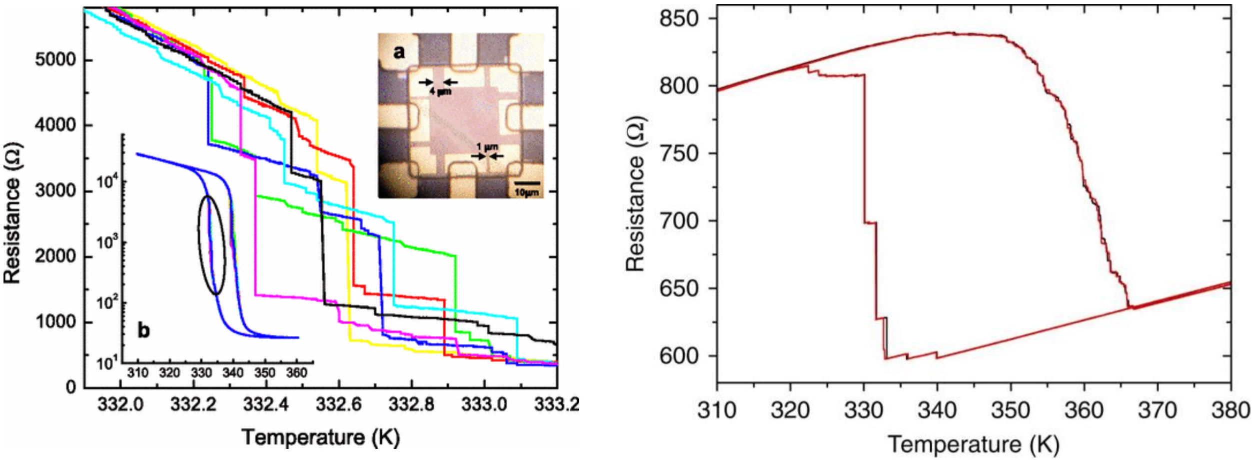

Figure 16. (Left) R vs. T measurement of a 90 nm thick VO_2 film on r-cut sapphire, emphasizing the avalanche behavior during the MIT. The film was 1 micron long and 6 microns wide. Inset a shows the physical device geometry used, while inset b shows the full R vs. T profile. Reprinted from Ref. [218]. (Right) R vs. T measurement of 50nm thick FeRh on MgO substrate, with 0.22 micron width and 2.6 micron length. There is an applied field of 1 T in plane. Reproduced from Ref. [187].

1.5 Magnetostriction and inverse magnetostriction

The normal magnetostriction effect occurs when a material that is exposed to a magnetic field changes size. The original discovery of this effect was made back in 1842, during Joule's work on iron rods. He was able to show that the length of the rods changed under the application of a magnetic field that magnetized the rods lengthwise. In general, longitudinal magnetostriction is characterized by the equation

$$\lambda = \frac{\Delta L}{L} \qquad 1$$

where λ is the magnetostriction coefficient, ΔL is the change in the length of the material along the direction of the applied field, and L is the original length of the material in a demagnetized state also along the direction of the applied field. $\lambda > 0$ indicates an increase in length of the sample, and $\lambda < 0$ a contraction. In addition to the longitudinal magnetostrictive effect, the volume is approximately preserved, such that there will be a corresponding decrease in length in the perpendicular directions. It is worth stressing that in this section, care should be taken when referring to a 'demagnetized' state. In general, this traditionally refers to any magnetic configuration where the net magnetization is 0. In this section, 'demagnetized state' refers to one in which each potential domain orientation is present in equal volume. Not using this so called ideal demagnetized state can lead to significant deviations in measured magnetostrictive quantities.

For transition metal based ferromagnets (Ni, Co, Fe), λ is on the order of $10^{-5} - 10^{-6}$ and can be either positive or negative. For Ni, typical values of λ are $\lambda_{100}^{si} = -46 \cdot 10^{-6}$, $\lambda_{111}^{si} = -24 \cdot 10^{-6}$, and $\lambda_{p}^{si} = -34 \cdot 10^{-6}$, where the subscripts refer to the direction in relation to Ni's crystal axes, and λ_p for polycrystalline Ni. The superscript s stands for saturation magnetization values, and the i indicates the measurement was done from the ideal demagnetized state as discussed earlier. For this work, we take the polycrystalline value. Ni has one of the largest values of magnetostriction for a simple ferromagnet. Rare earth metals with strong spin orbit coupling can have large magnetostrictive constants but are expensive and difficult to obtain at sufficient purity. Giant magnetostrictive compounds such as Terfenol-D ($Tb_xDy_{1-x}Fe_2$, $x \approx 0.3$) and Galfenol ($Fe_{1-x}Ga_x$, $x \approx 18.4$) can have magnetostrictive constants that are 10s to 100s of times larger than Ni but are difficult to synthesize.[219]

Fundamentally, magnetostriction is a direct consequence of spin-orbit coupling. This coupling leads to domain wall motion and particularly domain rotation, rather than changes in the spin moments directly. This spin-orbit coupling also means that along with the magnetostrictive effect, it can also mediate the inverse effect, inverse magnetostrictive effect. The inverse magnetostrictive effect is when an applied stress causes a change in the magnetization of a material. This effect also has several other consequences. For example, the magnetization vs. applied field (M vs. H) curve of a polycrystalline Ni film is shown in Figure 17. The applied stress influences the magnetization at some fixed field, in the case of Ni an increase (decrease) in magnetization for compressive (tensile) stress. But also note that it influences the overall shape of the M vs. H curve changes as a function of the applied field.

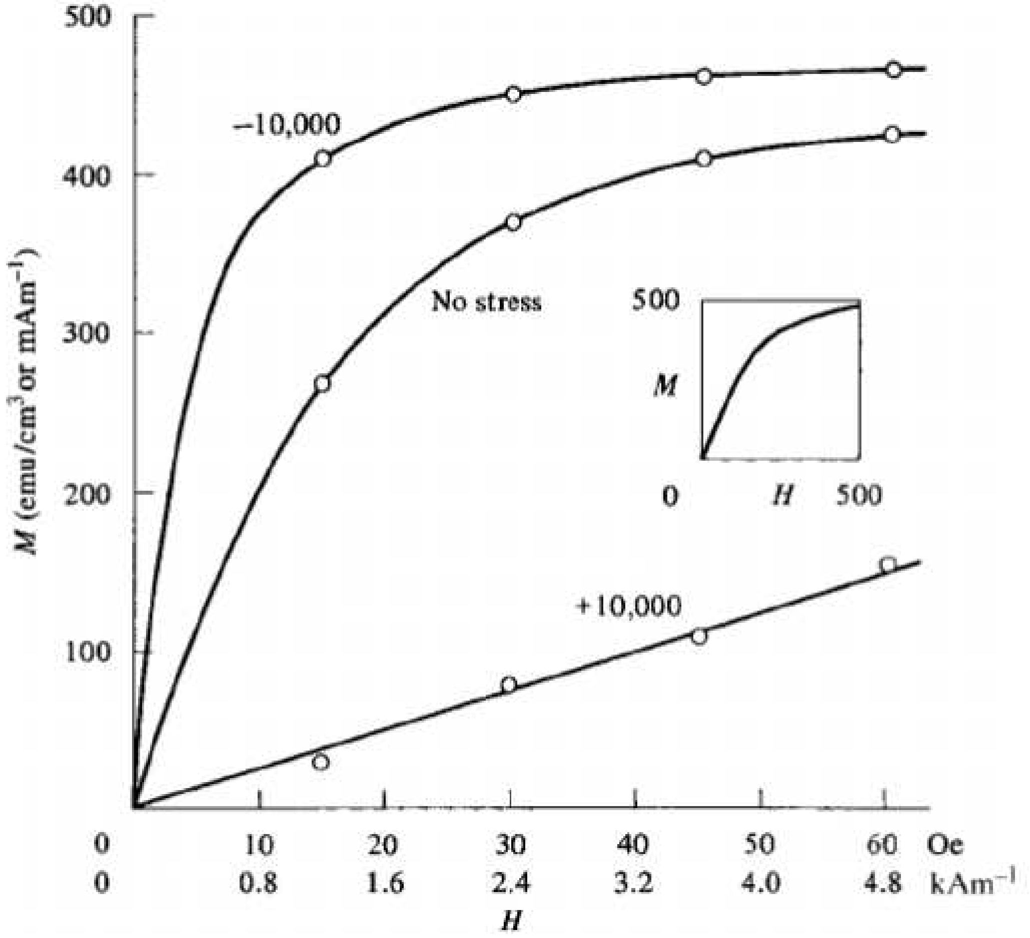

Figure 17. Effect of tensile (+) and compressive (-) stress of the magnetization vs. applied field of a polycrystalline Ni film. Reproduced from Ref. [220], originally unpublished work by D. K. Bagchi.

In addition to the previous effects, there will be an effective induced stress anisotropy. For small deformations, the magnetoelastic energy in general can be expanded in powers of the deformation [221–223]

$$E_{anis} = \sum_{ijkl} K_{ijkl}\varepsilon_{ij}\alpha_i\alpha_j + \ldots \qquad 2$$

where K_{ijkl} are the coupling coefficients, ε_{ij} is the strain tensor, and α_i are the direction cosines of $\overrightarrow{M_S}$ relative to the crystal axes. Keeping the lowest order terms in ε and noting that the cubic symmetry of the crystal will greatly simplify this expression to

$$E_{anis} = -\frac{3}{2}\lambda_{100}\,\sigma(\alpha_1^2\gamma_1^2 + \alpha_2^2\gamma_2^2 + \alpha_3^2\gamma_3^2) \\ -3\,\lambda_{111}\,\sigma(\alpha_1\alpha_2\gamma_1\gamma_2 + \alpha_2\alpha_3\gamma_2\gamma_3 + \alpha_3\alpha_1\gamma_3\gamma_1) \qquad 3$$

where σ is the magnitude of the applied elastic stress, γ_i are the direction cosines for the stress $\vec{\sigma}$ relative to the crystal axes. For a polycrystalline film, it is often reasonable to approximate the magnetostriction as isotropic, i.e. $\lambda_{100} = \lambda_{111} = \lambda_{si} = \lambda_p$. λ_{si} denotes the saturation magnetostriction from an ideal demagnetized state. Eq. 3 simplifies dramatically, into the form

$$E_{anis} = -\frac{3}{2}\lambda\,\sigma\cos^2(\theta_{M\sigma}) \qquad 4$$

where $\theta_{M\sigma}$ is the angle between the magnetization and the applied stress. Utilizing the identity $\cos^2(\theta) + \sin^2(\theta) = 1$ and dropping the constant term, we can rewrite Eq. 4 as

$$E_{anis} = \frac{3}{2}\lambda\,\sigma\,\sin^2(\theta_{M\sigma}) \qquad 5$$

Next, we would like to find an expression for the effective field H due to some applied strain applied perpendicularly to the magnetization. This effective field will move the magnetization some angle θ. The full expression for the energy E is given by

$$E = E_0 + \frac{3}{2}\lambda\,\sigma\,\sin^2(\theta_{M\sigma}) - M_S H\sin(\theta_{MH}) \qquad 6$$

where the first term includes any terms without angle dependence, including the magnetocrystalline anisotropy for a polycrystalline sample. The second term is the magnetoelastic energy from Equation (4), and the final term is the Zeeman energy with θ_{MH} as the angle between the magnetization and applied magnetic field. In the case where the stress is parallel (this approach applies as well for a perpendicular stress with minor changes) to the magnetic field, we can take $\theta_{M\sigma} = \theta_{MH} = \theta$ and minimizing the energy with respect to θ yields

$$\frac{dE}{d\theta} = 3\lambda\,\sigma \sin(\theta)\cos(\theta) - \mu_0 M_S H\cos(\theta) = 0 \tag{7}$$

Eliminating θ and utilizing $M = M_S \sin(\theta)$ brings us to this form for the magnetization M

$$M = \frac{\mu_0 {M_S}^2\,H}{2\,K_\sigma} = \frac{\mu_0 {M_S}^2\,H}{3\,\lambda_{si}\sigma} \tag{8}$$

In the case where $M \approx M_S$, we can solve for the effective stress anisotropy field, relabeled H_σ, as

$$H_\sigma = \frac{3\,\lambda_{si}\sigma}{\mu_0 M_S} \tag{9}$$

The total effective field H_{eff} can be written as

$$H_{eff} = H_{app} + H_\sigma = H_{app} \pm \frac{3\,\lambda_{si}\sigma}{\mu_0 M_S} \tag{10}$$

where the sign of the stress anisotropy field will depend on whether the stress is compressive or tensile. With this expression in hand, we can now estimate the effective field due to an applied stress.

A number of models are able to successfully capture the effects of ferromagnetic hysteresis.[224–227] A mesoscopic mean field model originated by Jiles and Atherthon has proven to reproduce hysteresis curves in good agreement with experimental data.[228,229] In this model, hysteresis arises when domain wall motion is inhibited by pinning sites such as lattice defects.

By statistically averaging over the entire sample, the model maintains a certain simplicity while still fundamentally connecting to the underlying physical nature of the problem. The main insight of this idea of pinning is that the ferromagnetic response can be broken up into two parts, a reversible and irreversible one. The reversible part captures the effects of domain wall bending, which requires no loss of energy. The irreversible part represents the effect of pinning defects, which will hinder domain wall motion and consume energy. For brevity, in the following we highlight only resultant equations relevant to modeling. For a detailed derivation, see Refs. [228,229].

An idealized version of the magnetic response can be well represented by the so-called anhysteretic curve. This curve represents the global minimum energy response, where the domain walls are able to freely move without pinning to a true equilibrium. From this idealized response, in the Jiles-Atherton theory the full magnetization is constructed as reversible and irreversible deviations from the anhysteretic. The anhysteretic $\mathrm{M_{an}}$ is well represented by a modified Langevin function

$$\mathrm{M_{an}} = \mathrm{M_S}\,\mathcal{L}\left(\frac{\mathrm{H_{eff}}}{\mathrm{a}}\right) = \mathrm{M_S}(\coth\left(\frac{\mathrm{H_{eff}}}{\mathrm{a}}\right) - \frac{\mathrm{a}}{\mathrm{H_{eff}}}) \tag{11}$$

where $\mathrm{H_{eff}}$ is an effective field with form $\mathrm{H_{eff}} = \mathrm{H_{app}} + \alpha\mathrm{M}$. The second term is analogous to a Weiss molecular field term, where the parameter α characterizes the strength of coupling between magnetic domains. For Ni, $\alpha \approx 0.004969$.[230] a is a parameter which characterizes the shape of the anhysteretic curve. The theory was later extended by Jiles to include magnetomechanical effects, including an effective stress anisotropy term very similar to the one given above.[231] The model has since been further, with large contributions by Sablik, and is now able to capture features such as the Villari effect.[232–237] The full model is now referred to as the

Jiles-Atherton-Sablik (J-A-S) model and has been widely adopted for modeling magnetic responses to stress. Here, we restrict ourselves to the effective field description given by Jiles, which largely captures the major features we are interested in. The full effective field $\mathrm{H}_{\mathrm{eff}}^{*}$ is then

$$\mathrm{H}_{\mathrm{eff}}^{*} = \mathrm{H}_{\mathrm{app}} + \alpha\mathrm{M} \pm \frac{3\,\lambda_{\mathrm{si}}\sigma}{\mu_0 \mathrm{M}_{\mathrm{S}}} \qquad 12$$

An important property of the anhysteretic is that it is identical for some applied field H and stress σ to the effective field $\mathrm{H}_{\mathrm{eff}}^{*}$ and no applied stress.[231] From the anhysteretic, the full magnetization M can be constructed from the reversible ($\mathrm{M}_{\mathrm{rev}}$) and irreversible ($\mathrm{M}_{\mathrm{irr}}$) components. M can be written simply as

$$\mathrm{M} = \mathrm{M}_{\mathrm{rev}} + \mathrm{M}_{\mathrm{irr}} \qquad 13$$

with $\mathrm{M}_{\mathrm{rev}}$ and $\mathrm{M}_{\mathrm{irr}}$ given as

$$\mathrm{M}_{\mathrm{rev}} = c(\mathrm{M}_{\mathrm{an}} - \mathrm{M}_{\mathrm{irr}}) \qquad 14$$

$$\mathrm{M}_{\mathrm{irr}} = \mathrm{M}_{\mathrm{an}} - k\delta\frac{d\mathrm{M}_{\mathrm{irr}}}{d\mathrm{B}_{\mathrm{e}}} \qquad 15$$

where c is a constant given experimentally by the ratio of the initial ($\mathrm{H}_{\mathrm{app}} = \mathrm{H}_{\mathrm{eff}}^{*} = 0$, and M=0) susceptibilities of M and M_{an}. k is a parameter which characterizes the pinning, being proportional to the number of pinning sites and the average pinning energy. $\delta = +1$ for $\frac{dM}{dH} > 0$ and $= -1$ for $\frac{dM}{dH} < 0$, and ensures the pinning always opposes changes in magnetization. Taking the differential forms with respect to $\mathrm{H}_{\mathrm{app}}$ of Eqn. 14 and Eqn. 15 and plugging them back into Eqn. 13 yields, with some algebraic rearrangement

$$\frac{dM}{dH_{app}} = \frac{1}{1+c}\frac{(M_{an}(H^*_{eff}) - M)}{k\delta - \alpha(M_{an}(H^*_{eff}) - M)} + \frac{c}{1+c}\frac{dM_{an}(H^*_{eff})}{dH_{app}} \qquad 16$$

Conveniently, the first term corresponds to changes in M due to irreversible changes, and the second to reversible ones. The entire equation can be numerically integrated, or each computed separately and added together. Further, it shows that irreversible changes are proportional to the distances from the anhysteretic and vanishes if $M = M_{an}$. This is called the "law of approach". It is closely connected to how the anhysteretic curve can be obtained experimentally. In experiment, the anhysteretic can be obtained by applying a decaying AC oscillation on top of the DC applied field, allowing domain walls to move past pinning sites.

A similar differential equation can be obtained for the change of magnetization as applied stress, and is given as[231]

$$\frac{dM}{d\sigma} = \frac{1}{\epsilon^2}(M_{an} - M_{irr}) + \frac{cdM_{an}}{d\sigma} \qquad 17$$

where $\epsilon = (E\xi)^{1/2}$ is a parameter involving Young's modulus E and a parameter ξ which characterizes the relationship between the derivative of M_{irr} with respect to elastic energy and $M_{an} - M_{irr}$.

The above differential equations can be readily numerically integrated to find how the magnetization evolves under applied field or strain, including hysteresis loops. The model has shown strong agreement with experiment for materials such as steel. For materials like Ni, used here, the inability to capture domain rotation among other difficulties means the model is more qualitative .[238] Therefore, for the work presented in this dissertation it will largely be sufficient to consider the anhysteretic curve, from which we will be able to extract useful information such as approximate values of the strain applied to magnetic thin films.

Chapter 2. Thin film deposition and characterization

2.1 Introduction

Due to their unique properties, the synthesis of high quality VO_2 and FeRh thin films has been an area of intense research. High quality VO_2 films have been successfully grown via chemical vapor deposition,[239] sol-gel,[101] sputtering,[240] pulsed laser deposition,[241], ion beam deposition,[242] e-beam evaporation,[243] and molecular beam epitaxy (MBE).[244] Sputtering is the dominant technique in growing FeRh films,[182] although MBE,[183] electron beam melting[182] and electron gun codeposition[182] has been used as well. While there are many techniques to grow thin films, sputtering enjoys several advantages. It is a relatively simple growth technique while also being easily scalable for industrial use. Despite that simplicity, it can be used to grow extremely high-quality films with good uniformity. Deposition rates can be tuned to grow films from a few nanometers to microns in thickness. The process is also highly tunable, allowing for a wide range of conditions for many different target materials to achieve the desired film properties. For these reasons, we chose sputtering as our growth technique for both the VO_2/Ni and FeRh/Ni heterostructures. While there are many reasons to find sputtering an attractive method for film growth, it also comes with downsides. For example, a target material made up of different atoms such as an alloy or oxide can lead to preferential sputtering of certain atoms rather than maintaining a stoichiometric balance, due to the fact that sputtering rates are specific to the atomic mass. This might require a presputter procedure to allow the sputtered flux to reach a stoichiometric steady state or co-sputtering from separate target materials. Sputtering also lacks some control compared to a technique such as MBE, where the terminating composition can easily be tailored at an atomic level.

Both VO_2 and FeRh phase transitions are highly sensitive to the quality of the film. To ensure the high quality of our films and therefore strong transitions, it’s important to characterize them via several techniques. The main method for characterization for the VO_2 films is resistance vs. temperature (R vs. T) of the film. The MIT’s extreme sensitivity to growth conditions means that even slight changes can lead to varying R vs. T profiles. Growth conditions can affect not only the absolute magnitude of the transition, but also characteristics such as the sharpness and thermal hysteresis width. Care was taken to maintain a 4 orders of magnitude resistive transition. In addition to the R vs. T, the crystalline quality measured from X-ray diffraction (XRD) experiments help to confirm the high quality of the VO_2 films. X-ray reflectivity (XRR) was used to determine the thickness of the films. Atomic Force Microscopy (AFM) allows us to characterize the surface roughness directly, which plays an important role at the VO_2/Ni interface. Once the quality of the VO_2 is confirmed, we are interested in looking at the magnetic properties of the VO_2/Ni heterostructures. A vibrating sample magnetometer (VSM) was utilized for these measurements.

Like VO_2, the FeRh MSPT is highly sensitive to growth conditions, and it is important to verify the quality of the films. The main method to do so was measuring magnetization vs. temperature (M vs. T) using either a VSM or a superconducting quantum interference device (SQUID) magnetometer. Again, the sharpness of the transition as well as the magnitude of the transition is a strong indicator of film quality. The magnetic properties of the FeRh/Ni heterostructures were similarly measured in a VSM or SQUID magnetometer. In order to further study the FeRh/Ni heterostructures, both XRR and polarized neutron reflectivity (PNR) were used. These techniques provide a wealth of information about the exact chemical composition and interfaces between the two materials. PNR also provides information on the magnetic composition, with depth dependence. Details for these techniques is provided in the rest of this chapter, with procedures provided in the appendices.

2.2 Sputtering

Traditional diode sputtering works by utilizing a target material inside a chamber with a gas. Typically, an inert noble gas such as Ar is used as the sputtering gas. A voltage is applied, utilizing the target itself as a negatively biased cathode, and the gun walls as the anode. Stray electrons subjected to this voltage difference will be accelerated and collide with the Ar gas atoms. If the electrons have enough energy, they will knock off an electron from the Ar atom, ionizing it. These ionized atoms form a weak plasma, which leads to a characteristic glow during the process. The negatively charged electrons are pushed away from the negative cathode target, whereas the positively charged Ar atoms will collide with the target. This collision will knock off atoms of the target material, and it is these pieces that ultimately get deposited as the thin film onto the substrate. It will also knock free more stray electrons, creating a feedback loop to sustain the plasma. This simple picture of sputtering leaves out many details, but nevertheless captures the essential parts of the process.

While this diode type sputtering is very effective at growing thin films, there are several improvements that can be made to increase the quality of films. One is the so-called “magnetron” sputtering, where magnets are placed near the target material. An example of magnetron sputtering is shown schematically in Figure 18. These magnets are shaped so that their magnetic fields confine the stray electrons close to the target. This produces two large advantages. Firstly, it reduces the ability of the stray electrons to collide with the substrate. These electron collisions are sufficiently energetic to cause structural damage and heating of the substrate. Secondly, by confining the electrons, the magnetron configuration dramatically increases the chances of collisions between electrons and Ar atoms by orders of magnitude. This greatly increases the deposition rate, while also allowing to maintain the plasma at lower pressures. Typically, the magnets are arranged with one magnetic pole in the center of the target, and a ring of magnets around the edges. These magnets can either be of roughly equal strength (‘balanced’ configuration), or ‘unbalanced’, by making the outer ring of magnets stronger than the center. This ‘unbalanced’ configuration allows for some lines of magnetic flux to not be contained to the target, and some secondary electrons can travel towards the substrate. This greatly increases the ion bombardment rate onto the substrate, which in some cases can improve film quality. The alternative ‘unbalancing’ by making the center magnet stronger than the ring isn’t often studied due to the low deposition rate. One trade off with the magnetron configuration is that sputtering magnetic materials often requires adjusting the magnet configuration. Strongly magnetic materials such as Fe are difficult to sputter. The interaction of the magnetic field of the magnetron and the target tends to lead to shunting and a focusing of the magnetic flux lines. Rather than a smoothly distributed ‘racetrack pattern’, the sputter becomes highly concentrated in a narrow ring region, and can cut through the target, wasting most of the sputter material.

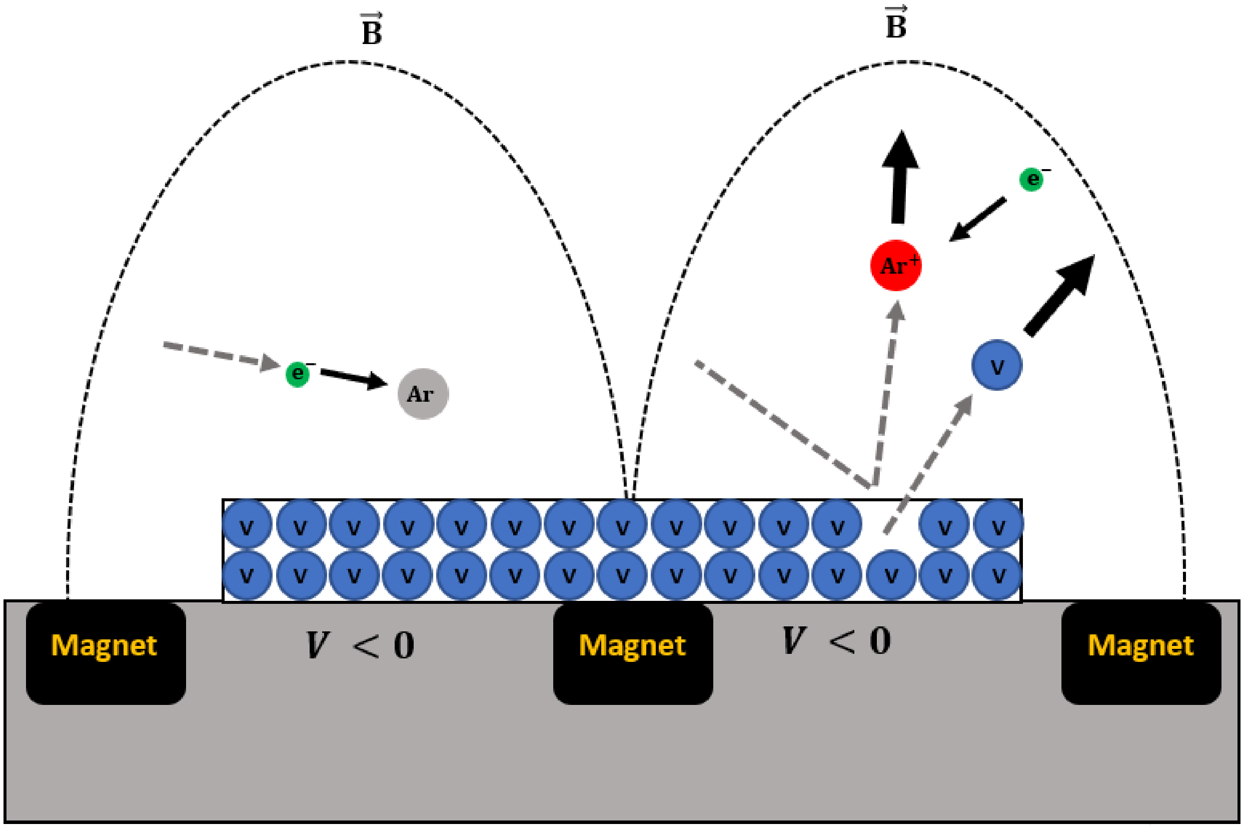

Figure 18. Schematic drawing of magnetron sputtering, with a vanadium (V) target. In our system, the target is 0.25 inches thick and 2 inches wide in diameter.

Another adjustment that can be made is using a radio frequency (RF) applied voltage, rather than direct current (DC). DC sputtering has the disadvantage of requiring current flow to apply the voltage, which means that it is only suitable for metals. Applying an RF voltage allows for the use of insulating targets, particularly oxides and ceramics. This opens up a much larger range of target materials than traditional DC sputtering. However, this flexibility comes with tradeoffs. RF sputtering typically has roughly half the rate of deposition of a comparable DC configuration. In addition, the entire electronic circuit that handles the voltage needs to be specially designed in order handle the RF signal. This requires special shielding of components from each other, as well as tuning capacitors to prevent damaging the power source. Our sputtering system utilizes an automatically adjusting load and tuning set of capacitors in an ‘L’ configuration. The load (shunt) capacitor, consisting of a variable capacitor in series with several fixed capacitors, acts to drive the impedance of the plasma to 50 Ω. The tuning capacitor consists of a fixed impedance inductor in series with a variable vacuum capacitor to nullify the reactance. The matching network is equipped with input sensors to detect the magnitude and phase of the incoming RF signal from the plasma, which then is transformed into a DC steering signal to control servo motors that adjust the variable capacitors. This acts to hold the plasma at 50 Ω resistance and 0 reactance, and thus 0 reflected power.

The last potential modification to the standard sputtering process that we utilize is reactive sputtering. Reactive sputtering works by introducing a reactive gas to the chamber during the sputtering process, typically oxygen. As the sputtered material is traveling towards the substrate, it collides and reacts with the reactive agent, forming some compound. By controlling the ratio of reactive gas to sputtering gas, one can tune the resulting product composition with very high accuracy. Reactive sputtering allows for a wider range of sputtering products, even if a target of the desired compound cannot be easily made. In a similar vein to reactive sputtering, another means of control is cosputtering, where multiple targets of potentially different materials are sputtered at the same time, only reacting together in transit and the substrate surface.

In this work, we utilize reactive RF magnetron sputtering for the VO_2 films. In our experiments, we utilize a pure metallic V target, and rely on reactive O_2 gas to form VO_2. This allows for the precise tuning of the oxygen stoichiometry in the VO_x films. This is particularly important for VO_2 in order to avoid the Magnéli and Wadsley phases. As was discussed in some detail in Section 1.2 and shown in the oxygen concentration phase diagram of Figure 2, there are a number of vanadium oxides which are stoichiometrically very close to VO_2, leaving only a tiny window to obtain pure VO_2 without contaminants. While the target is metallic and could potentially be used in DC mode, the RF ensures a stable sputter if the surface becomes slightly oxidized by the reactive O_2 gas or the target becomes ‘poisoned’. Poisoning of the sputtering target refers to the gettering of the reactive gas by the target material, either by chemical reaction, adsorption, or ion implantation. Poisoning changes the voltage and deposition rate of the target as well as the partial pressure of the reactive gas, sometimes drastically. It can also lead to hysteresis in deposition characteristics when parameters such as reactive gas partial pressure are varied, since there is a competition between the gettering and the sputtering processes. A two-step ‘presputtering’ process prior to film deposition can help to reduce the chance of target poisoning and improve reproducibility between depositions. First, a sputter is performed without the reactive gas introduced to the chamber. This has the direct benefit of cleaning the surface of the target of any remanent oxide but can also improve the initial sputtering rate since oxides often have lower sputtering rates than their metallic counterparts. This improved initial sputtering rate can help avoid a feedback loop where the gettering rate is greater than the sputtering rate. However, it won’t prevent target poisoning if the gettering rate is still greater than the sputtering rate in steady-state equilibrium. A second presputter is then performed with the reactive gas environment to allow the process to come to a steady-state equilibrium, and then the film deposition is performed. By contrast, the Ni and FeRh films are done using DC magnetron sputtering since they are metallic targets in a pure Ar environment. Details of the sputtering procedure are given in the next section and Appendix B (Sputtering Deposition Procedure).

Our system is a commercial Orion system by AJA international which contains 4 sputtering guns with 2 inches diameter, located at the bottom of an ultra-high vacuum chamber arranged in a confocal geometry. The confocal geometry along with a gimble system for each gun allows for flexibility in the incident angle of the sputtered material. For example, off-axis sputtering can improve film quality at the cost of deposition rate. The guns are equipped with pneumatic shutters that allow stabilization of the sputtering plasma without contaminating the substrate surface. At the top and center of the chamber is a rotating substrate holder with an adjustable height along the z axis. The substrate holder consists of a 3 inches Inconel plate rotated at 40 rotations/min to improve uniformity. Heating is provided by 2 lamps located behind a quartz plate, and the temperatures reported here are those recorded by a thermocouple located next to the 2 lamps. The total pressure is maintained by a gate valve in front of the pumping system which automatically adjusts to maintain the setpoint pressure. The partial pressure of each sputtering gas is maintained by 2 separate mass flow controllers, one for Ar and one for O_2 gas.

2.3 Deposition Procedure

In this section, we describe the actual conditions used to deposit the films. The step by step deposition procedure is provided in Appendix B (Sputtering Deposition Procedure). There are two types of films to consider. The first are VO_2/Ni heterostructures grown on Al_2O_3 and TiO_2 substrates. The second are FeRh/Ni films grown on MgO (001) substrates. All substrates used in this work were purchased from MTI Corporation. We will begin by describing the VO_2/Ni films, and then the FeRh/Ni films.

All VO_2 films fabricated in this thesis were grown via reactive RF magnetron sputtering. The Ni layers in the VO_2/Ni hybrid films were grown via DC magnetron sputtering with the gun in ‘unbalanced’ configuration, where the magnetic core is removed but the magnetic ring is untouched. Prior to use, the Al_2O_3 and TiO_2 substrates were stored in air. Both types of substrate are stable in air, and there is no risk of degradation. To prepare them for deposition, all substrates were cleaned to reduce contamination of the surface. First, they were ultrasonicated in an acetone bath for approximately 15 minutes, which is particularly effective at removing oils and organics on the surface. However, acetone is known to leave residue, so the first 15 minute sonication is followed by 15 minutes of sonication in methanol. The substrate is then blow dried with N_2 gas and immediately mounted onto the substrate holder and the substrate holder is loaded into a Load-Lock chamber to begin pumping down. It was found that 2 holder fingers on opposite corners of a substrate helped improve the reproducibility by enhancing the thermal contact with the Inconel plate. The Load-Lock reaches $\approx 1.5 \times 10^{-7}$ Torr before the substrate is transferred to the main chamber for deposition. The films were grown in a high vacuum chamber, with a base pressure of approximately 2×10^{-7} Torr. The target used in the VO_2 deposition was a pure (99.95%) V target with dimensions 2 inches diameter and 0.25 inches thickness purchased from Kurt J. Lesker company. The Ni target was a pure (99.995%) Ni target 2 inches diameter and 0.25 inches in thickness, also from Kurt J. Lesker.

For the FeRh films, MgO (001) substrates were stored in a vacuum desiccator as it is known to react to air. Prior to deposition, the substrates were cleaned by ultrasonication in 10 minutes of acetone, 10 minutes of methanol, and 10 minutes of isopropanol. Substrates were then dried with N_2 gas and then mounted onto the substrate holder and loaded into the Load-Lock. The FeRh target is a pure (50/50 ratio) FeRh target with 99.9% purity from ACI Alloys Inc. The FeRh is also operated in a DC magnetron sputtering gun in the unbalanced magnetic configuration.

For the VO_2 depositions, the Ar gas flow was fixed at 31 standard cubic centimeters per minute (sccm) while the O_2 flow was varied to alter the ratio between the two gasses. The flow of both gasses was maintained by two mass flow controllers accurate to 0.05 sccm. The pressure during deposition was maintained at 4 mTorr automatically by a gate valve in front of the turbo pump inlet. The substrate temperature was another parameter used to tune the properties of the VO_2 films. The gun tilt was set 17.7 ° from the horizontal which corresponds to direct line of sight sputtering to the substrate for our confocal sputtering geometry. The sample height was to 35 mm from the top of the chamber. The gun was operated at 200 W RF by setting the power as the set point variable. The thicknesses of the films are nominally fixed to 100 nm, calibrated using XRR. As the V target erodes through use, this leads to a variation in deposition time. Typically, roughly 30 minutes for a fresh target, whereas a well-used target would require closer to 45 minutes.

The Ni conditions are simpler. The Ar gas flow was fixed at 31 sccm, with a pressure of 4 mTorr. The deposition temperature was either room temperature (≈ 26 ℃) or 200 ℃. The gun tilt and sample height were maintained at 17.7 ° from the horizontal and 35 mm respectively. The gun was operated at 50 W DC by setting the power. The thickness is fixed at either 10 nm or 15 nm, calibrated in-situ via a quartz crystal thickness monitor.

Lastly are the FeRh conditions. The Ar gas flow was fixed at 31 sccm, and 4 mTorr pressure. The gun tilt and sample height were fixed at 17.7 ° from the horizontal and 35 mm respectively. The substrate temperature as well as the annealing temperature and annealing time were varied to optimize the quality of the films. The gun was operated at 20 W DC by setting the desired power.

For both the VO_2 and FeRh, the Ni was not able to be performed in situ. In the case of VO_2, despite the UHV there were concerns of chemical hysteresis due to the fact that the oxide and metal sputtering both occur in the same chamber. This hysteresis was undesirable if we wished to deposit Ni onto two VO_2 samples at different temperatures. A Ni deposition prior to a VO_2 deposition will act to leach O_2 from the environment during the vanadium oxide sputter as the Ni in the chamber oxidizes. An O_2 deficient atmosphere will lead to an O_2 deficiency in the vanadium oxide film which may alter the material properties, particularly in the case of VO_2 which is sensitive to O_2 stoichiometry. This is often avoided by utilizing separate chambers and transferring the sample between the two chambers when the option is available. As a compromise, when making a heterostructure, one sample was made, and then cut in half, with one half to be deposited in the RT configuration, and the other in the HT configuration. Thus, ensuring that the samples were directly comparable. Due to VO_2's relative stability in air, this was not expected to cause much change at the interface as long as the Ni depositions happened soon after the VO_2 was introduced to atmospheric conditions. In the case of FeRh which metallic, chemical hysteresis is was not a concern. However, samples showed a considerable variation in T_c, despite having strong transitions. FeRh samples were characterized prior to Ni deposition in order to find T_c and ensure that HT samples were made when the sample was fully transitioned. This likely leads to a thin oxide layer at the interface of the FeRh. This variation was later found to be correlated with the sample plate, which was used in both oxide and metal depositions. The elevated temperature annealing process lead to significant outgassing and flaking of the holder, which was significant enough to affect the quality of the films.

2.4 Resistance vs. Temperature

R vs. T measurements were made by mounting a VO_2 sample without Ni onto the top of a sample holder via copper tape, next to a temperature sensor. The sensor is a platinum RTD style detector with class A tolerance (± 0.15 to ± 0.35 °C), bolted to the sample holder in a brass sheath. A 1 cm by 1 cm heater was clamped to the bottom of the sample holder. The size of the heater is larger than the sample being measured, helping to minimize any lateral thermal gradients. The substrates themselves also have relatively large thermal conductivities. 2 leads are then soldered directly onto the sample using indium solder. The entire apparatus is isolated inside an unsealed box to reduce thermal noise. The leads were then attached to a Keithley 6221 model current source and model 2182A nanovoltmeter, in a 2-probe set up. While 4 point probes can eliminate the effects of contact resistance, 2 point measurements are simpler and do not affect the MIT scaling.[245,99] Even in the metallic state, the resistance of the VO_2 is relatively high. The resistance is measured by applying a 10 μA current to the sample and using $R = \frac{V}{I}$ to calculate the resistance. 10 μA is sufficiently small that Joule heating effects are negligible.

The temperature is controlled by a Lakeshore model 335 temperature controller utilizing a PID feedback loop, with the PID values determined empirically. The measurements were made in air using a rate of 1 K/min for both heating and cooling, sufficiently slow to ensure no spurious results. There is no active cooling element, which sets an upper limit to how quickly the sample can cool. This isn't a significant barrier for the chosen rate, particularly near T_c of the VO_2. 1 K/min thus strikes a nice balance between proper characterization of the films while still being time efficient. The temperature controller and Keithley systems are all controlled by an integrated custom LabVIEW program which records the temperature while sweeping the temperature at some fixed current.

2.5 X-ray Diffraction

Ever since the pioneering work of W. H. Bragg and W. L. Bragg following Von Laue et al., it has been known that X-rays can be used to obtain a characteristic diffraction pattern unique to the atomic order of a crystalline sample. X-rays, which are low enough energy to be nondestructive while simultaneously being of the order of atomic spacings, are perfect for the probing of crystalline solids.

The phenomena of high intensity peaks appearing for a specific incident X-ray beam was explained by W. L. Bragg by considering a crystal as being formed of planes of atoms, with a spacing d between the planes. Shown schematically in Figure 19, an X-ray is incident at some angle θ onto 2 planes in a simple crystal. The constructive interference between an X-ray beam specularly reflected by a specific plane and its neighbors would occur when the path length difference due to the extra distance traveled is an integer multiple of the incident wavelength. This leads to the Bragg equation

$$2\, d \sin(\theta) = n\, \lambda \tag{2.1}$$

where d is the separation between 2 crystallographic planes, θ is the angle of incidence, n is any positive integer corresponding to the order of diffraction, and λ is the wavelength of the incident light. By considering each possible plane formed by the crystalline structure, one can identify at what angles intensity peaks should appear.

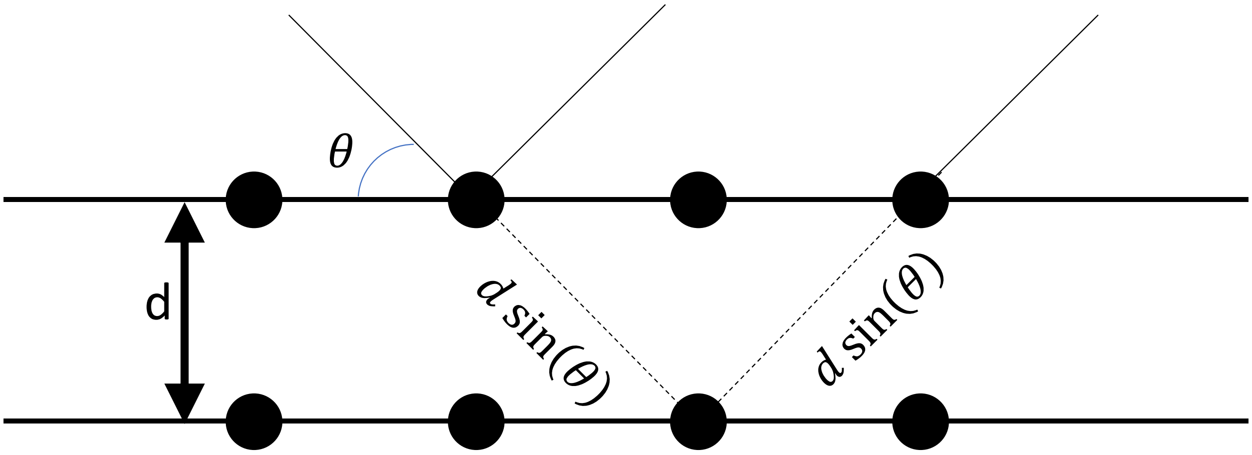

Figure 19. Schematic drawing showing Bragg diffraction between two planes of a lattice.

An equivalent method was given by von Laue by considering atoms placed at the sites of a Bravais lattice. The von Laue construction begins by considering the path difference of an incident X-ray onto two scatterers separated by displacement vector $\vec{\mathbf{d}}$, as in Figure 20. These atoms can reradiate in all directions; however sharp peaks will only be observed when rays constructively interfere.

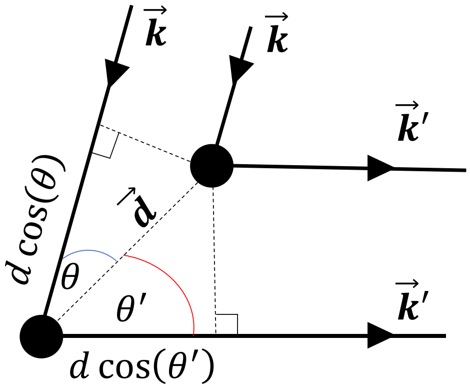

Figure 20. Two scattering elements, labeled to illustrate the path difference for an incident wave scattered off the two.

Incident on the scatterers is an X-ray propagating along the $\hat{\mathbf{k}}$ direction. The path displacement required for constructive interference is given by

$$|\vec{\mathbf{d}}|\cos(\theta) + |\vec{\mathbf{d}}|\cos(\theta') = \vec{\mathbf{d}} \cdot \left(\frac{\hat{\mathbf{k}}}{|\vec{\mathbf{k}}|} - \frac{\hat{\mathbf{k}}'}{|\vec{\mathbf{k}}'|}\right) = \mathrm{m}\lambda \qquad 2.2$$

where we've introduced $\hat{\mathbf{k}}'$ as the wave vector for some specularly scattered wave. θ is the angle between $\hat{\mathbf{k}}$ and $\vec{\mathbf{d}}$, θ' the angle between $\hat{\mathbf{k}}'$ and $\vec{\mathbf{d}}$. Or alternatively

$$\vec{\mathbf{d}} \cdot (\vec{\mathbf{k}} - \vec{\mathbf{k}}') = \vec{\mathbf{d}} \cdot \vec{\mathbf{Q}} = 2\pi\mathrm{m} \qquad 2.3$$

Extending this condition for an entire Bravais lattice whose atoms are separated from each other by lattice vector $\vec{\mathbf{G}}$ yields

$$\vec{\mathbf{G}} \cdot (\vec{\mathbf{k}} - \vec{\mathbf{k}}') = \vec{\mathbf{G}} \cdot \vec{\mathbf{Q}} = 2\pi\mathrm{m} \qquad 2.4$$

For each lattice vector $\vec{\mathbf{G}}$ and integer m. Due to the nature of the Bravais lattice, this condition states that for some change in wave vector, constructive interference occurs when that change in wave vector $\vec{\mathbf{Q}}$ is a vector $\vec{\mathbf{G}}$ of the reciprocal lattice, or

$$\vec{\mathbf{Q}} = (\vec{\mathbf{k}} - \vec{\mathbf{k}}') = (\vec{\mathbf{k}}' - \vec{\mathbf{k}}) = \vec{\mathbf{G}} \qquad 2.5$$

While the Bragg and van Laue conditions are useful for determining where the peaks in the diffraction pattern should appear, they don't give any information about the observed intensity. However, this information can be found from electromagnetic scattering considerations.

XRD takes advantage of classical elastic Thompson scattering, where the electrons of the sample oscillate as tiny nearly free dipoles under the field of the incoming x-rays, at frequencies characteristic to the radiation. The free electron approximation is appropriate since the natural frequency of bound electrons is on the order of $\omega_0 \approx \frac{\mathrm{v}}{\mathrm{a}}$, where v is the characteristic electron velocity and a the dimension of the atom. This is much less than the frequency of the incident X-ray.[246] More detailed derivations will of course provide valuable corrections. But the classical description is sufficient for typical XRD crystallography where we are only concerned with identifying the phase and quality of the grown samples. In addition, we suppress the phase shift relative to the incoming beam as well as the time dependence in the following section as they don’t contribute meaningfully.

For a plane wave with amplitude $\vec{\mathbf{E}}_i e^{-i\,\vec{\mathbf{k}}_i\cdot\vec{\mathbf{R}}_i}$, the scattered wave amplitude at some point $\vec{\mathbf{R}}$ is given by

$$\vec{\mathbf{E}}(\vec{\mathbf{R}}) = \vec{\mathbf{E}}_i \frac{r_e}{|\vec{\mathbf{R}}|} \sin\left(\theta_{\vec{\mathbf{E}}_i,\vec{\mathbf{R}}}\right) e^{-i\,\vec{\mathbf{k}}\cdot\vec{\mathbf{R}}} \tag{2.6}$$

With r_e being the classical electron radius, given by $r_e = \frac{e^2}{4\pi\epsilon_0 mc^2}$. $\theta_{\vec{\mathbf{E}}_i,\vec{\mathbf{R}}}$ is the angle between the electric field vector $\vec{E}_i$ and $\vec{r}$. The above expression is general for a free charged object of size much smaller than the incident wave front acting as a scatterer, but the inverse mass dependence ensures that we need only consider the electrons and not the nuclei.

To obtain the measured intensity of an actual crystal, several other factors need to be considered. The most obvious is that we need to sum over all the atoms in the crystal lattice that will contribute to the signal. This involves summing Eq. 2.6 for each scatterer, with the replacement of $\vec{R}$ to $\vec{R} - \vec{r}_{n_1n_2n_3}$. If we set some reference atom to be point $\vec{R}$, we can define the position of each other atom in relation to it using a lattice vector $\vec{r}_{n_1n_2n_3}$ which can be defined using the crystal coordinate unit vectors $\vec{\mathbf{c}}_i$ or alternatively defined using the hkl Miller indices and the fractional coordinates of the jth atom. $\vec{r}_{n_1n_2n_3} = n_1 a\vec{\mathbf{c}}_1 + n_2 b\vec{\mathbf{c}}_2 + n_3 c\vec{\mathbf{c}}_3 = hx_j + ky_j + lz_j$. This amounts to relating the phase difference due to all the scatterers back to the atom at $\vec{R}$.The scattered wave amplitude then becomes

$$\vec{\mathbf{E}}(\vec{\mathbf{R}}) = \vec{\mathbf{E}}_{\mathrm{i}} e^{-i\vec{\mathbf{k}}\cdot\vec{\mathbf{r}}_{n_1n_2n_3}} \frac{r_e}{|\vec{\mathbf{R}} - \vec{\mathbf{r}}_{n_1n_2n_3}|} \sin\left(\theta_{\vec{\mathbf{E}}_i,\vec{\mathbf{R}}-\vec{\mathbf{r}}_{n_1n_2n_3}}\right) \sum_{n_1n_2n_3} e^{-i(\vec{\mathbf{Q}})\cdot\vec{\mathbf{r}}_{n_1n_2n_3}} \qquad 2.7$$

In the Fraunhofer regime we can approximate $\vec{R} - \vec{r}_{n_1n_2n_3} \approx \vec{R}$ in the $\frac{1}{|\vec{\mathbf{R}}|}$ term as well as in the $\sin\left(\theta_{\vec{E}_i,\vec{R}}\right)$ term. $\vec{R}$ is on the order of our measurement distance $|\vec{R}| \approx 10^{-1}$ m, whereas $\vec{r}_{n_1n_2n_3}$ is on the order of the interatomic spacing, so $|\vec{R}| \gg |\vec{r}_{n_1n_2n_3}|$. The $\vec{R} - \vec{r}_{n_1n_2n_3}$ in the summed exponents must be maintained since $\vec{r}_{n_1n_2n_3}$ is on the order of the wavelength of the incoming radiation. The simplified scattered field is now

$$\vec{\mathbf{E}}(\vec{\mathbf{R}}) = \vec{\mathbf{E}}_{\mathrm{i}} e^{-i\vec{\mathbf{k}}\cdot\vec{\mathbf{R}}} \frac{r_e}{|\vec{\mathbf{R}}|} \sin\left(\theta_{\vec{\mathbf{E}}_i,\vec{\mathbf{R}}}\right) \sum_{n_1n_2n_3} e^{-i(\vec{\mathbf{Q}})\cdot\vec{\mathbf{r}}_{n_1n_2n_3}}$$

We can now construct the intensity $I(\vec{\mathbf{R}}) = \vec{\mathbf{E}} \cdot \vec{\mathbf{E}}^*$ .We can further simplify the sum of exponentials by utilizing the definition of a geometric series

$$\sum_{n=0}^{N-1} x^n = \frac{1-x^N}{1-x} \qquad 2.9$$

along with Euler's identity and a trigonometric identity. The intensity is then

$$I(\vec{\mathbf{R}}) = I_0 \sin^2\left(\theta_{\vec{\mathbf{E}}_i,\vec{\mathbf{R}}}\right) \frac{{r_e}^2}{|\vec{\mathbf{R}}|^2} \prod_{i=1}^{3} \frac{\sin^2\left(\frac{N_i a_i \vec{\mathbf{Q}} \cdot \vec{\mathbf{c}}_i}{2}\right)}{\sin^2\left(\frac{a_i \vec{\mathbf{Q}} \cdot \vec{\mathbf{c}}_i}{2}\right)} \qquad 2.10$$

The product term, or interference function, contains the essence of the Bragg and von Laue conditions. The large value of N_i's causes the function to be highly localized to values that satisfy the conditions, and essentially zero elsewhere.

There are a number of other factors that should be considered that will influence the overall intensity:

1. A polarization factor P, which accounts for the polarization of the incoming beam.

2. A structure factor S, which accounts for the shape of the crystal lattice.
3. A multiplicity factor M, to account for the fact that multiple Bragg planes can contribute at a specified Bragg angle.
4. A texture factor T, which accounts for any preferred orientation in the sample.
5. A geometric factor G, which accounts for certain geometric considerations.
6. An absorption factor A, to account for any loss inside the material.
7. A temperature factor, which accounts for the reduction in signal due to thermal motion.

We first address the polarization factor. $\vec{E}_i$ can be decomposed into two components, π polarization, which is confined to the scattering plane, and σ polarization normal to the plane. The sine of the angle between the π component and $\vec{r}$ can be expressed as $\cos(2\theta)$, and the sine of the angle between the σ component and $\vec{r}$ is always 1. If the polarization of the source is random as in X-ray generators, the wave will be composed equally of π and σ polarizations on average. Thus, using $\overline{\vec{E}_\sigma^{\,2}} = \overline{\vec{E}_\pi^{\,2}} = \frac{I_0}{2}$ and $I_{total} = I_\pi + I_\sigma$, the total intensity I will be modified by the average of the square of P

$$\overline{P^2} = \frac{1 + \cos^2(2\theta)}{2} \qquad 2.11$$

We now need to account for the structure of the unit cell itself in a crystal lattice. The structure factor S is an integration of the charge density in the unit cell, and can be written

$$S = \int_{\text{unit cell}} \rho(\vec{\mathbf{r}})\, e^{-i\vec{\mathbf{Q}}\cdot\vec{\mathbf{r}}} d\vec{\mathbf{r}} = \sum_{j=1}^{N} f_j\, e^{iQr_j} = \sum_{j=1}^{N} f_j\, e^{2\pi i(hx_j + ky_j + lz_j)} \qquad 2.12$$

The left most expression for S gives the general integration of the charge density, accounting for phase differences due to different particles. The middle expression is equivalent, but explicitly decomposes the integration into a sum over the contributions due to the individual atoms in the crystal. The term f_j is a so-called atomic form factor to account for the charge distribution around the jth atom, the details of which will be given momentarily. The rightmost term simplifies further, expressing S in terms of the hkl Miller indices and fractional coordinates given earlier. S is in general a complex quantity but appears in the intensity as $S \cdot S^* = S^2$, a real quantity.

A typical form for the atomic form factor is[247]

$$f_j(\vec{\mathbf{Q}}) = -\frac{1}{e}\int_{atom} \rho_j(\vec{\mathbf{r}})e^{-i\,\vec{\mathbf{Q}}\cdot\vec{\mathbf{r}}}d\vec{\mathbf{r}} \qquad 2.13$$

This is simply the Fourier transform of the electronic charge distribution, normalized such that if $\vec{\mathbf{Q}} = 0$, this reduces to

$$f_j(\vec{\mathbf{Q}}) = Z \qquad 2.14$$

The multiplicity factor M allows for the fact that multiple different Bragg planes can cause reflections for the same Bragg angle. For example, in an fcc single crystal structure, the $(\bar{1}11)$ $(1\bar{1}1)$ $(11\bar{1})$ would normally give distinct peaks. However, in a polycrystalline sample with random orientation, these peaks would be smeared out into a ring. This ring corresponds to a cone with the tip originating at the sample and an opening of 4θ that intersects a sphere with the sample at the center of the sphere. A short table of multiplicity factors for cubic, monoclinic and tetragonal crystals is listed below. The format is (Miller indices): # multiplicity factor. A term such as hhl stands for planes such as (112) or (211), which are equivalent. *'s are indicated for planes which can have the same Bragg spacing but differing structure factors depending on the crystal, meaning the indicated number should be divided by 2.

Table 1. Multiplicity factors for the cubic, monoclinic, and tetragonal crystal symmetries.

Cubic	(hkl):48*	(hhl):24	(0kl):24*	(0kk):12	(hhh):8	(00l):6	-
Monoclinic	(hkl):4	(h0l):2	(0k0):2	-	-	-	-
Tetragonal	(hkl):16*	(hhl):8	(0kl):8	(hk0):8*	(hh0):4	(0k0):4	(00l):2

The texture factor T accounts for any preferential orientation of the Bragg planes. For randomly oriented grains as in powder, it simply reduces to T=1. However, it is typical in most thin films to have some preferential orientation. In general, to know the texture factor, one must know the statistical distribution of orientations in the sample. A more detailed analysis is given in Ref. [248].

Next, an absorption factor handles the attenuation of the signal due to absorption as the X-ray travels through the material. An X-ray with initial intensity I_0 that travels a distance 2L will become attenuated by a factor of $e^{-2\mu L}$, where μ is an empirically determined attenuation coefficient, and 2L the total path length traveled. The absorption factor A is then given by

$$A = \int_0^{L_{max}} e^{-2\mu L} dL \qquad 2.15$$

In the $\theta/2\theta$ geometry, $L = \frac{z}{\sin(\theta)}$ where z is the depth of the film. $z = 0$ corresponds to the surface of the film, and $z_{max} = t$ where t is the thickness of the film. Upon integration 2.15 simplifies to

$$A = \frac{1}{2\mu}\left(1 - e^{\frac{-2\mu t}{\sin(\theta)}}\right) \qquad 2.16$$

It is worth emphasizing that A therefore has an explicit θ dependence. μ and t are often of roughly similar order to each other, so the exponential should not be neglected.

The geometrical factor G arises from certain trigonometric considerations during the measurement. As mentioned in the discussion of the multiplicity factor, for a given Bragg plane, the intensity will be smeared out in a circle, given by the intersection of a cone and sphere. The circumference of this ring will vary depending on the angle of measurement as $\sin(2\theta)$. To correct for this, we need to normalize by a factor of $\frac{1}{\sin(2\theta)}$. By a similar argument, the scattering vectors Q will themselves also lie on a cone. The density of these Q vectors will scale proportionally as $\sin\left(\frac{\pi}{2}-\theta\right)=\cos(\theta)$. Therefore, the overall geometric factor G is given by

$$G = \frac{\cos(\theta)}{\sin(2\theta)} = \frac{1}{2\sin(\theta)} \qquad 2.17$$

The last factor is temperature, which will affect the intensity due to thermal noise. This thermal noise will have the effect of causing the atomic ions to oscillate around their equilibrium positions. This oscillation can be taken into account by modifying the atomic form factor with a temperature dependent Debye-Waller factor

$$f_{j,\mathrm{therm}} = f_j e^{\frac{-8\pi^2\overline{u^2}\sin^2(\theta)}{\lambda^2}} = f_j e^{\frac{-Q^2\overline{u^2}}{2}} = f_j e^{-B\left(\frac{\sin^2(\theta)}{\lambda^2}\right)} \qquad 2.18$$

$\overline{u^2}$ represents the mean quadratic displacement from the equilibrium position $\vec{\mathbf{r}}_j$ of that atom and f_j is the atomic form factor defined previously. The factor $8\pi^2\overline{u^2}$ is often abbreviated as B in the literature. Exact analytic determinations of B are difficult, and it’s common to reference a database for an empirically determined value of B when it’s required. The main effect of this Debye-Waller factor is to lower the intensity of Bragg peaks, particularly at high angles. In addition, it also leads to an increase in the diffuse background scattering. We can finally give an expression for the final measured intensity

$$I(\vec{\mathbf{R}}) = I_0\overline{P^2}S^2 MTGA\frac{{r_e}^2}{|\vec{\mathbf{R}}|^2}\prod_{i=1}^{3}\frac{\sin^2\left(\frac{N_i a_i \vec{\mathbf{Q}}\cdot\vec{\mathbf{c}}_i}{2}\right)}{\sin^2\left(\frac{a_i\vec{\mathbf{Q}}\cdot\vec{\mathbf{c}}_i}{2}\right)} \qquad 2.19$$

The equipment setup for XRD is relatively simple, consisting of an X-ray source, a sample holder, and a detector. The measurements presented here were taken using a Bruker D-8 Series-I diffractometer in the $\theta/2\theta$ configuration. X-rays are typically produced using a cathode ray tube, where a filament is heated to produce electrons which are then accelerated by an applied voltage and collide with the source material. These collisions excite inner shell electrons which produce X-rays of a well-known characteristic wavelength and random polarization. A Cu source emits 3 characteristic wavelengths of radiation, the $K_{\alpha1}$,$K_{\alpha2}$ and K_{β}. In the case of a Cu source, the K_{β} can be greatly attenuated with a Ni filter, but it isn't practical to eliminate the K_{α} lines. However, the two are close enough in wavelength that the distortion off a monochromatic beam is small, and their intensities are 2:1. After production, the x-rays are collimated and sent towards the sample using a Göbel mirror with a divergence of 0.05°. The signal is then collected in a NaI detector.

In the $\theta/2\theta$ configuration, the source and detector are rotated in sync at a fixed radius to maintain the $\theta/2\theta$ geometry. In our system, the measuring circle is set to 0.8 m. Equivalently, one can instead rotate the sample rather than the source to maintain the proper geometry. Practically speaking, this is often easier to do, and it is the case for the Bruker Discover system, which has a fixed source. The system is also equipped with a full Eulerian cradle which allows for complete freedom in sample adjustment and orientation. The cradle is capable of step sizes as small as 0.005° in the angular directions, and 0.01 mm in Cartesian adjustments, for both sample and detector arm. Figure 21 contain several views of the geometry of our system. Panels a) and b) depict schematic views of the $\theta/2\theta$ scan. c) shows the actual system, in the geometry used in the scan. d) shows a schematic with a coordinate system in the sample reference frame that will be referred to during the sample alignment.

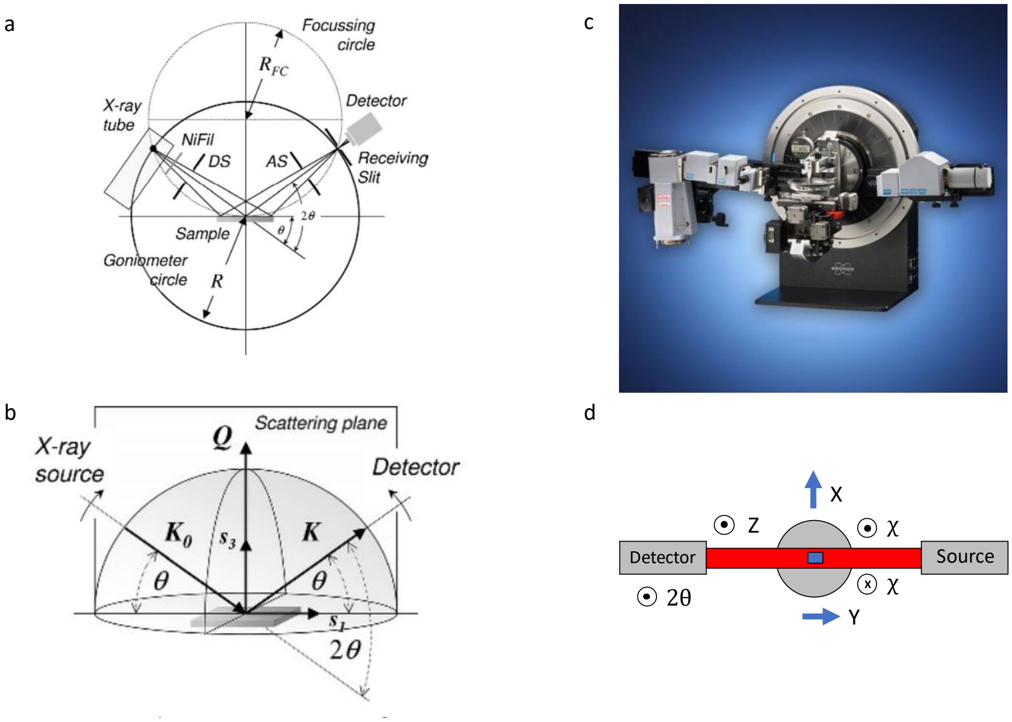

Figure 21. a) Schematic view of a $\theta/2\theta$ scan, in a top down view. b) Schematic view of a $\theta/2\theta$ scan, with emphasis on the momentum vectors.[248] c) An example of a Bruker D8 series XRD system.[249]b d) schematic view, with coordinate system used in the procedure.

The procedure for a typical XRD scan is given in Appendix C.

2.6 X-ray Reflectivity

X-ray Reflectivity (XRR) is another technique that can be used to characterize a wide range of thin film properties. XRR can provide valuable information about chemical composition, surface and interface roughness, and most commonly, film thickness. Rather than comparing to a known database, many of these parameters can be obtained via fits to the data. There are a number of different software packages for this fitting, including GenX,[250] Motofit,[251] or Refl1D.[252] XRR operates in the same geometry as the $\theta/2\theta$ XRD method, but at very low angles of incidence. A defining difference between the two techniques is that XRR relies on the reflective properties of the film, rather than diffraction.

A typical example of an XRR measurement is given in Figure 22. The main figure gives the reflected intensity measured as a function of 2θ. A log scale is used on the y-axis to accommodate the fact that the intensity varies over many orders of magnitude for a fixed intensity of incident radiation. The inset shows the same figure but emphasizes the region of 2θ from 0 to 1.5 degrees. As is clear from the inset, there are in general 3 regions with drastically behavior. In region I, we see an increase in the intensity as 2θ increases. This is due to the finite size of the sample. The lateral footprint F of a rectangular incident beam with length h as $F = \frac{h}{\sin(2\theta)}$. For a typical beam width of 0.1 mm and $2\theta = 0.2$, this leads to a footprint of nearly 3 cm. In region II, we see a plateau in the intensity. The exact slope of this plateau is related to the ratio $\frac{\beta}{\delta}$, where δ and β are the real and imaginary parts of the dielectric susceptibility. For X-rays, it is typical to represent the index of refraction of a material as $n = 1 - \delta - i\beta$. Both δ and β are small for X-rays, and the index of refraction is a small deviation from unity. δ is typically $\approx 10^{-5} - 10^{-6}$, and β is roughly a factor of 10 smaller. These values for β and δ can be calculated by considering the electron densities at the surface of a material as damped harmonic oscillators. Region II ends at $2\theta_c$, where θ_c is the critical angle. Due to the fact that the index of refraction is less than one, materials experience total internal reflection up to some critical angle, analogous to the phenomenon seen in optics. Snell's Law in the small angle approximation and taking $\beta \approx 0$ yields $\theta_c \approx \sqrt{2\delta}$. Finally, Region III shows sharp decreases in the intensity, along with the trademark Kiessig fringes. For an ideal smooth surface, the intensity in this region scales as $\frac{1}{Q^4} =$

$\left(\frac{\lambda}{4\pi\sin(\theta)}\right)^4$, which leads to the sharp decrease in intensity known as Fresnel decay or Porod slope as the angle increases.

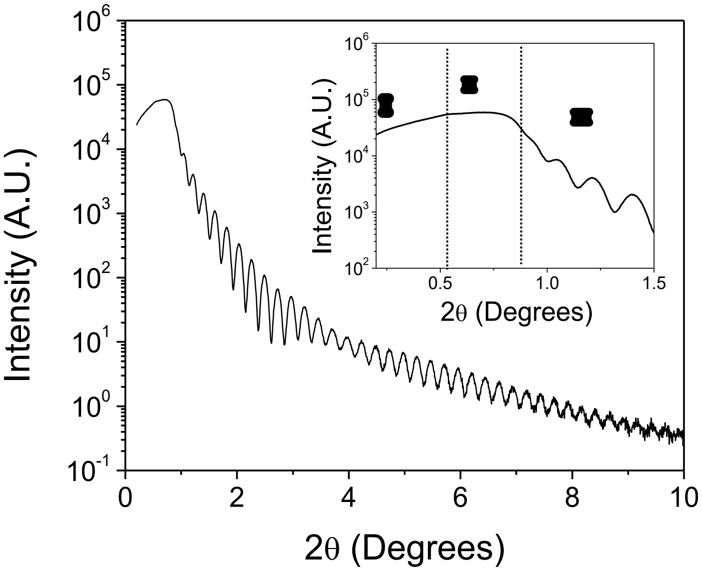

Figure 22. Typical XRR measurement on an FeRh thin film on MgO (001) substrate. (Inset) A narrower region of the same scan, to emphasis 3 regions of interest.

Kiessig interpreted these fringes in Region III as interference maxima due to a path difference between portions of the beam reflected at the surface of the thin film, and reflection at the interface between film and substrate. The situation is shown schematically in Figure 23.

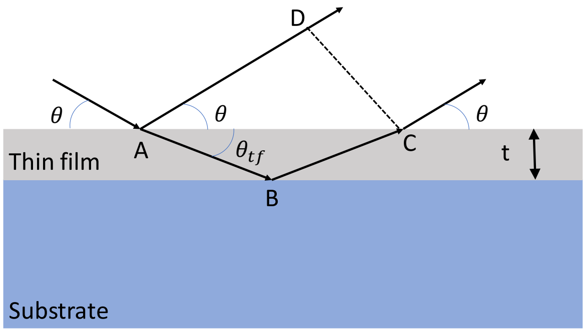

Figure 23. Schematic drawing for the path difference leading to Kiessig fringes in a thin film due to interference.

The phase difference due to this path difference is

$$\Delta = (\Delta_{AB} + \Delta_{BC})n - \Delta_{AD} = 2t\sin(\theta_{tf})$$

Where Δ_{xy} is the phase difference along the path from point x to point y, t is the thickness of the film, and θ_{tf} is the angle of refraction inside the film. A maximum is seen when $\Delta = m\frac{\lambda}{n} \approx m\lambda$, or an integer multiple of the wavelength. This is condition is identical to the Bragg condition constructed earlier, but for a thin film rather than atomic planes. This formulation is particularly useful for determining film thickness accurately. The x-ray wavelength is known to very high precision in addition to the fact that the thickness t in the above formula is uncoupled to the absorption coefficient as in most optical measurements. These facts, along with the fact that n is close to unity, allows for the estimation of t with reasonable precision. However, experimental limitations heavily limit practical measurable thicknesses of a single layer to around 100 nm for Cu K_α radiation. The smaller spacing of the fringes at larger thicknesses will be limited by the resolution of 2θ spacing of the instrument. One can move to higher order fringes to compensate but then beam divergence, source intensity, and surface roughness among other factors will degrade the signal until the fringes are lost beneath the noise floor. This approximate 100nm restriction is more than sufficient for the film thicknesses considered in this work. Estimations of thicker films can also be made by measuring a test sample under normal deposition conditions but only ~50 nm thickness. Sputtering rates are fairly consistent from sample to sample, so the thickness of full samples can easily be extrapolated from the test sample measurement.

Up to now, all of the analysis of XRR results has assumed perfectly smooth interfaces. In general, one can adequately take roughness into account using the Distorted Wave Born Approximation.[253,254] This gives a good approximation of the roughness for a wide range of in-plane correlation lengths in the roughness. In practice, it's often sufficient to consider the two limiting cases where the correlation length is much smaller or much larger than the x-ray extinction length of $\approx$ 1 micron. The theory greatly simplifies to a simple factor, and we can decompose the intensity I into a specular component and a diffuse component. In the case of large correlation lengths, one obtains a Debye-Waller like term $e^{-\sigma^2 Q^2}$ where σ is the RMS (root-mean-square) roughness defined as $\sigma = \frac{\int \sqrt{z(x,y)^2 - \bar{z}^2}\, dxdy}{\int dxdy}$ and Q the wave vector transfer $Q = \frac{4\pi \sin(\theta)}{\lambda}$. In the opposite limit and assuming a Gaussian roughness distribution, a Nevot-Croce (NC) factor can be used $e^{-2k_{j-1}k_j\sigma^2}$, where $k_j = \sqrt{k_i{}^2 - |\vec{k}|^2 (1-n)^2}$ is the z component of the wave vector in layer j and k_i the incident wave vector. These terms multiply the specular component of the intensity. In both cases, the main result is a large reduction in intensity, and each limit will give different results near θ_C. The roughness should also be much less than the layer thickness.

The physical XRR measurements taken use the same system and procedure as in XRD, with some minor differences mainly due to XRR's sensitivity to alignment as compared to XRD. See Appendix C (XRD/XRR Procedure) for the detailed procedure.

Notably, one needs to be rather careful about adjusting parameters such as the slit size through the scan, particularly when comparing to simulated data. However, the detailed XRR results presented later were done on a Rigaku SmartLab system that did not require the same adjustments. This procedure was mainly used to obtain thicknesses of the films. The manual adjustments of slit size, Soller slits, copper foil, and knife edge will change the overall intensity and scanning region from scan to scan and in general would need to be accounted for in any detailed modeling. However, they do not have a major effect on the spacing of the Kiessig fringes from which the film thickness can be obtained.

For detailed chemical analysis, the XRR data was fit using the Refl1d software, details of which will be given in the Polarized Neutron Reflectometry section.[252] The procedure to fit multilayer films is analogous between the two methods, with the Helmholtz equation taking the role of the Schrödinger equation.

2.7 Magnetometry

Perhaps the most essential measurement pieces of equipment are those used to measure the magnetic properties of the samples. Here, we use two magnetometry techniques to measure the magnetic properties of the films. The first is a Vibrating Sample Magnetometer (VSM), and the other is a superconducting quantum interference device (SQUID) magnetometer. For this work, the choice of magnetometer is mostly one of convenience, as the magnetic signal is robust.

The main consideration is that hysteresis loops are slow to perform in the SQUID and wasteful of helium, and so the VSM is always used for M vs. H measurements.

The VSM used in this work was a commercial Quantum Design VSM, a module of the physical properties measurement system (PPMS). A schematic of the system is shown in Figure 24, for reference.

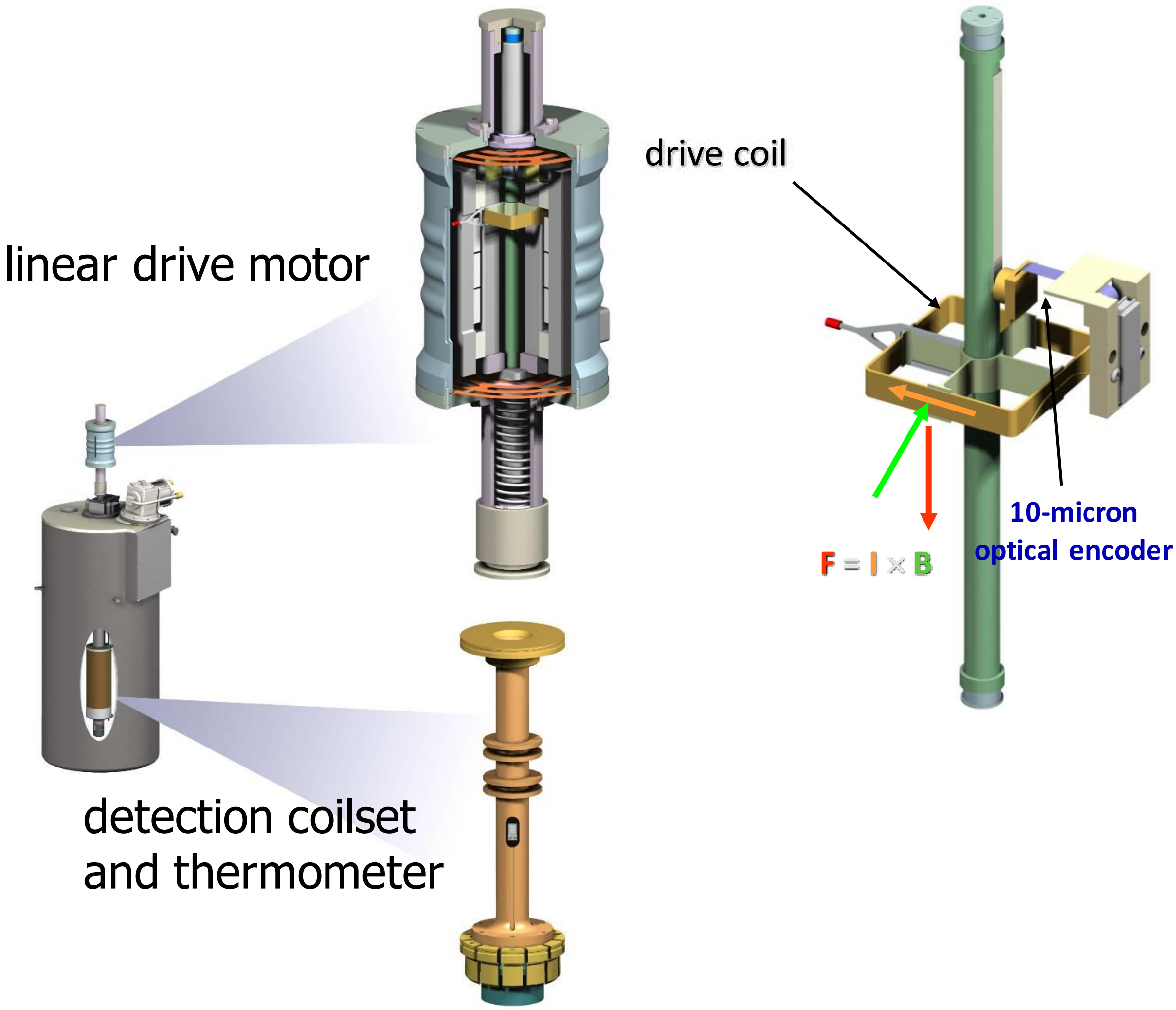

Figure 24. Schematic of VSM option in a Quantum Design PPMS. (Courtesy: Quantum Design)

In VSM magnetometry, the magnetic moment of the sample can be measured by vibrating the sample between pickup coils. This moving magnet will cause a change of flux in the coils, and thus an emf via Faraday's Law for a sinusoidal signal

$$V_{\text{induced}} = -\frac{d\phi}{dt} = -\left(\frac{d\phi}{dz}\right)\left(\frac{dz}{dt}\right) = \omega C m A \sin(\omega t) \qquad 2.20$$

As is usual, ϕ is the magnetic flux, ω the frequency of oscillation, and A is the amplitude of oscillation. The DC magnetic moment of the sample is given by m, and C is a coupling constant to account for the measurement geometry. In this system, a linear motor is isolated from the rest of the system by a spring suspension system with a resonant frequency of 5 Hz. The position of the motor is monitored using an optical linear encoder. This motor magnetically locks to a carbon fiber sample rod via magnets that attach to the top of the rod. The sample rod is sinusoidally oscillated at 40 Hz with an amplitude of 2 mm via a drive coil. The sample rod runs through a sample tube which provides a low friction guide, reducing measurement noise by reducing transmission of vibrations to the coil set. The sample itself is attached to a quartz sample mount via Dow Corning high vacuum grease which is stable to ~400 K. Initial sample positioning is accurate to ± 0.5 mm, and the quartz mount is then screwed into the sample rod. Carbon fiber is chosen for the rod due to its low rate of thermal expansion. However, the VSM chamber itself is stainless steel, and the sample is re-centered at each temperature to minimize the effects of thermal expansion.

For detection, the VSM utilizes a first order gradiometer, consisting of two coils. The sample is then vibrated along the central axes of these coils in order to generate a sinusoidal signal. The coils are spaced 7.1 mm from the bottom of one coil to the top of the other, and each coil is 1.7 mm thick with inner radius 3.865 mm and outer radius 6.85 mm. The voltage signal from the coils is then run through a pre-amp. The VSM utilizes the position of the linear motor as a lock-in signal accurate to 0.1 microns and compares both the in-phase portion as well as a 90 degree out of phase portion of the voltage to this lock-in value. At a 40 Hz oscillation, 40 measurements are taken and averaged per 1 s data point.

In cases where a temperature above 400 K is required, the VSM is equipped with an oven option that can run as hot as 1100 K. Only minor modifications are required, namely the sample rod, sample mount, and sample rod guide are replaced with high-T components, and the VSM is run under high vacuum. The sample mount is made up of yttria stabilized zirconia, a ceramic with low thermal conduction, ensuring low heat transfer to the linear motor portion of the system and maintain it below 315 K. Heating is achieved via a platinum resistor heating element with a dielectric upper coating that is patterned onto the sample mount. Embedded into the ceramic is a type S $Pt/Pt_{0.9}Rh_{0.1}$ thermocouple which measures the temperature right near the sample, corrected by a thermistor at the top of the rod to account for heating of the cold junction. It is electrically connected to the sample rod, which connects to a custom cap on the top of the linear motor. The temperature is controlled via a PID feedback system. In order to accommodate the increased temperature, the Dow Corning grease is replaced by a water-soluble alumina cement from Zircar to attach the sample to the sample mount. Both sample and sample mount are wrapped in a piece of low emissivity Cu foil to improve temperature homogeneity.

There are two main types of measurements done in the VSM, and their procedures are provided in Appendix D (VSM Magnetometry Procedure). The first type is magnetization vs. temperature, or M vs. T. For M vs. T measurements, the magnetization is recorded as the temperature is swept through some range, with a fixed field applied. The second type are magnetization vs. applied field, or M vs. H. At various temperatures above, during and below T_c of the SPT material, a hysteresis loop is taken.

The SQUID system is conceptually rather similar to the VSM, but with some key differences. The system used in this work is a Quantum Design MPMS-XL model SQUID magnetometer. To detect a magnetic signal, a 2nd order balanced gradiometer set up is used, with 2 sets of coils arranged with their axes aligned. The total separation of the coils is 3 cm from top to bottom. This set up is specifically chosen to be insensitive to the field applied by the superconducting magnet with an accuracy of 0.1%. The coils pick up a voltage utilizing Faraday's law, just as in the VSM case, by moving the sample through the coils. In this set up however, the oscillations are much slower. Signals from the pickup coils are then run through a superconducting RF interference isolation transformer, which has a rolloff frequency of -3 dB at 20 kHz. This transformer prevents erroneous flux jumps during the measurement, even in noisy RF environments. It also allows tuning of the input inductance of the SQUID. The transformer is also attached to a heater which drives it normal during magnetic field changes during the magnet initiation and the start of sample measurements. This voltage then drives a current through an input coil (inductor), which is ultimately what generates the flux measured by induced voltage response in the SQUID. The SQUID is coupled to another input coil which acts to flux lock the SQUID by applying an equal and opposite flux to the external signal. This voltage profile is then fit and compared to calibration samples to determine the magnetic moment of the sample.

In order to heat or cool the sample, helium gas is allowed to flow into the chamber. Heating the chamber can be done by flowing preheated helium gas directly into the chamber, as well as a chamber heater wrapped around the sample chamber. The temperature control is run by a PID system, with temperature measurements provided by 2 thermometers. The main sensor is positioned at the null point of the pickup coils, and a secondary sensor is placed at the bottom of the sample chamber. At room temperature or higher, the main control is provided by the primary thermometer, which has an accuracy of 0.01%.

Samples are mounted in commercial plastic drinking straws, which have negligible magnetic moments compared to strong ferromagnetic signals. Several smaller sections of straw are used to wedge the sample inside the straw in the middle of a full straw length. The straw should be sufficiently long that edge effects do not affect the signal, and the sample secure such that it cannot move around in the straw during use. The straw is then attached to the sample rod via Kapton tape.

Magnetic fields are applied by a superconducting magnet, which is always operated in no overshoot mode unless demagnetizing the pickup coils. Wait times of several minutes before measurement as well the built-in compensation in the MPMS pickup coils minimize any relaxation drift due to field creep in the coils. Control of the magnet is on the order of 0.1-1 gauss, measured via the current flowing through the magnet rather than the magnetic field itself. The helium level in the system is often limited to less than 50% which soft limits the magnet to a maximum applied field of 1 T during operation. The magnet also has a full reset option that sequentially allows portions of the magnet to go normal but uses too much helium to be used in the standard procedure. The procedure for a M vs. T measurement in the SQUID is given in Appendix E (SQUID Magnetometry Procedure).

2.8 Atomic Force Microscopy

Ever since its invention in 1986 by combining Scanning Tunneling Microscopy techniques with a profilometer tip, Atomic Force Microscopy (AFM) has been a powerful tool to investigate the surface topography of materials.[255,256] The strength of the technique lies in its flexibility combined with the incredible resolution it provides. Indeed, the original design was motivated by the inability of STM to measure insulating materials. Various forms of AFM have been used to probe metallic surfaces of films, insulators, nanoparticles, biologic samples including in liquid, and more. The first AFM had resolutions of 0.3 nm laterally, and vertical resolution less than 1 angstrom. Top of the line AFM systems today boast a resolution on the order of 20 pm-5nm in the lateral direction, and 30 pm in the z direction under ideal conditions. The original AFM utilized what would today be called contact mode, but quickly spawned several variations, including tapping mode (where the tip oscillates near the surface), magnetic force microscopy utilizing a magnetic tip to scan magnetic materials, lateral force microscopy, and a zoo of other techniques. Here, we focus on tapping mode AFM on a Bruker di Innova system with the large area scanner option. The main advantage of tapping mode over contact mode is the reduced wear and tear of tip and sample by reducing any lateral shearing forces during measurement. The cantilever is oscillated such that it touches the surface only at the bottom of the oscillations.

The setup required for AFM is relatively simple and is shown schematically Figure 25. The main probe in the AFM technique is a small cantilever, with a micromachined tip on one end of it. The cantilever is mechanically vibrated by a piezoelectric element so that it oscillates near the resonant frequency of the tip. The piezo is driven by a drive voltage. In order to measure the z height of the end of the cantilever, a diode shines a laser beam at the back of the cantilever. The reflection of this beam is picked up by a position sensitive photo detector. In the Innova system, this is a 4-segment array of detectors. As the cantilever oscillates this produces an AC voltage which is then rectified, then low pass filtered, converting it to an RMS DC voltage. This DC voltage is a direct measurement of how close the tip is to the surface, since the electrostatic interaction and thus deflection between tip and sample will vary as a function of distance. This measured DC voltage is compared to a setpoint voltage by a differential amplifier, and an error signal is generated, which is multiplied by a gain multiplier to improve responsiveness to the error signal. The motion of the cantilever is controlled by a piezo controller under the sample, which moves the sample in such a way as to maintain that set point RMS voltage, very similar to contact mode. This motion is controlled by a PID feedback loop, whose values were determined empirically.

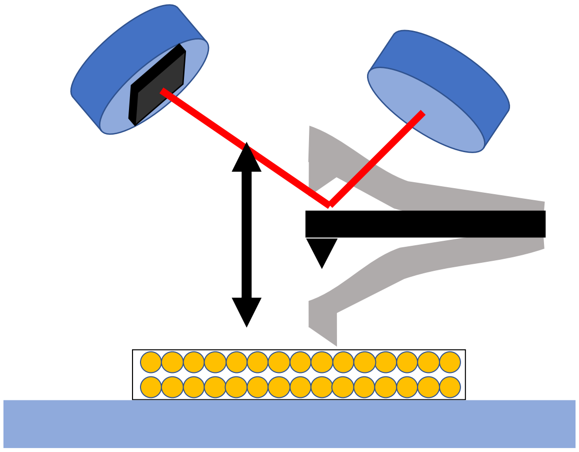

Figure 25. Schematic drawing of tapping mode AFM.

The tips used in this work are Bruker model RTESPA-300 tips. These are silicon tips with an aluminum reflective coating on the back to enhance the reflected laser signal. Bruker cites these tips as having a cantilever width 40 ± 2 microns in width, and 115 ± 10 microns in length with a resonant frequency of 300 ± 100 kHz. The tip radius is 10 ± 2 nm, with angles of between 15 and 25 degrees upwards. The tip shape was not externally verified via SEM or similar techniques, and no corrections for the finite tip radius were done in the images. The actual procedure for measurements is provided in Appendix F (AFM Procedure).

Once the image is taken, a .flt file is generated with the x, y, z data. This can then be loaded into software such as WSxM[257] or Gwyddion.[258] Images presented in this work were analyzed in WSxM. The images presented are mostly unaltered. The only corrections that are performed is a parabola flattening along the row direction, which levels the image. This eliminates the piezo nonlinear bowing, as well as any tilt from the sample not being perfectly horizontal. Then an equalize function is applied, which sets limiting cut-off values for z-height extrema.

2.9 Polarized Neutron Reflectometry

Polarized Neutron Reflectometry (PNR) is a relatively new technique but has quickly proven to be an extremely powerful one. Most techniques to probe magnetic materials involve a fundamental tradeoff between bulk averaged sensitivity as in magnetometry, or surface sensitivity due to the strong interactions with the materials as in magnetic force microscopy or XPEEM. PNR is one of the rare techniques that allows depth dependent probing of a thin film with atomic resolution, while still being able to probe the entire thickness of the film.

Conceptually, PNR is very similar to the XRR techniques of the previous sections. Physically, our electromagnetic wave is replaced by a neutron represented by a plane wave with de Broglie wavelength λ , incident wave vector $k_0 = \frac{2\pi}{\lambda}$, and energy $E_0 = \frac{\hbar^2 k_0^2}{2m}$. m is the mass of the neutron, and $\hbar$ Planck's constant. In principle, this could be generalized into a localized wave packet via superposition of plane waves with varying wave vectors. However, it is fortunately the case that the plane wave description is sufficiently accurate for our needs, and the following will take advantage of the plane wave formulations' simplicity and clarity. In addition, the PNR results to be presented in future chapters rely solely on the specular (coherent) reflection, which is due solely to elastic collisions. This specular data is sufficient to fully characterize the magnetic properties through the depth of the film. Off-specular reflection, while it can offer a wealth of other extra information, isn't necessary.

The scalar wavefunction Ψ can be written, for a plane wave, as

$$\Psi(\vec{\mathbf{k}}, \vec{\mathbf{r}}) = e^{i\vec{\mathbf{k}}\cdot\vec{\mathbf{r}}} \qquad 2.21$$

with wave vector $\vec{\mathbf{k}} = k_x\vec{\mathbf{x}} + k_y\vec{\mathbf{y}} + k_z\vec{\mathbf{z}}$ and position vector $\vec{\mathbf{r}} = x\vec{\mathbf{x}} + y\vec{\mathbf{y}} + z\vec{\mathbf{z}}$. As is typical, the modulus squared of the wavefunction, $|\Psi|^2 = \Psi^* \Psi$ gives the probability of finding the neutron at some location in space, with a momentum $p = mv = \frac{h}{\lambda} = \hbar k$. The neutron wavefunction obeys Schrodinger's equation, with the elastic condition reducing it to the time-independent version

$$\left[\frac{-\hbar^2}{2m}\nabla^2 + V(\vec{\mathbf{r}})\right]\Psi(\vec{\mathbf{r}}) = E\Psi(\vec{\mathbf{r}}) \qquad 2.22$$

where m is the neutron mass, E the neutron's total energy, and $V(\vec{\mathbf{r}})$ the interaction potential. V consists of two main components, the interactions with nuclei via the strong interaction, and magnetic interactions between the spin-$\frac{1}{2}$ neutron and both nuclear and electronic magnetic moments in the sample. $\nabla^2 = \frac{\partial^2}{\partial x^2} + \frac{\partial^2}{\partial y^2} + \frac{\partial^2}{\partial z^2}$ in Cartesian coordinates. The first term on the left-hand side (LHS) corresponds the particle's kinetic energy, and the second to the potential energy of the neutron. In vacuum where there is no interaction potential, (2.20) immediately reduces and the initial energy E_0 is given solely by the kinetic energy as $E_0 = \frac{1}{2}mv_0^2 = \frac{\hbar^2 k_0^2}{2m}$.

To simplify the problem without compromising the results, we will assume that the nuclear spins are completely disordered, and therefore don't contribute to the specular reflection. Even for relatively large applied magnetic fields, nuclear polarization is typically less than 1%.[259] In addition, we will make the same assumption as in the X-ray scattering case that the atomic form factor, i.e. the spatial distribution of electrons around atoms, can be neglected. Lastly, for the materials considered in this work, neutron absorption is negligible and can be neglected.

First, we deal with the scattering caused by the nuclear interaction. The nuclei are sufficiently localized relative to the neutron wavelength that they can be represented by a Fermi pseudo-potential in the impulse approximation. A convenient choice for a single atom, applying a Born approximation, is

$$V_F(\vec{\mathbf{r}}) = b\frac{2\pi\hbar^2}{m}\delta(\vec{\mathbf{r}}) \qquad 2.23$$

where b is a scattering length, and $\delta(\vec{\mathbf{r}})$ a Dirac delta function. This impulse approximation is much easier to work with, while maintaining the appropriate scattering cross section.[260] Formally, b is usually given as

$$b = b_c + \frac{1}{2}b_N I \cdot \sigma \qquad 2.24$$

where the first term on the right-hand side (RHS) is the coherent scattering length due to the strong interaction. The latter term is the magnetic interaction with the nucleus, which as stated earlier, can be neglected in the specular response when the nuclear spins are sufficiently disordered.

The mean potential V, or potential energy, can be given by integrating V_F over the volume of the scattering material

$$V_N = \frac{1}{\mathcal{V}}\int_{\mathcal{V}} V_F(\vec{\mathbf{r}})d^3\vec{\mathbf{r}} = \frac{2\pi\hbar^2}{m}Nb = \frac{2\pi\hbar^2}{m}\rho \qquad 2.25$$

where ρ is now a scattering length density (SLD) for the material. For a material made of m different constituent atoms, ρ is immediately generalizable as

$$\rho = \sum_{i=1}^{m} N_i b_i \qquad 2.26$$

This new formulation allows us to recast the Schrodinger equation in a simpler fashion as a 3-D wave equation

$$\left[\nabla^2 + k_0^2 - 4\pi\rho\right]\Psi(\vec{\mathbf{r}}) = 0 \qquad 2.27$$

In addition, this now allows us to write down the energy inside the medium as

$$E = \frac{\hbar^2 k^2}{2m} + \frac{2\pi\hbar^2}{m}\rho \qquad 2.28$$

From conservation of energy, a useful relationship between the wavevectors is

$$k^2 = k_0^2 - 4\pi\rho \qquad 2.29$$

In direct analogy to optics, we can define a refractive index $n = \frac{k}{k_0}$ or

$$n(k_0) = \sqrt{1 - \frac{4\pi\rho}{k_0^2}} \qquad 2.30$$

The Schrodinger equation becomes more compact, as

$$\left[\nabla^2 + k^2\right]\Psi(\vec{\mathbf{r}}) = 0 \tag{2.31}$$

We are now ready to begin solving for the reflection. Consider a perfectly smooth, flat and homogenous slab with some thickness L, and infinite length in the lateral directions. Further, we will assume that variations in the scattering length density (SLD) are only a function of z. This scenario is sketched out in Figure 26.

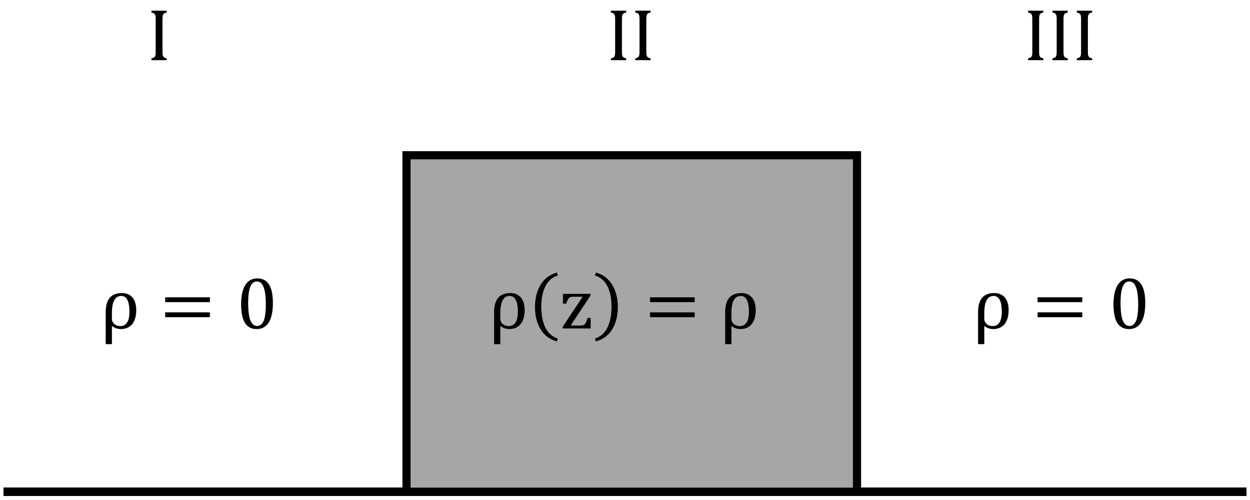

Figure 26. Schematic for a single slab with constant nonzero SLD and surrounded by vacuum.

No variation of the SLD in the x and y directions implies that there can be no gradient in the potential, and therefore the momentum and wave vector in the x and y directions are constant. An appropriate choice of wave function is of the form

$$\Psi(\vec{\mathbf{r}}) = e^{ik_{0,x}}e^{ik_{0,y}}\psi(z) \tag{2.32}$$

The Schrodinger equation then simplifies into the 1-D form

$$\left[\frac{\partial^2}{\partial z^2} + k_{0,z}^2 - 4\pi\rho(z)\right]\psi(z) = 0 \tag{2.33}$$

It is instructive to consider the special case when $\rho(z)$ inside the slab is constant, which permits a simple solution $\psi(z) = e^{ik_z z}$. A more general approach will be discussed momentarily.

The total wave function in region I can be written as the sum of the incident wave, and a reflected wave with amplitude r

$$\psi_I(z) = 1e^{ik_I z} + re^{-ik_I z} \tag{2.34}$$

With the sign convention indicating the direction of travel. Similarly, for II we can write

$$\psi_{II}(z) = ce^{ik_{II} z} + de^{-ik_{II} z} \tag{2.35}$$

Where c and d are as yet undetermined amplitudes. And lastly, for III,

$$\psi_{III}(z) = te^{ik_{III} z} \tag{2.36}$$

Where again t is an undetermined amplitude. We now need to pick appropriate boundary conditions. We require that the wave function and its first derivative are continuous in order to satisfy conservation of the probability density current (i.e., number of neutrons) and conservation of momentum, respectively. These two equations at each interface will establish 4 equations to fully determine the 4 complex amplitude coefficients r, c, d, and t as

$$1 + r = c + d \tag{2.37}$$

$$\left(\frac{k_I}{k_{II}}\right)(1 - r) = c - d \tag{2.38}$$

$$ce^{ik_{II}L} + de^{-ik_{II}L} = te^{ik_{II}L} \tag{2.39}$$

$$ce^{ik_{II}L} - de^{-ik_{II}L} = \left(\frac{k_{III}}{k_{II}}\right)te^{ik_{II}L} \tag{2.40}$$

A bit of algebra allows us to eliminate any explicit dependence on c and d. Isolating the t dependent terms on the LHS, and r on the RHS, yields, in matrix form

$$\begin{pmatrix} t \\ ik_{III}t \end{pmatrix} e^{ik_{III}L} = \begin{bmatrix} \cos(k_{II}L) & \frac{-1}{k_{II}}\sin(k_{II}L) \\ -k_{II}\sin(k_{II}L) & \cos(k_{II}L) \end{bmatrix} \begin{pmatrix} 1+r \\ ik_I(1-r) \end{pmatrix} = T \begin{pmatrix} 1+r \\ ik_I(1-r) \end{pmatrix} \qquad 2.41$$

The matrix in the above equation is the well-known transfer matrix, T, and contains all the material parameters of the slab. These equations can be solved for t and r simultaneously, and the intensity of the reflection that is experimentally accessible, R, is given by $R = |r|^2 = r^*r$. The above treatment was only given for a single slab, in the specific case where the SLD was constant along the slab. However, the extension to an SLD with variations along z can be done by dividing any SLD profile up into infinitesimal bins with length δL and solving each slab successively by induction. Experimental setups impose a natural limit to minimum bin size due to the maximum depth resolution. This depth resolution is directly tied to the range of Q measured, since the maximum Q is given by $Q_{max} = \frac{\pi}{\delta L}$ due to the Fourier nature between space and momentum.[261] The transfer matrix T for n bins can be generalized as

$$T = \prod_{i=1}^{n} T_i = T_n T_{n-1} \dots T_2 T_1 \qquad 2.42$$

The resulting product is also a 2x2 matrix. Notably, the individual transfer matrices T_i should be applied in the order that the neutron travels through the slab.

We now have a method that can be used to calculate r, and therefore R. However, in practice, we wish to do the inverse problem where, given some measurement of R, one constructs a model of their SLD profile and attempts to match the data via nonlinear least squares fits. Even with a good fit, however, there is no guarantee to uniqueness of the solution. Luckily in many cases, including ours, a reasonable amount of detail of the films is previously known via the deposition process and XRR analysis, which can compensate for the lost phase information. These constraints are often enough to obtain reasonable fits where useful information can be extracted. More recent research is ongoing into finding ways to find the phase data lost in the measurement, such as via the use of fronting and backing plates,[261] but for this experiment we stuck with previously known data to constrain the fits. More details into the fitting procedure will be given in at the end of the section, as well as in Chapter 6.

The above provides a dynamical solution to the main nonmagnetic interactions between the neutron and the sample. The neutron is a spin $\frac{1}{2}$ particle, with spin $|\vec{\mathbf{s}}| = \pm\frac{\hbar}{2}$. This spin will be quantized along the direction of the local magnetic field and can be represented by the appropriate Pauli spin matrices as $\vec{\mathbf{s}} = -\frac{\hbar}{2}\vec{\boldsymbol{\sigma}}$. We can incorporate this description of spin into the neutron wave function by adopting the spinor notation, and the wave function can be written as

$$\Psi(\vec{\mathbf{r}}) = \mathrm{C}_{+}\begin{pmatrix}1\\0\end{pmatrix}\Psi_{+}(\vec{\mathbf{r}}) + \mathrm{C}_{-}\begin{pmatrix}0\\1\end{pmatrix}\Psi_{-}(\vec{\mathbf{r}}) \qquad 2.43$$

C_{+} and C_{-} are complex probability amplitudes, normalized such that $|\mathrm{C}_{+}|^2 + |\mathrm{C}_{-}|^2 = 1$. $|\mathrm{C}_{+}|^2$ and $|\mathrm{C}_{-}|^2$ represent the probability of finding the neutron in a spin “up” or spin “down” state.

The magnetic interaction is a dipolar one, between the neutron and unpaired electrons of the material. This leads to a Zeeman energy term[262]

$$\mathrm{V}(\vec{\mathbf{r}})_{\mathrm{mag}} = -\vec{\boldsymbol{\mu}} \cdot \vec{\mathbf{B}} \qquad 2.44$$

Where $\vec{\boldsymbol{\mu}}$ is the neutron's magnetic moment due to its intrinsic spin angular momentum. $\vec{\boldsymbol{\mu}} = -g_n\mu_n\vec{\boldsymbol{\sigma}}$, where $g_n = -1.913$ is the gyroscopic ratio, $\mu_n = \frac{e\hbar}{2mc}$ is the nuclear magneton, and $\vec{\boldsymbol{\sigma}}$ is a Pauli spin operator represented by the three Pauli spin matrices. $|\vec{\boldsymbol{\mu}}| = -9.66 \times 10^{-27} \frac{J}{T}$ in magnitude. $\vec{\mathbf{B}}$ is the total magnetic induction given by both the applied field as well as that generated by unpaired electrons acting as tiny current loops and can be written as $\vec{\mathbf{B}} = \vec{\mathbf{H}} + \mu_0\vec{\mathbf{M}}$. The field due to the electrons is given by[247]

$$\vec{\mathbf{B}}_e(\vec{\mathbf{r}}) = \frac{\mu_0}{4\pi}\left[\boldsymbol{\nabla} \times \left(\frac{\vec{\boldsymbol{\mu}}_{\mathbf{e}} \times \vec{\mathbf{r}}}{|\vec{\mathbf{r}}|^3}\right) - \left(\frac{\vec{\mathbf{v}}_e \times \vec{\mathbf{r}}}{|\vec{\mathbf{r}}|^3}\right)\right] \qquad 2.45$$

Where μ_0 is the vacuum permeability. $\vec{\boldsymbol{\mu}}_{\mathbf{e}}$ is the electron magnetic moment with magnitude $|\vec{\boldsymbol{\mu}}_{\mathbf{e}}| = -g\mu_B$, where g is the Landé g-factor and μ_B the Bohr magneton. For electrons, $g = 2$. $\vec{\mathbf{v}}_{\mathbf{e}}$ is the electron's velocity. The first term in the expression on the RHS is the electron's spin contribution to the field, and the second term due to the orbital contribution. Experimentally, PNR is sensitive to the overall field, with no way to isolate or resolve each component. We next need to integrate $V(\vec{\mathbf{r}})_{mag}$ for the slab, as we did for $V(\vec{\mathbf{r}})_N$. In general, this is trickier than in the case of the Dirac delta function. Fortunately, the electromagnetic interaction is a weak, long range, force, and is thus amenable to a Born approximation.[259] Writing $\vec{\mathbf{B}}_e(\vec{\mathbf{r}})$ in its Fourier representation and integrating over the slab of length L with constant atomic density ρ yields[247]

$$V_M(\vec{\mathbf{r}}) = \frac{2\pi\hbar^2}{m}\frac{|g_n r_e|}{2}\rho\vec{\boldsymbol{\sigma}}\cdot\vec{\mathbf{M}}_{||}[\theta(L) - \theta(0)] \qquad 2.46$$

Where θ represents the Heaviside step function. This expression shows that we will only be sensitive to the in-plane magnetization. In addition, the expression is localized completely inside the slab, which makes it possible to solve each bin separately in our multislab model as we did earlier. The above expression only considered $\vec{\mathbf{B}}_e(\vec{\mathbf{r}})$, rather than $\vec{\mathbf{B}}(\vec{\mathbf{r}})$. If we define an effective field $\vec{\mathbf{B}}_{\mathrm{eff}}(\vec{\mathbf{r}}) = \vec{\mathbf{H}}(\vec{\mathbf{r}}) + \mu_0\vec{\mathbf{M}}_{||}(\vec{\mathbf{r}})$, we can recast the expression for $V_M(\vec{\mathbf{r}})$ and interpret it in terms of a SLD as

$$V_M(\vec{\mathbf{r}}) = -\mu_N \cdot \vec{\mathbf{B}}_{\mathrm{eff}}(\vec{\mathbf{r}}) = \frac{2\pi\hbar^2}{m}\rho_M \qquad 2.47$$

From here on out, for conciseness, we will drop the subscript on $\vec{\mathbf{B}}_{\mathrm{eff}}(\vec{\mathbf{r}})$, but unless otherwise specific, any mention of a magnetic induction $\vec{\mathbf{B}}(\vec{\mathbf{r}})$ should be understood as referring to $\vec{\mathbf{B}}_{\mathrm{eff}}(\vec{\mathbf{r}})$.

The 1-D wave equation from the previous results now becomes a pair of coupled equations of the form

$$\left[\frac{\hbar^2}{2m}\frac{\partial^2}{\partial z^2} + V_{++}(z) - E\right]\psi_+(z) + V_{\pm}\psi_- = 0 \qquad 2.48$$

$$\left[\frac{\hbar^2}{2m}\frac{\partial^2}{\partial z^2} + V_{--}(z) - E\right]\psi_-(z) + V_{\mp}\psi_+ = 0 \qquad 2.49$$

The subscripts of V denote the orientation of the spin, such that + − corresponds to a spin that is incident in the “up” direction, undergoes a spin flip, and leaves in the “down” orientation. Or in the more compact matrix notation

$$\left[\frac{\hbar^2}{2m}\frac{\partial^2}{\partial z^2}\check{I} + \begin{bmatrix} V_{++}(z) & V_{\pm}(z) \\ V_{\mp}(z) & V_{--}(z) \end{bmatrix} - E\check{I}\right]\begin{pmatrix}\psi_+ \\ \psi_-\end{pmatrix} = 0 \qquad 2.50$$

Where $\check{I}$ is the identity operator. The net potential operator $\check{V} = \check{V}_N + \check{V}_M$ is composed of both the nuclear and magnetic components. We solved for $\check{V}_N$ earlier, and it in matrix notation it is given as

$$\check{V}_N = \frac{2\pi\hbar^2\rho_N}{m}\check{I} \tag{2.51}$$

Whereas $\check{V}_M$ can be written as (writing $\vec{\mathbf{B}}$ in terms of the Pauli matrices)

$$\check{V}_M = -\mu\check{\sigma}\cdot\vec{\mathbf{B}} = -\mu\begin{bmatrix} B_z & B_x - iB_y \\ B_x + iB_y & B_z \end{bmatrix} = \frac{2\pi\hbar^2}{m}\begin{bmatrix} \rho_{M,z} & \rho_{M,x} - i\rho_{M,y} \\ \rho_{M,x} + i\rho_{M,y} & -\rho_{M,z} \end{bmatrix} \tag{2.52}$$

And thus $\check{V}$ is

$$\check{V} = \frac{2\pi\hbar^2}{m}\begin{bmatrix} \rho_N + \rho_{M,z} & \rho_{M,x} - i\rho_{M,y} \\ \rho_{M,x} + i\rho_{M,y} & \rho_N - \rho_{M,z} \end{bmatrix} = \frac{2\pi\hbar^2}{m}\begin{bmatrix} \rho_{++} & \rho_{\pm} \\ \rho_{\mp} & \rho_{--} \end{bmatrix} \tag{2.53}$$

We can immediately write down the free space solution for the incident beam as

$$\Psi_{0z}(z) = e^{ik_0z}\begin{pmatrix} C_+ \\ C_- \end{pmatrix} \tag{2.54}$$

Returning to Eqn. 2.48 and Eqn. 2.49, it is useful to recast them in uncoupled form by isolating an expression for ψ_- and substituting it in the lower equation (and vice versa for ψ_+), at the expense of obtaining two 4th order differential equations. The uncoupled forms are given as

$$\left[\frac{\partial^4}{\partial z^4} + a\frac{\partial^2}{\partial z^2} + b\right]\psi_{\pm}(z) = 0 \tag{2.55}$$

With

$$a = \left(\frac{Q^2}{2} - 4\pi\left(\rho_{++} - \rho_{--}\right) \right) \qquad 2.56$$

$$b = \left(\frac{Q^2}{4}\right)^2 - Q^2\pi\left(\rho_{++} - \rho_{--}\right) + \ (4\pi)^2\left(\rho_{++}\rho_{--} - \ \rho_{\pm}\rho_{\mp}\right) \qquad 2.57$$

An appropriate ansatz for this situation is given by $\psi(z) = \ e^{cz}$, which yields a characteristic equation of the form

$$c^4 \ + \ ac^2 \ + \ b = 0 \qquad 2.58$$

The roots to this characteristic equation are

$$c_1 \ = \ \sqrt{4\pi(Nb + Np) - \frac{Q^2}{4}} \quad , \quad c_2 \ = \ -\sqrt{4\pi(Nb + Np) - \frac{Q^2}{4}} \qquad 2.59$$

$$c_3 \ = \ \sqrt{4\pi(Nb \ - \ Np) - \frac{Q^2}{4}} \quad , \quad c_4 \ = \ -\sqrt{4\pi(Nb + Np) - \frac{Q^2}{4}} \qquad 2.60$$

Solutions to the wave equation are then

$$\psi_+(z) = \sum_{j=1}^{4} A_j e^{c_j z} \quad , \quad \psi_-(z) = \sum_{j=1}^{4} B_j e^{c_j z} \qquad 2.61$$

Substituting these forms for the wave functions back into (2.46,2.47) allows us to determine B_j in terms of the A_j as

$$B_j = \left[\frac{c_j^2 + \frac{Q^2}{4} - 4\pi(\rho_{++} - \ \rho_{\mp})}{c_j^2 + \frac{Q^2}{4} - 4\pi(\rho_{--} - \ \rho_{\pm})} \right] A_j = \ f_j A_j \qquad 2.62$$

The A_j can be found in terms of known quantities ($c_j, \rho, \psi(0), \frac{\partial\psi}{\partial z}(0)$) by applying the boundary conditions at z=0.

$$\psi_+(0) = A_1 + A_2 + A_3 + A_4 \tag{2.63}$$

$$\frac{\partial\psi_+}{\partial z}(0) = c_1A_1 + c_2A_2 + c_3A_3 + c_4A_4 \tag{2.64}$$

$$\psi_-(0) = f_1A_1 + f_2A_2 + f_3A_3 + f_4A_4 \tag{2.65}$$

$$\frac{\partial\psi_-}{\partial z}(0) = c_1f_1A_1 + c_2f_2A_2 + c_3f_3A_3 + c_4f_4A_4 \tag{2.66}$$

We can solve the above linear equations for A_j in terms of $\psi_\pm$, c_j , f_j and denote those coefficients α_j , β_j , γ_j , η_j such that

$$A_j = \alpha_j\psi_+(0) + \beta_j\psi_-(0) + \gamma_j\frac{\psi_+}{\partial z}(0) + \eta_j\frac{\psi_-}{\partial z}(0) \tag{2.67}$$

The wave functions can then be constructed as

$$\psi_+(z) = \psi_+(0)\sum_{j=1}^{4}\alpha_j e^{c_jz} + \psi_-(0)\sum_{j=1}^{4}\beta_j e^{c_jz} + \frac{\partial\psi_+}{\partial z}(0)\sum_{j=1}^{4}\gamma_j e^{c_jz} + \frac{\partial\psi_-}{\partial z}(0)\sum_{j=1}^{4}\eta_j e^{c_jz} \tag{2.68}$$

In full matrix form,

$$\begin{pmatrix}\psi_+(z)\\ \psi_-(z)\\ \psi'_+(z)\\ \psi'_-(z)\end{pmatrix} = [T]\begin{pmatrix}\psi_+(0)\\ \psi_-(0)\\ \psi'_+(0)\\ \psi'_-(0)\end{pmatrix} \tag{2.69}$$

Where T is again the (now 4x4) transfer matrix, given below:

$$\begin{bmatrix} f_3C^1 - f_1C^3 & C^1 - C^3 & \frac{f_3}{c_1}S^1 - \frac{f_1}{c_3}S^3 & \frac{1}{c_1}S^1 - \frac{1}{c_3}S^3 \\ f_1f_3C^1 - f_3f_1C^3 & f_1C^1 - f_3C^3 & f_1f_3S^1c_1 - f_3f_1S^3c_3 & \frac{f_1}{c_1}S^1 - \frac{f_3}{c_3}S^3 \\ f_3S^1c_1 - f_1S^3c_3 & S^1c_1 - S^3c_3 & f_3C^1 - f_1C^3 & C^1 - C^3 \\ f_1f_3S^1c_1 - f_3f_1S^3c_3 & f_1S^1c_1 - f_3S^3c_3 & f_1f_3C^1 - f_3f_1C^3 & f_1C^1 - f_3C^3 \end{bmatrix} \qquad 2.70$$

In the above, C^j, S^j represent hyperbolic trigonometric functions $C^j = \cosh(c_jL)$ and $S^j = \sinh(c_jL)$ respectively. Where L is the size of the bin slice used. We can immediately make the generalization for N slices as before. Our incident, reflected, and transmitted wavefunctions can be written as $\psi_{\pm,I}(z) = I_\pm e^{i\frac{Qz}{2}}$, $\psi_{\pm,r}(z) = r_\pm e^{-i\frac{Qz}{2}}$, $\psi_{\pm,t}(z) = t_\pm e^{i\frac{Qz}{2}}$, and $\psi'_{\pm,I}(z) = \frac{iQ}{2}I_\pm e^{i\frac{Qz}{2}}$, $\psi'_{\pm,r}(z) = \frac{-iQ}{2}r_\pm e^{-i\frac{Qz}{2}}$, $\psi'_{\pm,t}(z) = \frac{iQ}{2}t_\pm e^{i\frac{Qz}{2}}$. Our final matrix equation is then

$$\begin{pmatrix} \psi_{+,t} \\ \psi_{-,t} \\ \frac{iQ}{2}\psi_{+,t} \\ \frac{iQ}{2}\psi_{+,t} \end{pmatrix} = T \begin{pmatrix} \psi_{+,I} + \psi_{+,r} \\ \psi_{-,I} + \psi_{-,r} \\ \frac{iQ}{2}\psi_{-,I} + \frac{-iQ}{2}\psi_{-,r} \\ \frac{iQ}{2}\psi_{-,I} + \frac{-iQ}{2}\psi_{-,r} \end{pmatrix} \qquad 2.71$$

This equation is easily solvable by a computer program, and can simulate arbitrary SLD profiles for multilayer structures, with a few caveats. The first is that this solution was presented assuming vacuum in the fronting and backing layers. While no magnetic fronting or backing was used in this experiment, it is often necessary to introduce an artificial bin to ensure that $\vec{\mathbf{B}}$, particularly the component perpendicular to the sample, is continuous. In addition, the above derivation assumes that the quantization axis for the neutron is along the z direction. It is often the case that the local magnetic field may be in a different direction. This is can be accounted for by applying a similarity transformation via a rotation operator.[261]

The above formalism is implemented into the Refl1D software package.[252] This software suite offers a number of fitting algorithms, in particular the DiffeRential Evolution Adaptive Metropolis (DREAM) algorithm and the Nelder-Mead (NM) method.[263,264] The details of how individual samples were co-refined will be given in a following chapter. Given some reasonable initial parameters, we first apply the DREAM algorithm, which is an extension of Markov Chain Monte Carlo Methods (MCMC), which are well known workhorses. However, while MCMC's are a powerful technique, they are quite sensitive to proposal distributions used to generate trial moves and can converge quite slowly. To improve convergence, a variety of methods that adapt the proposal distribution have been developed but have various pitfalls. A recent improvement was made by adding the Differential Evolution component, in which multiple Markov Chains are run in parallel, and jumps are computed from randomly chosen members of the population. The DREAM algorithm builds on this further by including randomized subspace sampling in candidate point generation and trimming outlier chains. Remarkably, it is able to preserve detailed balance and ergodicity. In this work, about 1000 steps were used, depending on the parameter space. The DREAM algorithm thus provides a robust way to quickly sample a potentially large parameter space, which can then be further refined by the NM method. The NM method is a simplex method, which begins with a simplex of N+1 vertices and nondegenerate volume for an N dimensional function space. Steps are made by reflecting away from the largest point in the simplex while maintaining a fixed volume but with the option to take larger steps in certain directions when possible. Once the simplex is located inside a valley minimum, it will contract until it reaches some termination criteria. The NM method thus provides a relatively computationally cheap way to find a minimum of a multidimensional function without requiring the calculation of derivatives. However, it is also known to converge poorly and become stuck in local minima for some problems. Avoiding false minima is a particularly important concern due to the degeneracy of PNR modeling. Combining the two fitting techniques thus provides a robust way to find a local minimum, particularly when combined with a reasonable starting guess. Ideally this will be a global minimum, although it is not guaranteed.

In the previous derivation, it was assumed that the interfaces between each layer were sharp, causing a step function behavior. Refl1D allows interfaces to be blended using an error function profile, made up of individual slabs. Roughness of the interface is calculated within the NC limit. It is worth noting that the condition for optical smoothness, $\sigma \ll \frac{\lambda}{1-n}$, is much less strict as compared to X-rays, even with a comparable wavelength. In the NC formalism, the index of refraction is scaled as $e^{-2k_{j-1}k_j\sigma^2}$ as defined in the XRR section. Roughness of an interface is propagated through the layer as in Ref. [265].

Before the data was fitted, several corrections to the raw data were made using the reductus software package.[266] First, background scans were subtracted from the data. Then corrections were made to account for the polarization efficiency of the source. The footprint of the beam was also accounted for.

The physical PNR measurements were taken at NIST's Center for Neutron Research (NCNR) at the Polarized Beam Reflectometer (PBR) instrument, which has been characterized elsewhere.[267] Thermal neutrons were monochromated to 4.75 Å, and polarized. For direct comparison, it was attempted to mimic the procedure outlined for VSM as closely as possible. The procedure (not including alignment and background scanning) used was

1) First, the sample was heated above T_c, to 450 K with zero field applied.

2) Then a large field (H = 0.7 T, the maximum for the system) was applied in-plane to saturate the sample. This is lower than the VSM field, but considering the magnetic profile of the FeRh, it likely is more than sufficient.
3) The field is reduced to 0.1 T,
4) PNR measurements were taken for a select temperature, in our case 430 K
5) The temperature is reduced to the next select temperature and measured. This process was done for 390 K, 375 K, and 340 K, corresponding to different parts of the FeRh phase transition.

Only the “up-up” and “down-down” reflectivity intensities were collected. The range of Q values collected was $0.1 - 1.2$ Å^{-1}, spanning a 10^{-7}range in the magnitude of the intensity, normalized to the incident beam. In addition to the above, additional PNR measurements were made to measure magnetic switching at various applied fields. The procedure is the same as the above up to step 4. The magnetic field was then cycled to -0.1 T, and back up to 0.25 T, before a measurement was taken.

Chapter 3. Conditioning

3.1 Motivation

In order to prepare our VO_2/Ni bilayers, the first requirement is to grow high quality VO_2. In this chapter, we present the results of a study to tune the MIT, morphology and structural quality of VO_2 films. The goals in this work were two-fold: first was the need to grow high quality VO_2, evidenced by 4 orders of magnitude MIT. The sensitivity of VO_2 transition to deposition conditions means that optimized VO_2 growth is a challenge, even without other constraints on e.g. the morphology. However, in order to eventually combine VO_2 into hybrid structures, control of the interface is also a crucial parameter. Interfacial roughness is often a key parameter for proper coupling in multilayer magnetic systems dominated by interfacial interactions. Therefore, in addition to maintaining a high quality VO_2 transition, the secondary goal was to reduce the surface roughness of the VO_2 for eventual deposition of Ni onto the VO_2 itself.

r-cut (1-102) Al_2O_3 substrates are an ideal choice for extensively tuning the quality of VO_2 growth. While the epitaxial match is not quite as good as c-cut (0001) Al_2O_3 or TiO_2, it is still possible to grow high quality VO_2 and the r-cut is relatively low cost. The first section of this chapter focuses on tuning the quality of VO_2 on r-cut Al_2O_3 via deposition temperature and O_2 flow rate. VO_2's sensitivity to these conditions allow them to be used as efficient tuning knobs in controlling both the VO_2 MIT while simultaneously tuning the surface morphology. The second section focuses specifically on higher temperature (> 575 ℃) depositions, which show a unique morphology. In the final section, we show that substrate choice can also heavily influence VO_2 morphology and MIT characteristics, offering another tuning knob to achieve desired properties in VO_2. Various cuts of Al_2O_3 (a-cut, m-cut, c-cut) as well as TiO_2 (101) substrates are investigated.

The VO_2 films were deposited via magnetron sputtering following the process described in Chapter 2. R vs. T measurements are used to characterize the electrical properties of the VO_2 as a function of temperature. In particular, R vs. T measurements give information about the size of the MIT, the T_c of the film, the width of the thermal hysteresis, and the overall shape of the hysteresis as a function of temperature. The roughness and film morphology are probed directly via AFM. XRD is used to probe the crystalline quality and preferred orientation of the films.

3.2 Tuning of VO_2 films via temperature and oxygen concentration

The sensitivity of the vanadium oxides to growth temperature and O_2 environment has been known ever since the original discovery and synthesis by Morin. The wide family of vanadium oxides in such similar stoichiometries mean that these parameters are of even more importance than in most typical thin film growths. They also therefore act as both constraints and tuning knobs, as high quality VO_2 with the required MIT/SPT properties will only be obtainable in a very narrow region of temperatures and O_2 flow rates. It is therefore common practice to individually vary temperature[268–275] or O_2 flow rate,[276–279] while keeping the other parameters fixed. This has the advantage of isolating the effect of one growth parameter, while still allowing a wide range of control in achieving high quality VO_2. A much smaller number of studies have varied both T and O_2.[280–283] The references given above are restricted to studies that utilized magnetron sputtering and no post deposition treatment (such as by annealing[284], which has become an extremely popular method for obtaining high quality VO_2 thin films) in order to be directly comparable. They thus serve as notable highlights rather than a comprehensive list of deposition conditions in the literature. We refer the reader to Ref.s [284,285] for deeper literature reviews, including alternative deposition methods.

As discussed in Section 2.4, we utilize a heating and cooling rate of 1 K/min in the R vs. T measurements. This is sufficiently slow to ensure no spurious results due to e.g. thermal lag. There is no active cooling element, which sets an upper limit to how quickly the sample can cool. This isn't a significant barrier for the chosen rate, particularly near T_c of the VO_2. Figure 27 shows typical R vs. T profiles for various heating and cooling rates on the same sample. While there are slight changes in the width of the hysteresis, they're relatively minor for rates less than 1 K/min. Notably, there seems to be a bigger effect in the heating curve, as opposed to the cooling. For rates larger than 1 K/min, the widening of the hysteresis begins to become notable. 1 K/min thus strikes a nice balance between proper characterization of the films while still being time efficient and avoiding any stochastic switching.[286] Another sign that there are no spurious results are the close match in T_c that will be seen in the VO_2/Ni heterostructures later, which are done in low vacuum.

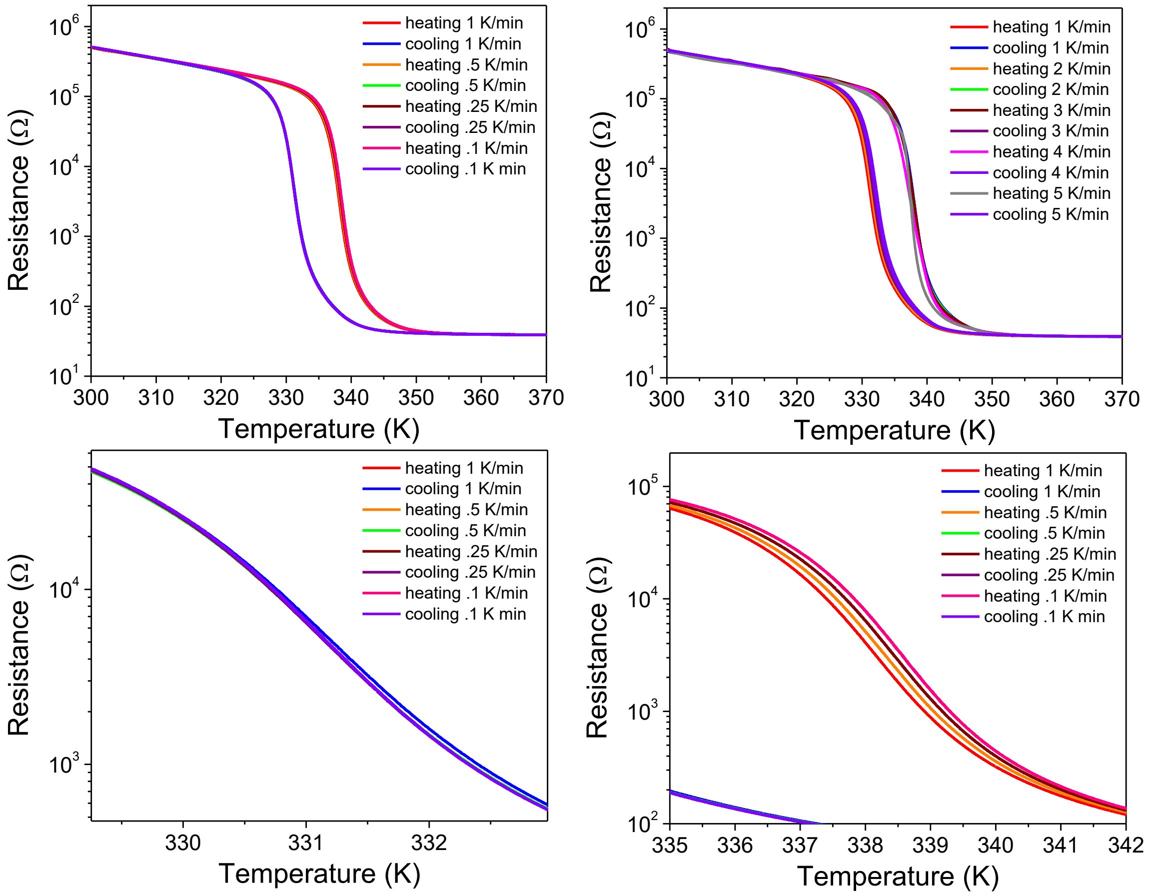

Figure 27. (Top Left) RvsT using various heating rates less than 1 K/min. (Top Right) RvsT using various heating rates greater than 1 K/min. (Bottom Left) Enhanced view of RvsT using various cooling rates less than 1 K/min, cooling branch. (Bottom Right) Enhanced view of RvsT using various heating rates less than 1 K/min, heating branch.

The sensitivity of the VO_2 MIT to temperature and O_2 flow rate can be seen in Figure 28 and Figure 29, which show VO_2 films for various temperatures and O_2 flow rates respectively. Figure 28 shows several 100 nm VO_2 samples grown on r-cut Al_2O_3 substrates, for a range of deposition temperatures. Many of the trends seen in the VO_2 MIT are broadly representative over various choices of deposition temperature. Most obviously, there is a clear reduction in the resistance of the semiconducting state with lower deposition temperature, when T is below T_c of the VO_2 transition. The reduction of resistance in the semiconducting state also corresponds to a reduction in the amplitude of the VO_2 MIT, leading to a smaller overall transition. Above T_c in the metallic state, a similar trend is seen for the 525 ℃ and 575 ℃ sample, but not the 475 ℃ sample. A decrease in resistance with lower deposition temperatures is also common for the metallic state, but at low enough temperatures the pattern is no longer monotonic. The increase (decrease) of resistance with varying conditions is not necessarily directly proportional between the semiconducting and metallic states, and so does not necessarily cancel out when comparing the overall effect on the MIT amplitude. We emphasize that the y-axis is on a log scale, which is nonlinear. Along with the change in amplitude of the MIT, we can see a rather large change in the characteristics of the thermal hysteresis between films. Higher temperatures show a much sharper MIT, which is linked to the variation of local T_c's in individual grains. A sharp MIT corresponds to most grains having very similar T_c, which causes most of the grains transition at the same temperature. A broadened MIT such as in the 475 ℃ sample is indicative of a larger variation in local grain T_c, where some grains will transition at higher temperatures, and some at lower temperatures relative to the average T_c. For the higher deposition temperatures, the thermal hysteresis is generally relatively symmetric. For the 475 ℃ sample, there is some minor asymmetry in the cooling loop as compared to the heating loop.

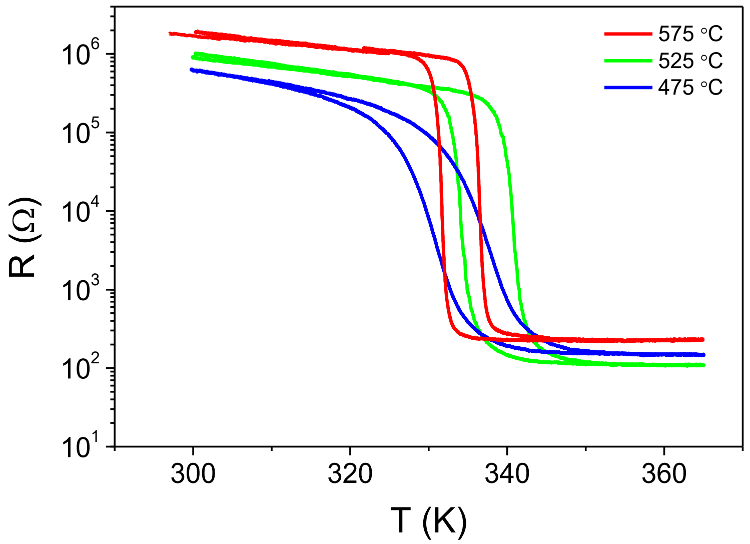

Figure 28. R vs. T for 100 nm VO_2 on r-cut Al_2O_3 substrate with varying deposition temperature but fixed O_2 flow rate at 2.75 sccm. The absolute sputter pressure was fixed at 4 mTorr, the Ar flow rate to 31 sccm, and the gun power to 200 W RF.

We now turn our attention to Figure 29 which shows variation in O_2 flow rate during deposition at a fixed 525 °C deposition temperature. With a fixed 31 sccm of Ar gas, these flow rates correspond to a variation from 7.92%-8.4% partial pressure of O_2 gas. Even for such minor changes, we see drastic changes in the VO_2 R vs. T characteristics. Some samples display a divergence or irreversibility in the resistivity at room temperature, particularly noticeable in the sample with 2.83 sccm O_2. The potential origins of this irreversibility will be the focus of a future chapter. Somewhat intuitively, in both the semiconducting and metallic states a higher oxygen concentration leads to a higher resistance in the film. As mentioned previously, these do not necessarily leave the overall amplitude of the MIT unchanged. A sample may therefore have a larger MIT with a higher resistance in the metallic state, due to the overall increase in resistance of the semiconducting state. This is particularly clear in the sample with 2.83 sccm O_2. While it starts with a higher resistance than the previous two samples, above T_c its resistance only drops to ≅ 5000 Ω, leading to an MIT of only 2-2.5 orders of magnitude. Similar reductions in the MIT amplitude are seen if the temperature or O_2 concentration is varied too low or too high. This is indicative of contamination from various other vanadium oxides. These other oxides may not have the same resistivity as VO_2 and won't show the VO_2 MIT. These factors will reduce the measured magnitude of the MIT of a nominally VO_2 film contaminated with other vanadium oxides since it's a bulk average measurement. Overall, the hysteresis loops are generally largely symmetric as before, but the exact shape varies with different O_2 conditions. The average T_c varies nonmonotonically within a small window close to 335 K. Samples with higher O_2 content show sharper transitions, indicating more uniformity between grains.

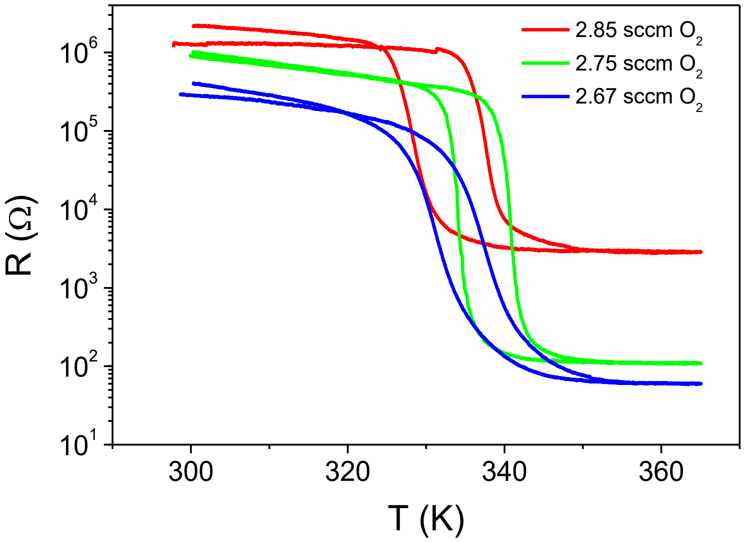

Figure 29. R vs. T for 100 nm VO_2 on r-cut Al_2O_3 substrate with varying O_2 flow rate but fixed temperature at 525 °C. The absolute sputter pressure was fixed at 4 mTorr, the Ar flow rate to 31 sccm, and the gun power to 200 W RF.

In addition to changes in the R vs. T properties of the films, altering the deposition temperature or O_2 content influences the morphology. The AFM images corresponding to the R vs. T profiles shown in the previous two figures are shown in Figure 30 and Figure 31. Figure 30 corresponds to the VO_2 samples deposited at various temperatures (575 °C, 525 °C, and 475 °C respectively). The AFM image for each sample is shown on the left, and a line profile corresponding to the green line in the AFM image is displayed to the right. The 575 °C sample shows the largest surface roughness, with an RMS roughness of 17.6 nm, and an average subtracted height of 55.4 nm. The average height refers to the height relative to the lowest value measured by the AFM scan, not relative to the substrate, since AFM is a surface technique. A perfectly flat 100 nm thick film would have an average subtracted height of 0, not 100 nm. The larger clusters are roughly 0.25 microns long in the $+1\hat{\imath} - 1\hat{\jmath}$ direction of the image, and roughly 0.6-0.8 microns in the $+1\hat{\imath} + 1\hat{\jmath}$ direction. The clusters are then divided up into smaller tightly packed columns. The grains are rather columnar in form and display some clear faceting, although they protrude at an angle. Some grains display something like a triangle-like symmetry. In addition, some areas show deep gaps in the film. The 525 °C sample shows a relatively similar structure, although the grains are less oriented along a global pair of axes, indicating less long-range ordering. The grain clusters are elongated, around 1.6 microns and 0.25 microns laterally. The sample still shows deep holes film in places. The depth of these holes is at least 40-50 nm, although exact depth determination may be limited by tip geometry. The average roughness is lower than the higher temperature sample, with an RMS roughness of 13.6 nm, and an average height of 37.4 nm. The 475 °C sample improves this smoothness even further, with an RMS roughness of 10.9 nm and average height of 27.8 nm. In this sample, the deep holes are greatly reduced as compared to the previous two, with near universal coverage across the film. One of the characteristic length scales for the grains is maintained at 0.25 microns.

For completeness, we also report the skew and kurtosis in the height distributions of the images. The skew represents some asymmetry in the distribution, with a negative skew representing a shoulder to the right, and positive skew a shoulder to the left. Roughly speaking, kurtosis corresponds to the 'peakedness' of the distribution. There can be complications with this definition in general, but our samples are close enough to a Gaussian distribution and sufficiently sampled that this definition is sufficient. For comparison, a Gaussian distribution corresponds to a kurtosis of 3. The 575 ℃, 525 ℃, and 475 ℃ have skews of 0.15, 0.32 and 0.13 and kurtosis of 3.43, 2.98 and 2.5 respectively. There is no clear trend in the skew values between samples, although it is clear all of them have a slight heavier weighting on the left shoulder in the height distribution. The kurtosis values are all relatively close to a Gaussian value of 3 but show a clear trend of decreasing kurtosis with lower deposition temperature. The decreasing kurtosis, indicating a flatter distribution, agrees well with the broader R vs. T results which would correspond to more variation between grain properties. A sharply peaked distribution such as a delta function would correspond to all grains being identical and a step-like MIT. There is a clear limitation in using a parameter such as the kurtosis sampled from AFM as it only gives information in the z direction and not in the lateral statistics. Nevertheless, there tends to be a clear correlation between the kurtosis in films' height distributions and their MIT properties, particularly for directly comparable samples where one parameter is varied.

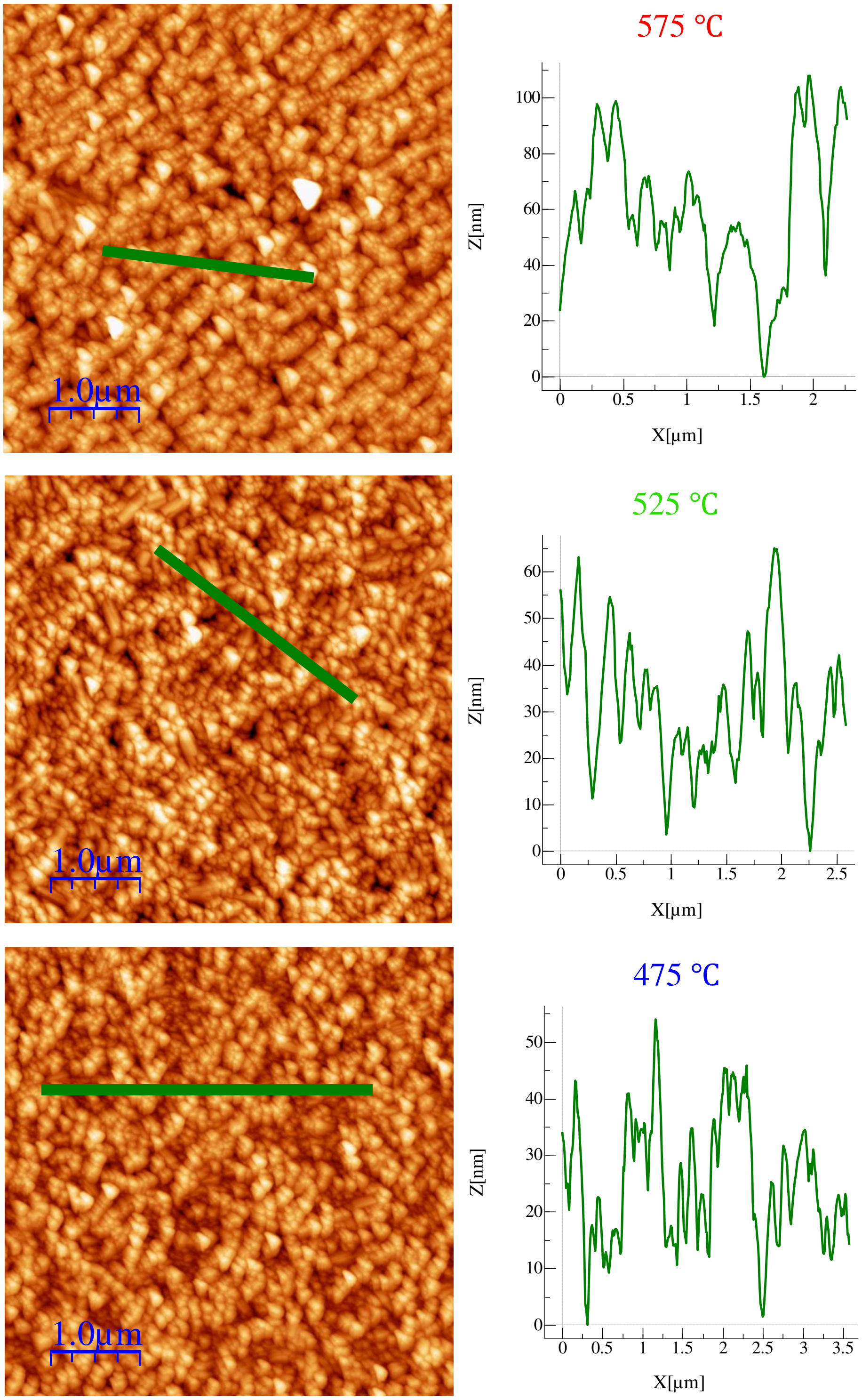

Figure 30. (Left) AFM images for 100 nm VO_2 on r-cut Al_2O_3 substrate with varying deposition temperature but fixed O_2 flow rate at 2.75 sccm. (Right) Line profiles displayed to the right are cuts along the green line in the AFM images. Samples correspond to those shown in Figure 28.

Figure 31 shows the AFM results for varying O_2 flow rates, rather than varying temperatures. The temperature was fixed at $525\ ℃$. The middle sample, for $525\ ℃$ and 2.75 sccm O_2 is the same control sample as shown in the temperature variation which allows for easy direct comparison. The 2.83 sccm sample shows clear texturing, although of a more cubic (rutile) symmetry rather than the more columnar growth of the previous runs. The rows of grains also show some amount of ordering. The roughness is lower than all the samples at 2.75 sccm, at only 8.2 nm RMS roughness and average height of 23.36 nm. The 2.67 sccm sample by contrast shows a very different morphology from the other samples. While still textured, the sample has lost the high degree of symmetry seen in the previous samples. There is some weak row-like alignment parallel to the $+1\hat{\imath} - 1\hat{\jmath}$ direction. In addition, the sample surface is wavy, almost 'melted' in appearance. The roughness in this sample is drastically lower than all previously discussed samples, at 2.1 nm RMS roughness, and an average height of only 6 nm.

The variation in surface morphology also impacts the statistical properties of the surface height. The samples show a varying skew of 0.72, 0.32, and 0.21. Again, we see all positive skew values. The kurtosis also shows a fairly large difference, from 4.47, to 2.98 and then 2.72 for the 2.83 sccm, 2.75 sccm, and 2.67 sccm samples respectively. Again, we see that a higher kurtosis is correlated to a sharper transition in the MIT, as expected. However, the fact that the high kurtosis of the 2.83 sccm sample isn't reflected in a noticeably sharper transition shows the limitations of this simplistic correlation.

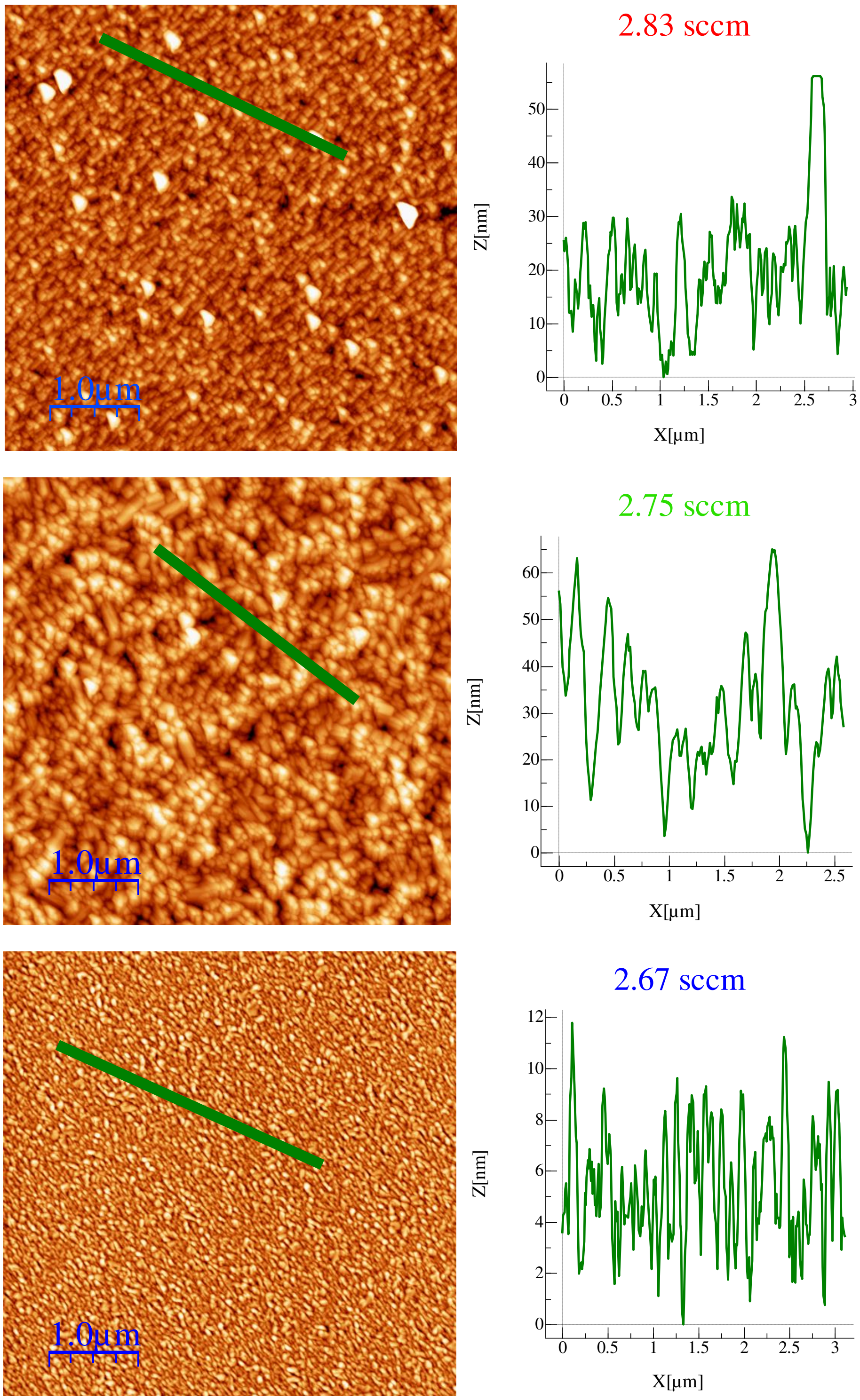

Figure 31. (Left) AFM images for 100 nm VO$_2$ on r-cut Al$_2$O$_3$ substrate with varying O$_2$ flow rate but fixed temperature at 525 °C. (Right) Line profiles displayed to the right are cuts along the green line in the AFM images. Samples correspond to those shown in Figure 29.

Overall, these results hint at a potential method for tuning the surface morphology of VO_2 while maintaining a full 4 orders of magnitude transition. If only one parameter is tuned, the MIT in VO_2 is quickly lost, offering only a very small window to affect the surface morphology. However, higher deposition temperatures have an analogous effect to higher O_2 concentrations of increasing the overall resistance of the film both above and below T_c, and vice versa. Therefore, higher deposition temperatures might be able to compensate for a lower O_2 concentration, or a lower deposition temperature might be compensated by a higher O_2 concentration. This would allow for maintaining the VO_2 transition, while potentially influencing the morphology differently from a high T, low O_2 sample compared to a low T, high O_2 sample.

In addition to using the R vs. T as an indirect measure of the quality of the VO_2, the structural quality can be characterized via XRD. Figure 32 presents XRD measurements for two films deposited at 475 ℃ and 525 ℃ with the O_2 flow rate fixed at 2.67 sccm. The single crystalline r-cut (1-102) Al_2O_3 substrate is prominently peaked at 25.58 °. Beam contaminant peaks are marked by a star. A strong peak belonging to VO_2 is apparent at 37.2 °. This peak belongs to the (200) monoclinic VO_2 peak as well as a twinned (-211) peak which causes some additional broadening to the peak. Along with the strong VO_2 peak, there are traces of other peaks belonging to other vanadium oxides. While the VO_2 peak is notably larger in the 525 ℃, it has come at the cost of stronger contamination from other oxide phases. The close stoichiometry of the various Magnéli and Wadsley phases to VO_2 make some amount of contaminant phases common during VO_2 growth. V_2O_5 seems likely a potential match, with the (001) peak at 20.2 ° and (101) at 21.44 °, and higher harmonics at 41.2 ° and 43.86 °. Therefore, at a fixed oxygen concentration, the higher temperature sample contains more V_2O_5, as the deposition conditions move away from the narrow window for pure VO_2. Peaks labelled with a star correspond to the substrate.

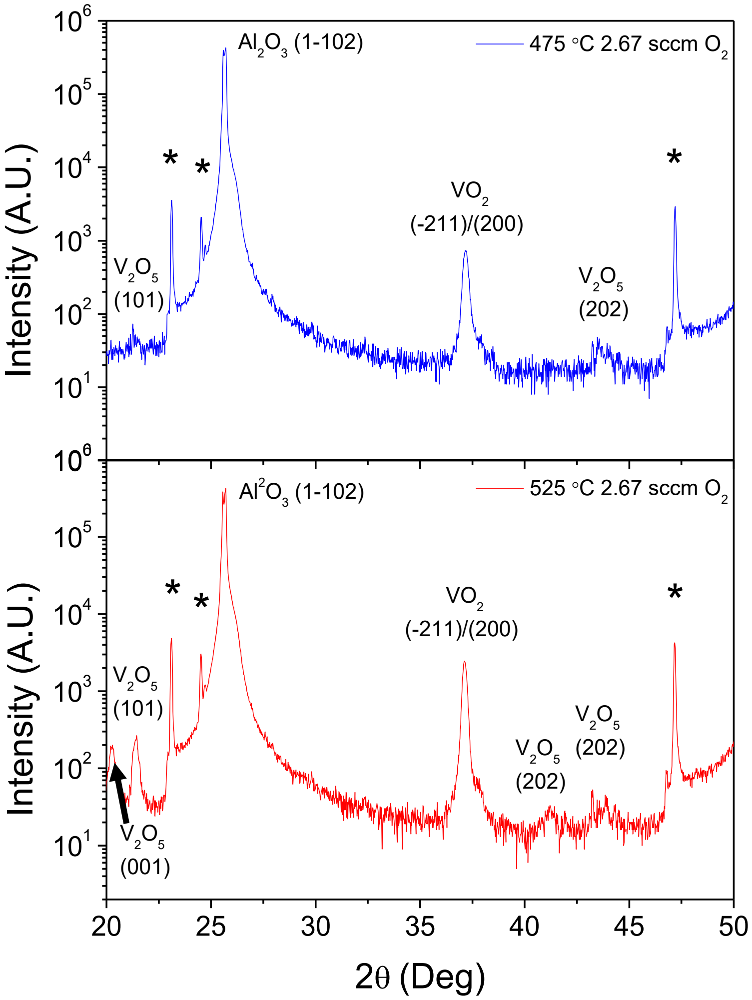

Figure 32. XRD of two sputtered VO_2 onto r-cut Al_2O_3 substrate. (Top) VO_2 deposited at 525 ℃ and 2.67 sccm O_2. (Bottom) VO_2 deposited at 525 ℃ and 2.67 sccm O_2. Peaks labelled with a star correspond to the substrate.

3.3 Films with "melted" texturing at high deposition temperatures

In the previous section, increasing the temperature while simultaneously lowering the O_2 has led to smoother films, although the smoothest films tend to be slightly more metallic than desired. An obvious extension is to continue to increase the temperature to compensate for this lower resistance. Another set of samples was made during a different batch, which we label Batch 2. Between batches, it is often necessary to open the sputtering chamber for maintenance, such as cleaning the sputtering gun or replacing the V target. It was observed that opening the chamber can lead to a permanent shift in the O_2 flow rate required to obtain a particular desired morphology. This shift did not seem to have an obvious correlation with any specific maintenance operation. Even if the chamber was simply opened, resealed, and reconditioned (including a 30-minute presputter in pure Ar environment), there can be a permanent shift in the O_2 requirement. This shift does not occur with every chamber opening and can happen to either increase or decrease the required O_2, although decreases from the typical value of ~2.75 sccm seemed more common. The fact that decreases were more common potentially signifies a leak, but this shift happens even if the chamber is easily able to recover the 2×10^{-7} Torr base pressure. The shift is typically on the order of -0.2 to +0.15 sccm. This corresponds to a range of 7.46% to 8.55% O_2 content, from a nominal 8.15%. Fortunately, the sensitivity of the VO_2 MIT and morphology to O_2 content allowing for a direct comparison between batches and therefore allows to tune back to comparable conditions between batches. A comparison of R vs. T and AFM to Batch 1 in the previous section indicates a shift equivalent to requiring a 0.7 sccm O_2 lower flow rate in Batch 2 for the batches to be at comparable conditions.

We can now explore the effects of higher deposition temperatures. Figure 33, Figure 34, and Figure 35 present the R vs. T and AFM measurements for a set of samples with increasing temperature, from 525 ℃ to 675 ℃. The O_2 is held fixed at 2.57 sccm for this series. Beginning with the AFM for the first sample at 525 ℃, we see the film has a low RMS roughness of 1.38 nm. However, the R vs. T shows that the film is metallic, with a resistance of less than 1 kΩ.

There is some sign of the VO_2 transition with a resistance change from 500 Ω to 50 Ω at temperatures 300 K and 365 K respectively, although it is nearly completely suppressed. In addition, we again see that the high temperature metallic state can be more resistive compared to the other films even if the low temperature state is also metallic. Last, we note that this metallic behavior is seen at a deposition temperature of 525 ℃, which again shows that the temperature and O_2 flow rate are linked. Higher temperatures are required for lower O_2 flow rates in order to see high quality VO_2.

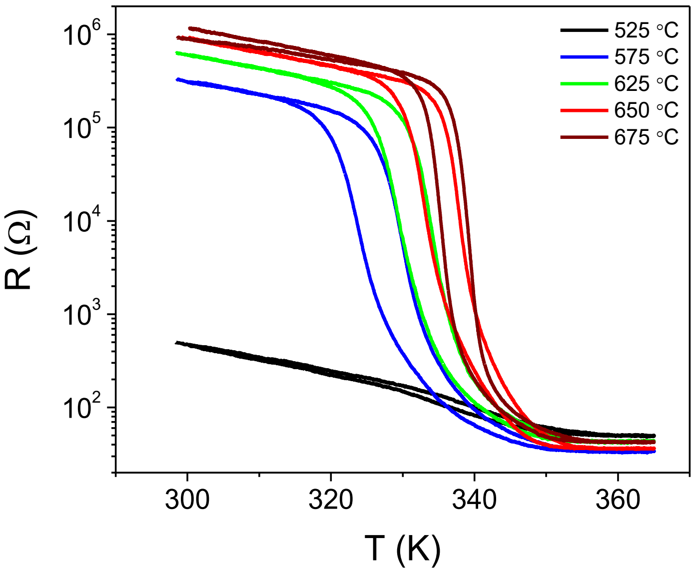

Figure 33. R vs. T for 100 nm VO_2 on r-cut Al_2O_3 substrate, for various temperatures. The O_2 flow rated was fixed at 2.57 sccm O_2. All samples are from Batch 2. The absolute sputter pressure was fixed at 4 mTorr, the Ar flow rate to 31 sccm, and the gun power to 200 W RF.

The second film, deposited at 575 ℃, shows a very similar morphology with an RMS roughness of 1.66 nm. However, the R vs. T is drastically improved, with a strong orders of magnitude MIT. The size of the thermal hysteresis is typical for a sample on r-cut substrate, although there is a clear asymmetry in the cooling branch due to a lack of supercooling. As discussed in Section 1.2, the thermal hysteresis in VO_2 thin films is usually attributed to the martensitic nature of the transition and the various morphological features of the grains. Typically, this hysteresis is symmetric in heating and cooling branches, at least in resistivity measurements. Asymmetry in the thermal hysteresis of resistivity has been observed but is somewhat more common in features such as the optical properties. We refer the reader to Ref. [109] and the references therein for a deeper discussion. To date, it's not clear which mechanism is most plausible, particularly since the mechanism behind thermal hysteresis isn't itself well understood. However, we can observe that this asymmetry causes the higher temperature portion of the MIT to show a severe tail-like feature, as the cooling branch isn't pushed to lower temperatures as in previous samples.

Increasing the temperature further, as in the third film deposited at 625 ℃, shows a drastic change in the morphology. Previously, we had noted that some films had a slightly "melted" characteristic. This third film takes this to the extreme, with the entire film having a melted look. Large grains with a width of approximately 200 nm have formed, with clearly defined grain boundaries between the regions. These grain boundaries have a depth of at least 15-20 nm. The texture of the grains themselves are rather smooth in comparison, with very few features on the grains themselves. Any symmetry in the texturing is weak, although there does seem to be some preference for grain boundaries roughly along the $+1\hat{\imath} - 1\hat{\jmath}$ direction of the image. This film shows a negative skew of -0.37, and a kurtosis of 2.79. The overall roughness of the film is only 4.99, despite the high amount of texturing provided by the grain boundaries. Turning to the R vs. T plot, we see a strong 4 orders of magnitude transition, larger than the previous film. This seems to be common, with films with the melted texture showing larger transitions than more typical films. The tail-like characteristic has also gotten more extreme, with the cooling branch developing a noticeable kink. In addition to the larger MIT amplitude, the R vs. T properties between ‘melted’ films tends to be relatively consistent, providing a means for identifying when the transition from smooth to melted texture has taken place. The larger than expected transition amplitude and kink in the cooling branch generally indicated a melted type film morphology.

The 4th film in the series is somewhat anomalous, with the morphology reverting back to the smooth morphology, despite an even higher deposition temperature of 650 ℃. This is likely due to minor drift in the conditions of the chamber, even though this sample is part of the same batch as the prior three samples. In addition to changes in conditions when opening the chamber as discussed previously, there is a smaller longer-term drift between samples. This hysteresis in deposition conditions happens despite the precaution of a 15-minute total presputter with each sample. It also seems to be more prevalent when changing from higher to lower O_2 concentrations, which then requires an increase in the O_2 flow rate. One possibility is the interaction of the pure V target with O_2 in the chamber, as oxidation of the target surface can influence sputtering rates and oxidation of the final film. The fact that the sample morphology has changed is evident in the R vs. T characteristics of the sample. While the MIT is as large and featuring the tail feature as expected, the tail is not quite as severe as in the previous sample or in the next sample which will also display a melted texture. The melted texture can be recovered by increasing the temperature, or the O_2 flow rate.

In the final film of this batch, the deposition temperature has been increased further, to 675 ℃. The AFM imaging shows that the film has recaptured the melted appearance. In addition, the texturing is further enhanced, with a trough to peak height closer to 30-35 nm. This also has the effect of increasing the overall RMS roughness, to 9.53 nm. Turning to the R vs. T, we see a strong VO_2 MIT. In this film, we see a greater than 4 orders of magnitude change in the resistance from 0.92 MΩ at 300 K to 42 Ω at 365 K- nearly 5 orders of magnitude.

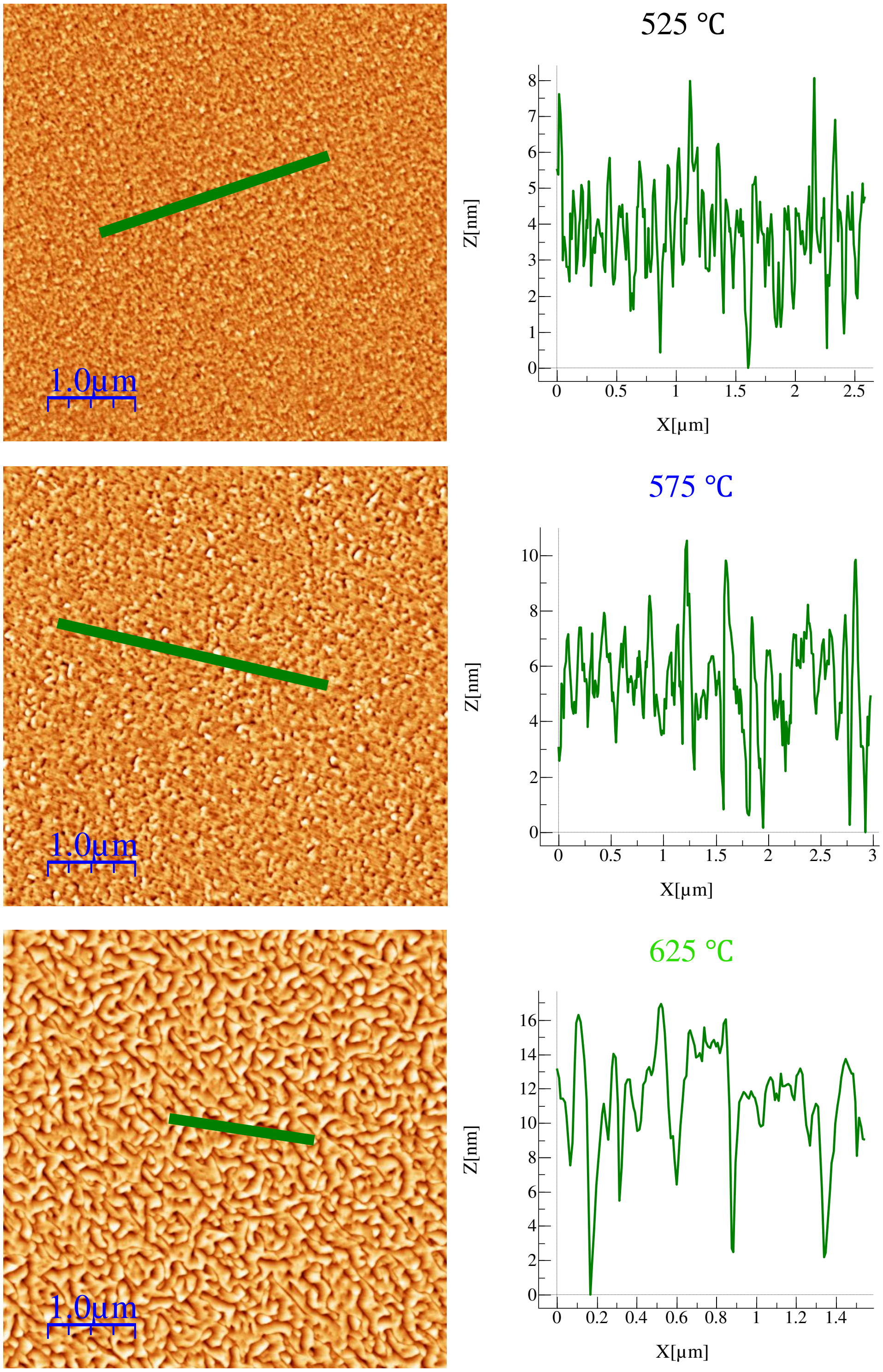

Figure 34. (Left) AFM for 100 nm VO_2 on r-cut Al_2O_3 substrate, for various temperatures. (Right) Line profiles displayed to the right are cuts along the green line in the AFM images. The O_2 flow rated was fixed at 2.57 sccm O_2. All samples are from Batch 2.

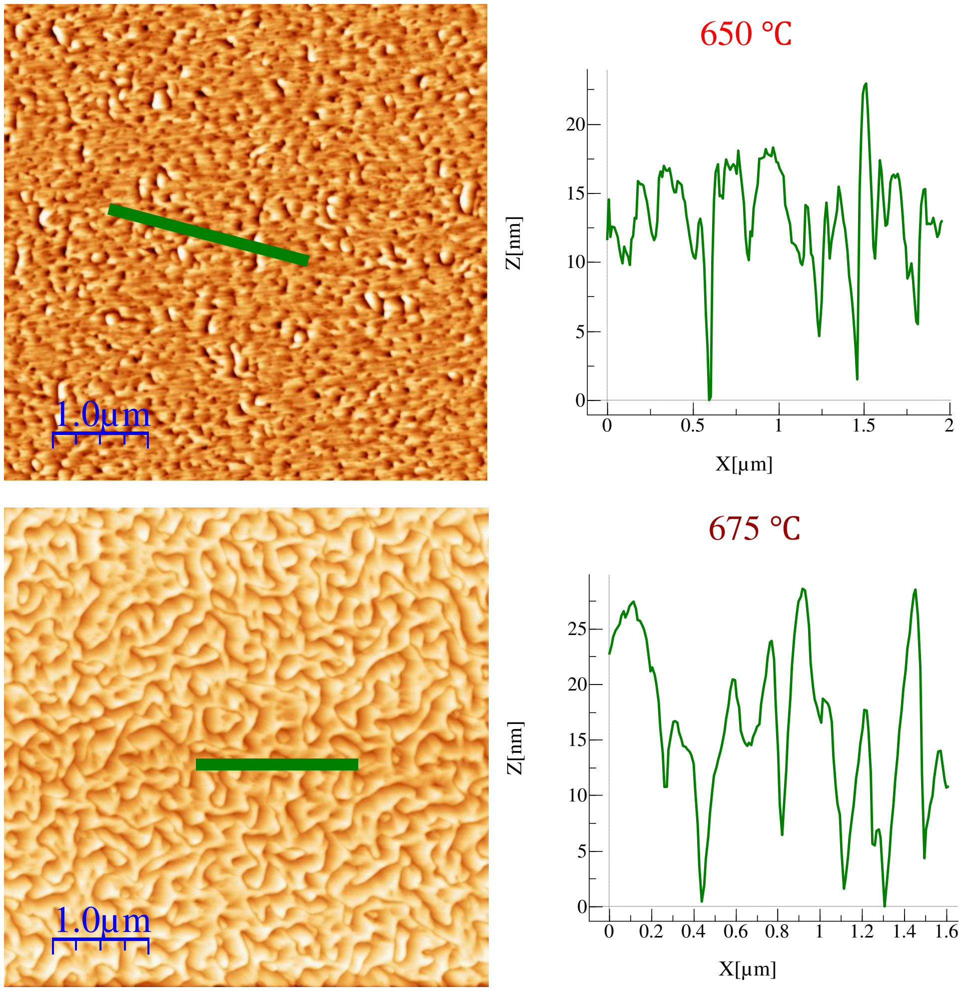

Figure 35. (Left) Additional AFM for 100 nm VO_2 on r-cut Al_2O_3 substrate, for various temperatures. (Right) Line profiles displayed to the right are cuts along the green line in the AFM images. The O_2 flow rated was fixed at 2.57 sccm O_2. All samples are from Batch 2.

It is possible to continue increasing the deposition temperature even further. However, for a deposition temperature of 725 °C, the Inconel sample plate itself began to experience heavy flaking, which makes difficult to carefully control the conditions during deposition. It's not clear if this is due to different thermal expansion rates between the Inconel plate and VO_2 deposited onto the substrate holder, or if the VO_2 is losing structural integrity at the higher temperatures. At such higher temperatures or higher O_2 flow rates, the VO_2 begins to peel away from the substrate and form full micron sized islands with very smooth surfaces and heights around 150 nm. For the conditions tested, these islands are sufficiently connected to allow the percolation behavior required for a R vs. T measurement and show a full 5 orders of magnitude MIT.

There have been only a few reported cases in the literature with a larger than 4 orders MIT in VO_2 thin films.[99,287,288] While they used c-cut or m-cut Al_2O_3 substrates (and in the case of the latter two references, PLD as their deposition method), we note that the conditions are very similar to those of the "melted" films, with high temperatures and relatively low O_2 content. Kim et al. in Ref. [[288]] reproduced the conditions used by Ref. [[287]] using PLD on m-cut, and their SEM results show a very similar morphology to our "melted" films. In addition, their films deposited at higher temperatures show a full 5 orders of magnitude MIT, and progress to isolated nanoislands at the highest temperatures as expected. Unfortunately, Kim et al. only include one branch of the R vs. T measurement, so direct comparisons of asymmetry in the thermal hysteresis cannot be made. They do not comment on any such asymmetry in the text. High temperature (> 550 ℃) depositions are often underexplored, as low temperature depositions are desired for low cost industrial application and avoid many complications such as diffusion or dewetting.[243] However if high temperature depositions yield films with unique properties, they may need to be reconsidered.

It is worth noting that this "melted" texturing in VO_2 is not entirely unexpected. While the melting point of phase pure VO_2 is quite high at 1545 ℃,[77,202] the melting point of VO_{2+x} is drastically lower, closer to 700 ℃ in bulk equilibrium. This can also be seen on the phase diagram presented earlier in Figure 2, with the "VO_2 and a liquid phase" label in the upper right, above 708 ℃. We are therefore quite close to the melting temperature for these impurity phases, and it is not uncommon for melting temperatures to be lowered in thin films as compared to bulk equilibria. The lower melting temperature can be attributed to phases such as V_6O_{13} or V_3O_7 which contain V^{+5} and therefore leads to the drastically lower partial melting temperature.[82,289] This process occurs as a peritectic decomposition into VO_2 and a liquid phase.[82] The reduction of phase impurities into phase pure VO_2 would also naturally lead to the enhanced MIT seen for these films. Lastly, this suggests there may be additional optimizations for phase pure VO_2 and a full 5 orders of magnitude MIT with further tuning of deposition conditions.

3.4 Utilizing alternate substrates to tune the VO_2 transition

In addition to tuning the processing conditions of the VO_2 film deposition, the choice of substrate is another avenue for tuning the VO_2. The epitaxial relationship and preferential orientations can have a large impact on the morphology, crystalline quality and MIT properties of a VO_2 film. The R vs. T for two films grown on a-cut (11-20) Al_2O_3 substrate are shown in Figure 36. Nominally, these films were both produced with 525 °C and 2.67 sccm O_2. The second film was done during the course of Batch 2, whereas the first was in a batch which had lower base O_2. In addition, it is only 50 nm thick. As in the r-cut case, the sensitivity of VO_2 to the local deposition conditions means that it isn't sufficient to have the same deposition parameters unless samples are compared in the same batch. However, one can directly infer the local conditions by comparing the results of measurements such as AFM and R vs. T and use them to orient and relate different batches. From these comparisons, the desired film properties can be recreated. Shown alongside is an r-cut sample deposited with the same conditions in the same batch for comparison. Looking to the top film, we see the 4 orders of magnitude change in the resistance typical of a VO_2 film, from 0.86 MΩ at 300 K to 92 Ω at 360 K. The amplitude of the transition is slightly smaller than the r-cut, suggesting that the conditions may need slight tuning specific to the a-cut substrate, but overall the quality of the transition is quite high. Looking to the MIT, we see a thermal hysteresis comparable but slightly smaller than that of the r-cut. The net T_c of the film is also close to but slightly below the r-cut value due to the different substrate lattice strain. In addition, we see a greater spread to the MIT, indicating a larger spread in local T_c for the a-cut grains. The transition is largely symmetric, although the lower portion has slightly more of a tail than the upper portion.

In the bottom film we see that the transition has gotten slightly smaller in amplitude from 1.06 MΩ at 300 K to 111 Ω at 365 K. This is an indication that the conditions have moved away from the ideal conditions on a-cut substrate and is likely tied at least in part to the vastly different morphologies that will be shown in the AFM since the comparable r-cuts in each panel are nearly identical. In addition to the smaller amplitude, the shape of the thermal hysteresis has changed. While the thermal hysteresis begins at roughly the same temperature in the heating loop, the transition is much broader in temperature, indicative of a broader range of T_c's for the grains. This wider transition also pulls the average T_c of the film to slightly higher temperatures, although the thermal hysteresis is similar to the top sample.

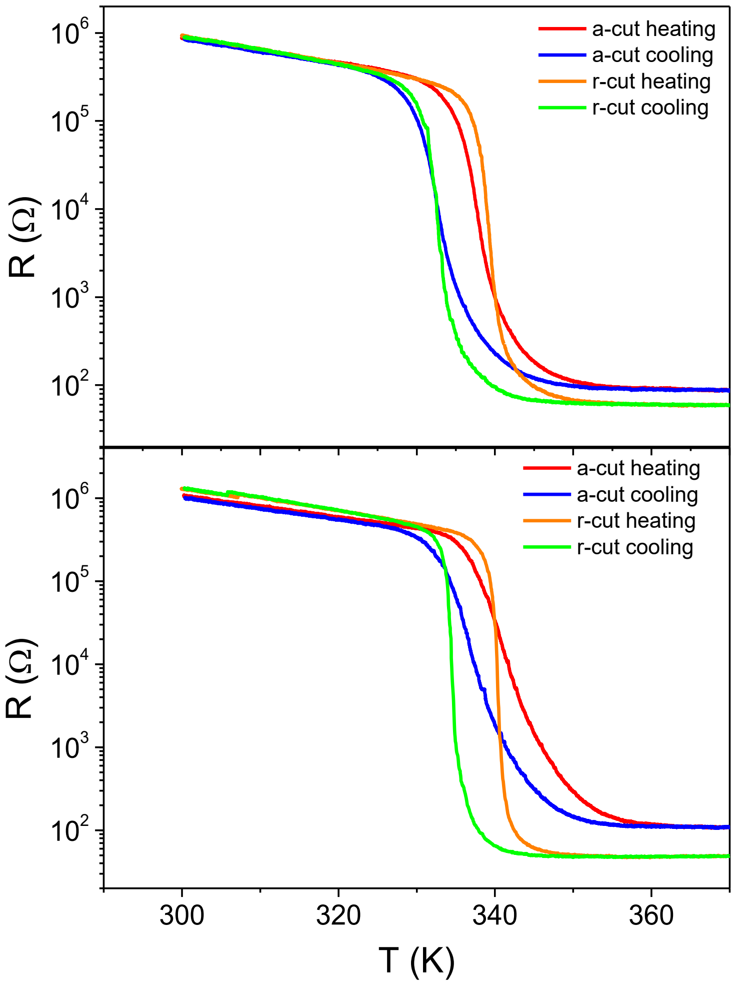

Figure 36. R vs. T for a 100 nm VO_2 film on a-cut substrate. Samples on r-cut provided for comparison. The absolute sputter pressure was fixed at 4 mTorr, the Ar flow rate to 31 sccm, and the gun power to 200 W RF.

Figure 37 shows the AFM results for two films grown on a-cut Al_2O_3 substrate with strikingly different morphologies. The top film corresponds to the top film shown in Figure 36, and similarly with the bottom figures. The top film shows a relatively low RMS roughness of 2.8 nm, whereas the bottom is much rougher, at 5.8 nm roughness. In contrast to the r-cut films shown earlier, both show a positive skew in their height distribution, of -1.70 and -0.20 for the top and bottom film respectively. The top film has a relatively large kurtosis at 7.65, and the bottom film one very close to a Gaussian distribution at 3.06. Both films show a high density of pinhole defects with a 20 nm depth, although the top film favors less holes with a deeper trough, whereas the bottom film shows many shallower dips. Outside of these defects, the top film shows very plateau like behavior, with the plateaus showing a smooth top surface with sub 0.7 nm RMS roughness. The plateaus have a characteristic length scale of around 0.4 microns in the lateral directions. In the bottom sample, the grains are more strand-like, with a width of around 125 nm and length 200 nm or so. Neither morphology displays any obvious crystalline symmetries.

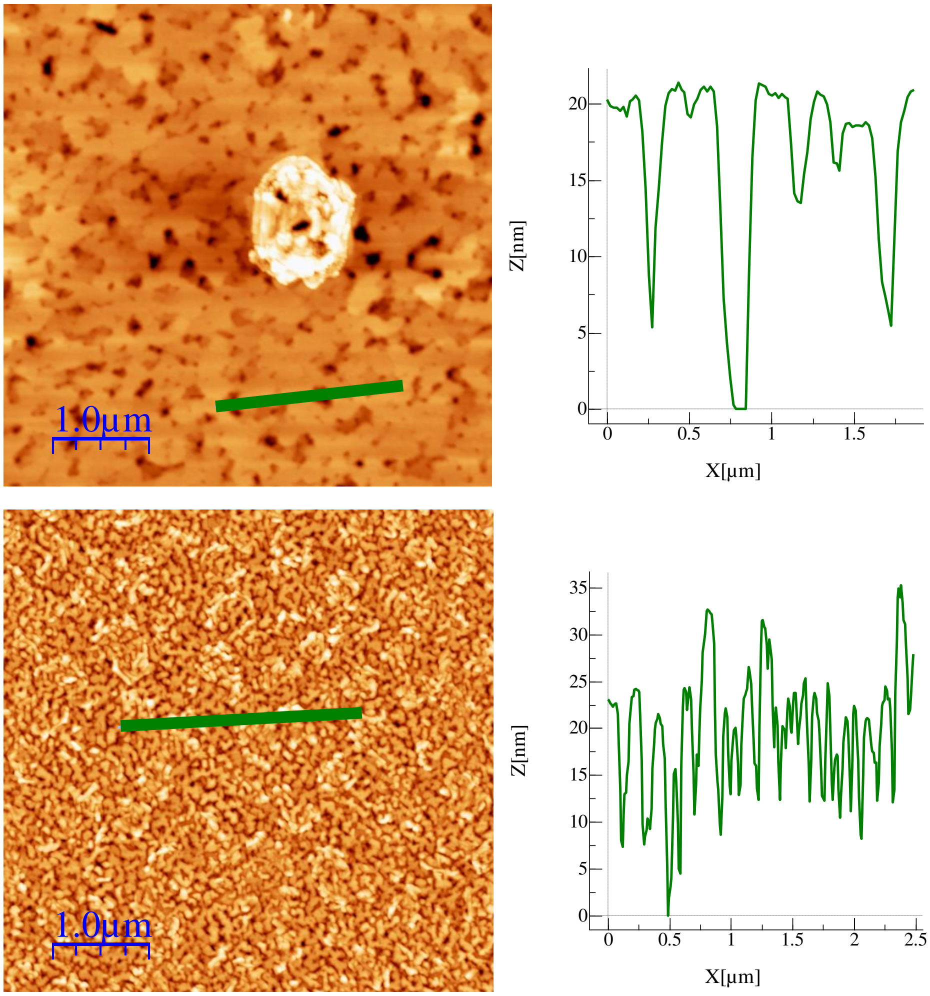

Figure 37. (Left) AFM images for 100 nm VO_2 on a-cut Al_2O_3 substrates, from different batches. (Right) Line profiles displayed to the right are cuts along the green line in the AFM images. Both films were deposited at a nominal 525 °C and 2.67 sccm O_2, but the bottom film is at an effective higher O_2 content. The top film is 100 nm thick, the bottom 50 nm thick.

In Figure 38 we show the XRD for two samples deposited on a-cut (11-20) Al_2O_3 substrate. The top figure, in blue, corresponds to VO_2 deposited at 475 °C. The bottom, in red, corresponds to a deposition temperature of 525 °C. The 525 °C film is a part of the same batch as the 525 °C film shown in the top AFM in Figure 37 and the top R vs. T in Figure 36. Both show the expected peak for the 0.5 mm thick single crystalline substrate at 37.86 °, but there is different behavior at the VO_2 peaks. The sample deposited at 475 °C and 2.67 sccm O_2 shows poorer crystalline quality, with only a small peak seen at 44.14 ° that can be indexed to the VO_2 (12-1) or (120) monoclinic planes. By contrast, when the temperature is increased to 525 ℃ as in the bottom panel, a clear monoclinic VO_2 (020)/ (002) peak is seen at 39.88 °. In addition, the minor peak at 44.14 ° seen in the previous sample is largely suppressed, indicating that the (020)/(002) peak is more favorable under these conditions. This is similar to what was seen on r-cut substrates, with temperatures above roughly 475 ℃ being required for the VO_2 to crystallize on Al_2O_3 substrates. In contrast to the r-cut, the peak is much more pronounced.

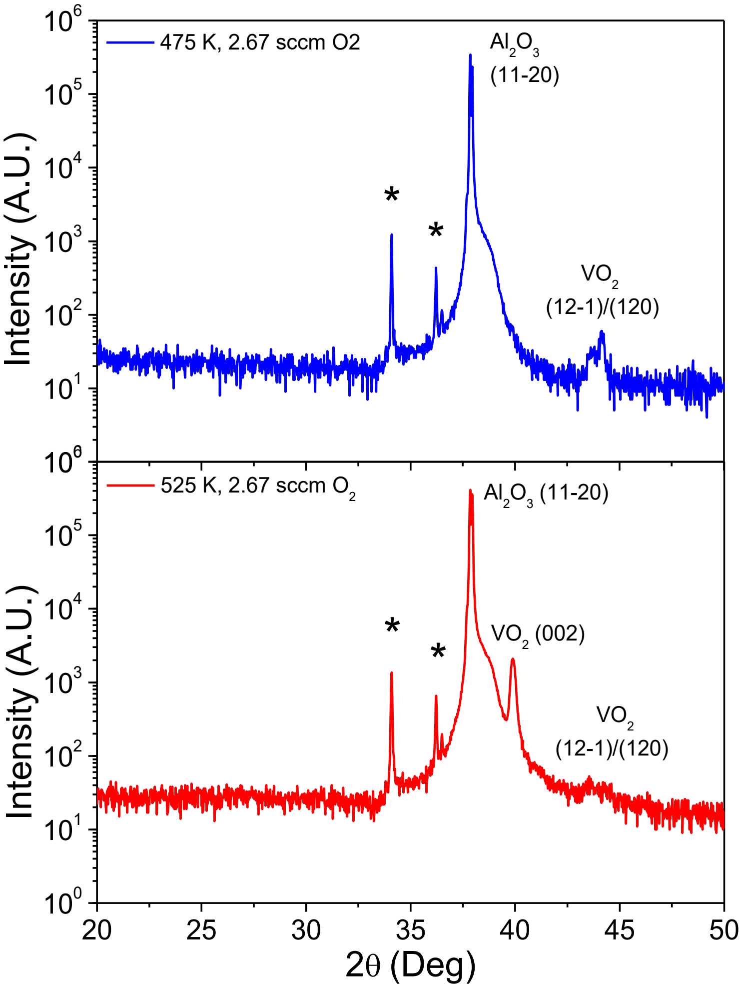

Figure 38. XRD of two sputtered VO_2 onto a-cut Al_2O_3 substrate. (Top) VO_2 deposited at 475 ℃ and 2.67 sccm O_2. (Bottom) VO_2 deposited at 525 ℃ and 2.67 sccm O_2. Peaks labelled with a star correspond to the substrate.

Another less studied Al_2O_3 plane is the m-cut, or (1-100) plane. Looking to the R vs. T characteristics shown in Figure 39, the m-cut also shows a strong MIT, larger than even the comparable r-cut sample without any additional tuning. The r-cut sample is slightly below 4 orders of magnitude in the amplitude of the transition, indicating a slightly O_2 deficiency for optimal MIT. Overall the two substrates show relatively similar shapes to the thermal hysteresis, with the average T_c pushed to higher temperatures relative to the r-cut and the m-cut thermal hysteresis being a bit smaller. There is some asymmetry in the MIT, with a cooling branch transitioning slightly faster than the heating branch counterpart. As in the a-cut case, we see that the conditions for a high-quality m-cut sample is close but slightly different from the conditions one would use for an r-cut substrate.

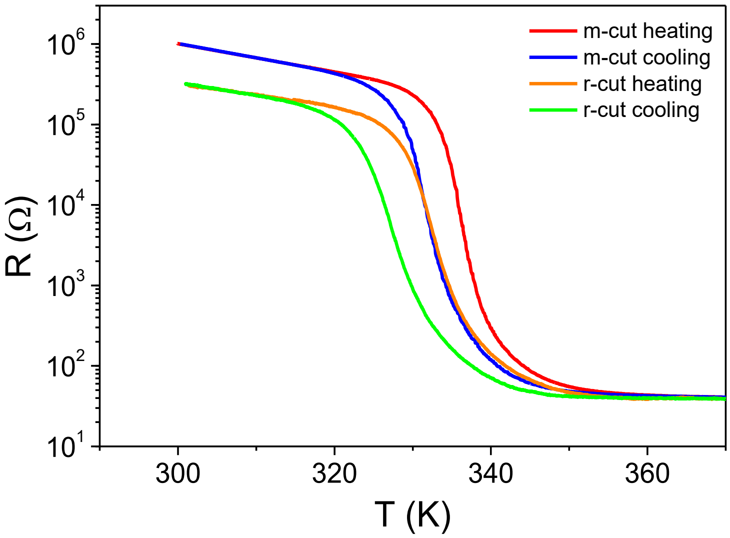

Figure 39. R vs. T for a 100 nm VO_2 film on m-cut substrate. Sample on r-cut provided for comparison. The absolute sputter pressure was fixed at 4 mTorr, the Ar flow rate to 31 sccm, and the gun power to 200 W RF.

A typical AFM measurement for 50 nm VO_2 on an m-cut substrate is shown in Figure 40. This sample was deposited at 525 ℃ and 2.67 sccm O_2, as a part of Batch 2. For these conditions, m-cut shows rather small, clearly defined grains. The grain size is on the order of 50-100 nm, with a clear distribution in grain size. The sample is also rather smooth, with an RMS roughness of 1.99 nm. The height distribution has a slightly positive skew, at 0.14, and a nearly Gaussian kurtosis of 2.83. The roughness is quite a bit smaller than the corresponding a-cut and similar to the r-cut samples made in the same batch shown in the bottom of Figure 37 and Figure

34 respectively. The film also shows good coverage, with few to no pinhole style defects common on the other substrates.

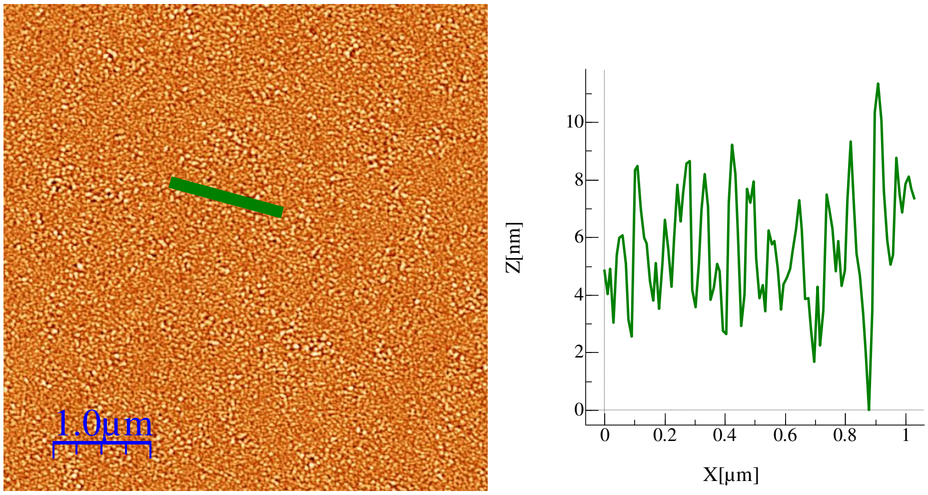

Figure 40. (Left) AFM images for 50 nm VO_2 on m-cut Al_2O_3 substrate. (Right) Line profiles displayed to the right are cuts along the green line in the AFM images.

The XRD results for a typical 100 nm VO_2 on m-cut substrate is shown in Figure 41, with deposition conditions 525 ℃ and 2.75 sccm O_2. As expected, the substrate peak is seen at 68.3 ° for the m-plane of Al_2O_3. A strong VO_2 peak is seen at 33.44 °, which indexes to the monoclinic (10-2) VO_2 peak. The higher harmonic (20-4) peak is also seen in the shoulder of the Al_2O_3 peak, at 70.46 °.

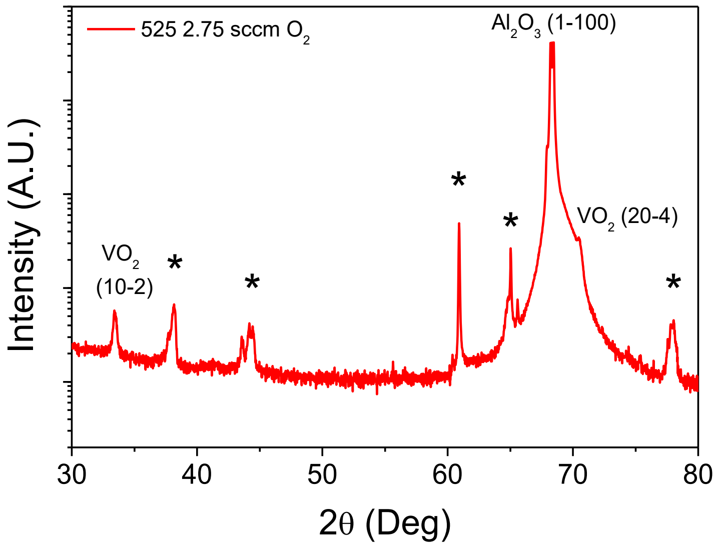

Figure 41. XRD of 100 nm sputtered VO_2 onto m-cut Al_2O_3 substrate. Peaks labelled with a star correspond to the substrate.

The two previous substrates are somewhat unusual choices, but c-cut (0001) Al_2O_3 is a very common choice due to the excellent epitaxial relationship between this plane and the VO_2 crystal structure. A R vs. T for a sample grown on c-cut substrate at 525 ℃ and 2.75 sccm O_2 is provided in Figure 42 along with a sample on r-cut for comparison. The c-cut shows a strong 4 orders of magnitude MIT, with a sharp transition. The T_c relative to the r-cut is shifted upwards, along with a slightly larger thermal hysteresis. The thermal hysteresis is also nearly perfectly symmetric, unlike the VO_2 deposited on other substrates shown thus far.

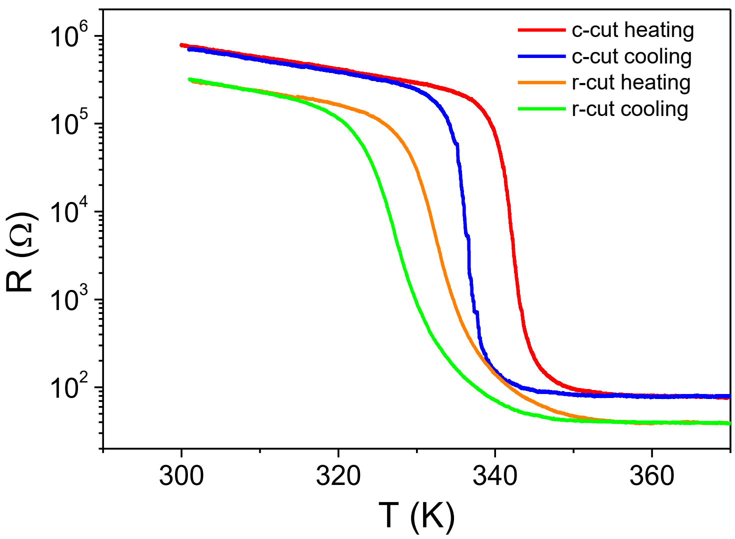

Figure 42. R vs. T for a 100 nm VO_2 film on c-cut substrate. Sample on r-cut provided for comparison. The absolute sputter pressure was fixed at 4 mTorr, the Ar flow rate to 31 sccm, and the gun power to 200 W RF.

AFM for a 100 nm VO_2 film deposited on c-cut Al_2O_3 substrate at 525 ℃ and 2.75 sccm O_2 is shown in Figure 43. This sample was grown as a part of Batch 1. The surface morphology in these samples is not unlike those shown previously for similarly conditioned samples on r-cut substrate, despite the much-improved epitaxial relationship seen in the XRD pattern. The sample is rather rough, with an RMS roughness of 11.04 nm, and grains on the order of 100-225 nm in size. There are some regions with the cylindrical symmetry seen in some of the samples with r-cut substrates presented earlier. The skew of the height distribution is low but positive, at 0.44. The kurtosis is nearly Gaussian, at 3.24. While the areal coverage is high, there are some pinhole defects that can be seen in portions of the film.

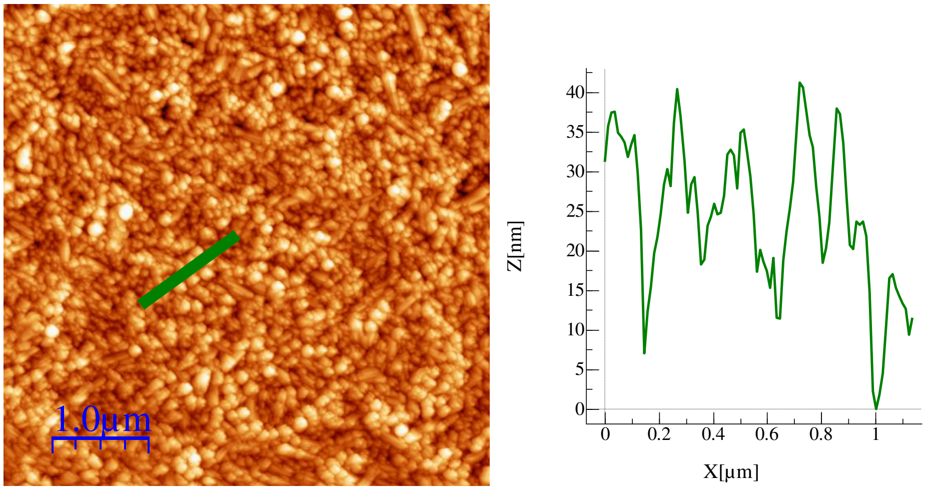

Figure 43. (Left) AFM images for 100 nm VO_2 on c-cut Al_2O_3 substrates. (Right) Line profiles displayed to the right are cuts along the green line in the AFM images.

Figure 44 shows a typical XRD pattern for VO_2 deposited at 525 °C and 2.75 sccm O_2 on c-cut substrate. The c-cut (0001) peak is displayed prominently at 41.72 °. The monoclinic VO_2 (020)/(002) peak is seen at 39.88°, just like was seen previously in the a-cut samples. The positioning of the c-cut substrate peak means that the VO_2 peak overlaps with a contaminant peak of the substrate, unlike in the a-cut case. Nevertheless, we can definitively identify this peak based on the width of the peak, whose broadening is characteristic of VO_2 rather than a contaminant peak. In addition, a direct comparison with a blank c-cut substrate shows the peak is much stronger in the VO_2/Al_2O_3 film. A minor peak belonging to another oxide is visible at 20.5 ° that can be indexed to the V_2O_5 (001) orientation, indicating some slight contamination.

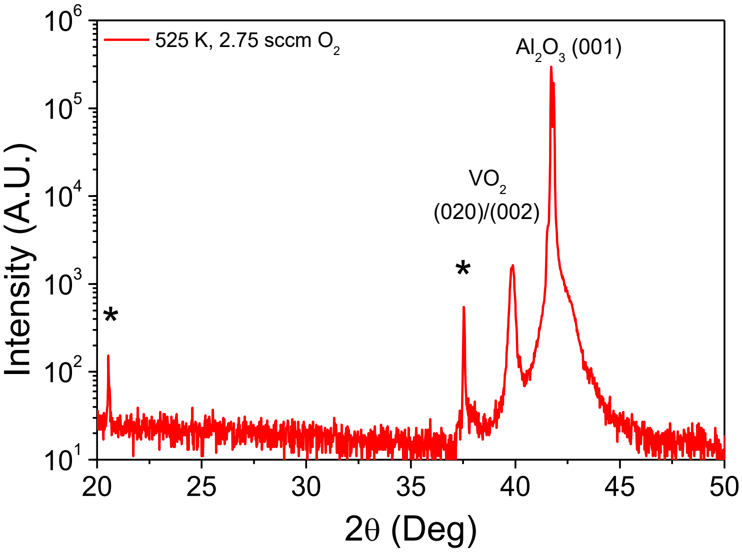

Figure 44. XRD of 100 nm sputtered VO_2 onto c-cut Al_2O_3 substrate. Peaks labelled with a star correspond to the substrate.

The last substrate we considered in this work was TiO_2 (101) (equivalent to (011)), in a switch away from the various Al_2O_3 cuts. TiO_2 is another standard substrate for VO_2 due to the epitaxial relation- the rutile naming is derived from the TiO_2 mineral. Ti and V are also right next to each other on the periodic table, which means that the crystal structures are nearly an exact match, with a slight difference in lattice parameters due to the atomic mass.

In Figure 45, a 100 nm VO_2 films on TiO_2 (101) substrate is shown. Turning our attention to the bottom film, we see that it has formed plateaus, not unlike those seen in one of the a-cut samples. Unlike the a-cut sample, there is clear anisotropy and the plateaus have a roughly tetragonal symmetry which manifests with a stripe-like top down pattern. The film shows deep indentations between the plateaus. These trenches have a depth of at least 50 nm and an opening width of roughly 200 nm. The overall roughness of the film is quite high, at 11.3 nm, however the plateaus have a much lower roughness on their top face, closer to 3-4 nm. Like the a-cut sample, the film shows a large negative skew of -1.04 and a clear tail in the height distribution, although this should be understood by decomposing the film into two distributions for the plateaus and valleys separately. The film shows a mild kurtosis of 4.05.

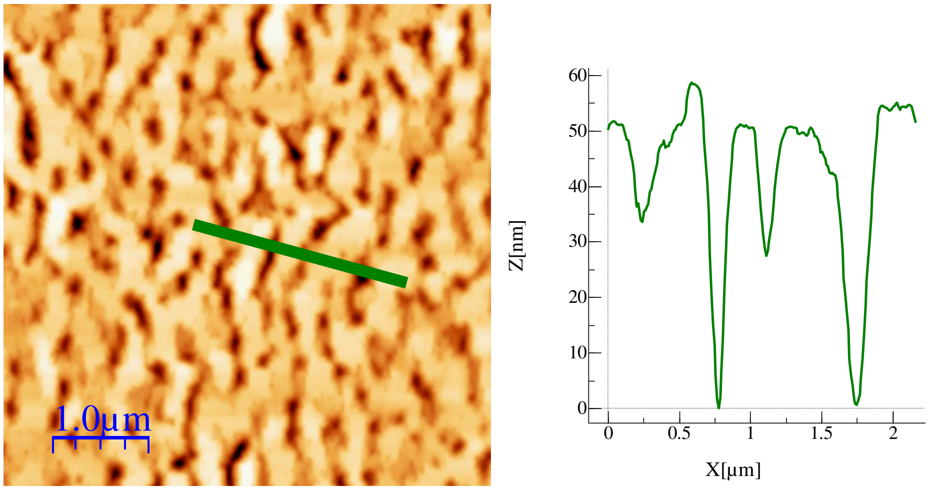

Figure 45. (Left) AFM images for 100 nm VO_2 on TiO_2 (101) substrate. Deposited at 525 °C and 2.67 O_2 sccm. (Right) Line profiles displayed to the right are cuts along the green line in the AFM images.

The R vs. T measurement for a typical VO_2 film on TiO_2 (101) substrate is shown below in Figure 46 along with a r-cut comparison film. We see a strong 4 orders of magnitude MIT, although with a number of notable features. Interestingly, the slope of the resistance in the semiconducting state is different than that of the r-cut. This contrasts with the previous 3 samples on various Al_2O_3 substrates, which showed roughly the same slope as each other. The film transitions from its semiconducting state to the metallic state at around 328.7 K, typical for VO_2 on TiO_2 (101) substrate.[110] While the transition is rather sharp, roughly comparable to the r-cut sample, the thermal hysteresis is much thinner at only 2.55 K. Below the transition we see the typical metallic behavior in VO_2.

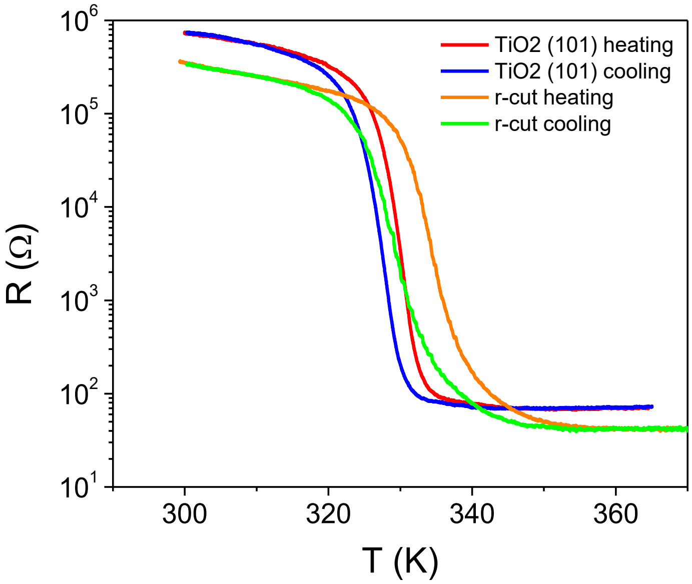

Figure 46. R vs. T for 100 nm VO_2 on TiO_2 (101) substrate deposited at 475 ℃ and 2.67 sccm O_2. The absolute sputter pressure was fixed at 4 mTorr, the Ar flow rate to 31 sccm, and the gun power to 200 W RF.

The XRD pattern for a 100 nm VO_2 film on TiO_2 (101) is shown in Figure 47. As expected, the TiO_2 (101) peak is apparent at 36.12 °. The similarity in crystal structure means that any VO_2 peak will be rather close, and indeed there is a VO_2 peak visible in the right-hand shoulder at 37.22 °. In the monoclinic phase, this peak indexes to the (200) or (21-1) twinned peaks. Across the SPT these orientations will correspond to the rutile (101) in VO_2, utilizing the appropriate unit vector conversion. The fact that the VO_2 peak is visible despite the relatively low deposition temperature contrasts with the Al_2O_3 substrates.

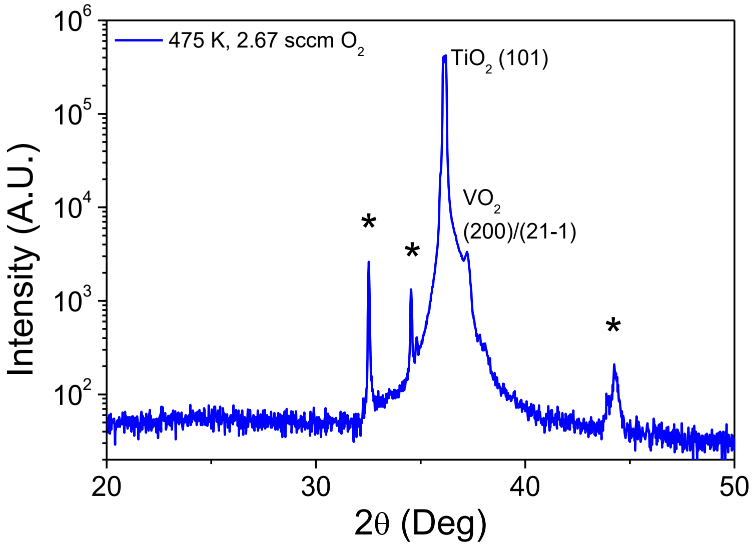

Figure 47. XRD of 100 nm sputtered VO_2 onto TiO_2 (101) substrate. Peaks labelled with a star correspond to the substrate.

3.5 Conclusions

In this chapter, we showed the tunability of the deposition of VO_2 thin films on various substrates via magnetron sputtering. These films show the 4 orders of magnitude or larger MIT concomitant with high quality VO_2. Tuning the temperature and oxygen concentration in the vacuum chamber during the deposition proved to be an effective method for tuning both the R vs. T properties of the films, but also the surface morphology. Whereas most works individually tune the temperature or O_2 flow rates, we show that equally strong MIT behavior can be seen at different deposition equilibria. However, different temperature and O_2 concentration combinations lead to very different surface morphologies, with higher O_2 and lower T showing more columnar textured growth and high T low O_2 conditions showing smoother morphology. O_2 concentration is shown to be a key way to control the roughness and morphology in VO_2 sputtered films. Increasing the temperature allows to compensate and maintain roughly the same stoichiometry, a critical feature in the vanadium oxide system. To fully optimize the VO_2, it is also beneficial to iterate between changing the deposition temperature and O_2 concentration rather than to fix one and tune the other as is common in other studies. We were able to achieve a sub 2 nm RMS roughness while maintaining most of the VO_2 MIT, however films in these conditions only showed a weak preferential orientation as measured by out of plane XRD. We also show that drifts in deposition conditions, either between samples or due to opening the vacuum chamber can be corrected for by studying the surface morphology and R vs. T characteristics.

Further increases of deposition temperature beyond 575 ℃ lead to a sharp change in morphology, with the films showing a “melted” type texturing. In the extreme case, this nanopatterning leads to nanoislands of VO_2 that leave portions of the substrate exposed. This type of nanopatterning is common in thin films when it is energetically favorable as a way to reduce the total surface energy.[290–292] The total surface energy minimum, and therefore growth mode, is determined by the competition between the film free surface energy, the substrate-film interface energy, and substrate free surface. Temperature is also a relevant tuning parameter, as low deposition temperatures can limit or freeze out undesirable kinetics such as dewetting.[293–295] In addition to the texturing, these films show very asymmetric MIT, with greater than 4 orders of magnitude MITs. While this nanopatterning and MIT characteristics show promise for future work, they’re unsuitable for the clean interface required in this work.

While alternative deposition parameters such as absolute deposition pressure, substrate biasing, and annealing were explored as potential tuning knobs, they did not show as much promise as temperature and O_2 concentration for obtaining smooth VO_2 interfaces. On the other hand, alternative substrates showed much more promise. Various planes of Al_2O_3 substrates led to improved structural quality as measured by XRD, with strong peaks. They also maintained the 4 orders of magnitude MIT while each showed a different morphology as compared to the r-cut substrate. TiO_2 (101) substrates were also explored, and also showed a strong structural quality while providing a very anisotropic but smooth surface. The different epitaxial lattice strain also leads to a lower T_c of 330 K.

Taken together, control of deposition parameters and choice of substrate allow for very different types of interfaces in VO_2 films. These interfacial properties can be used to tune the magnetic properties of VO_2/Ni hybrid bilayers, as we show in the next chapter.

Chapter 4. Magnetic properties of VO_2/Ni Bilayers

4.1 Motivation

As was discussed in Chapter 1, magnetic hybrid heterostructures consisting of an SPT material and a FM are an underexplored but competitive alternative as compared to other more well studied coupled magnetic heterostructures such as piezoelectric/FM or AF/FM bilayers.[25,26,47] SPT materials such as the vanadium oxides would allow for manipulation of the magnetic properties of the FM layer in a heterostructure without the need for an external applied magnetic field. Alternative stimuli such as light, electric field and temperature which can trigger the SPT can be used instead of applied magnetic fields to modify magnetic properties via magnetoelastic coupling between the SPT material and the FM layer. These SPT materials also show sharp switching like behavior, in contrast to the more gradual response of materials such as piezoelectrics.

VO_2 is a promising choice of SPT material, with its T_c of ~340 K. In addition to being close to but above room temperature, the T_c is easily tunable via deposition conditions, substrate, or methods such as doping. In previous work, it was shown that the magnetic properties of Ni deposited on VO_2 and V_2O_3 can be modified by interfacial stress due to the SPTs of these vanadium oxides.[296,297] Here we further explore the VO_2/Ni system, studying the effects of substrate choice and tuning the VO_2 deposition conditions and morphology. Ni is the FM of choice due to its high magnetostrictive coefficient for an easily grown FM.

The section begins by discussing the sputtering of the metallic Ni layer onto VO_2 films, following the procedure laid out in Chapter 2. We then reconfirm the crystalline quality of the

VO_2 layer via XRD after Ni deposition, as well as checking for any preferential orientation of the Ni. AFM is used to characterize the Ni surface morphology in the heterostructures, which will influence the magnetic properties. Magnetometry measurements taken at various temperatures for representative samples are shown for three substrates: c-cut Al_2O_3, TiO_2 (101) and r-cut Al_2O_3. The influence of the substrate on the magnetic properties are discussed. Finally, magnetic measurements for alternative substrates m-cut and a-cut Al_2O_3 are presented.

4.2 Characterization and Ni deposition

VO_2 films were first deposited via magnetron sputtering following the procedure laid out in Chapter 2, and optimized as described in Chapter 3. Once the desired conditions were reached, several VO_2 samples were fabricated, with the Ni added only after all VO_2 samples for that batch were deposited. As mentioned in Chapter 3, the delicate sensitivity of VO_2 to any contaminant that could influence the O_2 of the chamber should be avoided. Sputtering metallic Ni prior to a VO_2 deposition will act to leach O_2, leading to a O_2 deficient atmosphere and require reconditioning of the chamber. Fortunately VO_2 is metastable in ambient conditions for periods of several weeks or longer, even without a capping layer.[96,97] This stability allows for a later deposition, rather than a single VO_2/Ni heterostructure per conditioning cycle. In addition, outside the chamber the VO_2 films are stored in a low-pressure desiccator system to further slow any degradation.

After the VO_2 samples have been prepared, the Ni can be deposited on top of the VO_2 and are capped in-situ with Al capping layers to prevent oxidation of the Ni. The deposition for samples with Ni deposited well above Tc was done at 473.15 K and will be labeled as ‘HT’. The deposition for samples with Ni deposited below Tc were done at ambient temperature and will be labeled as ‘RT’, and will be discussed in the next chapter. The Al capping layer in the RT samples are done immediately following the RT deposition. The Al capping layer for the HT samples are done after cooling back to RT, typically approximately 1 hr after the deposition. The nominal thicknesses were 100 nm/15 nm/5 nm for the VO_2/Ni/Al heterostructures. Since the VO_2 deposition is a reactive process, the deposition rate was confirmed on test samples via XRR and assumed to be constant across depositions per batch. If the chamber is opened, the deposition rate is remeasured after the conditioning and tuning has taken place. It is important to calibrate the thickness after tuning since conditions inside the chamber such as the O_2 content can influence the sputter rate. The metallic Ni and Al deposition rates were measured using an in-situ quartz crystal balance. Prior to the first deposition or measuring the deposition rate, both metallic targets are presputtered for 30 minutes to eliminate any oxide layer on the surface of the target. Subsequent sputters are presputtered for 3 minutes immediately prior to deposition, to clean the surface and allow the plasma conditions to equilibrate.

With the Ni deposited, several HT samples were measured via XRD to confirm the crystalline quality of the VO_2, as well as determine any out-of-plane preferential orientation of the Ni. The results for several choices of substrate are shown in Figure 48. All three show the same vanadium oxide peaks as pure VO_2 samples from Chapter 3. In the top panel, the c-cut substrate shows a strong (020)/(002) monoclinic VO_2 peak at 39.88 °, to the left of the c-cut (0001) Al_2O_3 peak at 41.70 °. However, an additional broad peak has formed at 45.6 ° which belongs to the Ni (111) plane. In the middle panel in blue is the VO_2/Ni heterostructure grown on TiO_2 (101) substrate. Again, we see a VO_2 (200)/(21-1) twinned peak located at 37.22 °, to the right of the TiO_2 (101) peak at 36.16 °. Unlike the c-cut substrate, there is no clear peak attributable to Ni, indicating less preferred orientation. In the bottom panel of the figure is the sample grown on r-cut (1-102) Al_2O_3 substrate. As previously, the VO_2 on r-cut shows the same (200)/(21-1) peak as the TiO_2 (101) at 37.01 °. The slight discrepancy between the two can be attributed to slight differences in alignment of the XRD system as well as the different lattice strains of the substrates. The unstrained peak is predicted to be at 36.0969 °. As with the TiO_2 (101), no Ni peak is evident within the experimental limits of our detector.

Overall, all 3 samples show strong VO_2 peaks in the expected preferred orientation for their corresponding substrates. The (020)/(002) oriented VO_2 on c-cut substrate seems to encourage a Ni (111) orientation, whereas VO_2 (200)/(21-1) on r-cut and TiO_2 (101) substrates do not seem to greatly encourage a preferred orientation.

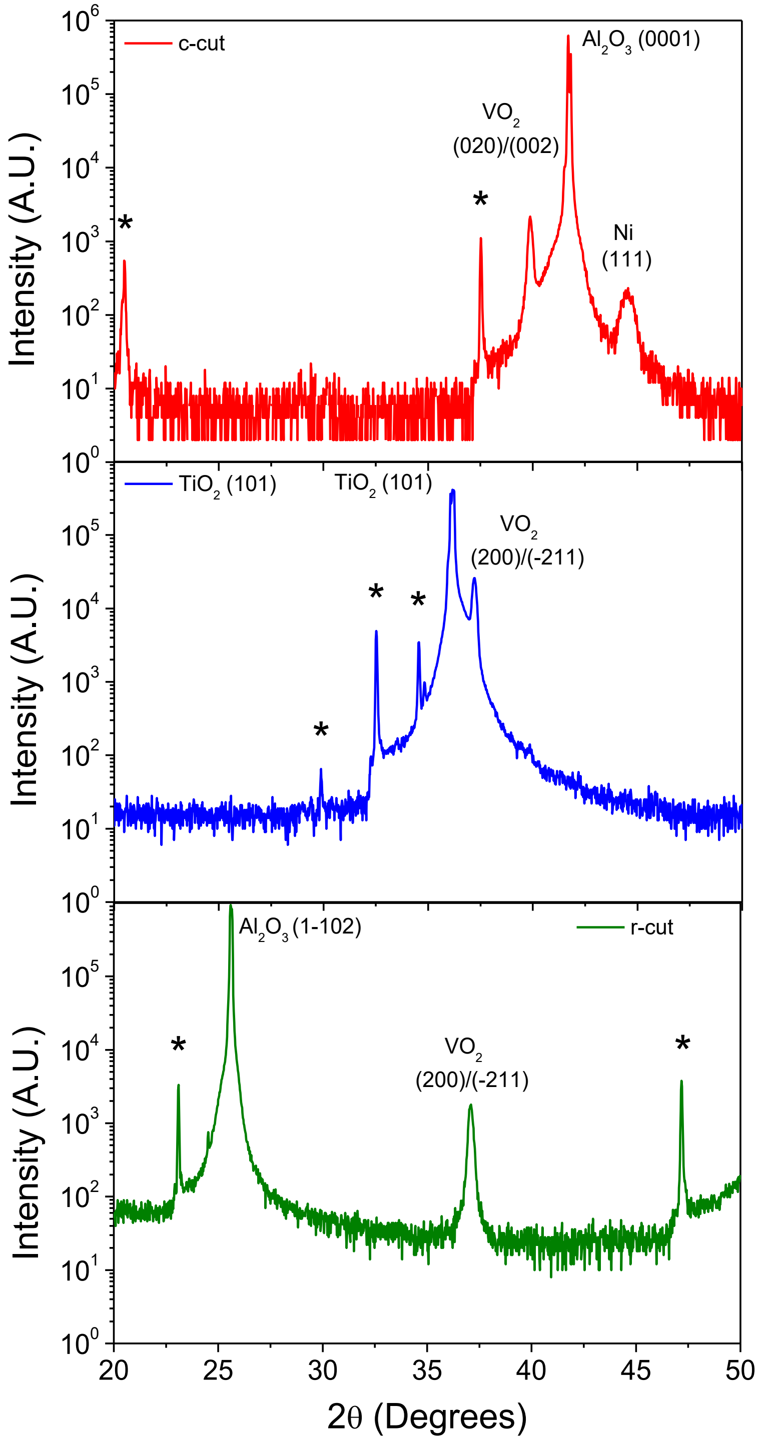

Figure 48. XRD of 100 nm/15 nm VO_2/Ni bilayers on: (Top) c-cut Al_2O_3 substrate, (Middle) TiO_2 (101) substrate, and (Bottom) r-cut Al_2O_3 substrate. Peaks labelled with a star correspond to the substrate.

After confirming the structural quality of the films, the surface morphology needs to be characterized. AFM for samples on c-cut Al_2O_3, TiO_2 (101) and r-cut Al_2O_3 substrates respectively are shown in Figure 49. It is immediately clear how important the substrate choice is, with each sample showing very different grain microstructure despite very similar deposition conditions and similar VO_2 quality. Examples of the underlying VO_2 morphology for each substrate was covered in Chapter 3. Even samples with the same preferred orientation such as the TiO_2 (101) and r-cut Al_2O_3 show different Ni morphology. The c-cut sample shows very small circular grains of 40-60 nm, and a low RMS roughness of 1.22 nm. The TiO_2 (101) sample goes to the other extreme, showing very large plateau like grains, separated by large grain boundaries. These boundaries show that the plateaus are roughly 15 nm tall, the nominal thickness of the Ni deposition. The overall film roughness is 4.53 nm, with the top of the plateaus showing less than 1 nm roughness. The grains themselves are on the order of hundreds of nm wide, typically 400+ nm wide. Lastly, the r-cut sample grain size is somewhere in between with moderately sized but visibly inhomogeneous regions of large grains interspersed between smaller grains. The RMS roughness is quite high, at 13.6 nm.

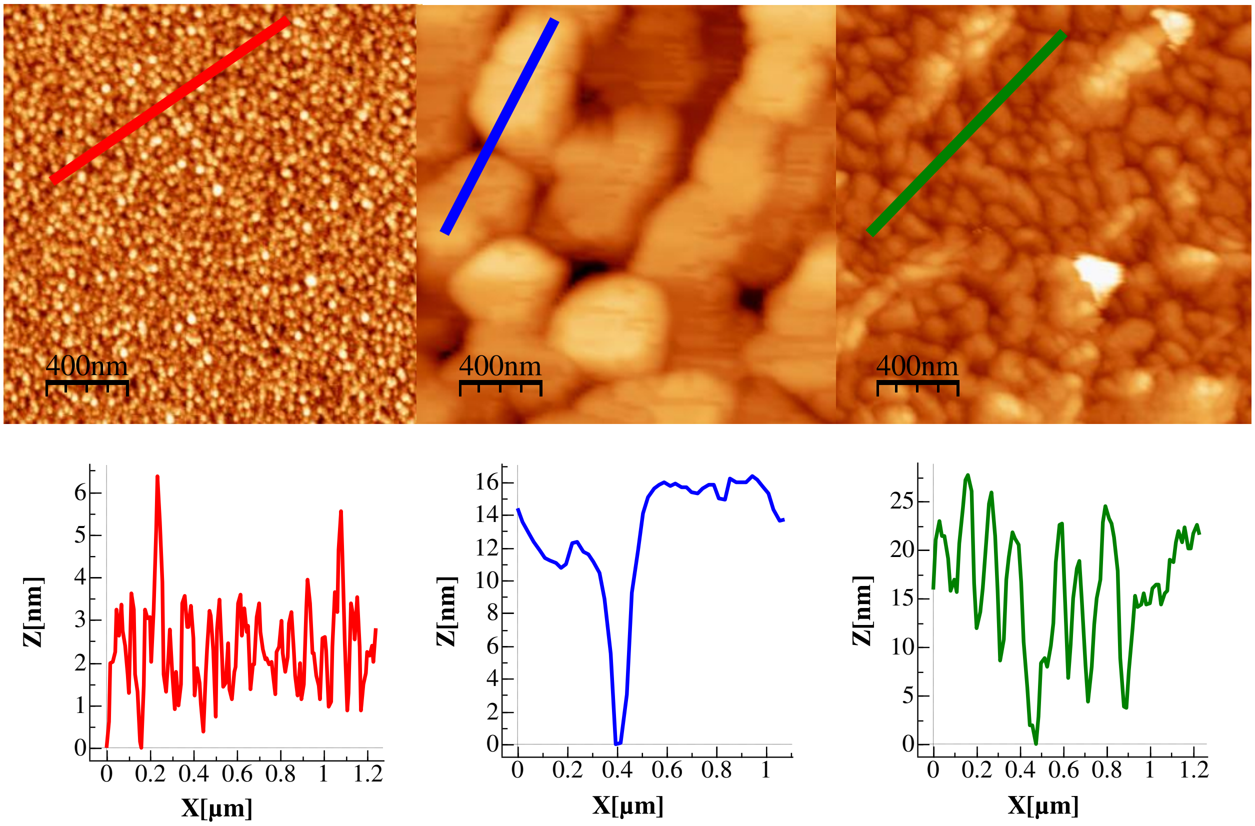

Figure 49. AFM for 100 nm/15 nm VO_2/Ni on (Left) c-cut Al_2O_3 substrate, (Middle) TiO_2 (101) substrate, and (Right) r-cut Al_2O_3 substrate. (Bottom) Line profiles are cuts along the colored lines in their respective AFM image.

Lastly, we provide R vs. T measurements for typical samples of bare 100 nm VO_2 films on TiO_2 (101), c-cut Al_2O_3, and r-cut Al_2O_3 substrates. These samples were optimized following the discussion in Chapter 3, with the conditions optimized for each substrate individually. All 3 show a strong 4 orders of magnitude MIT from roughly 1 MΩ to less than 100 Ω at 360 K. The details of the MIT follow the patterns established in the previous chapter for the respective substrate. The TiO_2 (101) sample shows the lowest T_c at less than 330 K, with a very sharp transition and low thermal hysteresis of 2.5 K. The r-cut Al_2O_3 sample is in the middle of the three, with a Tc of roughly 333.4 K, thermal hysteresis of 6 K and a rather wide tail on the upper portion of the MIT. The c-cut Al_2O_3 substrate has the highest T_c at approximately 338.4 K. It has a thermal hysteresis comparable to the r-cut Al_2O_3 at 5.8 K but doesn't display much of a tail in the MIT.

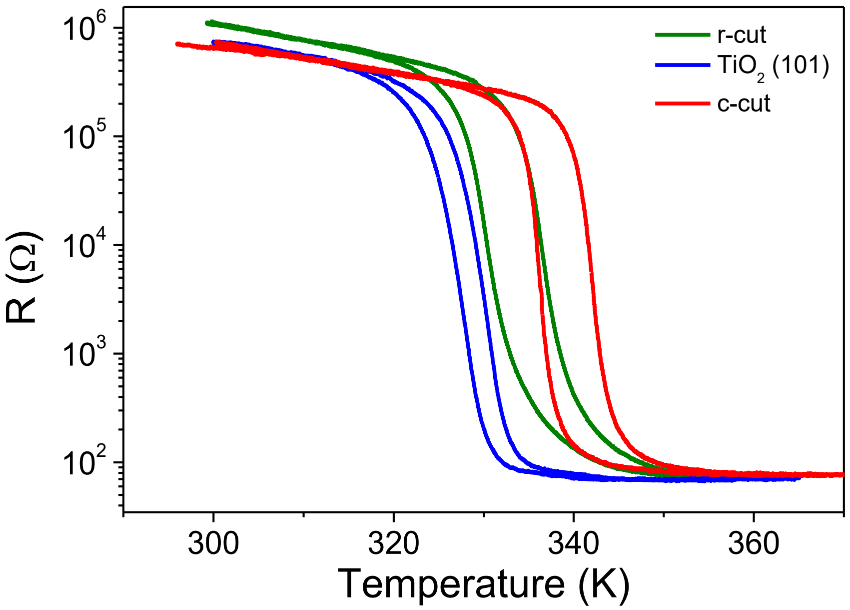

Figure 50. R vs. T for 100 nm bare VO_2 on TiO_2 (101), c-cut Al_2O_3, and r-cut Al_2O_3 substrates.

Having structurally characterized our VO_2/Ni bilayers as well as the R vs. T of the underlying VO_2, we are now ready to consider the magnetic properties in the bilayers.

4.3 Magnetic measurements for c-cut, r-cut, and TiO_2 substrates

In this section we present the magnetic measurements of HT VO_2/Ni bilayers taken in the VSM. RT samples show a different behavior and will be discussed in the next chapter. In particular, we focus our attention to the substrates characterized in the previous section: c-cut Al_2O_3, TiO_2 (101), and r-cut Al_2O_3. VO_2 is paramagnetic and therefore the majority of the magnetic signal will come from ferromagnetic Ni in any magnetometry measurement, even for thicknesses as thin as 10-15 nm. Magnetic hysteresis loops were taken at various temperatures beginning at 290 K and ending at 370 K, following the procedure given in Chapter 2. One full measurement consisted of the sample completing two full thermal 'cycles' of $290\ \mathrm{K} \rightarrow 370\ \mathrm{K} \rightarrow 290\ \mathrm{K} \rightarrow 370\ \mathrm{K} \rightarrow 290\ \mathrm{K}$. This temperature range is sufficient to ensure that the VO_2 is fully transitioned regardless of the substrate, and thus avoid traveling in a minor loop along the thermal hysteresis of the VO_2. The hysteresis loops are measured in-plane with an in-plane applied field.

Typical examples of the hysteresis loops for heterostructures grown on the three substrates are presented in Figure 51 for select temperatures. The magnetic data presented is the raw data, uncorrected for contributions from the sample holder, VO_2, or substrate. Note that the selected temperatures are slightly different between substrates. The temperatures shown were chosen to highlight changes in coercivity, which cluster close to the VO_2 T_c associated with that substrate.

For each substrate, these loops are from the first heating branch in the thermal cycling. At 300 K the hysteresis loops show a typical M vs. H response for a ferromagnet. As the temperature is increased, the overall shape of the hysteresis loop is maintained. However, there are slight changes in the saturation magnetization and more noticeably, large changes in the width, or coercivity, particularly near T_c for VO_2. The coercivity is the magnetic field required to reduce the magnetization to 0 from saturation. Here, we take the average for both negative and positive applied fields. This helps to reduce error, particularly from any stray bias fields. For example, there is often a small field (< 2 mT, often ~1 mT) due to remanent magnetization in the pickup coils of the VSM.

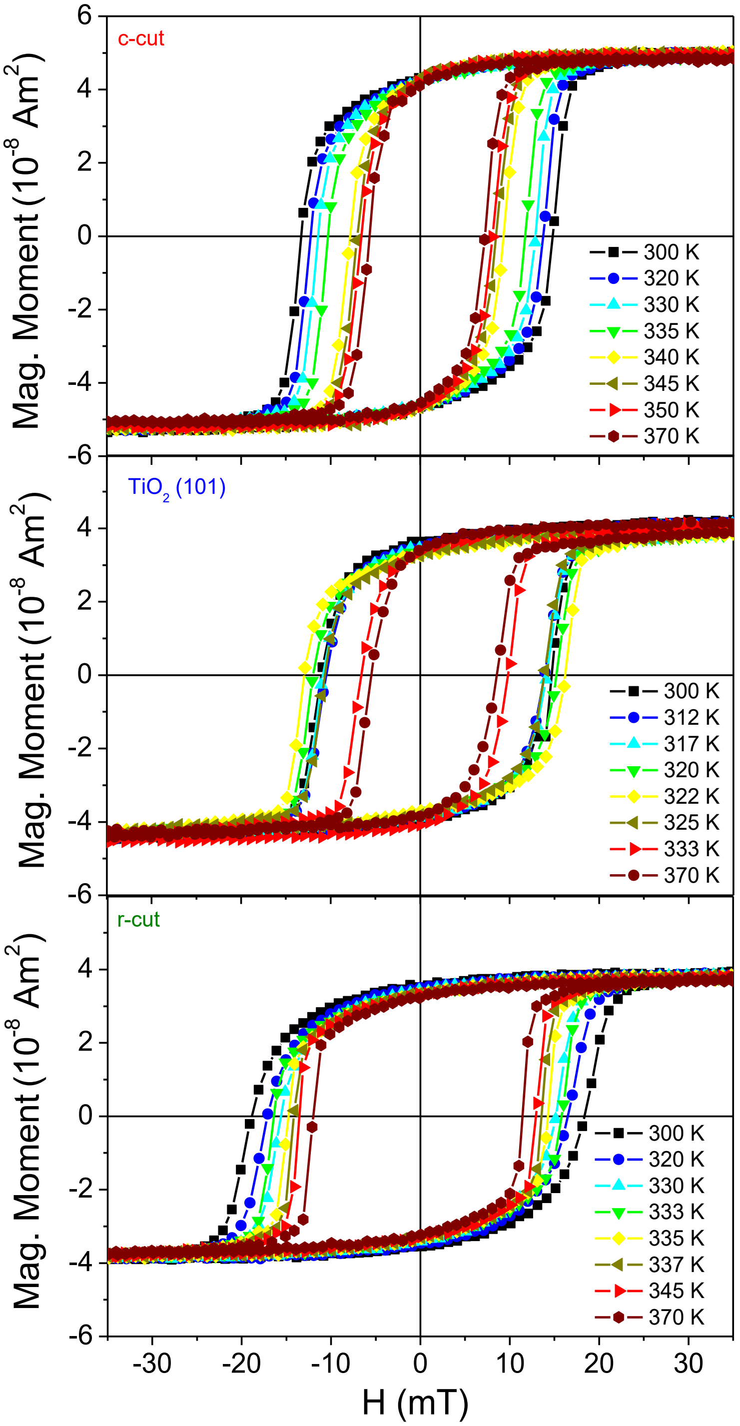

Figure 51. Magnetization vs. applied field (M vs. H) for various temperatures of HT 100 nm/15 nm VO_2/Ni bilayers on (Top) c-cut Al_2O_3, (Middle) TiO_2 (101), and (Bottom) r-cut Al_2O_3 substrates. First heating branch of 2 heating/cooling cycles.

In order to get a better look at the changes in coercivity, we can extract the coercivity from the hysteresis loops and plot it explicitly as a function of temperature for each thermal branch. This coercivity vs. temperature (H_C vs. T) behavior for both HT VO_2/Ni bilayers on all three substrates are plotted in Figure 52. The saturation magnetization changes will be discussed in a later section.

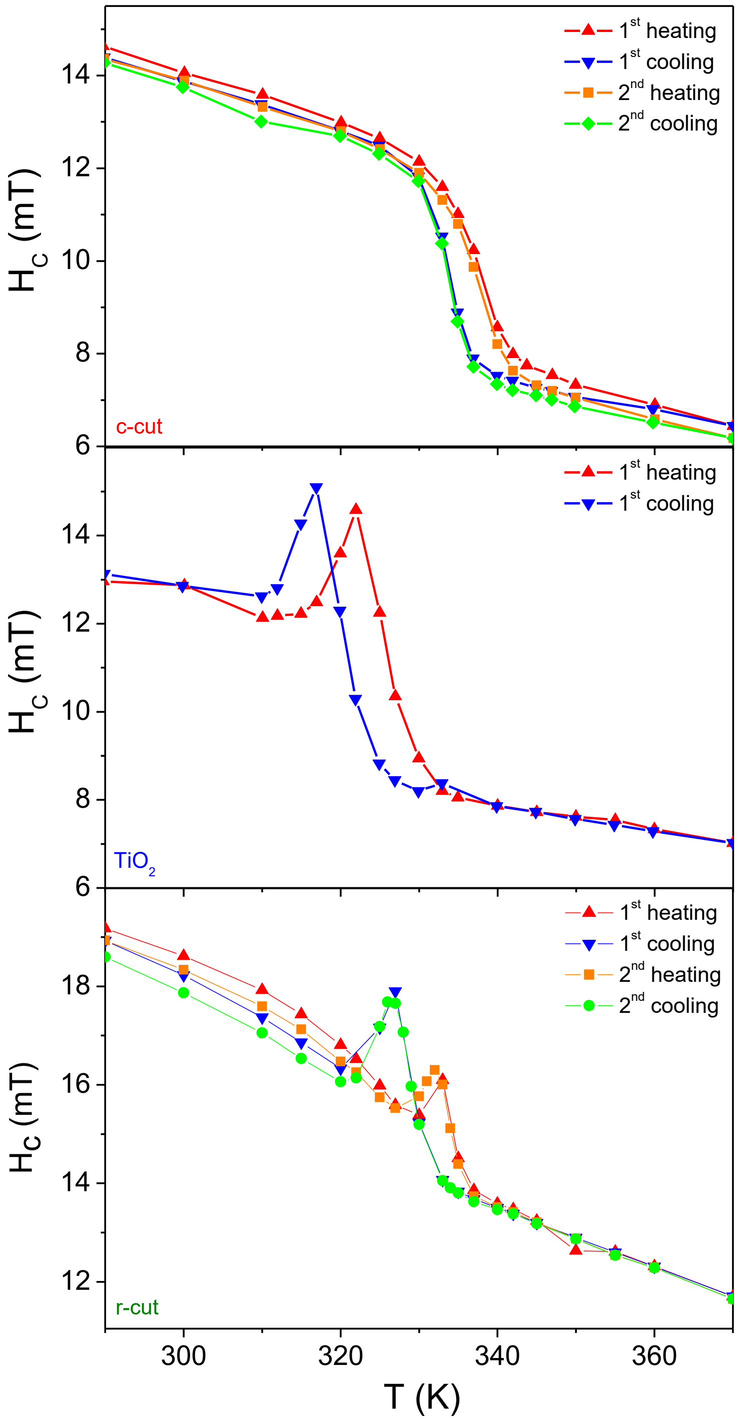

Figure 52. Coercivity extracted from M vs. H loops at various temperatures of HT 100 nm/15 nm VO_2/Ni bilayers on (Top) c-cut Al_2O_3, (Middle) TiO_2 (101), and (Bottom) r-cut Al_2O_3 substrates.

Looking first to the c-cut sample show in the top panel, we see the sample starts with a relatively large coercivity near RT, 14.6 mT at 290 K for the first heating loop. As the temperature is increased up to 330 K, the coercivity slightly decreases as is typical in ferromagnets. At roughly 330 K to 342 K, we see a sharp decrease in the coercivity to 7.54 mT at 347 K. This value is considerably lower than the previous trend as a function of temperature. A clear comparison can be made by linearly extrapolating the high temperature behavior back to 320 K. This yields an extrapolated coercivity of only 8 mT, a 37.5% decrease compared to the actual 12.8 mT measured. As the temperature is increased well past 347 K, the coercivity returns to its previous trend, although it has been permanently shifted lower. In the first cooling cycle shown in blue we see essentially the same behavior but with a 4 K thermal hysteresis. This hysteresis is a signature of the VO_2 phase transition and matches the one observed in the R vs. T of the bare VO_2. The sharp change in the coercivity at ~330-340 K that occurs can be attributed to the underlying VO_2, which will undergo its SPT as the temperature crosses T_c. Like the thermal hysteresis, this range agrees with the temperature range of the VO_2 MIT in the R vs. T measurements, as shown previously in Figure 50. As the VO_2 crosses from the monoclinic to rutile structure, it induces a shear strain due to the changes in V atoms along the c-axis. This shear strain then acts to apply an anisotropic stress at the VO_2/Ni interface, which can influence the Ni via inverse magnetoelastic coupling. This effect has previously been demonstrated in VO_2/Ni and V_2O_3/Ni bilayers.[296] The coercivity change therefore inherits many of the properties of the underlying SPT. Not only does it occur at T_c, it has a similar temperature spread to the complete the transition (as can be seen in e.g. R vs. T measurements), as well as the signature thermal hysteresis of the VO_2 SPT. This coupling to the SPT means that deposition conditions for the Ni becomes an additional tuning parameter. Recall that for HT samples, we deposit the Ni well above the T_c of VO_2. This will lead to the Ni seeing the rutile VO_2 during the initial deposition, and the Ni is relaxed when the VO_2 is in the rutile state. When cooling through the transition, the Ni becomes strained when the VO_2 is in the monoclinic structure. The HT deposition therefore determines the ‘high to low’ coercivity as the temperature increases. Below T_c, the Ni is strained, and above the Ni is able to relax. The baseline coercivity in this relaxed state will also be influenced by film features such as the roughness, defects, etc.

In the middle and bottom panels of Figure 52, the same type of coercivity vs. temperature profile is plotted for the VO_2/Ni on TiO_2 (101) and r-cut Al_2O_3 substrate. Following the first heating branch, both samples start with an elevated coercivity that decreases with increasing temperature. Close to the T_c for their respective substrates we again see a sharp drop in the coercivity, although the r-cut drop is smaller than in the c-cut or TiO_2 (101) case. However, in both of these samples, there is a coercivity enhancement that is strongly localized near T_c. Far above T_c, the samples return to the trend of slowly decreasing coercivity with increasing temperature after being permanently shifted to lower coercivity. The cooling branches show a similar behavior, but with thermal hysteresis values that match those seen in the R vs. T measurements for bare VO_2 on the respective substrates. We note that future thermal cycles for all substrates with HT VO_2/Ni heterostructures show the same features in the coercivity indicating that this process is repeatable and that the samples haven’t significantly degraded due to the thermal cycling.

The H_C vs. T profiles for these two samples are the product of two effects. In addition to the strain anisotropy field mechanism that led to the decrease in coercivity well above T_c, another effect accounts for the localized peak in coercivity close to T_c. We attribute this enhanced coercivity to the coexistence of both structural phases of VO_2 in the vicinity of T_c, as detailed in the next section.

4.4 Localized coercivity enhancement due to phase coexistence

The spike in coercivity seen in the previous section can be attributed to the nature of the SPT of the VO_2 that underlies the FM Ni. A first order transition implies a mix of both phases when the material is very close to T_c. The coexistence of both the monoclinic and rutile phase at fixed temperatures near T_c has been confirmed directly for polycrystalline thin film VO_2, as shown in Section 1.4. The domain size of the VO_2 monoclinic and rutile phases range from 10's-100's of nm, as seen in Figure 14. However, a VO_2/Ni hybrid heterostructure system introduces another fundamental length scale in the Ni's magnetic domain size.

The size of the Ni magnetic domain size will be directly related to the microstructure and morphology of the Ni film. The AFM shown earlier in Figure 49 of Section 4.2 is a direct probe of the Ni morphology and can therefore give insight into the typical expected magnetic domain size. In the c-cut sample, which has small Ni grains, we can expect the Ni magnetic domains to be of similar size to the grain size. If the VO_2 phase domains are roughly the same size of the Ni grains/domains or larger, then the magnetic behavior is largely governed by grain boundaries and the phase coexistence does not play a significant role in the magnetic pinning. By contrast, in the large smooth TiO_2 (101) plateaus, the Ni magnetic domains will be much larger, and will be able to see a larger portion of the boundaries between the two underlying VO_2 phases. The two VO_2 phases are under different amounts of strain, which leads to an inhomogeneous boundary between the two. This laterally inhomogeneous stress profile leads to disorder which will be inherited by the Ni layer, with phase boundaries acting as magnetic defects or pinning sites for domain wall motion during magnetic reversal. This disorder will be maximized when the border region between the two VO_2 phases are maximized, which should occur close to the middle of the transition and also explains why the phenomena is localized so sharply around T_c. The r-cut is somewhere between the two more extreme examples, with medium sized grains. Therefore, it shows a coercivity spike, but smaller than that of the TiO_2 (101). This coercivity enhancement had previously been seen in V_2O_3/Ni bilayers during the V_2O_3 SPT, as well as in $Nd_{0.5}Sr_{0.5}CoO_3$ on STO substrate, but not in VO_2/Ni.[298] The similar response despite the fundamentally different driving mechanisms for this phase separation is another sign that this coercivity enhancement is driven by phase coexistence across the VO_2 SPT.[299] The localized coercivity spike near T_c seen only in some samples is therefore driven by a competition between the length scales of the VO_2 structural phase domains, and the magnetic domains of the overlying Ni layers.

4.5 Magnetic anisotropy

The samples were also checked for any in-plane anisotropy by rotating the samples in-plane and remeasuring their magnetic properties. Typical hysteresis loops are shown in Figure 53 for both c-cut (Top) and r-cut (Bottom) Al_2O_3 substrates. The c-cut sample shows an identical hysteresis loop at various angles, indicating the lack of any strong anisotropy for in-plane rotations. The r-cut shows only a very minor change in the hysteresis loop at a 45 ° rotation. These measurements were taken at 300 K, indicating a lack of anisotropy even when the HT films are in the strained state due to the VO_2 SPT. The VO_2 SPT is highly anisotropic, so the lack of anisotropy can be tied to the polycrystallinity of the films.

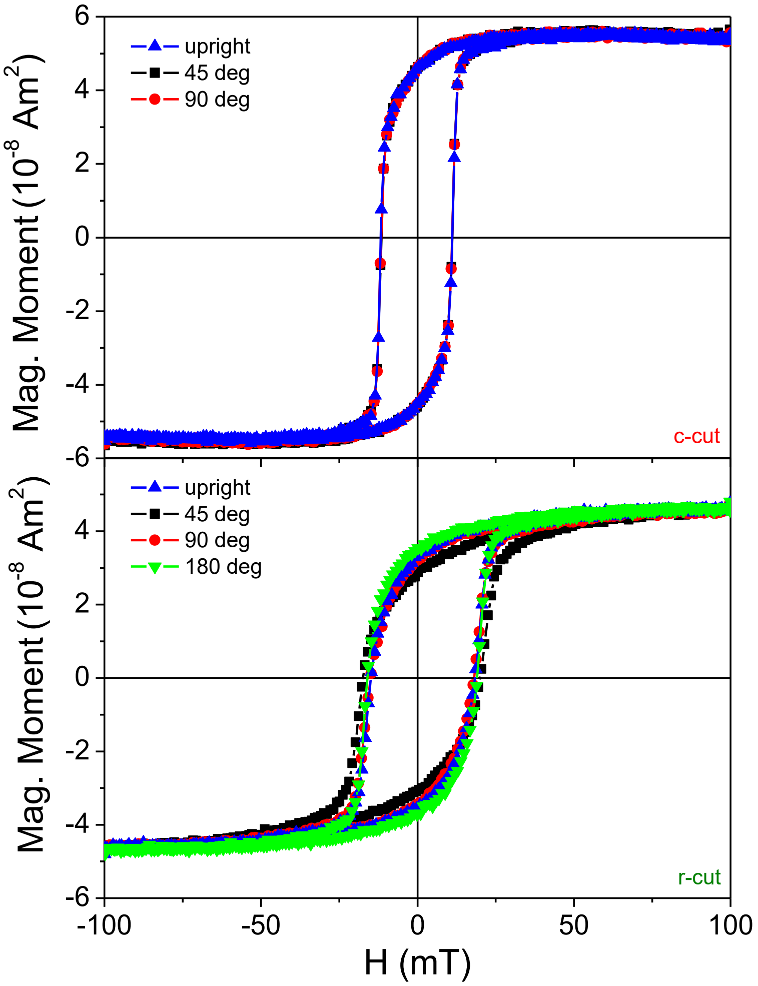

Figure 53. M vs. H measurements of HT 100 nm/15 nm VO_2/Ni bilayers on (Top) c-cut Al_2O_3 substrate and (Bottom) r-cut Al_2O_3 substrate, for various orientations inside the VSM. Taken at 300 K.

By contrast, the TiO_2 (101) samples inherit a very strong rutile symmetry anisotropy from the substrate. This symmetry was evident in the surface morphologies of both the VO_2 layer shown in Figure 45 of Chapter 3 as well as the Ni itself in Figure 49. Figure 54 shows M vs. H loops and their extracted coercivities for a fresh TiO_2 (101) sample, but with one rotated 90 ° in the sample holder relative to the other. Both measurements were taken with the same sample and measured consecutively. The left figure shows the hallmark rectangular shape of a magnetic easy axis, whereas the right figure shows a clear hard axis. In the easy axis orientation, the sample is relatively easy to saturate at less than 30 mT, but shows a large coercivity, greater than 12 mT at all temperatures measured. By contrast, in the hard axis orientation, the hysteresis loops do not close until nearly 50 mT. They also show a much lower coercive field, with a maximum less than 10.5 mT.

This anisotropy also has a strong influence on the H_C vs. T behavior. The measurement along the easy axis is similar to the measurement shown previously. The coercivity begins elevated, spikes close to Tc due to phase coexistence, and then decreases sharply across the VO_2 SPT. In the hard axis measurement, the sample still has a high to low coercivity profile across the temperature range measured, and the transition width is consistent with the easy axis measurement as well as the VO_2 transition width as measured in R vs. T measurements. However, the localized spike in coercivity close to T_c is suppressed. The fact that this is seen in the same sample rules out different surface morphology as a cause.

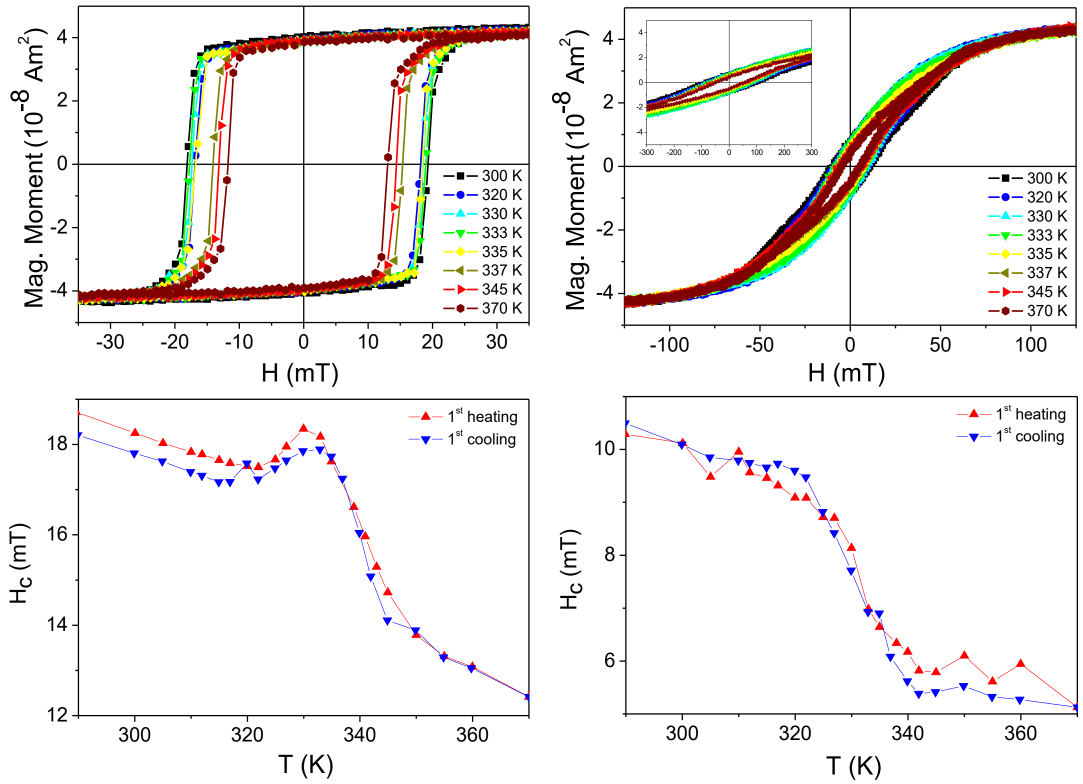

Figure 54. (Top) M vs. H for various temperatures of HT 100 nm/15 nm VO_2/Ni bilayers on TiO_2 (101) substrate. (Top Left) Easy axis and (Top Right) Hard axis, rotated 90 degrees relative to the easy axis. (Bottom) Extracted coercivities corresponding to the above loops.

4.6 Magnetization vs. Temperature

In addition to the various M vs. H measurements shown, measurements of M as a function of temperature (M vs. T) were also taken. As mentioned previously, there was a slight change in saturation magnetization visible in the hysteresis loops shown previously. Figure 55 shows M vs. T curves for (a) c-cut, (b) r-cut, and (c) TiO_2 substrates under an applied field of 50 mT. Here, all 3 samples show very similar behavior. As the temperature is ramped well below T_c, they show a slight decrease in the magnetization as thermal energy reduces the alignment of the magnetic moments. Near T_c, we see a sharp increase in magnetization that is maintained even as the temperature continues to increase above T_c. As with the coercivity changes, this magnetization change occurs at a temperature corresponding to the T_c of the bare VO_2 for each substrate. In the cooling branch, we see the opposite behavior, with characteristic thermal hysteresis. Lastly, we note that the process is repeatable through multiple thermal cycles (data not shown), as the M vs. H measurements were. Indeed, these measurements were taken after the M vs. H loops following the procedure laid out in Chapter 2 which means that the samples have already been thermally cycled prior to these M vs. T measurements.

As with the other changes in the magnetic properties of these VO_2/Ni heterostructures, the changes in magnetization are fundamentally tied to the VO_2 SPT via magnetoelastic coupling. In addition to the stress anisotropy field, there is the inverse magnetostrictive effect itself. As was discussed in Section 1.5, a FM under stress will undergo changes in its magnetization. For Ni, which has a negative magnetostrictive constant, a compressive (tensile) stress leads to an increase (decrease) in magnetization, for fixed applied magnetic field (See Figure 17). Since the Ni will be relaxed above T_c when deposited in the HT configuration, this indicates the Ni undergoing a tensile stress when the temperature is reduced below T_c.

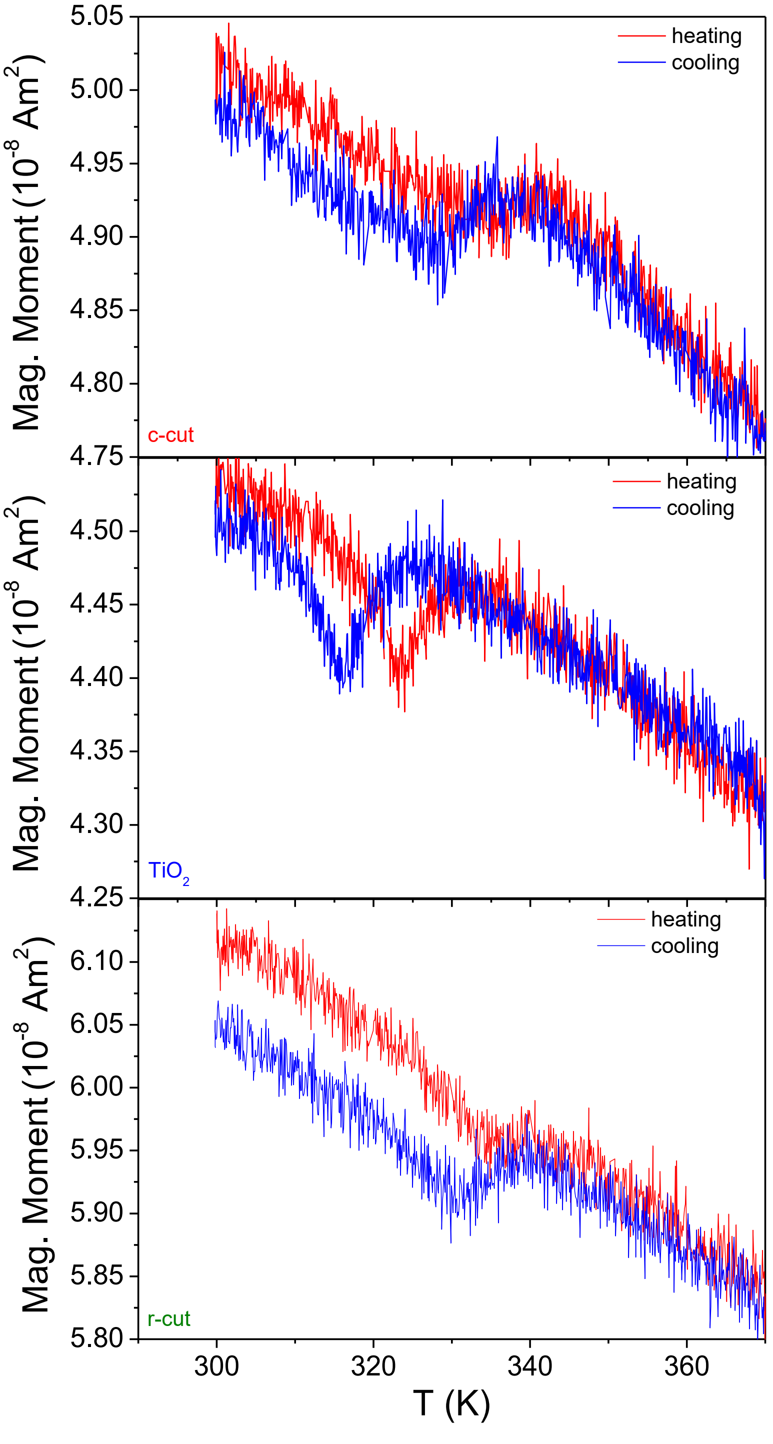

Figure 55. M vs. T for HT 100 nm/15 nm VO_2/Ni bilayers on (Top) c-cut Al_2O_3, (Middle) TiO_2 (101), and (Bottom) r-cut Al_2O_3 substrates. The applied magnetic field is fixed at 50 mT for all samples.

4.7 Estimates of strain

A rough quantitative estimate of the strain being applied to the Ni layer can be made utilizing Eqn. 12 from Section 1.5 if we assume the stress in the Ni is uniform and that change in magnetic properties is due to an effective stress anisotropy field

$$H_{eff}^{*} = H_{app} + \alpha^{*} M \pm \frac{3\,\lambda_{si}\sigma}{\mu_0 M_S} \qquad 4.1$$

One way to do so is to compare the change in the coercivity above and below the VO_2 transition. For the same Ni layer, the effective field should be same at the coercive point.

$$\mathrm{H}_{\mathrm{eff}_{\mathrm{below}}}^{*} = \mathrm{H}_{\mathrm{eff}_{\mathrm{above}}}^{*} \qquad 4.2$$

Conveniently, at the coercive point the term proportional to M drops out, leaving[238]

$$H_{app\_below} \pm \frac{3\,\lambda_{si}\sigma}{\mu_0 M_S} = H_{app\_above} \qquad 4.3$$

with the strain being provided by the VO_2 SPT. This yields

$$\Delta H_C = H_\sigma = \frac{3\,\lambda_{si}\sigma}{\mu_0 M_S} \qquad 4.4$$

Previously, in Section 4.3 the coercivity difference for the c-cut sample was estimated to be 4.8 mT. Taking the effective field H_σ to be the difference between measured and extrapolated coercivities and using the material parameters for Ni ($\mathrm{M_S} = 470 \cdot 10^3\ \frac{\mathrm{A}}{\mathrm{m}}$, $\lambda_{\mathrm{si}} = \lambda_{\mathrm{p}}^{\mathrm{si}} = -34 \cdot 10^{-6}$) yields a stress of 22 MPa required for the coercivity difference at 320 K in the c-cut sample shown previously. This value is in good agreement with previous work, and is a reasonable fraction of the directly measured stress of 380 MPa in single VO_2 films.[300]

A similar estimate of the strain in the Ni layer can be made utilizing the M vs. T data presented in the previous section and applying the J-A-S model developed in Section 1.5. For the field applied ($\mathrm{H_{app}} = 50\ \mathrm{mT}$), the sample is well saturated, as can be seen in the hysteresis loops of Figure 55. It is therefore reasonable to represent the total magnetization M by the anhysteretic magnetization $\mathrm{M_{an}}$, given as

$$\mathrm{M} = \mathrm{M_{an}} = \mathrm{M_S}\mathcal{L}\left(\frac{\mathrm{H^*_{eff}}}{\mathrm{a}}\right) = \mathrm{M_S}\left(\coth\left(\frac{\mathrm{H^*_{eff}}}{\mathrm{a}}\right) - \frac{\mathrm{a}}{\mathrm{H^*_{eff}}}\right) \qquad 4.5$$

with the parameters $\mathrm{M_S}$ and a given from fitting to experimental data. The effective field required to cause the change in magnetization seen in the M vs. T across the $\mathrm{VO_2}$ SPT can be found by numerically integrating the differential form of Eqn. 4.5. Either $\frac{\mathrm{dM}}{\mathrm{d}\sigma}$ or $\frac{\mathrm{dM}}{\mathrm{dH^*_{eff}}}$ can be used, since as mentioned in Section 1.5, $\mathrm{M_{an}}(\mathrm{H_{app}}, \sigma) = \mathrm{M_{an}}(\mathrm{H^*_{eff}}, 0)$. Indeed, one can switch from one to the other via application of the Chain Rule $\frac{\mathrm{dM}}{\mathrm{d}\sigma} = \frac{\mathrm{dM}}{\mathrm{dH^*_{eff}}}\frac{\mathrm{dH^*_{eff}}}{\mathrm{d}\sigma}$. In the case where the magnetization is along the anhysteretic, integration simply returns the closed form solution of Eqn. 4.2. An intuitive explanation for the equivalence between $\mathrm{M_{an}}(\mathrm{H_{app}}, \sigma)$ and $\mathrm{M_{an}}(\mathrm{H^*_{eff}}, 0)$ can be seen by considering what these two expressions represent on a hysteresis loop. The point on the M vs. T. at 345 K, just above the $\mathrm{VO_2}$ transition, would be equivalent to a hysteresis loop at $\mathrm{H_{app}} = 50\ \mathrm{mT}$ and 345 K. This loop for the c-cut sample, previously shown in Figure 51, is reproduced in Figure 56. For comparison, we also include the anhysteretic magnetization in red. As expected, the anhysteretic and experimental magnetizations overlap when the sample is saturated at roughly 25 mT or larger. Physically, this corresponds to completely reversible magnetization as the magnetic field is swept, which leads to no history dependence.

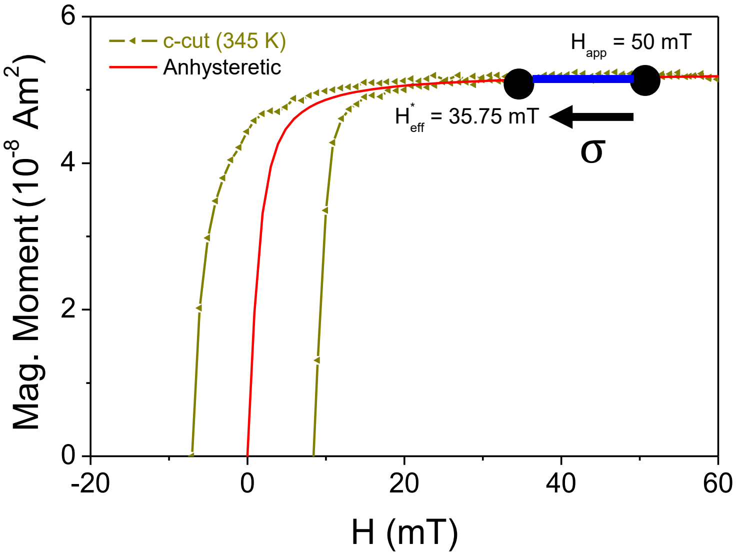

Figure 56. M vs. H for an HT 100 nm/15 nm VO_2/Ni bilayer on c-cut Al_2O_3. The experimental loop is the same 345 K loop shown in Figure 51, corrected for diamagnetic substrate contributions, and centered. The anhysteretic was found via fitting to the saturated portion of the data. It has parameters $M_S = 407\ \frac{kA}{m}$, $a = 582\ \frac{A}{m}$, and $\alpha = 0.0049695$.

On the hysteresis loop, the M vs. T equivalent point is the point labeled by $H_{app} = 0.05$ mT, with an effective field $H^*_{eff} = H_{app} + \alpha^* M$. As the temperature in the sample is reduced, the VO_2 SPT strain is applied, shifting the effective field by a factor of $\frac{3\,\lambda_{si}\sigma}{\mu_0 M_S}$. The change in magnetization was estimated to be 0.768% in the M vs. T, and the shift in effective field can be found by finding at what point along the upper branch the magnetization is reduced by this amount. Ultimately, the magnetization drop yields an $H_\sigma = 1.43$ mT or a tensile stress of 65.6 MPa. It is clear from the figure that a tensile stress is needed, since $\frac{3\,\lambda_{si}\sigma}{\mu_0 M_S}$ must be overall negative to reduce the magnetization and Ni has a negative magnetostrictive coefficient λ_{si}. Again, the estimated stress is a significant fraction of the VO_2 SPT stress and is of a similar order of magnitude to the previous estimate based on the coercivity changes. However, there is a clear disagreement between the two estimates. This is not too surprising, considering the assumptions that went into the form of stress anisotropy field used. For instance, it is known that there is a demagnetization field term in polycrystalline films that goes as $H_D = \frac{3\,\lambda_{si}\sigma M}{\mu_0 B_S}$, due to the effect of stress on grain alignment.[230] This term acts nearly identically to H_σ, but scales linearly with M. In addition, the percentage change in magnetization is very small, less than a percent at such high saturating fields. This makes any estimate rather sensitive to how the raw magnetic data is normalized.

The result of integrating the differentials (or using the equivalent values from the hysteresis loop) yields M as a function of H^*_{eff} or σ. To translate back to a function of temperature as in the M vs T, we need a form for the stress as a function of temperature. We assume that the distribution of T_C in the VO_2 grains is a Gaussian distribution. In an effective media approximation, the strain applied can be found by integrating this distribution, which will yield the percentage of grains in either phase. The integral of a Gaussian is the (complementary) error function, with parameters from fitting to the data. The stress as a function of temperature T can then be written as

$$\sigma(T) = \frac{\sigma_0}{2}\operatorname{erfc}\left(\frac{T - 337.4}{2}\right) \qquad 4.6$$

where σ_0 is the stress applied when the film is fully transitioned to the monoclinic state. A picture of Eqn. (4.3) is shown in the inset of Figure 57. M is now explicitly a function of T, given by

$$M(T) = M_{an}(T) = M_S\mathcal{L}\left(\frac{0.05 + \alpha^* M - \frac{3\,\lambda_{si}}{\mu_0 M_S}\frac{\sigma_0}{2}\operatorname{erfc}\left(\frac{T - 337.4}{2}\right)}{a}\right) \qquad 4.7$$

The result is shown below in Figure 57. For visual clarity, the theoretical magnetization obtained was then corrected with the approximately linear slope as a function of temperature, as our version of the J-A-S model does not explicitly capture the effects of temperature.

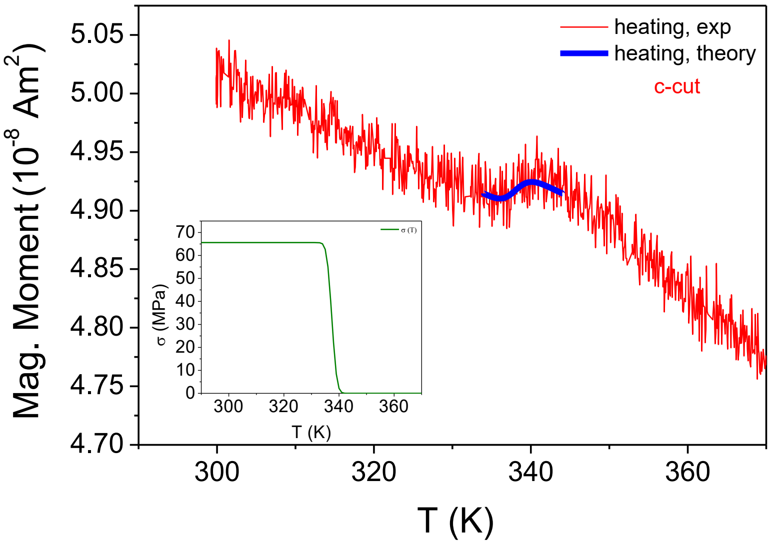

Figure 57. M vs. T for HT 100 nm/15 nm VO_2/Ni bilayers on c-cut Al_2O_3. The same data as the heating data shown in Figure 55 is shown in red. $H_{\mathrm{app}} = 0.05$ mT. The theoretical fit is shown in blue.

Taken together, these estimates serve as a reassuring sanity check that the effect is indeed due to the stress of the VO_2 SPT. Estimates on the other substrates will yield similar values, with variations due to factors such as Ni orientation, interfacial roughness, etc. However, it is worth stressing that a number of simplifying assumptions were made in these estimates. Theoretically, the expressions used assumed a uniaxial stress, and that the film was not textured with a preferred orientation. In addition, there is no guarantee the stress is uniform throughout the Ni layer. Therefore, even in the best case scenario these values should be considered an equivalent uniaxial stress. The order of magnitude reduction from the full SPT stress may also be indicative of a stress relaxation mechanism at the interface, such as grain boundaries. This would lead to only a partial transfer of strain across the interface. Lastly, thin film magnetostriction values can vary greatly from bulk values.[301]

4.8 Alternate substrates: m-cut and a-cut Al_2O_3 substrates

In addition to the previous 3 substrates that were fully structurally characterized, Ni was also deposited onto VO_2 on both m-cut and a-cut Al_2O_3 substrates following the same procedure as previously described. Their H_C vs. T curves are plotted in Figure 58. Both show responses that are very similar responses to the c-cut sample. Below T_c, they show elevated coercivities of around 15-16 mT. Across the VO_2 SPT we see a decrease in the coercivity with the T_c, sharpness of the coercivity change, and thermal hysteresis modified by the choice of substrate. Well above T_c, the coercivity returns to its previously slow decrease but stays shifted downward. Overall, the absolute values of the coercivity are very similar between these two samples as well as the c-cut. As in the previous samples, the process is completely reversible over multiple cycles.

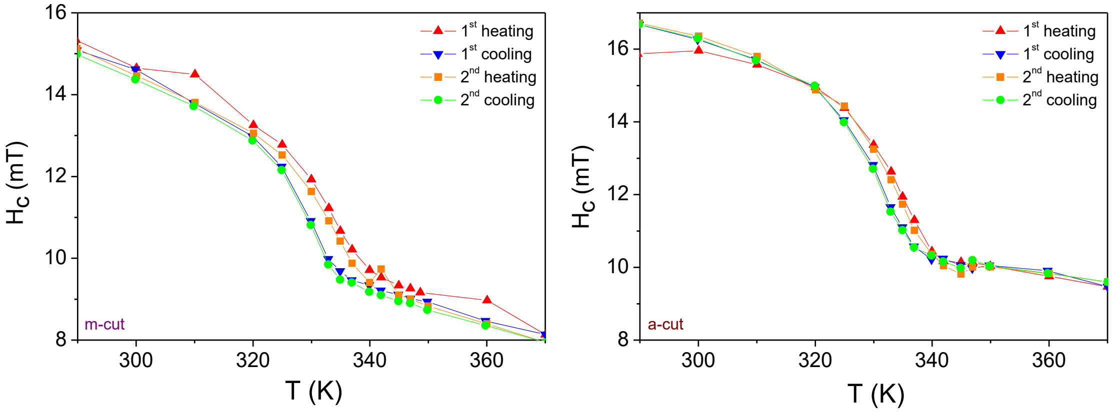

Figure 58. Coercivity extracted from M vs. H loops at various temperatures of HT 100 nm/15 nm VO_2/Ni bilayers on (Left) m-cut Al_2O_3, (Right) a-cut Al_2O_3 substrates.

4.9 Conclusions

In this chapter, we show a method for preparing structurally coupled VO_2/Ni heterostructures on various substrates via magnetron sputtering. A necessary precursor is the optimization of the VO_2 layer, which was described in the previous chapter. The structural quality and surface morphology were confirmed via XRD and AFM respectively. The VO_2 shows strong crystalline quality while the Ni tends to be polycrystalline for most choices of substrate. The Ni grains show a wide range of grain size and structure, from small grains on the order of 50 nm wide to several microns.

Magnetic measurements show that the VO_2 SPT affects the magnetic properties of the Ni via magnetoelastic coupling mediated at the interface of the two layers. This interfacial strain leads to several effects. In all samples, there is a sharp decrease in coercivity with increased temperature due to the strain anisotropy field generated by the SPT strain. The T_c for this process as well as the sharpness and resulting thermal hysteresis are dependent on the underlying VO_2 layer and is therefore tunable via choice of substrate and VO_2 deposition conditions. In addition, samples show an increased magnetization across the VO_2 SPT due to an inverse magnetostrictive effect. Last, some samples show a localized spike in the coercivity very close to T_c of the underlying VO_2. We attribute this to phase coexistence across the first order VO_2 SPT. Domain wall motion in samples with large Ni magnetic domains (grains) can be pinned by these phase boundaries which act as magnetic defects. Whereas samples with smaller grains are primarily influenced by grain boundaries.

In conclusion, VO_2/Ni bilayers show an effective means for tuning the coercivity of the FM layer with alternative stimuli such as temperature. Below the T_c for the VO_2 SPT, strain leads to a 4.8 mT (37.5%) increase in coercivity. In addition, phase coexistence of the VO_2 phases close to T_c leads to a sharply localized coercivity enhancement as large as 6.2 mT (73%) in samples with sufficiently smooth interfaces. The tunability of the underlying VO_2 SPT is inherited by the coercivity changes, allowing for control in the coercivity vs. temperature profile. Estimates of the interfacial strain show a reasonable fraction of the SPT strain is transferred, with room for enhancement with better control over e.g. the interface. All samples in this chapter had their Ni layers deposited in the ‘HT’ setup such that the Ni is deposited onto rutile VO_2 and show reproducible magnetic behavior over multiple thermal cycles.

Chapter 5. Irreversibility in VO_2/Ni Bilayers

5.1 Motivation

During the work presented in the previous chapter, the Ni was always deposited in the HT configuration, or above the VO_2 SPT. A twist on this concept is to consider depositing the Ni below T_c and therefore below the VO_2 SPT. In principle, doing so should reverse the effects of the VO_2 SPT. Rather than being relaxed above T_c and under compressive strain below T_c, the Ni will instead be relaxed below T_c and under tensile strain above T_c. This should reverse the magnetic effects in the VO_2/Ni bilayers, compared to the HT samples.

However, it was observed that the magnetic properties in these RT samples also show some interesting irreversibility after the first thermal cycle that was not observed in HT samples. This irreversibility can have drastic effects on the magnetic properties of the RT bilayers. A potentially related irreversibility after the first thermal cycle can also be seen in R vs. T measurements, with the resistance of the film below T_c being permanently shifted higher. We propose cracking in the VO_2 as a potential mechanism that would explain both types of irreversibility. We first review the literature on cracking in VO_2. While VO_2 has long been known to suffer cracking across the SPT in single crystalline form, there is considerably less data on cracking on thin film VO_2. We then compare the experimental R vs. T results to a theoretical percolation model that includes the effects of cracking. Cracks are known to be highly resistive, and therefore small amounts of cracks could influence the R vs. T properties of VO_2 films. To directly observe whether cracking occurred, the samples were then measured using AFM.

5.2 Magnetic Irreversibility in VO_2/Ni bilayers

In previous chapters it was shown that the VO_2 SPT caused a change in the magnetic properties of the Ni in VO_2/Ni bilayers. In those experiments, Ni was always deposited onto VO_2 at elevated temperatures which ensured the VO_2 was in the rutile state (‘HT’). Ni deposited on rutile VO_2 should be relaxed when the VO_2 is in the rutile state and become stressed as the VO_2 transitions to the monoclinic state. However, if Ni is initially deposited onto monoclinic VO_2, it will be relaxed when VO_2 is in the monoclinic state and stressed when VO_2 transitions to the rutile state (‘RT’). Rather than being under tensile stress as in the HT case, it will be under compressive stress.

Figure 59 shows hysteresis loops for RT VO_2/Ni bilayers at selected temperatures across the VO_2 transition, for 4 consecutive thermal branches. In the top left, corresponding to the first heating cycle, we see a typical ferromagnetic response for the Ni layer at all temperatures, with the hysteresis loops maintaining their overall shapes. As in the HT case, the changes in the Ni behavior is realized in changes in the saturation magnetization and coercivity of the sample. The magnetization at 327 K, below the transition, is notably higher than at temperatures above T_c, such as 370 K. Even more evident are the changes in coercivity, where a clear temperature trend is noticeable. The hysteresis loops for the other 3 thermal cycles show coarsely similar behavior to the first heating cycle but vary in the finer details. The coercivities are various temperatures have become much more homogenous relative to the first heating cycle, although they still follow the same trend. The difference in saturation magnetization has also largely disappeared. Relative to each other, the first cooling, second heating, and second cooling largely agree, although there are minor adjustments from the first cooling to the second heating cycle. This agreement is common, and we’ll hereafter refer to all 3 thermal cycles after the first heating as ‘future cycles’ when discussing them in aggregate. As before, we can extract the coercivity and plot it as a function of temperature (H_C vs. T), to more clearly observe the changes in the VO_2/Ni bilayer. The coercivities corresponding to the measurements in Figure 59 are shown in Figure 60, with a more complete temperature sampling.

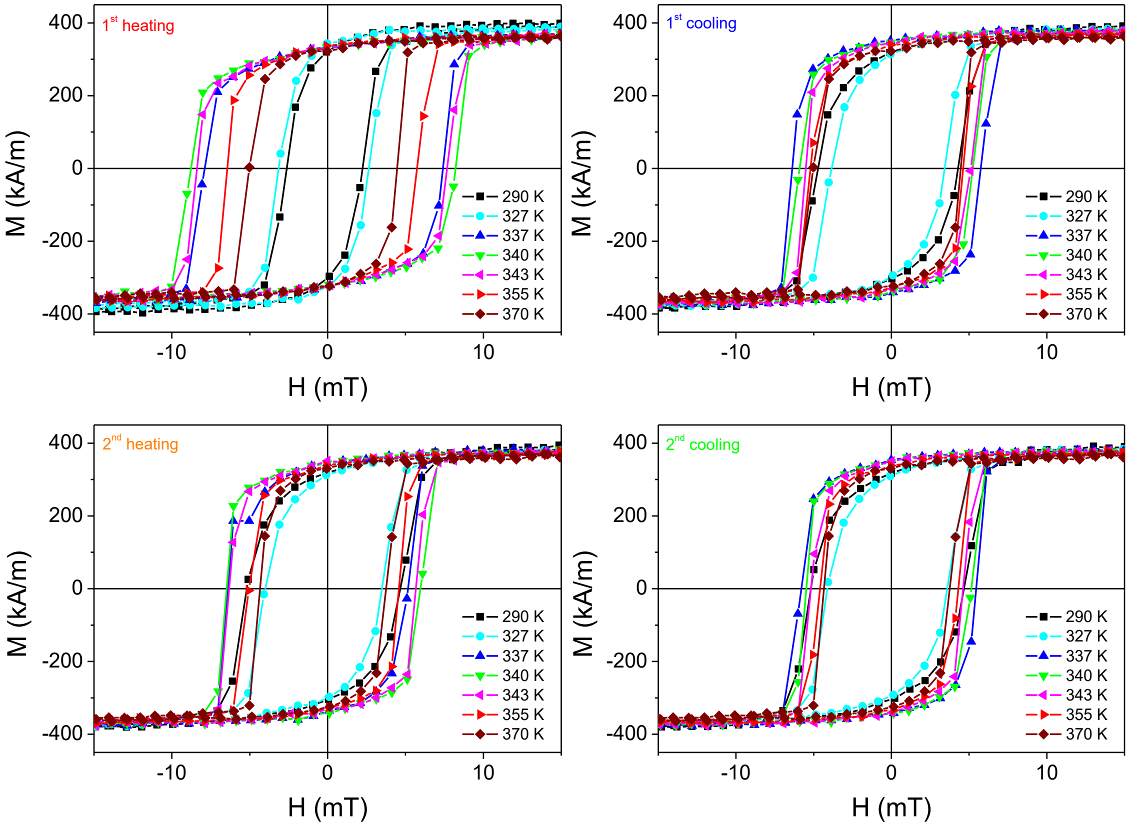

Figure 59. In-plane magnetization vs. applied field for a RT 100 nm VO_2/15 nm Ni bilayer grown on r-cut Al_2O_3. Select temperatures across the first heating cycle are shown.

The first heating measurement is shown in red. At room temperature, the sample exhibits a very low coercivity, only 2.4 mT. This coercivity is relatively constant until the temperature begins to approach T_c, culminating in a sharp ~340% increase to 8.5 mT at 340 K. This maximum is sharply peaked, and the coercivity decreases with increasing temperature, although not as sharply as the initial increase. This decrease in the coercivity is much broader, and still shows a significant slope even at 365 K, a temperature which is more than enough to fully transition the underlying VO_2. Once the film is fully transitioned, the coercivity remains at 4.7 mT, elevated relative to where it would be if the 300 K coercivity trend were simply extrapolated to higher temperatures. As we shift our attention to the first cooling loop shown in blue, we see an overall much different temperature profile. This contrasts with the results seen in the HT bilayers, where the heating and cooling loops mirrored each other apart from the thermal hysteresis. Above the transition, the coercivity maintains an elevated coercivity, but without the corresponding slope. Instead, we see only a peak very localized near T_c, much smaller than the one seen in the heating curve. This peak reaches a maximum value of 0.62 mT at 337 K. As the temperature is decreased further there is a sharp decrease in the coercivity, although it settles to a value that is still above the original values seen in the heating loop. The small dip slightly below T_c is common for samples, although it is often suppressed in the first heating cycle. At 300 K, the coercivity is nearly double the original RT coercivity, at 4.9 mT. After the first heating and cooling cycles the magnetic properties seem to largely stabilize, and the second heating and cooling show relatively similar profiles to the first cooling cycle. Notably, the second heating shows an enhanced slope in the coercivity with increasing temperature above T_c, mirroring the first heating on a smaller scale. Depending on the sample there can be variation, and the second cycles can show some residual minor irreversibility and ‘jitter’ in the coercivity.

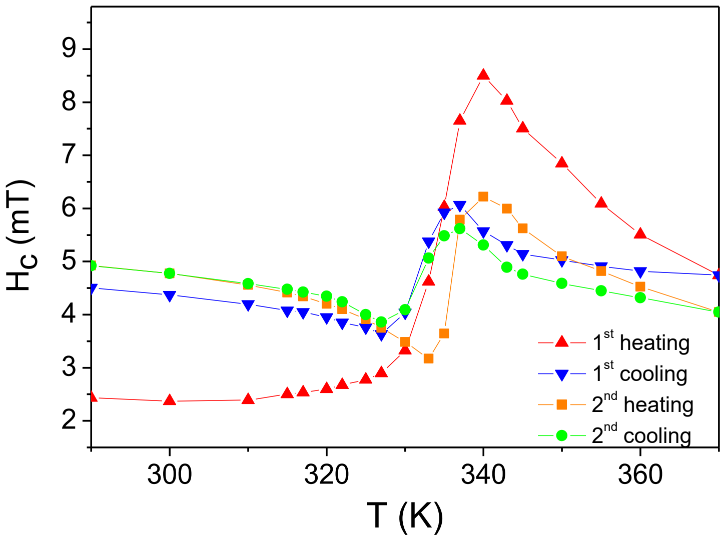

Figure 60. Coercivity vs. temperature of a RT VO_2/Ni bilayer on r-cut Al_2O_3 extracted from hysteresis loops taken at various temperatures.

Bilayer VO_2/Ni samples grown on other substrates also show magnetic irreversibility. The coercivities for several substrates other than r-cut are shown in Figure 61. We emphasize that the range of the y-axis on each panel varies, in order to emphasize the features for each sample. The base coercivity is largely a function of features such as the film roughness, which will be heavily influenced by the substrate and deposition conditions used to optimize the VO_2 transition, as we showed in Chapter 3. Changes in the coercivity due to strain applied by the VO_2 will cause coercivity changes on top of this baseline. However, the absolute scale is maintained between samples as well as with the r-cut sample shown in Figure 60, in order to allow easy direct comparison between features.

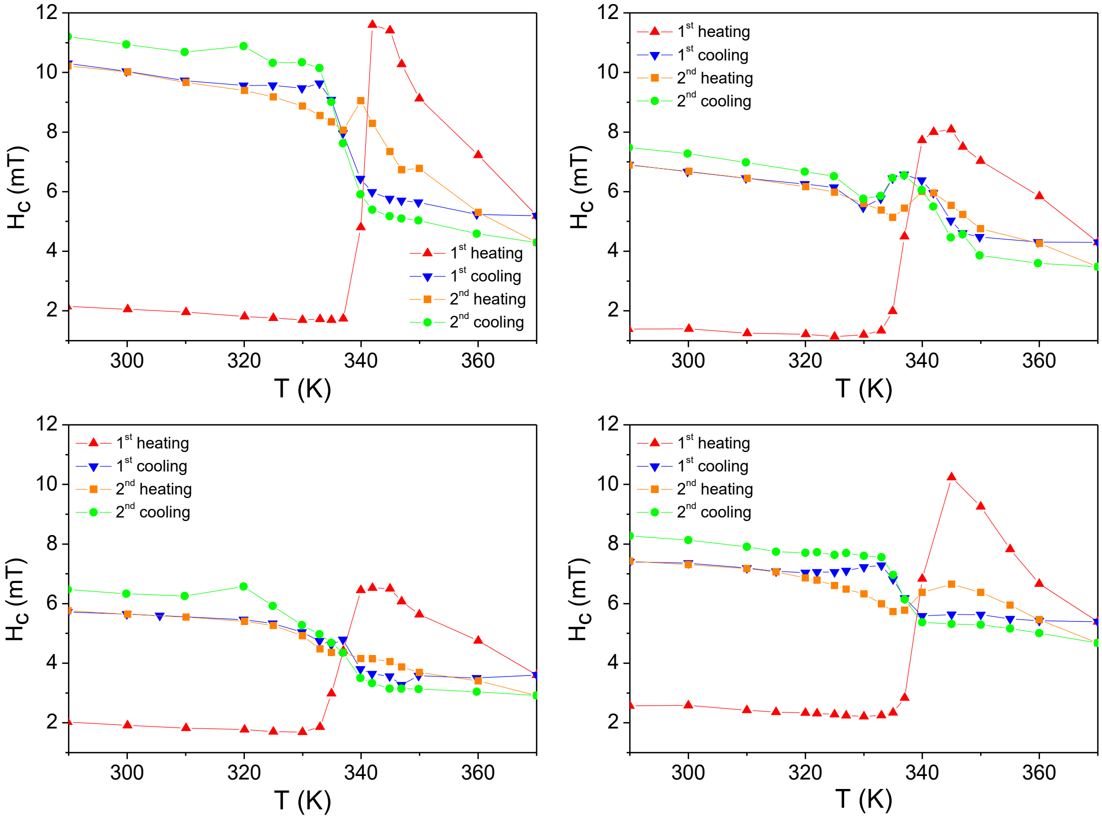

Figure 61. Coercivity vs. temperature of a RT VO_2/Ni bilayer on (top left) c-cut Al_2O_3, (top right) a-cut Al_2O_3, (bottom left) m-cut Al_2O_3, and TiO_2 (101) taken at various temperatures.

In the top left panel, we see the coercivity for a c-cut sample. In the first heating cycle, we see an overall pattern reminiscent of the r-cut behavior, where at lower temperatures there is a low coercivity of 0.33 mT at 300 K, followed by an increase in the coercivity close to T_c for VO_2 on c-cut Al_2O_3. This baseline low temperature coercivity is larger relative to the first heating coercivity in the r-cut. Compared to the r-cut Al_2O_3, the peak has also been shifted higher in agreement with the midpoint of the heating curve at 342 K as seen in the R vs. T for c-cut samples in Figure 42 or Figure 50. Above Tc, we see similar features as in the r-cut sample, with a peaked response close to T_c, followed by an enhanced slope in the coercivity with increasing temperature. At 3.11 mT, this peak is 163% of the extrapolated coercivity at 342 K. Due to the significant slope in the low temperature coercivity, it is a lower coercivity than the 300 K value. As in the r-cut, the future thermal cycles show behavior different from the first thermal cycling, indicating some sort of structural change in the bilayer. Beyond this superficial comparison, the post-first heating cycles in the c-cut sample show a very different behavior to the RT r-cut sample. Instead, they look more like an HT sample, with temperatures above T_c showing a reduced coercivity and temperatures below T_c showing coercivities elevated as compared to the high temperature coercivity as well as the initial coercivities in the first heating cycle. At 300 K, the new coercivity is roughly 4.14-4.36 mT, or 126% of the coercivity at 300 K in the first heating loop and 163% of the coercivity at 360 K in the first heating loop. For the two cooling loops, the shift largely corresponds to the midpoint of the R vs. T at 336 K. Interestingly, the heating loop is also shifted, instead of sharing the thermal hysteresis of the first heating. This is also very similar to the HT samples, which showed relatively minor thermal hysteresis outside of the phase coexistence coercivity spikes. The size of the change in coercivity for the future cycles is roughly equivalent in magnitude to what was seen in the first heating cycle. In these future cycles the spike due to phase coexistence seems to be absent, either suppressed or otherwise hidden. The sample also shows some of the “jitter” alluded to in the discussion of the r-cut sample. For instance, the increase seen at 310 K in both the first and third heating cycles. This jitter seems to be related to how the sample adjusts as it is thermally cycled, rather than a mismeasurement in the magnetic measurement itself. These jitters seem to have some sporadic correlation between cycles, as seen here for the 310 K measurement, but the behavior is inconsistent. Again, this behavior likely largely depends on the specifics of how the sample attempts to relieve strain across the VO_2 SPT.

In the top right panel of Figure 61 is the coercivity as a function of temperature for VO_2/Ni grown on a-cut Al_2O_3. This sample displays very similar behavior to the r-cut overall, with a baseline coercivity 6.26 mT at 310 K. As with the c-cut, the peak is shifted. In this case, the peak occurs at 350 K, rather than the midpoint of the heating loop which occurs at 339 K. The peak in the first heating seems to have some minor jaggedness to it, as well. The difference in the first heating peak and the heating curve midpoint is another sign that this first peak is related the strain across the transition. If the sample is in some sense less strained as compared to the previous samples, the sample might survive through more of the SPT before hitting the threshold strain required for cracking or deformation. A major difference from the r-cut sample is the behavior in the future cycles. While they maintain the profile of low coercivity below T_c, and elevated coercivity above T_c, the increase in coercivity is almost completely suppressed, as compared to the change in the r-cut sample. The low temperature coercivity has also developed a slight slope, for the future cycles. In the first cooling and second heating cycles, the coercivity at 350 K is only $\cong$ 6.6 mT, hardly larger than the extrapolated coercivity for either the first heating. It's also only 13% larger than the extrapolated 5.9 mT from the low temperature future cycle coercivity. In the second cooling cycle at 350 K, the coercivity is only 6.1 mT, reducing the difference in coercivity even further.

The bottom left panel of Figure 61 shows the coercivity vs. temperature response for a sample on m-cut Al_2O_3. The first heating cycle shows the now familiar response, with a base coercivity of 4.65 mT at 300K, a coercivity peak of 7.48 mT at 347 K, and a smaller slope in H_C vs. T at higher temperatures. This peak represents a 207% enhancement relative to the expected coercivity at 347 K. The future cycles show responses similar to the r-cut sample, where they maintain a low to high H_C vs. T profile across the VO_2 SPT, although reduced as compared to the first heating. The high temperature segment still shows a coercivity enhancement of 167% across the VO_2 SPT. All thermal cycles show the distinctive thermal hysteresis as well, of roughly 3.1-6 K depending where on the curve it's evaluated. However, the m-cut sample shows more jitter relative to the r-cut.

In a change from the Al_2O_3 substrates, the bottom right panel displays the H_C vs. T profile for a sample on TiO_2 (101) substrate. The first heating shows behavior typical to the other RT samples, with a low coercivity at low temperatures, a sharp increase peaked close to T_c, and a gradual decline with increasing temperature. At 300 K, the first heating cycle displays a coercivity of 13.94 mT. The increase across the VO_2 SPT peaks at 17.45 mT at 340 K, 138% of the extrapolated coercivity. The future cycles also show the low to high H_C vs. T profile, but with a reduction in the magnitude of the change. The low temperature coercivity has increased, to 15.3 mT at 300K. The high temperature coercivity decreased relative to the first heating cycle, to 15.77 mT at 340 K. The sample shows a 5 K thermal hysteresis that seems roughly consistent between cycles. Overall, the entire profile seems to have some broad curvature relative to the Al_2O_3 samples, with a distinctive slope even far from the VO_2 SPT. This seems likely to be tied to the VO_2 morphology and VO_2/Ni interface, which was very different from the Al_2O_3.

In the discussion of Figure 59, along with the coercivity changes, it was noted that there were changes in the saturation magnetization of the sample as well. This magnetization change can also be observed during an M vs. T measurement, as shown in Figure 62 for a VO_2/Ni bilayer on r-cut Al_2O_3. The applied field was set to +50.0 mT during the duration of the measurement. The value of the field is chosen to be large enough to ensure the sample is fully saturated, but not so large so that any changes (i.e., in anisotropy etc.) would be overwhelmed. In the first heating loop, there is a decrease in the magnetization with increasing temperature which is typical for a ferromagnet. At 335 K the VO_2 crosses its SPT and we see a sharp decrease in magnetization, which is the mirror opposite of the result seen in HT samples. This drop from $388.9\ \frac{\mathrm{kA}}{\mathrm{m}}$ to $380.8\ \frac{\mathrm{kA}}{\mathrm{m}}$ across the SPT represents a 2.1% change in magnetization. Previously, the Ni in the HT samples went from relaxed above T_c to compressed below T_c due to the VO_2 SPT and the reduction in volume and c-axis length. In RT samples, the Ni is relaxed below T_c, but undergoes a tensile stress due to the VO_2 SPT, which acts to reduce the magnetization via an inverse magnetostrictive effect. Above and far from T_c, the sample returns to its previous trend but is permanently shifted lower due to the strain of the VO_2 SPT. After the first heating cycle, the sample is cooled through a cooling cycle. Above T_c, the magnetization agrees well with the first heating curve until the temperature approaches T_c. In contrast to the heating cycle, there is little to no discernable change in the magnetization as the sample crosses the VO_2 SPT. Linear fits to the data above and below the transition, far from T_c, show a 0.1% difference in extrapolated magnetizations at 335 K. Below T_c, the sample maintains the same trend, and is permanently shifted lower relative to the magnetization prior to thermal cycling. This measurement corresponds to a piece of the same sample presented in Figure 59 and Figure 60, cut prior to any measurements. Because of the irreversibility, the normal procedure described in Chapter 2 means that any M vs. T measured after the hysteresis loops will not show irreversibility since the sample has already been thermally cycled.

In conclusion, some amount of irreversibility seems to be a feature of the RT deposition, regardless of substrate. In general, it seems to lead to a reduction in the coercivity change tied to the VO_2 SPT, although even post thermal cycling large changes in the coercivity are still detectable. This irreversibility is also seen in the M vs. T changes associated with the VO_2 SPT, where after one thermal cycle the magnetization no longer shows a noticeable change. The exact change in the magnetic response is likely intrinsically linked to the bilayer microstructure, grain morphology, and stoichiometry. How those features cause the film to respond to the strain of the VO_2 SPT would govern their different magnetic response. This would be consistent with the model of cracking, which allows the films to accommodate the strain of the SPT. This mechanism would then lead to a reduced response, since the coercivity changes are tied to the interfacial VO_2/Ni strain. As with the R vs. T characteristics and literature results, the c-cut seems to be in some sense more resilient to the VO_2 SPT relative to the TiO_2 and other samples, showing a smaller coercivity spike and overall less change in magnitude. The peculiar response of the c-cut sample which seemed to show HT-like characteristics will be revisited in the next section along with similar flipped H_C vs. T profiles on other substrates, which is not specific to the c-cut substrate.

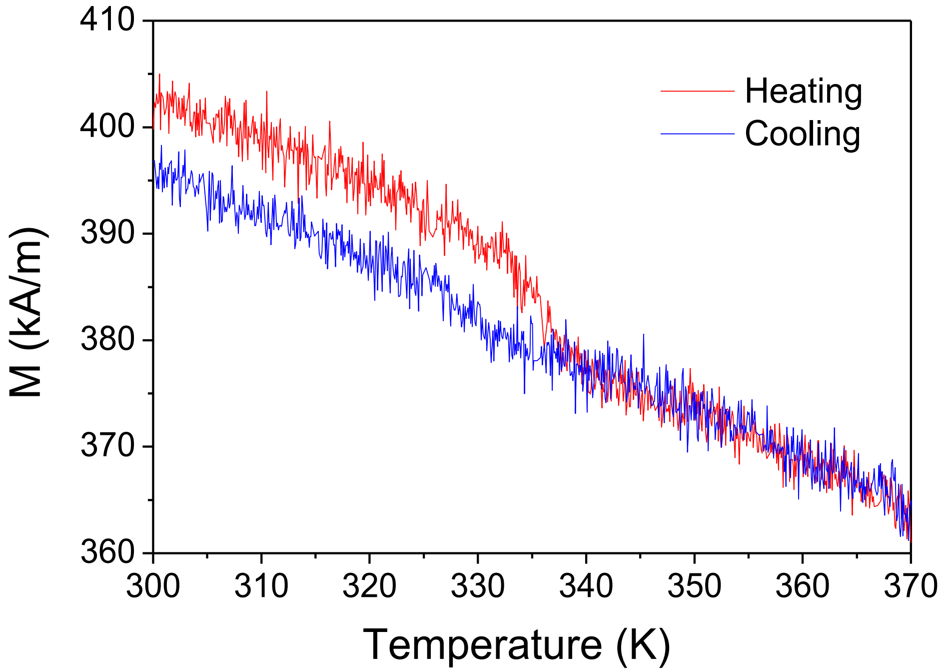

Figure 62. M vs. T measurement for a virgin RT VO_2/Ni bilayer on r-cut Al_2O_3.

5.3 Irreversibility in R vs. T of VO_2

An irreversibility that is in many respects similar to that seen in the RT VO_2/Ni bilayers is also seen in the R vs. T profiles of bare VO_2 films that have not been thermally cycled. Figure 63 shows 2 consecutive R vs. T measurements for bare VO_2 on r-cut Al_2O_3, following the procedure laid out in Chapter 2. Prior to this measurement, the samples were virgin VO_2, uncycled and fresh from the sputtering chamber. The first heating is presented in red, followed by the first cooling in blue. The second heating and cooling are shown in orange and green, respectively. Because there is such a heavy overlap on a logarithmic scale, the curves corresponding to the first measurement are marked by symbols. Enhanced views are shown in Figure 64. It's clear that the first heating branch has an overall lower resistance at each temperature below T_c, compared to the other 3 branches. This difference in resistance can be as large as 23% at 300 K on r-cut Al_2O_3. We see a similar spread maintained during the transition between the 1st and 3rd heating cycles. This change in behavior is a signature that something occurs after the 1st heating cycle, but prior to the 1st cooling branch. In order to exclude extraneous sources that could alter the resistivity (e.g., the indium contacts flexing or peeling), a control sample was measured after being thermally cycled on a hotplate. Samples which have been thermally cycled prior to the R vs. T measurement do not show this irreversible behavior, indicating an intrinsic change to the film properties.

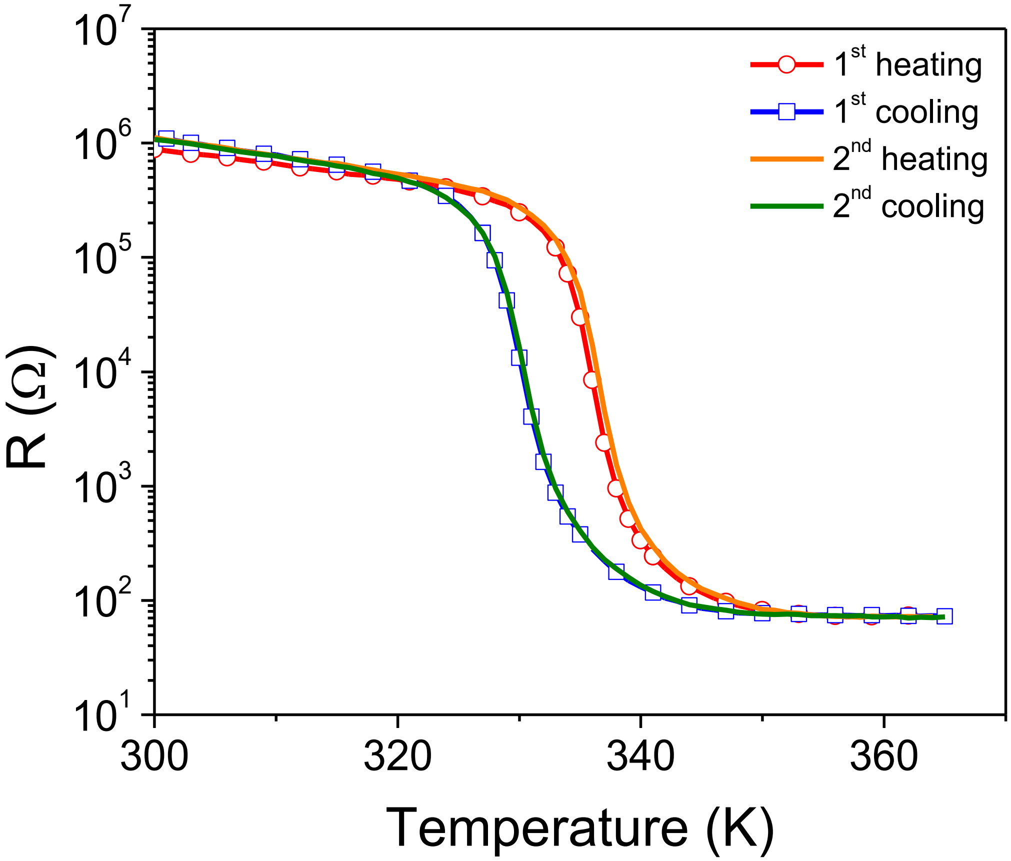

Figure 63. R vs. T measurement for 100 nm VO_2 on r-cut Al_2O_3, for 2 consecutive thermal cycles.

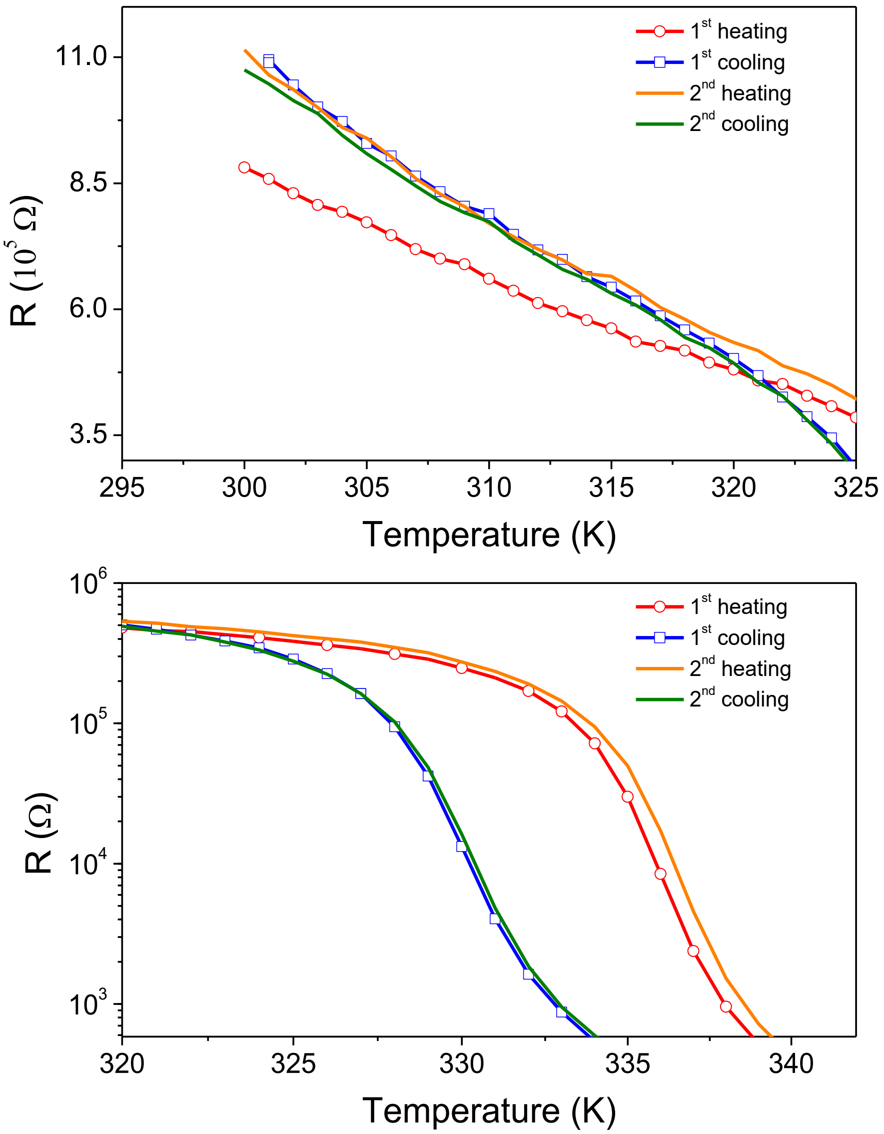

Figure 64. R vs. T measurement for 100 nm VO_2 on r-cut Al_2O_3, for select temperatures along the R vs. T curve. Note the different scales on the y-axis between the two plots.

While the majority of samples in this portion of the work was done with VO_2 on r-cut samples, we note that VO_2 on other substrates show this irreversibility as well. Figure 65 shows the R vs. T profiles for 100 nm thick VO_2 films on various substrates. Clear irreversibility is seen in resistance of the c-cut, a-cut, and TiO_2 (101) samples. The magnitude of this change is similar in magnitude between the samples, at 10.3 %, 18.8 %, and 27.7 %. The relatively larger change in the TiO_2 as compared to the c-cut agrees with the discussion in the previous section, suggesting the c-cut is able to stabilize the VO_2 with relatively less overall cracking as compared to epitaxial TiO_2. The TiO_2 (001) is harder to distinguish definitively due to its low T_c, which means the transition isn't fully complete at 300 K, the limit of our set up. However, even in this sample, the slope is suggestive.

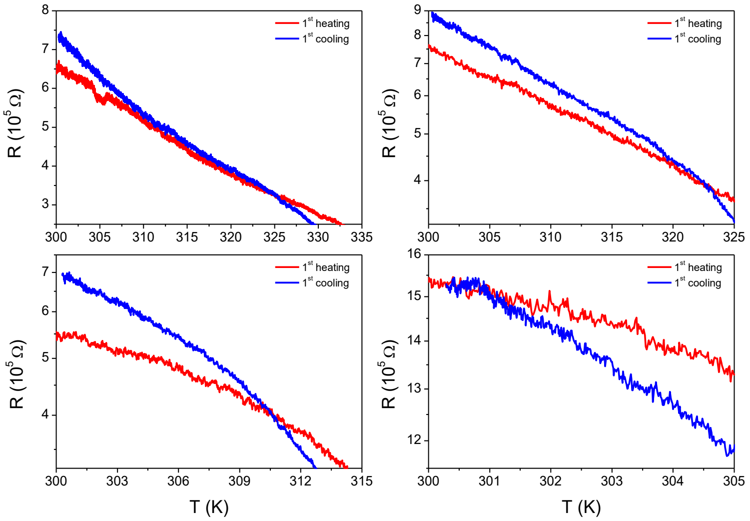

Figure 65. R vs. T measurements for select temperatures for 100 nm VO_2 on (Top Left) c-cut Al_2O_3, (Top Right) a-cut Al_2O_3, (Bottom Left) TiO_2 (101) and (Bottom Right) TiO_2 (001) substrates showing irreversibility.

It may be possible to suppress this irreversibility. In order to control the VO_2 morphology as was discussed in the previous two chapters, it was found that high temperatures and low O_2 concentration produced smoother VO_2 morphologies. However, these conditions have a drastic impact on the reversibility of VO_2 samples, as shown in the top of Figure 66 for a VO_2 film on r-cut Al_2O_3. In addition to broadening the transition, we see very little disagreement between the 1st heating and 1st cooling branches- certainly nowhere near the 20% as seen previously. In addition, films made under high O_2 conditions display the opposite effect, showing even larger irreversibility. Referring back to Figure 29 of Section 3.2, we consider the sample made with 2.83 sccm O_2 flow rate, reproduced for convenience on the bottom of Figure 66. This film only showed a 3 orders of magnitude MIT as the film was too resistive. However, this film shows a quite noticeable irreversibility, over 100% at 300 K.

This agrees with the explanation given in the paper by Shibuya et al., which attributed this reproducibility to oxygen deficiencies. It is also likely in agreement with the work done by Ko et al.. [99] Their deposition conditions are very similar to our optimized temperature and O_2 flow rates. More importantly, their 5 order of magnitude transition is a hallmark of the "melted" films which we discussed previously. It is rather fortuitous that the conditions for reversibility, a large MIT, and smooth films are all consistent. As the quality and control of the growth of VO_2 films improves, there does not seem to be a tradeoff between these 3 quantities which are all of critical importance to realizing VO_2 in multilayer structures.

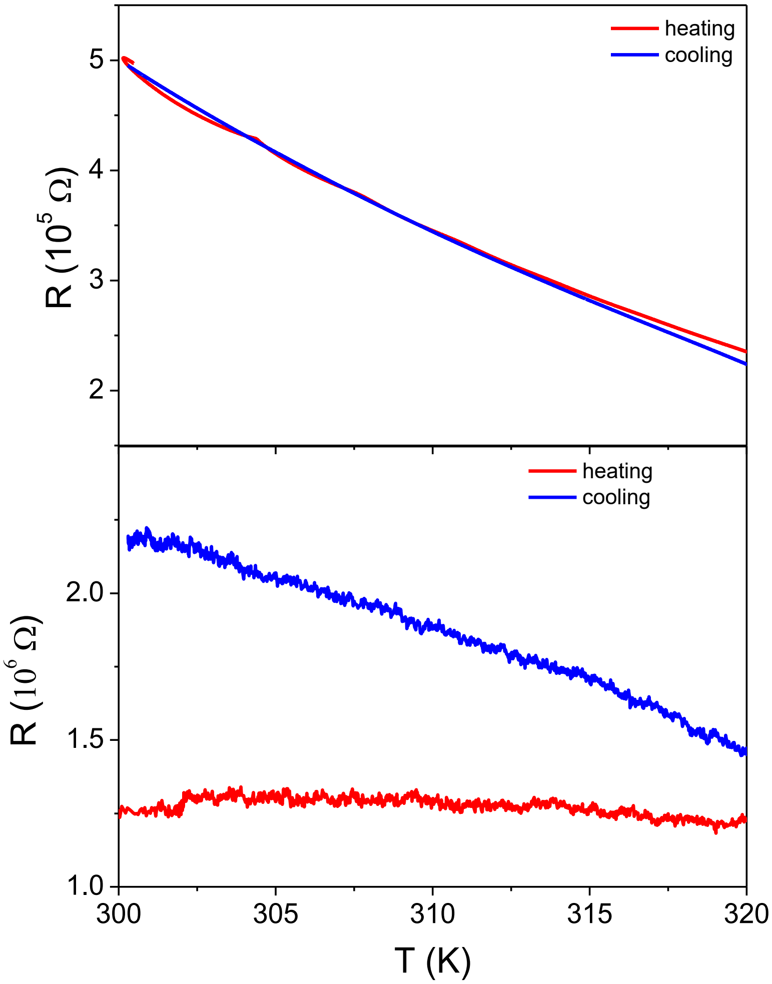

Figure 66. (Top) R vs. T measurement for 100 nm VO_2 on r-cut Al_2O_3, with optimized conditions for low roughness morphology (corresponding to a high T, low O_2 deposition atmosphere). (Bottom) R vs. T measurement for 100 nm VO_2 on r-cut Al_2O_3 deposited with high O2 flow rate.

5.4 Cracking in VO_2

One potential mechanism that would explain both types of irreversibility phenomena would be cracking in the VO_2 layer. VO_2 has long been known to crack as it crosses the SPT, due to self-induced strains. This was noted first in VO_2 single crystals as this often led to the crystals cracking or shattering along the rutile c-axis.[83,302–305] This cracking was so severe that it often rendered the macroscopic crystal sample unusable for further measurement after a single or small number of thermal cycles. VO_2 based ceramics also suffer from cracking due to the strains induced by the SPT.[306] An example of a cracked VO_2 single crystal is shown in Figure 67, reproduced from Ref. [[307]]. The top right of the figure shows a VO_2 single crystal before the initial cracking even, just after cracking, and in a future thermal cycle. Top left is the corresponding I-V curve, showing a drastic change in resistivity due to the cracking. The bottom panels show the same process for another VO_2 sample, with a focus on development of the crack across several seconds. The cracks are visible even to simple optical examination. For reference, the sample sizes of these single crystals are approximately $0.001\ \times\ 0.005\ \times 0.1\ \mathrm{cm}^3$.

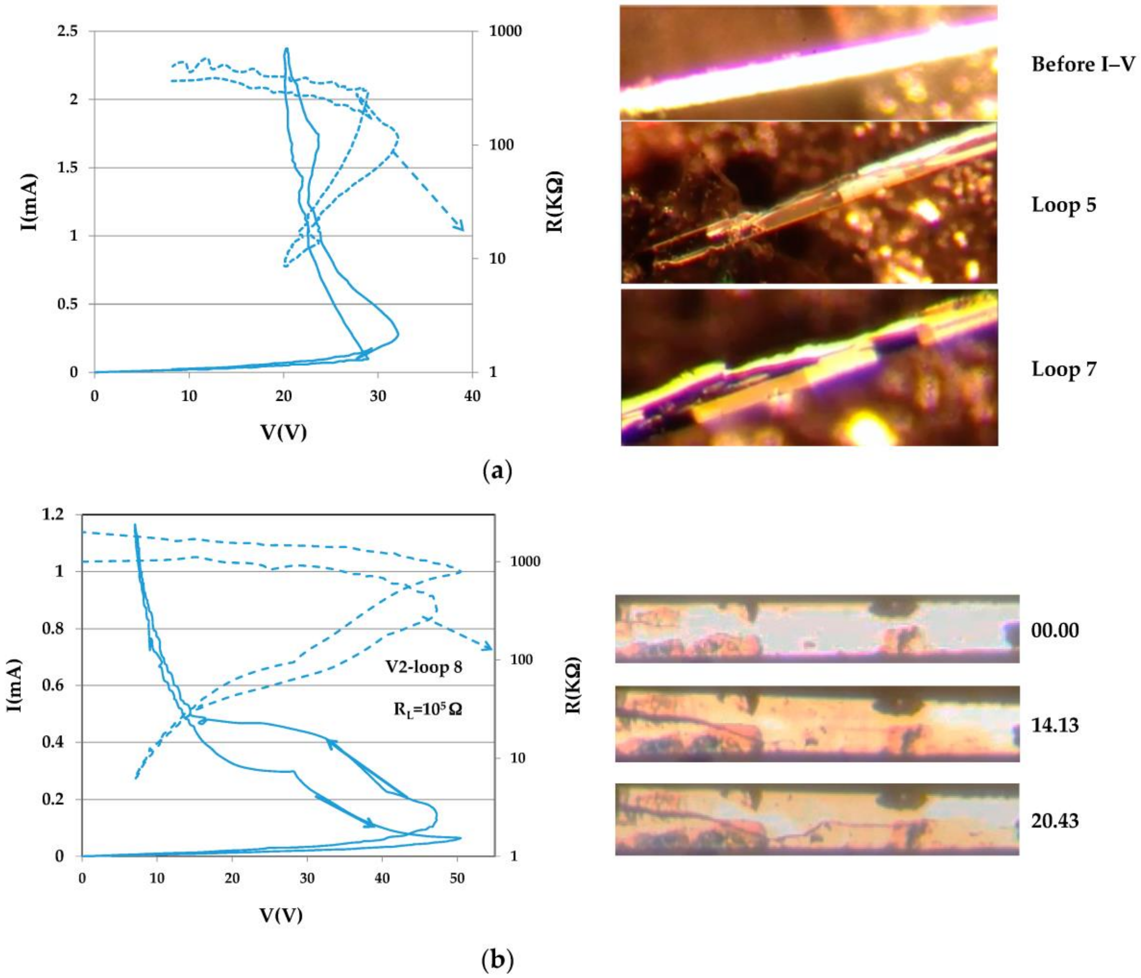

Figure 67. (Left) I-V curves for single crystal VO_2 crystals, which undergo cracking as the VO_2 crosses the SPT. (Right) Optical images of the VO_2 across the cracking event. Reproduced from Ref. [[307]].

One of the original motivations for developing VO_2 in thin film form was to structurally stabilize it as it crosses the SPT.[101,308,309] Thin films can be far more robust to strains than their bulk counterparts.[248] Thin film VO_2 has been shown to be very robust to repeated thermal cycling across the SPT, surviving hundreds to thousands of thermal cycles without major degradation.[300] Guzman et al. reported VO_2 films which survived more than 10^8 thermal cycles over the course of several months, without failure.[310]

The overall stability of the macroscopic resistive and optical properties meant that the problem of cracking in thin film VO_2 was relatively unexplored until more recently. The first direct observation of cracking came from Nagashima et al., who were able to obtain images of microcracks via AFM, reproduced in Figure 68.[311] These VO_2 films were grown by PLD to 10-30 nm in thickness, grown on TiO_2 (001) substrate. Their results indicate a minimum thickness for cracks to form, related to the energy for cracking as compared to the strain due to the substrate and SPT. Modeling the SPT as a thermal expansion coefficient, they theoretically calculate a minimum thickness of 15 nm for VO_2 on TiO_2 substrate, in good agreement with their experimental results. The real thermal expansion coefficients between VO_2 and TiO_2 are similar enough to be neglected. In Figure 68 (a), is one of their 10 nm VO_2 films, which displays no cracks as it is below the 15 nm critical thickness. In panel (b), a clear network of cracks has formed, following the VO_2/TiO_2 symmetry. Panel (c) shows an enhanced view of the same cracks. Panel (d) shows the scaling of density of cracks as a function of thickness. In these samples, they find a crack width of 10 nm. For the thickest films considered, they find a density of cracks 1-2%. Unfortunately, the paper does not comment on the morphology of films with thickness greater than 30 nm, which is roughly just before double the critical thickness.

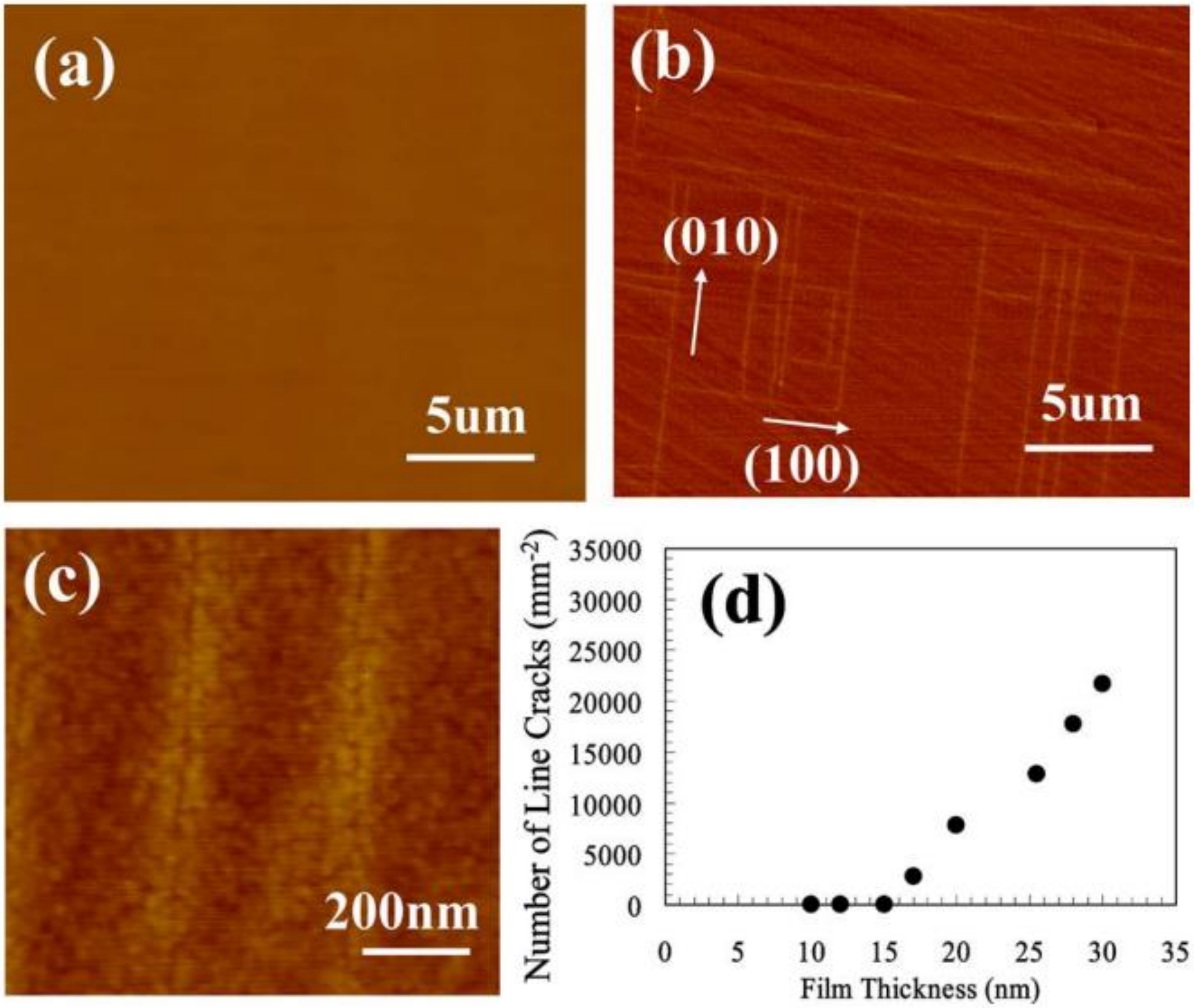

Figure 68. AFM images showing microcracks in (a) 10 nm VO_2 on TiO_2 (001) substrate. (b) and (c) show 30 nm VO_2 on TiO_2 (001) substrate. Reproduced from Ref. [311].

After the pioneering work of the Nagashima paper, a number of other papers have also reported observation of cracking, either with direct observation or in passing when discussing other results. A non-comprehensive list of papers with direct observations are listed in Table 2. Their direct imaging of cracks in VO_2 have been compiled into Figure 69. It is immediately clear that these films have much cleaner surface morphologies than those shown in the previous chapter, showing nearly single crystalline quality. This morphology quality is directly tied to the film growth conditions. It seems that up to this point, the focus on investigations of cracking in

VO_2 thin films is largely confined to ultrathin VO_2 made via PLD onto rutile TiO_2 substrate. From Table 2, the closest comparison to our system is Ref. [312], which utilizes sputtering of films in a comparable thickness to ours. Even here however, the film shows excellent quality, matching the rutile TiO_2 substrate. The cracks as well tend to follow the rutile symmetry in a regular pattern.

Table 2. List of publications that directly image cracks in VO_2 films. OM = optical microscopy, and HRTREM = High Resolution Transmission Electron Microscopy, and c-AFM=conducting AFM. * Ref. [318] also includes SnO_2 buffered TiO_2 substrates that do not show cracking.

Reference	Growth	VO_2 thickness	Substrate	Imaging
311	PLD	10-30 nm	TiO_2 (001)	AFM
312	sputtering	100,250 nm	TiO_2 (001)	AFM, SEM, OM
313	sputtering	170 nm	50 nm Si_3N_4	OM, TEM
314	PLD	10-50 nm	TiO_2 (001)	OM, HRTEM
315	PLD	10-45 nm	TiO_2 (001)	Kelvin probe FM
316	PLD	9-80 nm	TiO_2 (001)	OM
317	MBE	1.4-30 nm	TiO_2 (001)	AFM
318	PLD	300 nm	TiO_2 (001) *	TEM
319	PLD	12-48 nm	TiO_2 (001)	c-AFM

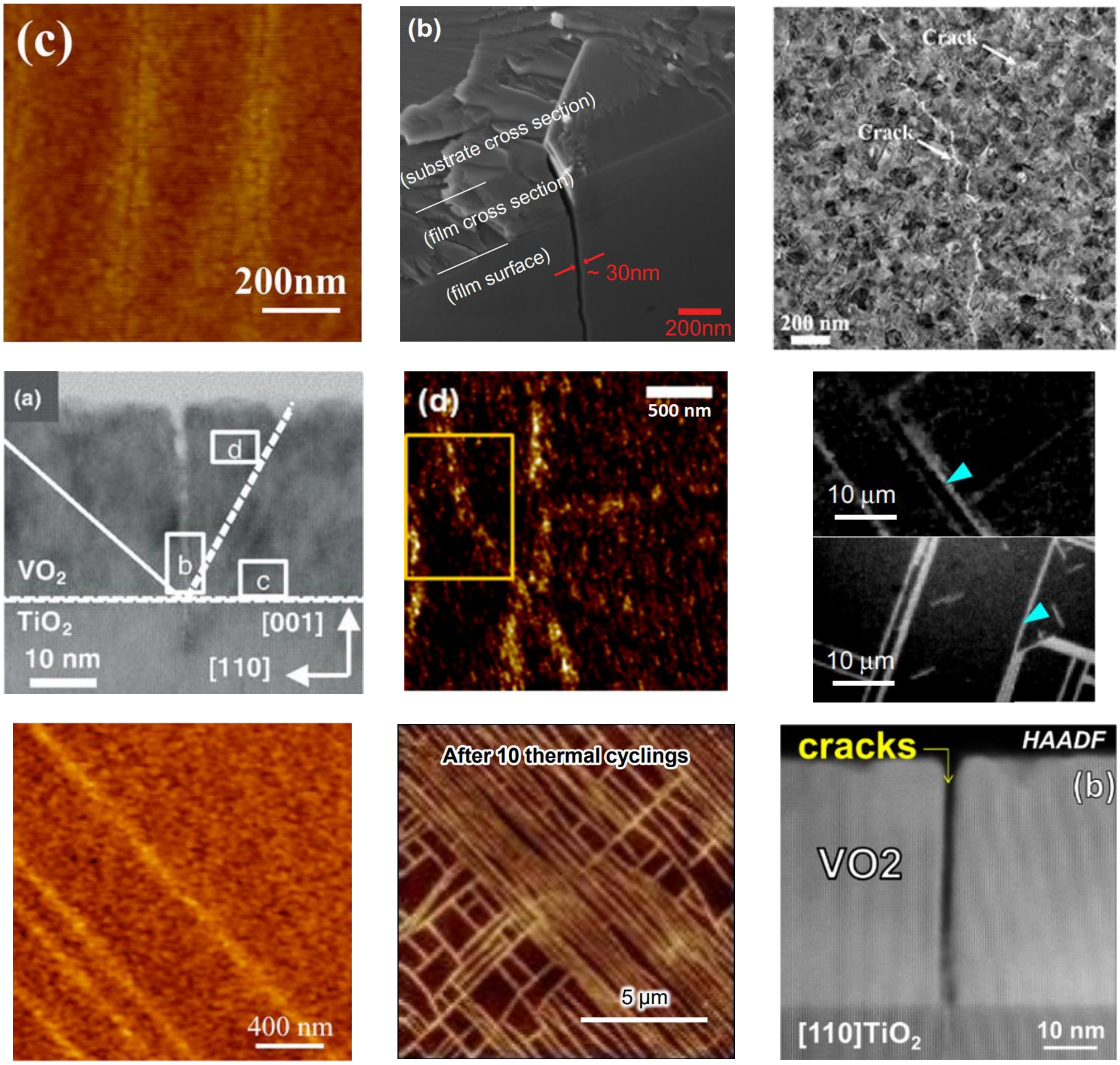

Figure 69. Compilation of images showing cracking in VO_2 thin films. From Ref.s [311–319]. All utilize TiO_2 (001) substrate, except the third image, on 50 nm Si_3N_4 membrane.

Several works also mention cracking in passing. Shibuya et al. note that reducing the oxygen pressure suppresses crack formation, which they attribute to an incorporation of oxygen vacancies.[320] They also found that samples doped by W above 4% don't seem to show cracking behavior. Work by Ko et al. and Jian et al. notice a lack of cracking in VO_2 on c-cut Al_2O_3, which they attribute to the polycrystalline nature of the film.[300,321] The former work only mentions this in passing, in the context of the excellent quality retained after multiple thermal cycles in their films. It is possible that any irreversibility in comparison to the orders of magnitude change was unnoticed. The latter work performed a much deeper analysis via in-situ TEM to study the structural properties of their VO_2 films. They find that while polycrystalline films have inherently worse MIT characteristics compared to a single crystal, there is a trade off as the domain boundaries provide a means of accommodating the SPT induced strain. Their TEM measurements track the strain induced in the film through the phase transition, and they find that when rutile VO_2 nucleates, the strain propagates to the grain boundaries, where it accumulates. This leads to grain boundaries having an elevated strain, that accumulates further with each thermal cycle. They find a noticeable change in film properties, particularly in the first 15 thermal cycles, which they attribute to accumulation of grain boundary strain which eventually saturates. They find that the films become more epitaxial with thermal cycling, which acts to increase the phase transition amplitude. This effect competes with the reduced amplitude due to defects at the domain boundaries which act to reduce the size of the phase transition. The result is a thin film which is robust to thermal cycling as compared to single crystals, and a roughly stable MIT amplitude. The grain boundaries therefore act in an analogous fashion as the cracks seen in the works shown in Table 2, accommodating the intrinsic stress of the SPT. The SnO_2 buffered substrates also lead to a more robust VO_2.[318] These results suggest cracking in VO_2 thin films may be controllable or suppressible depending on the details of the film. This controllability is likely to become increasingly important for applications that seek to harness the SPT portion of the VO_2 phase transition rather than simply the MIT properties.

5.5 Numerical Model R vs. T

In order to gain a better understanding of whether cracking is a plausible mechanism for the increase in resistance of the VO_2 thin films, we performed numerical simulations of the bare VO_2 film as a classical 2-D resistor network with random percolation.[322] The code for an implementation in Matlab, originally written in Matlab2016b, is provided in Appendix A (Resistor Network Code). Percolation methods have shown to be a useful theoretical method for describing a wide range of physical phenomena. It has also been successful when applied to the VO_2 resistivity, by considering a network of grains which can alternate between the metallic or insulating state.[216,323–325]

In our model, the VO_2 is discretized as a square lattice of size 1000 x 1000. Memory limitations prevented us from scaling it up further, however this size is more than sufficient to see macroscopic smoothing of the simulated R vs. T curves that is seen in experimental R vs. T data. Even for sizes as small as 100 x 100, the avalanche behavior typical of smaller devices begins to smooth out. Each site on the lattice represents a single homogenous grain, which will be entirely in a metallic or insulating state. Each grain is electrically coupled to its nearest neighbors (NN), but structurally independent (i.e., there is no mechanical coupling due to SPT strain from neighboring transitioned grains). We also neglect any effects of local Joule heating or voltage induced transitions. One grain consists of 4 resistors in a cross shape. A grain can be in one of 3 states: metallic, insulating or broken. Each state has a corresponding resistance. Metallic resistors have a resistance $R_M\ \Omega$, semiconducting resistance is given by $R_0 e^{\frac{-E}{k_B T}}\ \Omega$, and a broken resistance of $10^{13}\ \Omega$. The resistance value for a broken grain was chosen as finite but arbitrarily large. The value for $R_0 = 1{,}506\ \Omega$, $\frac{E}{k_b} = 2750$ K, and $R_M = 58.5\ \Omega$ were matched to the experimental data. When a grain breaks, it is only the solitary grain that changes, rather than e.g. a line crack as seen in the literature.

In order to assign each grain a T_c, a random value is sampled from a Gaussian distribution with mean value 330.3 K and a standard deviation of 8 K. The distribution captures the sensitivity of VO_2 to minor differences in its local environment, such as variations in oxygen content or strain due to grain boundaries. Without these variations, the film would act as a single crystal, with all grains switching simultaneously. The characteristics of the Gaussian was chosen to match the experimental data. The mean value corresponds to the measured T_c, and the spread of the Gaussian controls the sharpness of the MIT. At their local transition temperature, 6.25% of grains are randomly assigned to break instead of becoming metallic. A grain is only allowed to transition to a broken state from the insulating state in the heating cycle. This physically corresponds to being allowed to break due to the stress of crossing the transition, but if the grain survives the transition, it is no longer at risk of breaking.

Schematically, an example of the VO_2 lattice at various temperatures is shown in Figure 70. At each end of the film, the current is applied through metallic electrodes with zero resistance. The voltage drop across the films is also sampled at the electrode placement. Each square with cross resistors represents a grain, with the insulating state shown in blue, the metallic state shown in red, and a broken grain shown in brown. At 300 K, nominally all the grains are in the insulating state. As the temperature is increased like shown in the top right panel, a portion of the grains will transition according to their local T_c. As the temperature is increased further, eventually a percolation pathway is formed, as shown in the bottom left panel. This path corresponds to the rapid drop in resistance across the MIT, as the current is free to divert along the low resistance metallic pathway. Along with transitioning to the metallic state some grains will crack, which should act like an open portion of the circuit.

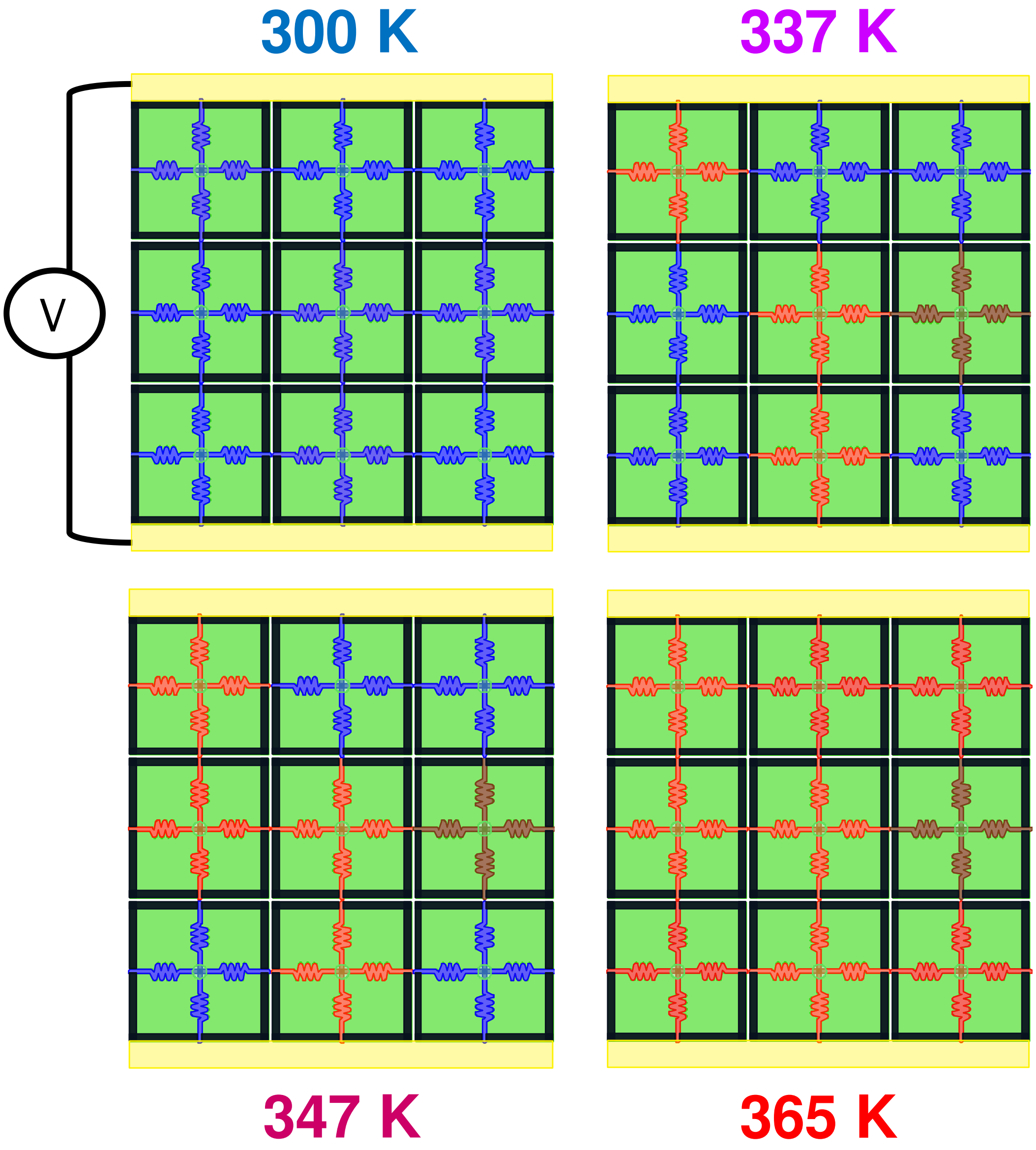

Figure 70. Schematic of a resistor network grid representing a VO_2 film, at various temperatures. Insulating grains are shown in blue (R=1000 Ω), metallic in red (R=1 Ω), and broken in brown (R=10^{13} Ω).

To solve for the resistance of the total film, we start by considering I_i, the total current at the ith lattice site, given by a generalized version of Ohm’s law

$$I_i = \sum_j^N g_{ij}(V_i - V_j)$$

which says that the total current at the ith site can be found via the sum of incoming and outgoing currents to all the other lattice sites. V_i is the voltage at the ith site. g_{ij} is the local conductance between the ith and jth site, given as the average of the two resistors from each grain. In a NN model $g_{ij} = \frac{2}{(R_i+R_j)}$ when the ith and jth sites are NN, and 0 otherwise since the sites are not connected. Each site on the lattice, including the metallic contacts, obeys this condition. The sum reduces to

$$I_i = \sum_j^4 g_{ij}(V_i - V_j)$$

Where j now sums the 4 nearest neighbors of the ith site. The reason for starting with the generalized Ohm’s law form is the ability to easily rewrite the entire network as a system of equations in matrix form as

$$\vec{I} = \overline{G} \cdot \vec{V}$$

where $\vec{I}$ is a $N^2 \times 1$ vector, with the ith element I_i. Similarly, $\vec{V}$ is a $N^2 \times 1$ vector, with elements V_i. $\overline{G}$ is an $N^2 \times N^2$ conductance tensor (matrix). For our situation, $\vec{I}$ is known, by invoking Kirchhoff’s current law (conservation of charge) as well as realizing that experimentally, we apply a fixed current at the electrodes. $I_i = 0$ for $i > N$ and $i < N^2 - N$. This allows for the current to enter/exit from the edge sites corresponding to the metallic strips, which is N elements long on either end of the sample. Inside the VO_2 film itself, there are no sources of current being injected, so they must sum to zero in equilibrium. $\overline{G}$ is similarly known a priori, and its elements are given as

$$\overline{G}_{ii} = \sum_{j=1,(j\neq i)}^{N^2} g_{ij}$$

else

$$\overline{G}_{ij} = -g_{ij} = \overline{G}_{ji}$$

In the case where there is only NN coupling, $\overline{G}$ is in general a large, sparse matrix. Despite being $N^2 \times N^2$, it will only have $O(5N^2)$ nonzero terms from the main diagonal, as well as the 4 off-diagonal terms corresponding to NN coupling. The gold leads will also have nonzero terms, but these are only of order 2N for each of the starting and ending strips. A schematic view of a typical $\overline{G}$ matrix is given in Figure 71. White blocks indicate 0 elements, and blue nonzero, as defined above. For readability, this is the grid for a relatively small network, 5 grains by 5 grains, or a $\overline{G}$ matrix of size $N^2 \times N^2 = 25 \times 25$ elements.

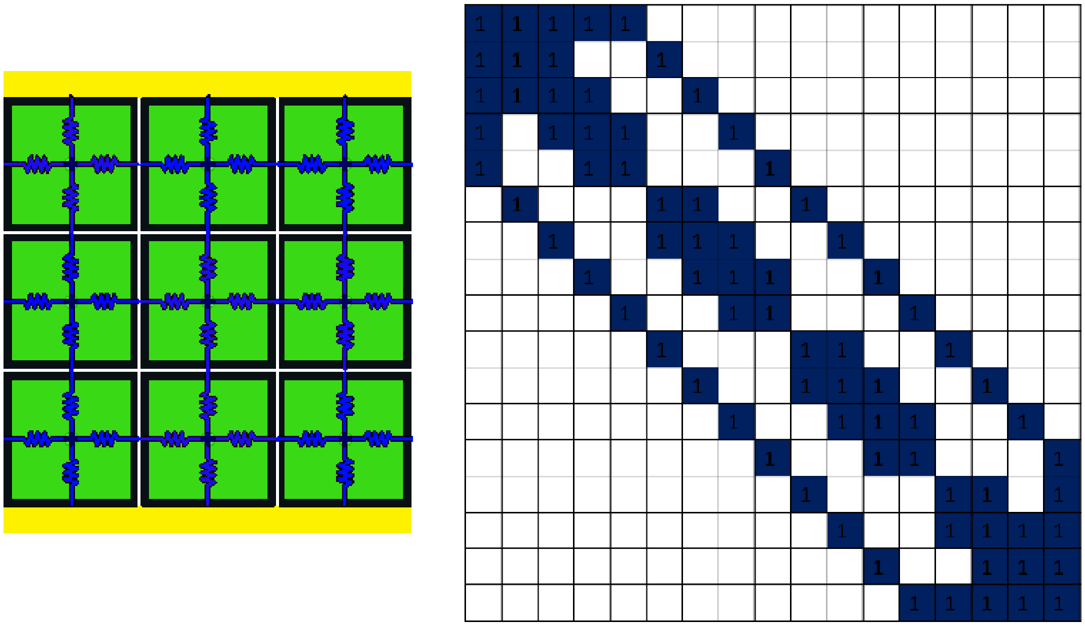

Figure 71. (left) A schematic of the resistor network. (right) Schematic view the sparse conductivity matrix such a network produces.

With $\vec{I}$ and $\overline{G}$ given, the problem is reduced to finding the V_i at each lattice site, which becomes a simple matrix inversion problem for the inverse of $\overline{G}$,$\overline{G}^{-1}$. In general, a preconditioned conjugate gradient (PCG) method can be employed iteratively to solve for $\overline{G}^{-1}$.[322] However, for several reasons, we found direct methods to be preferable. Relative to direct matrix inversion methods, the PCG method trades slower speed for smaller memory requirements. It can be shown that the convergence of the PCG method is bounded by the ratio of the largest and smallest eigenvalues of the matrix, which for G with large variations between elements is quite large. We were unable to find a preconditioning scheme that greatly improved performance. In addition, the size of $\overline{G}$ is a restriction for easily taking advantage of a graphical processing unit (GPU) for highly parallel implementations of PCG methods. Due to the sparse symmetric nature of $\overline{G}$, the extra memory requirements for the solver are comparable to that needed to originally construct $\overline{\mathrm{G}}$. Once $\vec{\mathrm{V}}$ is known, we need simply to apply Ohm's Law $\mathrm{V} = \mathrm{I} \cdot \mathrm{R}$ or $\frac{\mathrm{V}}{\mathrm{I}} = \mathrm{R}$. This process can be repeated for each temperature step to find the equivalent resistance of the film for each temperature. At the start of the simulation, the nonzero elements of G are allotted to avoid having to resize G in memory.

The results of the simulation are shown in Figure 72, along with a typical R vs. T curve from a real sample. The simulation results show quite strong agreement with the experimental data through the entire range of temperatures. For readability, only the first heating and cooling cycle of the simulation is shown, but future heating and cooling cycles show similar agreement with the data. Notably, there is some disagreement in the shoulders close to T_c in both the heating and cooling curves. This comes from the implementation of thermal hysteresis, discussed below. The inset focuses on the low-T region in order to emphasize the agreement between simulation and experiment. In the simulation, we can see that the initial heating starts off at a lower resistance relative to future heating and cooling cycles in the semiconductor range. As the temperature is increased, both simulated and experimental samples go through the MIT and its associated several orders of magnitude transition. During this heating, the majority of grains that will break are able to do so, at their designated breaking temperatures. Above around 350 K, the sample is in the metallic and largely post-cracked state. As the film is cooled, the system then goes back through the MIT, retaining any cracks that had formed due to the first thermal cycle. Returning to RT, we see good agreement between the experimental and simulation resistances for the first cooling cycle.

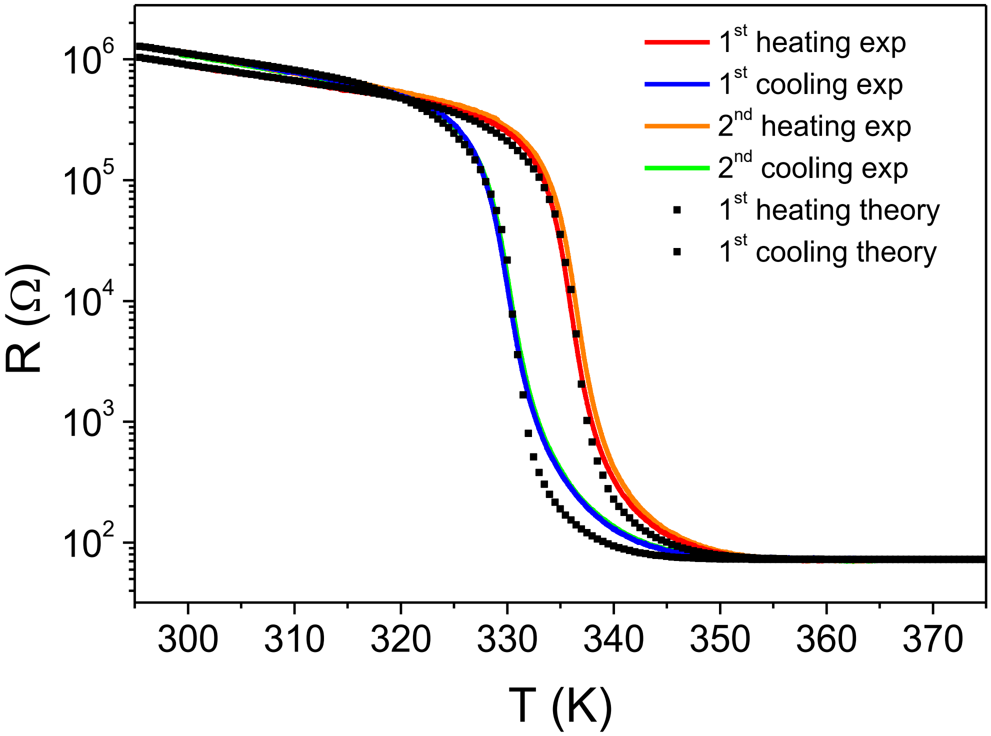

1st heating exp
1st cooling exp
2nd heating exp
2nd cooling exp
1st heating theory
1st cooling theory
R (Ω)
10^6
10^5
10^4
10^3
10^2
300
310
320
330
340
350
360
370
T (K)

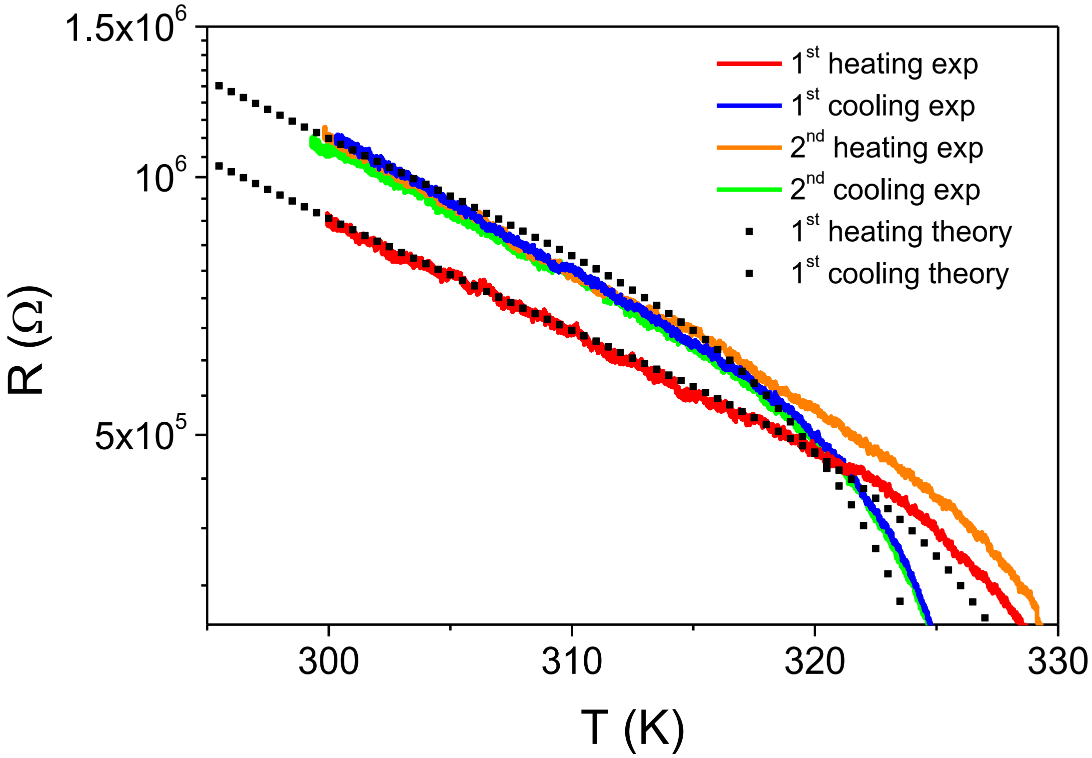

1st heating exp
1st cooling exp
2nd heating exp
2nd cooling exp
1st heating theory
1st cooling theory
R (Ω)
$1.5x10^6$
10^6
$5x10^5$
300
310
320
330
T (K)

Figure 72. Simulated R vs. T for a 1000 x 1000 square lattice. (Bottom) Enhanced view at lower temperatures.

While the agreement between such a simple toy model and the experimental data is heartening, it is worth commenting on several details of the model, the consequences of which may not be apparent in the bulk equivalent resistance. Currently, nothing previously mentioned would account for the thermal hysteresis. Physically, this is should be expected, as VO_2 single crystals show small to vanishing thermal hysteresis of 0.5 K or less. The physical origin of thermal hysteresis in VO_2 thin films is still not completely understood but is known to be heavily tied to grain size, substrate, thickness of the film, deposition conditions, oxygen content, and twin boundaries.[104–109] It has been argued that these properties will influence a supercooling or superheating phenomenon. To incorporate hysteresis, there are two generally accepted avenues. The most common is the Preisach model,[224,326] which has shown great success as a general method for modeling first order phase transitions including the VO_2 MIT.[327] In the Preisach model, the thermal hysteresis is taken as a fitting parameter, where grains have a T_c given as $T_C \pm \delta T_C$, where the ± refers to the heating and cooling, respectively. The thermal hysteresis is therefore taken as an inherent property of each grain. A more physically realistic approach is to directly include inter-grain interactions, such as in Ref. [[328]] where they utilize a mean-field approach. As far as we're aware, there is no developed formal theory for the interaction between grains in VO_2. For simplicity, we take the Preisach approach, and the thermal hysteresis is $\delta T_C =$ 3.05 K was found by fitting the experimental data. This hysteresis is applied uniformly to all grains. While not visible in the bulk data, this will alter the fraction necessary to form a percolation pathway. Rather than filaments forming preferentially, metallic puddles form randomly.

We also mention that this 2-D model potentially may not capture the correct semiconducting to metallic fraction scaling. Sohn et al. were able to directly measure the semiconducting to insulating fraction in VO_2 on TiO_2 films.[315] From their measurements, for VO_2 thicker than 30nm, a 3-D percolation model better captures the scaling law, whereas a 2-D model is more appropriate 15nm films. However, they did not consider inter-grain interactions, which may cause some of the difference they assign to the 2-D and 3-D models. Also, other measurements such as in Ref. [[324]] find good agreement with a 2-D model. This difference effectively gets compensated into the fitting parameters of the model and is impossible to derive from the bulk equivalent resistance presented, but we mention it for completeness.

5.6 AFM of thermally cycled VO_2

While so far cracking seems to be a plausible mechanism for these irreversible features in our VO_2 and VO_2/Ni films, if cracking is indeed occurring it should be possible to be probed directly. In an attempt to directly verify whether cracking was occurring in our VO_2 films, we turned to atomic force microscopy (AFM) to probe the microstructure of the film. The virgin VO_2 film is first measured using AFM prior to any thermal cycling to establish a 'background' comparison. The film is then thermally cycled on a hotplate in air at 5 K/min up to a maximum temperature of 400 K. 400 K was chosen in order to ensure that the film was fully transitioned, and to account for any temperature differential at the surface of the film and the thermocouple inside the hot plate that records the temperature. Resistivity measurements show that the film transitions to its fully metallic phase well below the 400 K set point, further confirming that this temperature is enough to transition the VO_2. The film is held at 400 K for 10 minutes, and then returned to room temperature at 5 K/min. All 3 parameters of the thermal cycling process were varied to rule out any variation due to dependence on the thermal cycling process, but no major changes were noted for the range of parameters measured. The ramp rate was varied from 5-10 K/min, the maximum temperature from 370 K-430 K, and the time held at max temperature from 5-10 minutes. After this thermal cycling treatment, the VO_2 sample is again measured under AFM, in roughly the same area as before. AFM scans were taken consecutively over several scanning ranges. The largest scan areas are 5-10 microns. While the system is equipped with a large area scanner, scans larger than 10 microns sacrifice significant fidelity. Smaller scans from 0.5-2 microns are then taken to improve the fidelity of the images further, which are linked to the scanning area.

The results of one such set of AFM measurement is shown in Figure 73 and Figure 74. The first figure depicts the full range (5 microns) scan for a typical VO_2 film on r-cut Al_2O_3 substrate both before and after thermal cycling. The measurement prior to thermal cycling is shown on top, and the measurement after cycling on the bottom. The green lines correspond to line profiles, shown to the right of the AFM images. Ovals denote features that will be shown in higher detail in Figure 74.

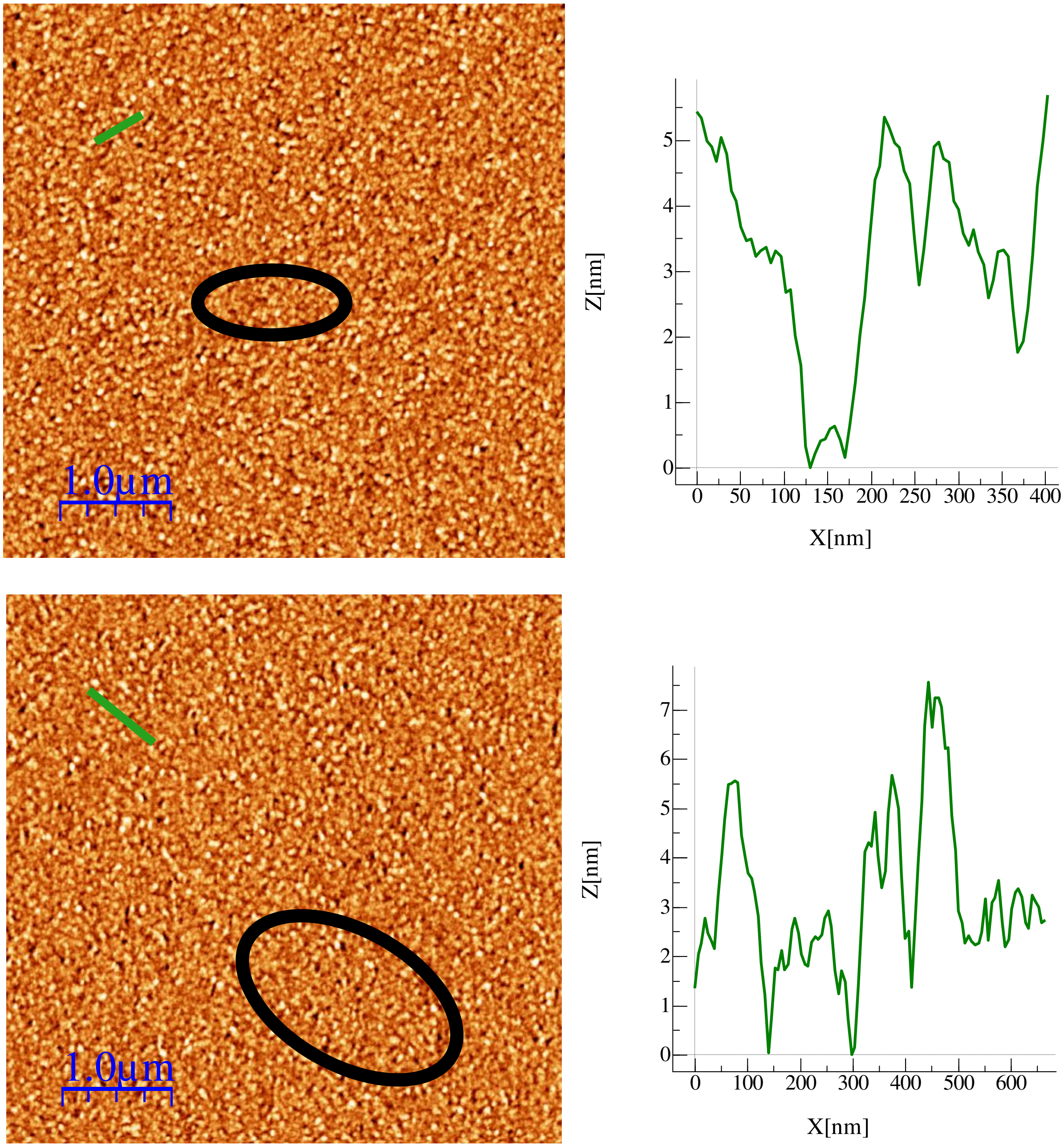

Figure 73. AFM images taken for a 100 nm VO_2 on r-cut Al_2O_3 substrate. (Top left) shows a film prior to thermal cycling. (Top right) The line profile displayed to the right is a cut along the green line in the AFM image. (Bottom left) depicts the same film after the thermal cycling treatment. (Bottom right) The line profile displayed to the right is a cut along the green line in the AFM image.

Immediately it becomes clear that distinguishing any type of cracking is difficult due to the highly polycrystalline nature of the films. Despite a low RMS roughness for each measurement at 1.2 Å and 1.3 Å respectively, the films show quite a bit of texturing due to the grains and grain boundaries. The difference in roughness alone is somewhat suggestive, but far from definitive especially as VO_2 is known to show small changes in microstructure when held above T_c, even at relatively low temperatures. While the post-cycle film shows features that might at first glance look like cracks, comparison to the pre-cycle film shows similar features. Examples are highlighted under the ovals for each measurement. There are numerous grain boundaries or other features that could easily be mistaken for cracking. While they may look superficially similar, clearly a film that has not been thermally cycled will not exhibit cracking due to thermal cycling. The polycrystalline nature and lattice mismatch with r-cut Al_2O_3 also make it less likely that any cracks will be distinct line cracks along the crystalline axes as in the literature for epitaxial VO_2 on TiO_2. Any cracking that would form will likely be influenced by the contours of the grains.

In order to provide a closer look, the same films are presented again in Figure 74, but with higher magnification. Again, the pre-cycle film is shown on the top half, with the post-cycle film shown in the bottom portion of the figure. The left images show two representative portions of the film at 2x the scale previously. The right images correspond to the ovals shown in Figure 73. The bottom right image shows a striation which might reasonably be interpreted as a crack. It has a similar width to the cracks measured by Nagashima, at $\cong$ 10 nm.[311] However, a very similar striation is seen in the top left. So, while the bottom may plausibly be caused or lengthened by the thermal cycling, we cannot definitively distinguish the two features as pre- and post- cycling. Unlike the literature VO_2 on TiO_2, they are not distinct enough to identify by inspection. They're also not easily distinguished by statistical image analysis in software such as Gwyddion.[258]

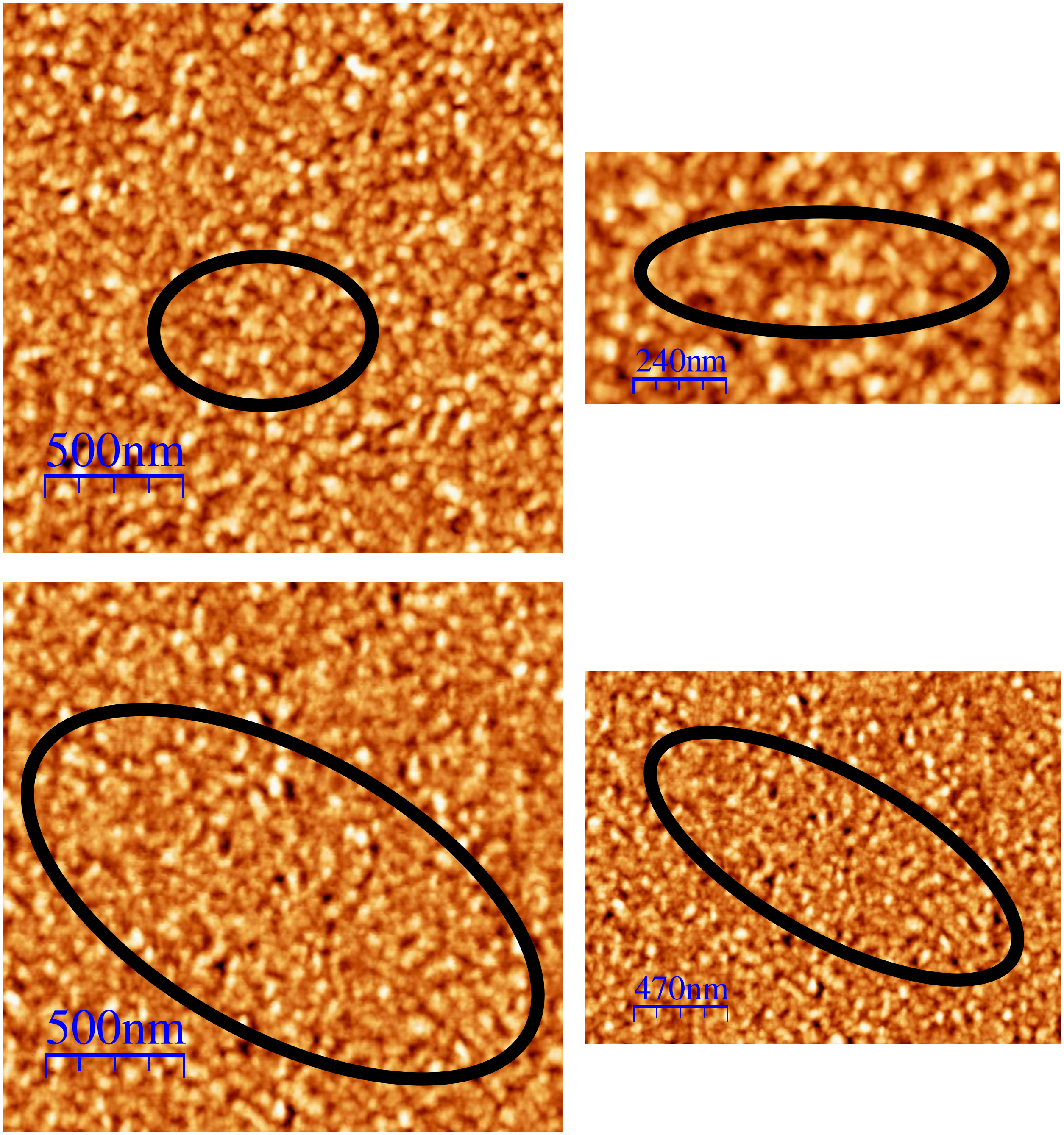

Figure 74. AFM images taken for a 100 nm VO_2 on r-cut Al_2O_3 substrate. (Top left) shows the same image in the previous figure but enhanced for clarity. (Top right) shows an example of a crack-like feature, but in an uncycled film. (Bottom left) depicts the same film after the thermal cycling treatment, also enhanced. (Bottom right) shows an example of a potential crack. The ovals correspond to their counter parts in Figure 73.

We are therefore unable to observe cracks in our VO_2 films within instrumental limitations. One major confounding factor is the highly polycrystalline nature of the films themselves, which makes it difficult to definitively distinguish features. Abreu et al. similarly found they could not detect their cracks with AFM, even with 30 nm crack widths and on TiO_2 substrate, due to lack of tip sensitivity. Their result in Figure 69 is the SEM result rather than the AFM they show.[312] There is also no guarantee that cracks will propagate to the surface layer, which would be undetectable in a surface technique such as AFM but could still influence structural properties. Other detection methods such as electron microscopy or in-situ AFM across the VO_2 SPT may therefore be necessary to confirm cracking in VO_2 films.

5.7 Conclusions

In this chapter, we explored whether it was possible to reverse the H_C vs. T profile in VO_2/Ni bilayers by depositing Ni below T_c of the VO_2, rather than above it. Samples with the Ni deposited at RT show a low coercivity due to their unstrained state below the VO_2 SPT, and a higher coercivity after the temperature is increased beyond T_c. This is the opposite of the profile seen in HT films, which display a high to low coercivity change. Therefore, deposition above or below phase transitions can act as an additional tuning parameter that has permanent effects on the overall properties of the bilayer. In previous work on materials with near room temperature phase transitions, this choice is often neglected since the default deposition temperature tends to be high and thus above T_c to ensure crystalline quality.

As was the case in the HT films, this effect is visible utilizing several different substrates, including various cuts of Al_2O_3 and TiO_2 (101). The exact details of the HC vs. T profile varies from substrate to substrate, although they share many common features. However, these RT bilayers show a clear irreversibility in the magnetic properties after the first heating across the VO_2 SPT that wasn't seen in the HT films. This irreversibility is seen in both the coercivity and saturation magnetization properties of the films. After multiple thermal cycles, there is still a reduced coercivity enhancement of around 0.626 mT (17%) at 360 K, as well as localized enhancement near T_c due to phase coexistence in the VO_2 layer. Changes in the magnetization across the VO_2 SPT are no longer observed within instrument resolution after thermal cycling.

A likely culprit seems to be cracking due to the stress of the VO_2 SPT, something that is well known due to the destruction of VO_2 single crystals. VO_2 thin films are known to be robust in most of their properties under repeated thermal cycling, although they have been shown to suffer some amount of less destructive cracking in order to accommodate the VO_2 SPT. Literature data on this cracking in thin films is also somewhat lacking, since it isn't a major concern for many of VO_2's interesting properties. We show that a similar irreversibility is seen in the resistivity of virgin VO_2 films, which shown an increase in the resistivity in the semiconducting state below T_c. Theoretical modeling using a percolation model shows that cracks would show exactly this type of behavior, since they can be expected to act as local open circuits. Therefore, cracking is a plausible link between both the irreversibility in magnetic properties in VO_2/Ni bilayers and irreversibility in resistivity in pure VO_2. Changes such as strain relaxing to grain boundaries seems less likely to be able to cause both behaviors. This irreversibility is not seen in HT samples. This is another hint towards cracking being the culprit, since in the procedure outlined in Chapter 2, samples are cooled below the VO_2 SPT, prior to being reheated for Ni deposition. HT samples would therefore already have cracked prior to deposition, since this reheating is essentially equivalent to a heating thermal cycle.

We attempted to find direct evidence of this cracking via AFM measurements, but no obvious cracking was observed. However, it is clear more study into the structural response to the VO_2 SPT in thin films is needed. In addition to suggestions in the previous section, reproduction of these results for magnetic structures in alternative forms such as single crystals, nanobelts, or powders might also offer some insight. Lastly, preliminary results show that it may be able to reduce or suppress cracking using a low O_2 environment, as O_2 deficient VO_2 seems more resilient to this irreversibility. More work needs to be done to understand whether this irreversibility is controllable if applications are going to take advantage of direct coupling to the VO_2 SPT.

Chapter 6. FeRh/Ni Bilayers

6.1 Motivation

While VO_2 provides a rich playground for exploration, both in fundamental physics and applications, there are many avenues for exploring magnetic heterostructures. In the case of our VO_2/Ni bilayers, the interaction is driven entirely by the SPT of the VO_2 since VO_2 is paramagnetic both above and below the transition. A natural extension is to add magnetic coupling in addition to the strain coupling provided by an SPT, via the use of a FM material. A number of materials undergo magnetic transitions in addition to their SPT, but a particularly interesting choice is FeRh. The AF to FM transition can be expected to potentially yield larger effects than more typical transitions such as AF to PM transitions. In addition, its T_c of 370 K makes it viable from an applications standpoint. Indeed, there have already been a number of studies on FeRh/FM bilayers after the pioneering work by Thiele et al..[199] However, they typically focus exclusively on the role of the magnetic coupling, and neglect any impact from the SPT. In addition, they do not consider any effects of depositing above or below the transition, as the magnetic transition isn't expected to have any permanent history effects if properly thermally and magnetically cycled.

In this section, we present the results of a study on FeRh/Ni bilayers. The FeRh films were magnetron sputtered following the procedure outlined in Chapter 2, and the sputtering conditions were optimized for high quality FeRh films. The main techniques used to characterize the quality of the FeRh were XRD to ensure high crystalline quality, and magnetometry measurements that show the magnetic transition is similar to that in bulk FeRh. While the high sensitivity of the transition to growth conditions is a challenge in growing FeRh, it also allows an avenue for monitoring the quality of the films. In addition to the above measurements, AFM scans show a textured single crystalline morphology, with the texture aligning along the substrate lattice directions. After sample quality was confirmed, a representative set of samples were grown, Ni was sputtered onto the samples to create a bilayer system, and measured consecutively with XRD/XRR, PNR, and then magnetometry. By using the same set of samples for each measurement, we can more confidently draw conclusions about the link between the structural characteristics such as the FeRh/Ni interface affect the magnetic properties of the bilayers. The sensitivity of the FeRh to growth conditions and effects such as the details at the interface necessitates this extra detail.

6.2 Sample Preparation and Characterization of Bare FeRh films

In order to find the proper conditions for high quality FeRh films, the FeRh samples were magnetron sputtered from a $Fe_{50}Rh_{50}$ target onto MgO (001) substrates, typically roughly 5 mm x 5 mm wide with a thickness of 0.5 mm. In principle, smaller pieces could be used, but it was found that 2 fingers in opposite corners of the sample greatly improved the homogeneity due to improved thermal contact. The high temperatures required in the annealing process and the sensitivity of the transition to the chemical ordering render the samples extremely sensitive to minor temperature gradients due to slight differences in thermal contact across the sample. A 5 mm x 5 mm sample is large enough that portions of the sample affected by shadowing effects of the finger can be removed, leaving only a uniform film. The sample conditions are the same as given in Chapter 2, with the deposition temperature and post-deposition annealing temperature used as tuning parameters. In prior work, it was found that an elevated but relatively low deposition temperature, followed by a high temperature anneal promotes high crystalline quality and a strong magnetostructural transition. The rate of the FeRh sputter was measured prior to deposition utilizing both a quartz crystal balance as well as XRR. In the case of the crystal, a 50/50 average between the Fe and Rh parameters were assumed, and deposition rates agreed well with the XRR results. The Ni and W values were measured using the quartz crystal balance.

Before any magnetic characterization, structural characterization via XRD was used to confirm the crystalline quality of the FeRh, since FeRh without the CsCl structure will not show a magnetic transition. A typical XRD pattern for a high quality FeRh film with strong CsCl chemical ordering is shown in Figure 75. This measurement was taken with the system described in Chapter 2. The largest intensity peak at 42.8 ° corresponds to the MgO (002) peak with Cu $K_{\alpha1}$ radiation, as expected for the 0.5 mm thick single crystal substrate. The MgO (001) peak is forbidden. The splitting of the peak to the right corresponds to the Cu $K_{\alpha2}$ signal. Peaks labeled with a star belong to the substrate or the powder Al sample backing plate. A strong FeRh (001) peak is evident at 29.81 °. The large intensity despite a thickness of only 50 nm is indicative of the high crystalline quality of the FeRh in the CsCl crystal structure. The minor peak to the left of the FeRh (001) is a contaminant beam from Cu K_{β} radiation.

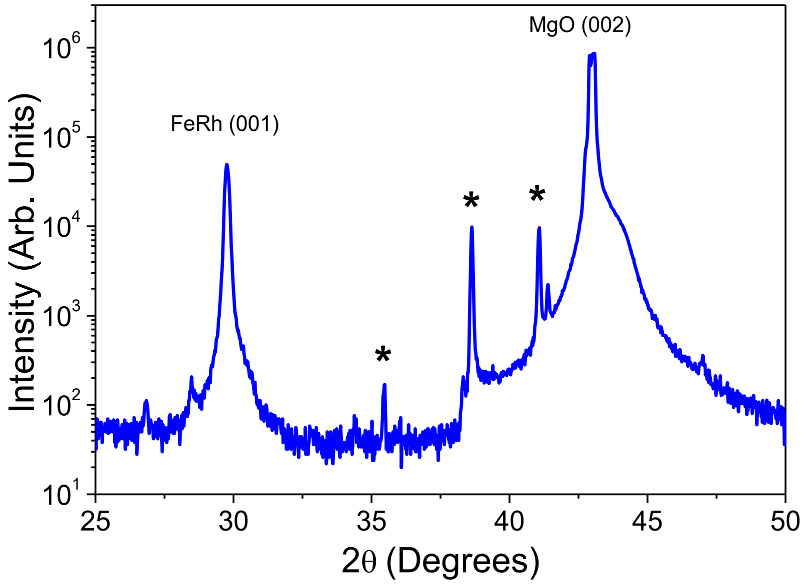

Figure 75. XRD of sputtered FeRh onto MgO (001) oriented substrate. Peaks labelled with a star correspond to the substrate or powder Al backing plate.

After confirming the structural quality of the films, it is still necessary to check the quality of the magnetic transition, as even films with a high quality XRD can still display poor transitions. A straightforward measurement of the transition is an M vs. T measurement, where the sharpness and magnitude of the AF to FM transition are highly sensitive to the FeRh quality. A high quality FeRh film will show temperature response similar to that shown in Figure 76, which shows an M vs. T measured in the SQUID system. Looking first to the 0.1 T measurement, the magnetic properties shows several hallmarks of a high quality FeRh thin film. At low temperature, below T_c, we see a very low remanent moment, only 32 $\frac{\mathrm{kA}}{\mathrm{m}}$. Averaging the midpoint of the heating and cooling branches at half the saturation magnetization of the FM phase, the MSPT shows a T_c of 378.4 K. This particular sample nearly completes the phase transition at 400 K, the maximum temperature of the SQUID. At 400 K, we see an estimated saturation magnetization of 1290 $\frac{\text{kA}}{\text{m}}$, in excellent agreement with the best FeRh films and bulk FeRh in the literature. Also shown in the figure, in black, is the same sample measured at 1 T. The sample displays identical behavior, except with T_c shifted to lower temperature due to the applied field which acts to stabilize the FM phase.[186] The data displayed is the raw data collection, without correction. Therefore the 1 T measurement is shifted lower due to the diamagnetic signal of the MgO substrate.

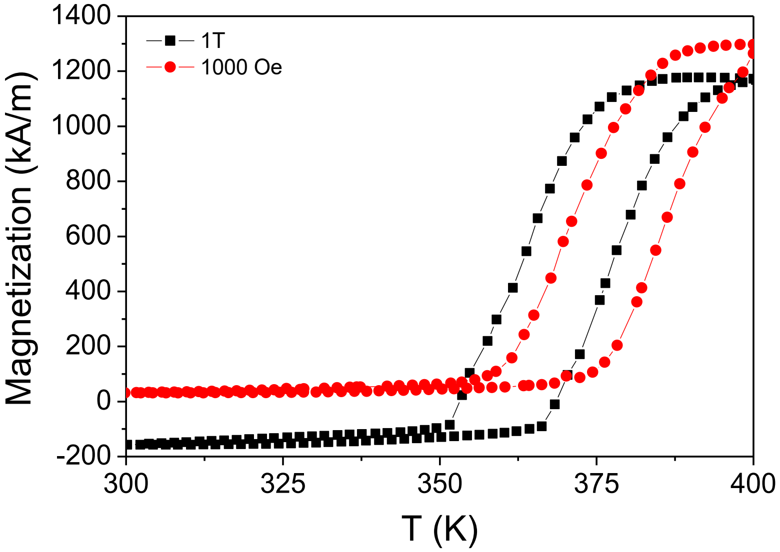

Figure 76. M vs. T for an FeRh film on MgO (001) substrate for 1 T and 0.1 T applied fields.

In order to fully characterize the magnetic properties of the FeRh film, we wish to know not just the temperature dependent magnetization, but also the magnetic behavior as a function of applied field. To that aim, we show uncorrected hysteresis loops at various temperatures across the FeRh transition in Figure 77. In order to highlight the features in the loops, the scale is varied from panel to panel, as the signal in the AF phase would be essentially flat on the scale of the FM measurement. For these measurements, the field was applied in-plane. In the top left panel, at 300 K, the film is nominally fully transitioned to the AF phase, although there is a clear remanent FM phase. The coercivity is rather large, approximately 17.13 mT. As the temperature is increased the magnetization increases as seen in the panel at 365 K. This corresponds to the onset of the transition, with only a small portion of the film having transitioned to the FM phase. At 375 K, a significant portion of the film is transitioned, and the sample is in the middle of the phase transition. The coercivity has widened, and the magnetization is a significant fraction of the saturation magnetization of the film fully in the FM phase. Above this midpoint in the transition, the coercivity begins to decrease again and the magnetization is close to the full FM value, as in the 395 K panel. Measurements during the transition are extremely sensitive to the local temperature, and a slight temperature drift causes the opening of the hysteresis loops for measurements too close to T_c. The corrections for this behavior will be discussed momentarily. At 420 K, the film is mostly transitioned to the FM state, and the FeRh shows a fairly typical hysteresis loop.

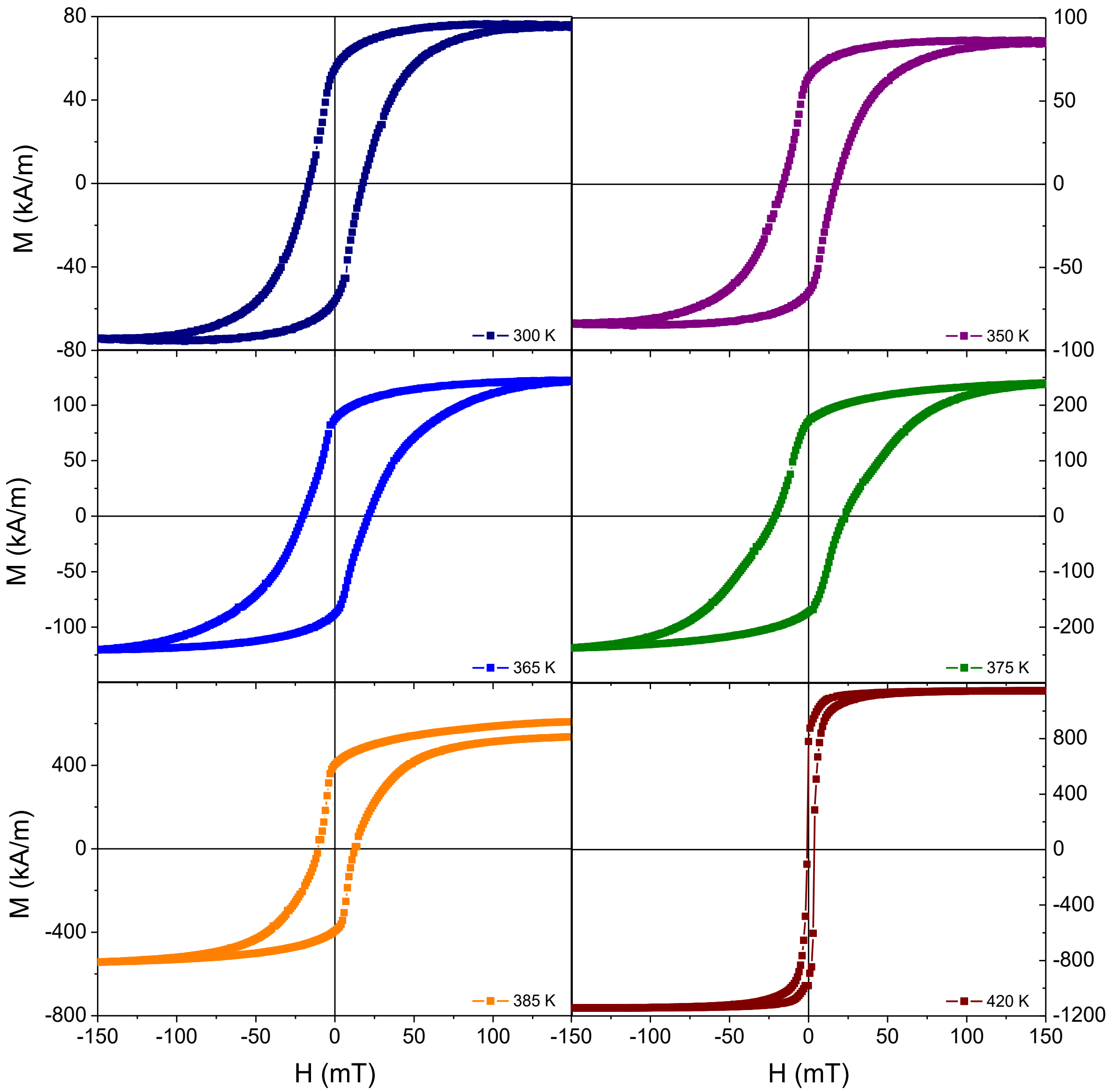

Figure 77. Hysteresis loops for an FeRh film on MgO (001) substrate, at various temperatures.

Figure 78 shows the extracted coercivities as a function of temperature. At low-T, the remanent FM phase leaves a relatively large coercivity at 17.1 mT. The absolute value of this coercivity is highly variable from sample to sample. The value of the coercivity at low-T in samples is strongly correlated with the amount of remanent FM moment measured and is inversely proportional to the magnetization. Therefore, samples with a large remanent FM phase at low-T tend to have a relatively lower coercivity and the highest quality samples with low magnetization have much larger coercivities, over 45 mT. The slope of the coercivity as a function of temperature in these highest quality samples also tends to be much more extreme. This coercivity behavior is likely tied to the local behavior experienced by remanent FM portions of the film. In a film with a very low remanent moment, a FM portion of the film is largely surrounded by AF bulk, which will act to pin the moment. Samples with a large remanent moment have sufficient neighboring FM phase to act more like a normal FM, but partially pinned relative to the high-T full FM phase.

With increasing temperature, the coercivity decreases slightly, until the bulk of the FeRh begins to transition as the temperature approaches T_c. As the onset of the AF to FM transition, the coercivity begins to increase, reaching a sharp peak. It seems likely that the spike in coercivity near T_c can be attributed to a phase coexistence effect in the MSPT, as was discussed in the previous work with VO_2/Ni bilayers. Since phase coexistence is a universal feature of first order transitions, it is unsurprising to see a similar effect occur here. The fact that it is not in the true midpoint is likely due to the magnetic interactions of various FeRh domains with each other, something that was not present in the VO_2. Rather than being a simple function of maximizing boundaries, an exchange spring effect or local demagnetization fields will influence the coercivity as well as strain. From this perspective it’s not surprising to see a peak when there is a significant AF phase present in the FeRh. In this sample, the measured coercivity peaks at around 22 mT. Due to the localized sharpness of the peak, even these close points might miss the ‘true’ peak, although it will be close. While there is variation between samples, this peak generally sits around 20-25 mT in magnitude, with the sharpness of the peak influenced by the quality of the FeRh. As the temperature is increased further and the FeRh transitions further to the FM state, the coercivity drops drastically. It is worth noting that even when the film is nominally fully transitioned as measured by the saturation magnetization, the coercivity is still slightly elevated. It is only when the film is far from where the heating and cooling branches meet in the thermal hysteresis do we see the coercivity reach its true value of 2.2 mT. This value for the FM coercivity is consistent between samples, if the quality of the films and the roughness are held roughly constant.

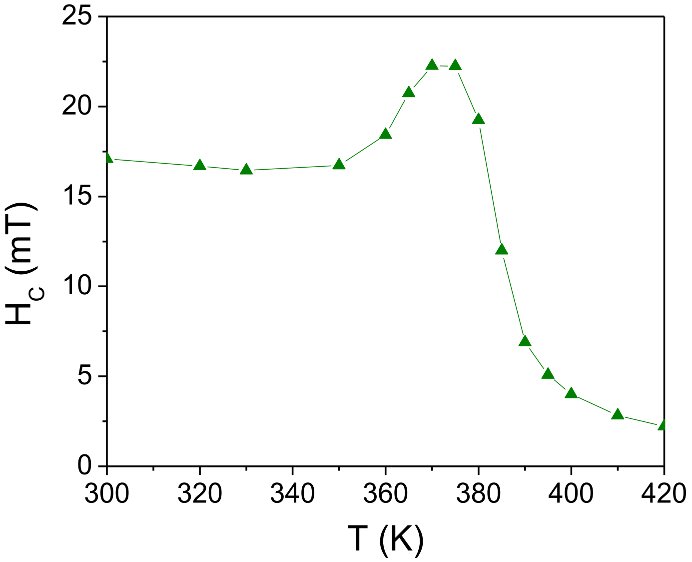

Figure 78. Coercivity vs. Temperature for an FeRh film on MgO (001) substrate.

We now take a moment to return to the opening of the hysteresis loop seen in the bottom left panel of Figure 77. This is purely an artifact of the QD VSM system. When setting a set point, there will be some overshoot of the temperature during the measurement, and the system will attempt to recover during the measurement. This overshoot is small, only 0.2 K over the entire measurement, but the FeRh film is sensitive to even this minor fluctuation in the middle of the transition. This overshoot feature happens regardless of the temperature stabilization procedure, including waiting manually for a given set of time. The overshoot only happens once the measurement itself begins. An example of this overshoot is shown in Figure 79, which shows both temperature as a function of time, and temperature as a function of field. For readability, only every 10th data point collected is shown. This measurement was taken during a nominal 380 K hysteresis loop. The overall offset from the nominal 380 K to ≅ 379.75 K isn't concerning, but the variation across the measurement is. The error bars are generated dynamically by the QD software, and represents the naïve error due to uncertainty in the thermometer etc. In both graphs, there is a clear overall dip in the temperature that is later recovered, although the ending temperature is slightly lower than the starting temperature. This is fairly typical, even for temperatures such as 380 K which require active heating (rather than any passive cooling). In order to correct for this, hysteresis loops near the FeRh MSPT are run 3 times in succession, and any future hysteresis loops shown in future sections of this chapter are the 3rd loop. Typically, the 2nd loop is sufficient to close the hysteresis, but a 3rd is done out of an abundance of caution. Outside of the initial opening of the hysteresis loops, all 3 loops identical in their magnetic properties.

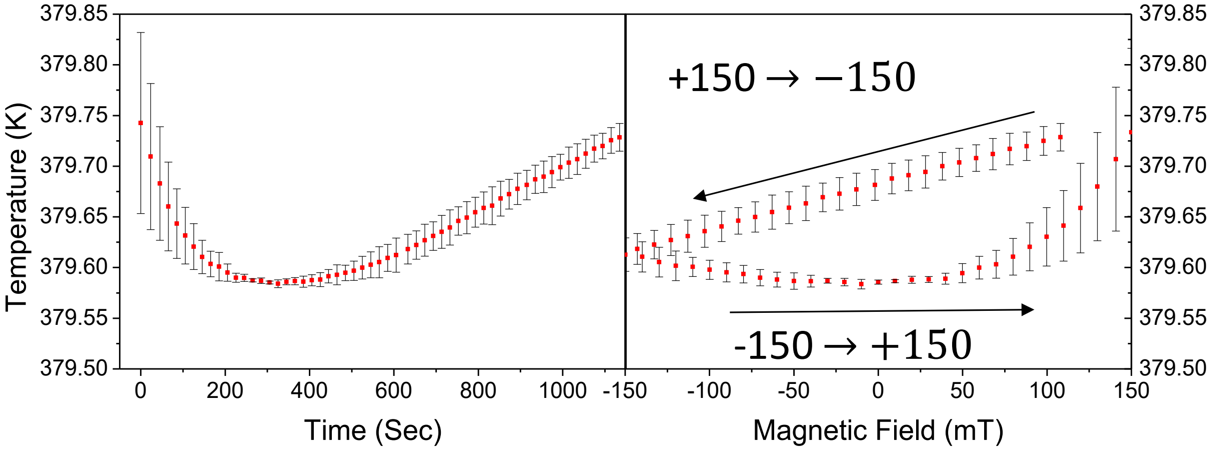

Figure 79. (Left) Temperature vs. time at a nominal 380 K setpoint. (Right) Temperature vs. applied magnetic field for the same measurement.

Having full characterized our bare FeRh films magnetically, we briefly consider the surface morphology. Presented below in Figure 80 are two FeRh films, with slightly different annealing conditions. Both AFM images are 2 × 2 μm scans. The top film was annealed for 2 hours at 800 °C, and the bottom 1 hour at 850 °C. Overall, both films are very smooth, despite no intentional tuning of the surface roughness. The top film shows an RMS roughness of 0.59 nm. The bottom is clearly rougher even just visually and has a roughness of 0.98 nm. In the top film, a subtle cubic symmetry is seen in the defects of the film. For the bottom film, there is clear cubic texturing of the film, following the substrate. Line profiles displayed to the right show that the absolute height difference in the films is quite small, ≅ 2nm for the top film, and ≅ 4.5 nm for the bottom. This texturing is similar to that seen in nanoislands that have been observed in prior works. However, those studies focus on much thinner films, on the other of 5 nm or less. In addition, the cubic symmetry in those ultrathin films is reduced considerably, although there is some. From these AFM studies, we can conclude that the surface roughness in our FeRh films is quite low, comparable or better than the previous VO_2 films. XRR results presented in the next sections will also show oscillations to very high Q values, confirming this interface smoothness. In addition, we can conclude that the films are relatively single crystalline, although with texturing and defects. It is unsurprising, considering the role of the single crystalline cubic MgO substrate in helping to promote high quality epitaxy. Finally, we note that despite the light texturing, we do not see large signs of in-plane magnetic anisotropy in the samples, cubic or otherwise.

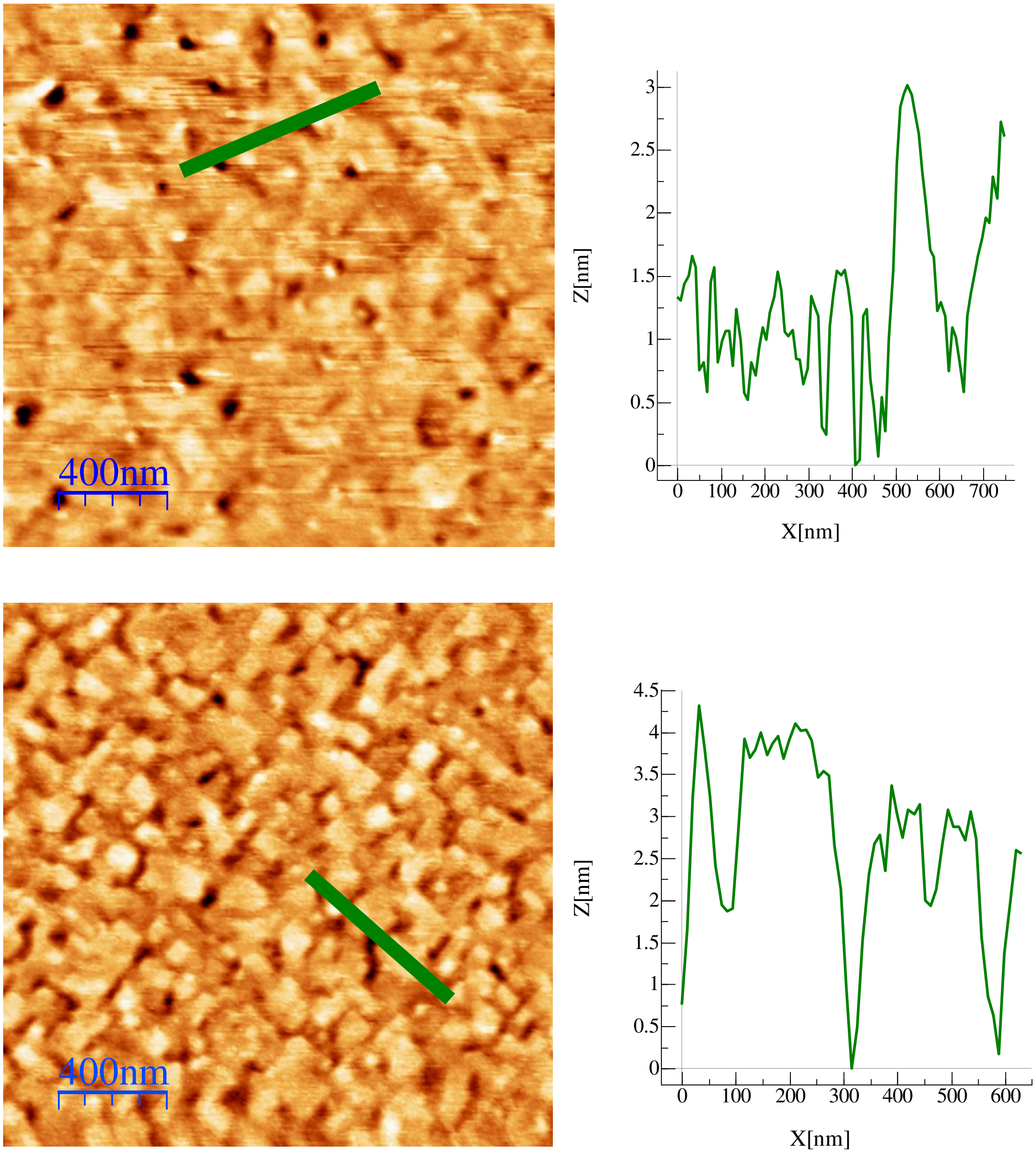

Figure 80. AFM for two FeRh on MgO samples. (Top) Annealed for 2h at 800 °C. (Bottom) for 1h at 850 °C. (Right) Line profiles displayed to the right are cuts along the green line in the AFM images.

This concludes the characterizations of bare FeRh films, which will form the base in the FeRh/Ni bilayer heterostructures to be discussed in the rest of the chapter.

6.3 FeRh/Ni Bilayers with Ni deposited above and below T_c

In order to study the effects of depositing Ni above and below T_c, two samples were completely characterized with a variety of techniques. Using the same samples for multiple measurements allows to minimize any variation between samples, and to directly correlate various parameters such as T_c between different measurements. Both samples were made sequentially, with deposition temperature 300 °C, followed by a 800 °C anneal for 1 hr. The MgO substrates were 1 cm x 1 cm, with minimal finger shadows in order to maximize the area and thus PNR signal, which is highly reliant on the total flux through the sample. The ramping during the heating and cooling required for the elevated annealing temperature was analogous to the procedure described in Chapter 2 for elevated deposition temperatures. Both samples were removed from the chamber, and sister samples made at the same time were measured to confirm the quality and the exact range of T_c. The samples were then reintroduced to the chamber and coated in Ni as well as the subsequent W capping layer in-situ. The deposition for the sample with Ni deposited below Tc was done at ambient temperature and will be labeled as 'RT' throughout this chapter. The deposition for the sample with Ni deposited well above Tc was done at 525 K and will be labeled as 'HT'. The W capping layer in the RT sample was done immediately following the RT deposition. The W capping layer for the HT sample was done after cooling back to RT, approximately 2 hrs after the deposition. The nominal thicknesses were 70nm/15nm/5nm for the FeRh/Ni/W heterostructure.

The crystalline quality of the RT and HT samples were confirmed via room temperature XRD, as shown in Figure 81. These measurements were done at NIST on a Rigaku SmartLab system utilizing a Cu K_α source, which allowed for higher resolution than XRD measurements shown previously. Figure 81 shows the XRD pattern for the RT sample, the HT sample, and then both overlaid for easier comparison by eye. Beginning with the RT sample, there are several notable peaks. The largest peaks correspond to the MgO (002) and (004) substrate peaks located at the nominally expected values 42.8 °and 93.8 ° respectively. The next highest intensity peaks belong to the FeRh (001), (002), and even (003) Bragg peaks at 29.81 °, 61.87 ° and 100.93 °. These FeRh peaks show a full width half max (FWHM) of $0.318\,° \pm 0.001\,°$. MgO grows with a NaCl-like cubic crystal structure, with lattice parameter 4.2140 Å. This lattice parameter allows for an epitaxial relationship between the FeRh and MgO, shown in Figure 82. Displayed is a single unit cell of FeRh on top of an MgO substrate, with each atom color coded as labeled in the legend. The c-axes of both FeRh and MgO are aligned and point out of the page. In-plane, it can be seen that the FeRh (110) is parallel to the MgO (100) axis. Thus, despite the large difference in lattice parameters (2.988 Å vs. 4.2140 Å for FeRh and MgO respectively, at room temperature) for these structures with cubic symmetry, there is an expected lattice mismatch of only ≅ 0.27%. Returning to the XRD pattern of the RT sample, a Ni peak corresponding to the (002) peak is observed at 51.84 ° indicating a preferential orientation. Despite Ni's fcc structure, the lattice mismatch between Ni and FeRh is quite large, the details of which will be discussed in more detail shortly. The Ni (004) peak, if present, would be entirely obscured by the much larger intensity of the MgO (004) peak. Finally, a W (011) shows in the left shoulder of the MgO (002) peak.

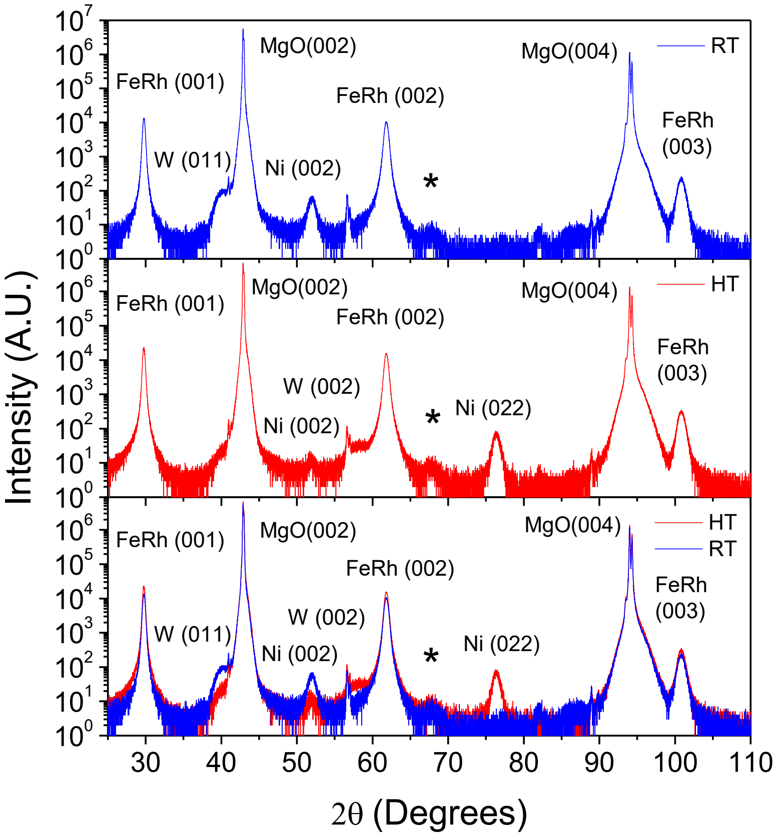

Figure 81. XRD of FeRh/Ni/W bilayers, for RT and HT Ni deposition conditions. Peaks labelled with a star correspond to the substrate or powder Al backing plate.

A similar analysis of the HT XRD scan shows large similarities, but also some features distinct from the RT sample as well. Again, the most prominent peak is the MgO substrate, as expected. The FeRh (001), (002) and (003) are again present, with roughly the same intensity and FWHM of 0.318 ° ± 0.001 ° as in the RT sample, indicating similar crystalline quality. However, analyzing the Ni peaks is shows there is a clear distinction between the RT and HT samples. In the HT, the Ni (002) peak is nearly completely suppressed in favor of the Ni (022) at 76.38 °, with this new peak having roughly the same intensity as the Ni (002) peak in the RT sample. Evidently, while depositing below the transition is energetically favorable for the Ni

(002), depositing above T_c with the associated change in lattice parameter stabilizes the Ni (022) orientation instead. This change in Ni texture also induces a change in the W capping layer to W (002). This subtle shoulder is seen to the left of the FeRh (002) peak and is more easily distinguished in the overlapping figure.

In the overlapping figure, a small difference can be seen in the right shoulder of the MgO peak, with the HT exhibiting a slightly larger intensity. This value is superficially close to where one might expect a Ni (111) peak at 44.5 °. Attempts were made to quantitatively fit a Ni (111) peak. Visually, a peak inserted at 43.5 ° improves the fit, but only marginally, with a reduction in the χ^2 of 0.3 %. However, the large intensities of the MgO peaks tend to dominant the signal. In addition, a peak at 43.5 ° as opposed to 44.5 ° would require a strain of $\cong 2$ % in the out of plane direction. Rudimentary strain analysis to be presented in 6.8 indicates largely relaxed Ni layers, so it would be unlikely for the Ni (111) to be uniquely strained. Further, the shoulder is present in both samples, so it is unlikely to be a result of the FeRh transition change in lattice parameter. All these points taken together point towards this shoulder being an artifact due to minor differences in the MgO substrate or slight differences in alignment between the samples rather than significant Ni (111) presence in the heterostructures.

A useful way to characterize the quality of the of a thin film is via its chemical ordering parameter $S = \sqrt{\frac{A_{001}/A_{002}}{1.07}}$, where S ratio of the integrated intensities of the 001 peak to the 002 peak, normalized to the theoretical ratio of 1.07 for a perfectly ordered film. A value of $S = 1$ would indicate a perfectly ordered film in the CsCl structure, and $S = 0$ a completely disordered one. The RT film yields an order parameter $S = 0.810 \pm 0.001$, and the HT a slightly larger value at $S = 0.866 \pm 0.001$. These values for the order parameter, as well as variation between samples are typical to those reported in the literature for high quality FeRh. The deviation from perfect order and variation between samples is typical due to the sensitivity of FeRh to the growth conditions. In addition, the HT sample receives a slight bit of what is essentially extra annealing due to the HT Ni deposition process. The order parameter can also be used to directly estimate the number of sites with the correct atoms vs. alloyed atoms via the relation

$$S = \frac{r_A - F_A}{1 - F_A}$$

Where r_A is the fraction of atoms of species A in their correct spots in the lattice, and F_A the fraction of atoms of species A in the alloy. The fraction of disordered phase is 9.5% for the RT sample, and 6.7% for the HT sample. This disordered phase can be associated with some remanent disordered bcc FeRh, rather than the desired CsCl structure.

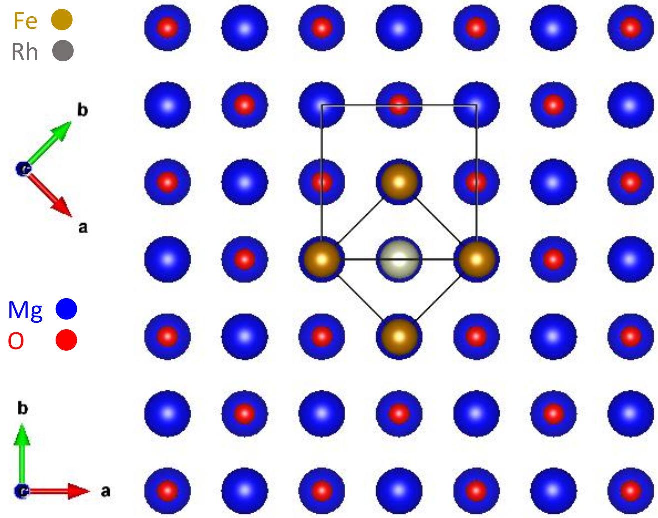

Figure 82. Schematic view of the epitaxial relationship between FeRh and MgO. FeRh (001)||MgO (001) is oriented out of the page, with FeRh (110)||MgO (100) in-plane.

Along with XRD, specular XRR measurements were also taken on the same SmartLab system, utilizing parallel beam optics and an 0.5 ° Soller slit. The results are presented in Figure

83. The raw measured data is displayed in black for both the RT and HT samples, and the theoretical fits shown in blue and red respectively. Looking at the raw data, we can already notice several features in the data. The main feature that stands out is how high angle both samples show specular reflection, an indication of smooth interfaces. Relative to each other however, it is clear that the RT must have a smoother interface since the oscillations in the HT sample damp out at much lower values of Q. In addition to the broader pattern, on can easily distinguish multiple oscillations superimposed on each other, a hallmark of multilayer systems that have different fundamental lengths in satisfying the Bragg condition.

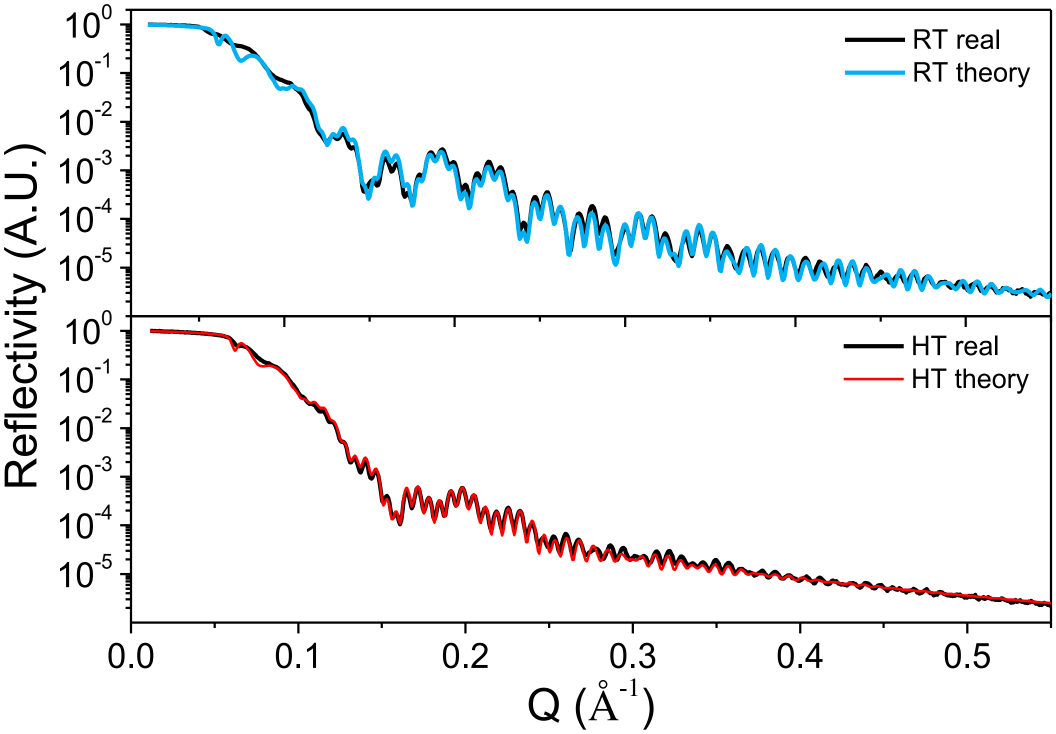

Figure 83. Specular XRR results for ‘RT’ and ‘HT’ MgO/FeRh/Ni/W thin films.

In order to construct the models of best fit, the raw data was imported and modeled in the Refl1D software discussed in Chapter 2. The starting profile was built roughly in line with expectations from the deposition process, but otherwise allowed to refine freely. The scattering length density (SLD) profile for the best models are shown in Figure 84. The real part of the SLD, ρ , is shown in dark blue and dark red for the RT and HT samples respectively. The imaginary part of the SLD, ρ_i, is shown in light blue and red. The sample depth is divided into 3 slab models of FeRh/interfacial-FeRh: Ni/Ni for both the RT and HT samples, bound on either end by the MgO substrate or the W cap and then air. Each interface (MgO: FeRh, FeRh: Ni) is allowed to vary separately from the bulk. From the model fits, the exact thickness of each layer can be extracted, showing a thickness for the FeRh/interfacial-FeRh/Ni/W stack of 70/3/11/7 nm and 70/0.7/13/7 nm for the RT and HT samples respectively. Starting at a depth of 0 and working upwards through the stack, a number of notable features can be deduced from the figure. Firstly, the MgO: FeRh interface in both samples shows an abrupt shift from MgO to FeRh, with the interfacial FeRh matching its bulk values. This is in contrast to previous work, which has tended to find a unique interfacial layer. Continuing upward, it can be seen that both the RT and HT samples converge to similar values in the SLD, despite being free to diverge independently. This is another sign that points to the high quality and reproducibility in the films. At the FeRh: Ni interface is where the samples start to show very different behavior. In the RT sample, a sharp dip is observed in the SLD. From the XRR data alone, several possibilities are indistinguishable. An Fe-rich FeRh layer, Ni diffusion into the FeRh, a native oxide layer, or a low-density Ni layer are all potential causes. We will return to this feature when discussing the PNR data, as PNR together with the XRR can be used to reduce the possibilities. Turning to the HT sample, no sign of this low-density layer is present, and instead a smooth transition from FeRh to Ni is seen. The higher deposition temperature can be expected to allow for more intermixing at the interface, so this result should not be too surprising. Finally, the W interface cap in the HT sample is noticeably rougher than the RT sample, with an RMS roughness of 0.9 nm compared to only 0.6 nm in the RT sample. This leads to the additional damping of the XRR signal in the HT sample shown in Figure 83.

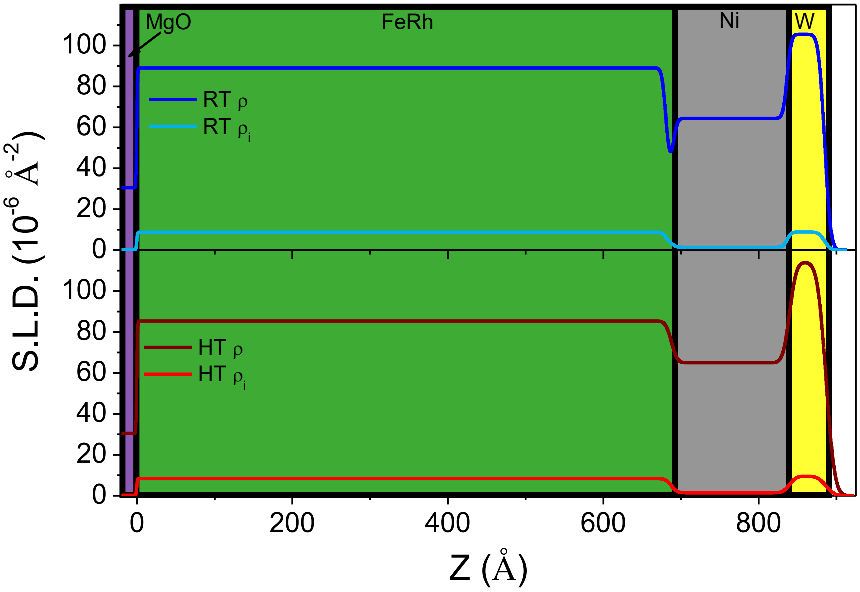

Figure 84. SLD profiles corresponding to XRR results for RT and HT MgO/FeRh/Ni/W thin films

While XRD and XRR provide a wealth of information about the RT and HT samples, they’re inherently limited to structural characterizations. While useful, if we wish to learn about the magnetic properties of the bilayers, we need to turn to a technique such as PNR as a way to probe the magnetic properties with depth dependence.

6.4 Magnetic Response of RT and HT FeRh/Ni Bilayers

In this section we present the results for the RT and HT FeRh/Ni bilayers. We begin with the M vs. T profiles shown in Figure 85, as the quality of the magnetic AF to FM transition is a good indicator of the quality of the underlying FeRh film. The procedure for the measurement was as given in Chapter 2. For the nominal thicknesses of 75 nm FeRh and 15 nm Ni, one can expect a magnetization of 78 $\frac{\mathrm{kA}}{\mathrm{m}}$ below T_c, when the FeRh is in the AF state and does not contribute to the magnetization, and 1136 $\frac{\mathrm{kA}}{\mathrm{m}}$ above T_c when the FeRh is in the FM state. In the data presented in Figure 85, we see magnetizations for both the RT and HT that are close to the nominal numbers but vary slightly from the theoretical values, as well as from each other. Below T_c, both samples show a magnetization elevated above 78 $\frac{\mathrm{kA}}{\mathrm{m}}$ at 139 $\frac{\mathrm{kA}}{\mathrm{m}}$ for the RT sample and 166 $\frac{\mathrm{kA}}{\mathrm{m}}$ for the HT sample. This discrepancy is indicative of a remanent FM phase at low temperatures, something commonly seen in the interfaces of FeRh thin film systems. The origin of this interfacial FM phase is discussed in 6.7. Across the transition the two samples show roughly similar behavior, with identical T_c, but a $\cong$ 12% difference in saturation magnetization once the MSPT is completed. If we define T_c as the average of when the heating and cooling branches reach half magnetization, we obtain a T_c of 383.5 K in the RT, and 385 K in the HT sample. The RT sample shows a quite good agreement with the theoretical saturation magnetization, at 1080 $\frac{\mathrm{kA}}{\mathrm{m}}$ at 430 K. The HT deviates from the theoretical value, showing a reduced magnetization of only 952 $\frac{\mathrm{kA}}{\mathrm{m}}$ at 430 K. This can likely be attributable to the slight differences in quality or stoichiometry of the samples, which can heavily affect the quality of the FeRh MSPT. In particular, slight differences in the Rh ratio can shift the magnetization without otherwise affecting the transition too heavily. While differences in magnetization can in principle be caused by differences in thickness of the samples, this 12 % difference is far too large to be caused by the minor differences in thicknesses as seen in XRR and PNR. The PNR results to be presented in 6.5 are accurate to 1% in the thickness and show similar thicknesses for both samples.

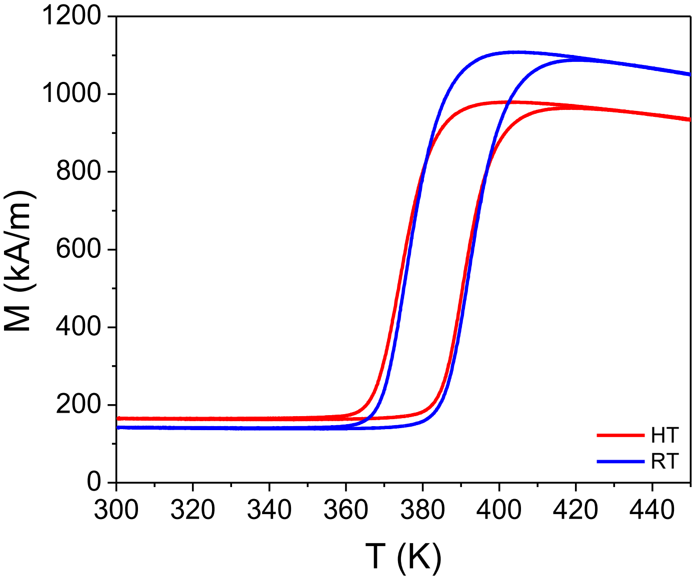

Figure 85. M vs. T for RT and HT FeRh/Ni samples under an applied 100 mT in-plane field.

Figure 86 shows results for magnetic hysteresis loops taken at various temperatures for the two types of samples. Starting at 450 K and cooling, hysteresis loops were measured at various temperatures following the procedure outlined in Chapter 2. Loops were collected every 3-5 K, particularly near T_c. For readability, only a select few are shown in Figure 1, which show features stereotypical of each portion of the transition. The chosen temperatures of 430 K, 390 K, 370 K, and 340 K correspond exactly to the values used in the PNR measurements that will be discussed in the next section, allowing a direct comparison. These temperatures correspond to being well above, just starting, mid, and below, the transition respectively. In the hysteresis loop taken at 430 K, we see a typical ferromagnetic response for a FM with a low coercivity. This is expected, as the FeRh is in its FM state, and will be strongly exchange coupled to the Ni layer.

Both FM FeRh and Ni have a relatively low coercivity, but in this bilayer structure, the response is largely dominated by the thicker FeRh. We also notice the same difference in magnetization as was seen in the M vs. T scan. Decreasing the temperature to 390 K, we see roughly a similar response, albeit with a slightly larger coercivity and lower magnetization. Continuing with the decrease in temperature, we start to see much more interesting behavior at 375 K, in the middle of the phase transition. Both samples have notably larger coercivities as compared to higher temperatures. At the start of the magnetization reversal, the samples begin with roughly similar behavior, but the HT diverges from the RT behavior, displaying a larger overall coercivity. The HT sample now has a higher saturation magnetization, in a reversal to what happened at higher temperatures, and as seen in the M vs. T. We can also begin to see some features or 'wiggle' in the HT sample, corresponding to a double switching event. A further decrease in temperature to 340 K, below the transition, further enhances the features we saw at 375 K. There is now a clear double-switching evident in the HT hysteresis loop, whereas the RT shows a single low coercivity switch. This double switching in the HT layer will be the subject of further discussion in Section 6.6. The hysteresis loops presented are the raw magnetic signal collected in the VSM, with no corrections (such as for the diamagnetic substrate) applied. Finally, we note that there is no sign of exchange bias, which is not surprising given the compensated AF state at the interface for FeRh (001).[329] However, these bulk measurements cannot determine if there is an exchange spring effect between the AF/FM system.[330]

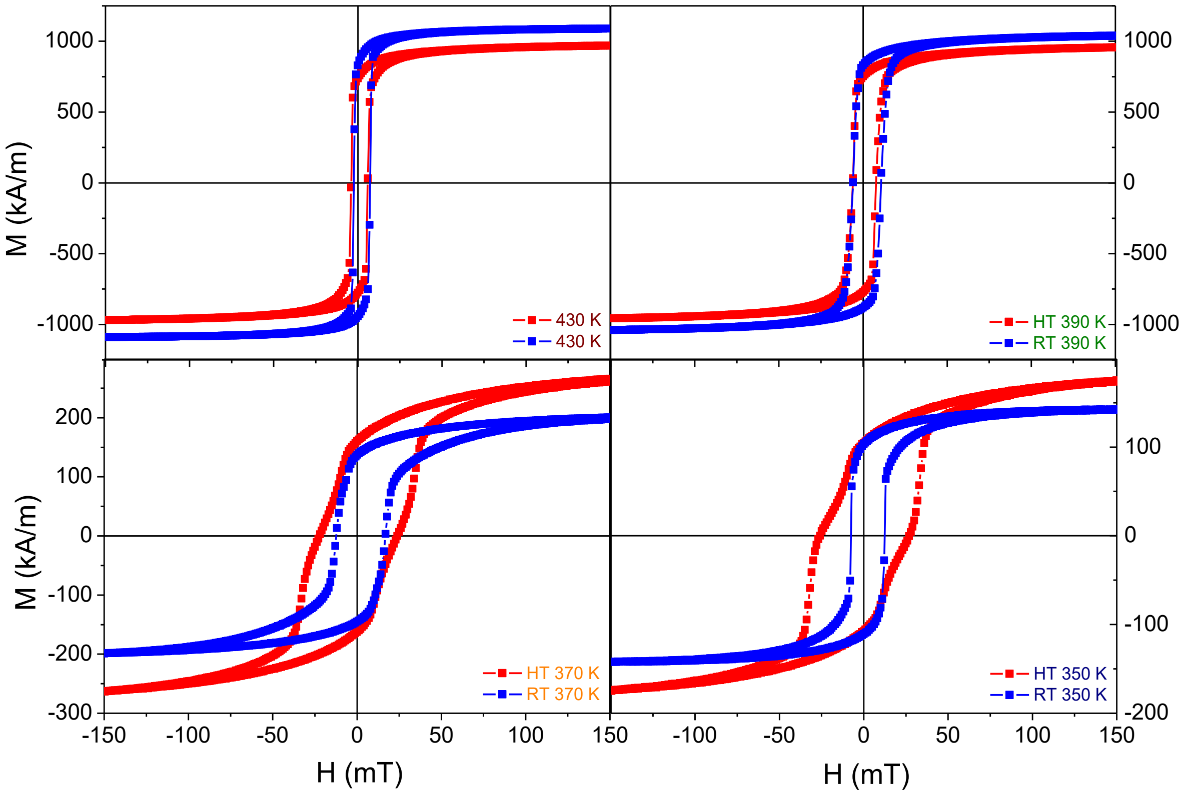

Figure 86. Hysteresis loops for RT and HT FeRh/Ni bilayers at various temperatures. (top left) at 430 K, (top right) at 390 K, (bottom left) 370 K, (bottom right) 350 K.

From these hysteresis loops, we can extra the coercivity at various temperatures, shown in Figure 87 in red and blue. In order to capture the full details across the FeRh MSPT, the coercivities are extracted from all the loops measured, not just the ones shown above. Above T_c, both the RT and HT samples follow roughly the same trend of a low 4.85 mT coercive field, dominated by the FeRh FM response. As the temperature is reduced, both samples start to show a sharp increase in the coercivity. In the case of the RT, this coercivity peaks at 18.83 mT at a temperature close to but below T_c, during the FeRh phase transition. This spike is then followed by a sharp decrease to 9.95 mT. This coercivity is stable at lower temperatures, with the typical FM slow increase as the temperature continues to be decreased. In the HT case there is an initial increase in the coercivity that also comes to a peak at 26.76 mT, however after the peak the coercivity remains elevated. There is often a shallow dip in the coercivity near but slightly lower temperature than the peak, before we see the normal FM behavior established. For both samples, as the temperature is reduced further, there is a slight increase in coercivity typical of FMs. The spike in coercivity near T_c can be attributed to a phase coexistence effect in the SPT, as was discussed in the previous work with VO_2/Ni bilayers and in bare FeRh. As in the bare FeRh, the peak occurs below T_c but during the phase transition. The coercive response far below T_c also seems similar to the response seen previously in VO_2/Ni bilayers. The Ni deposited at RT, which should correspond to a relaxed state, has a lower coercivity. In the HT sample, which should be relaxed above T_c and strained below T_c, we see a higher coercivity. One major difference between the previous work on VO_2 (as well as V_2O_3) is the FM nature of the FeRh. We would expect to see a high coercivity in the RT sample above T_c, but this is completely suppressed by the magnetic coupling due to the FM FeRh.

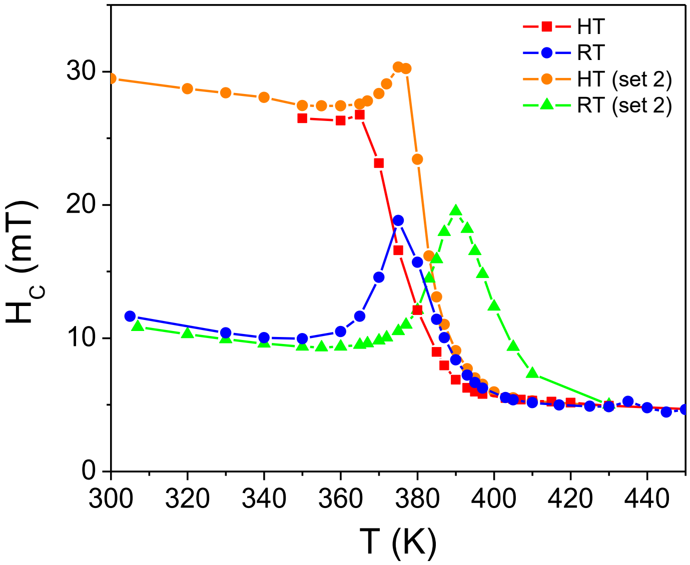

Figure 87. Coercivity of RT and HT FeRh/Ni bilayers extracted from hysteresis loops taken at various temperatures.

While we focus on only one set of samples in Figure 87, many of the features are broadly reproducible, as can be seen by the second set in the figure. There is a slight shift in the value of T_c, which we attribute to slight differences in FeRh stoichiometry or growth conditions. The value of the coercivity above T_c is consistently around the FeRh value of 5 mT for both RT and HT samples. The general features seen in the coercivity spikes are also robust, with the HT spike being more or less visible depending on its value relative to the low-T value of the coercivities as. The peak's strong localization also necessitates a fine temperature scan in the region. Because the peak and low-T HT coercivities are driven by different mechanisms, there is no consistent relationship between which is larger. In some samples, the low-T coercivity is greater than the peak, and in some samples the reverse is true. However, they are generally roughly similar in magnitude. The magnitude of the RT spike is fairly consistent between samples. The HT by contrast, shows more variability in the magnitude of the peak. In addition, the HT peak seems to always occur at a lower temperature than the corresponding RT sister sample. The low-T coercivities show quite a bit of variability in the absolute value. In the RT case, it can potentially be even lower than the corresponding RT high-T coercivity. In the hysteresis loops of the second set HT sample (data not shown), there is no double switching event.

Due to its nature as a bulk technique, magnetometry is limited in what else we might learn about what drives the difference between HT and RT magnetic behaviors. For more insight into the different systems, we turn to PNR. PNR's sensitivity to both structural and magnetic properties with nm resolution depth dependence can help to determine the cause of the different magnetic behavior in the two deposition conditions. It allows access to the interface, a critical region for magnetic properties in bilayers but one that is inaccessible by bulk magnetometry. The structural sensitivity, for instance, can be used to probe for chemical diffusion or differences in interfacial roughness. Whereas the magnetic sensitivity will be able to pick up any unusual magnetic behavior near the interface, such as a pinned layer or remanent FM phase in the FeRh. PNR is therefore an ideal probe into our FeRh/Ni bilayers.

6.5 Polarized Neutron Reflectometry of RT and HT FeRh/Ni Bilayers

In order to better understand the differing magnetic profiles between the RT and HT sample, PNR was measured at various temperatures across the FeRh MSPT for both samples. In order to correlate the results with later magnetometry measurements, care was taken to attempt to mimic the measurement sequence used during the magnetometry. Before measurement, the sample is heated to 450 K in zero applied field. Once the temperature is stabilized, a 700 mT in-plane field is applied in order to saturate the sample. This is slightly below the 1 T applied during magnetometry, limited by the magnet apparatus available during the measurement. However, this is far more than sufficient to ensure the sample is fully saturated. The field is then reduced to 100 mT. The temperature is reduced to the first measurement temperature. Once the temperature is stabilized, the PNR data is collected. The temperature is then reduced to the next measurement temperature, and the process is repeated. This process is thus a direct analog to a cooling branch in an M vs. T magnetometry measurement. 4 temperatures were measured: 430 K, 390 K, 375 K, 340 K, corresponding to above the transition, at the beginning of the transition, mid-transition, and below the transition. The raw data along with the theoretical values of the best fit model for both the RT and HT samples' specular 'spin-up' and 'spin-down' reflectivities at each temperature are shown in Figure 88, for a range of Q values up to 0.12 $Å^{-1}$. Note the log scale. While proper discussion of the modeling is needed to fully understand the features, a number of qualitative features can be seen even in the raw data. In both samples, above the transition, clear short oscillations can be seen. Translating from Q-space, the length of these oscillations correlates well to the thickness of the ferromagnetic FeRh/Ni bilayer structure. There is also a quite noticeable asymmetry between R^{++} and R^{--} signals the films, as expected for a ferromagnet. As the temperature decreases, these smaller oscillations broaden out, but remain due to the FM Ni and nuclear contributions to the SLD. The intensity covers a 5 orders of magnitude range, with noise being a limiting factor for the lowest intensities.

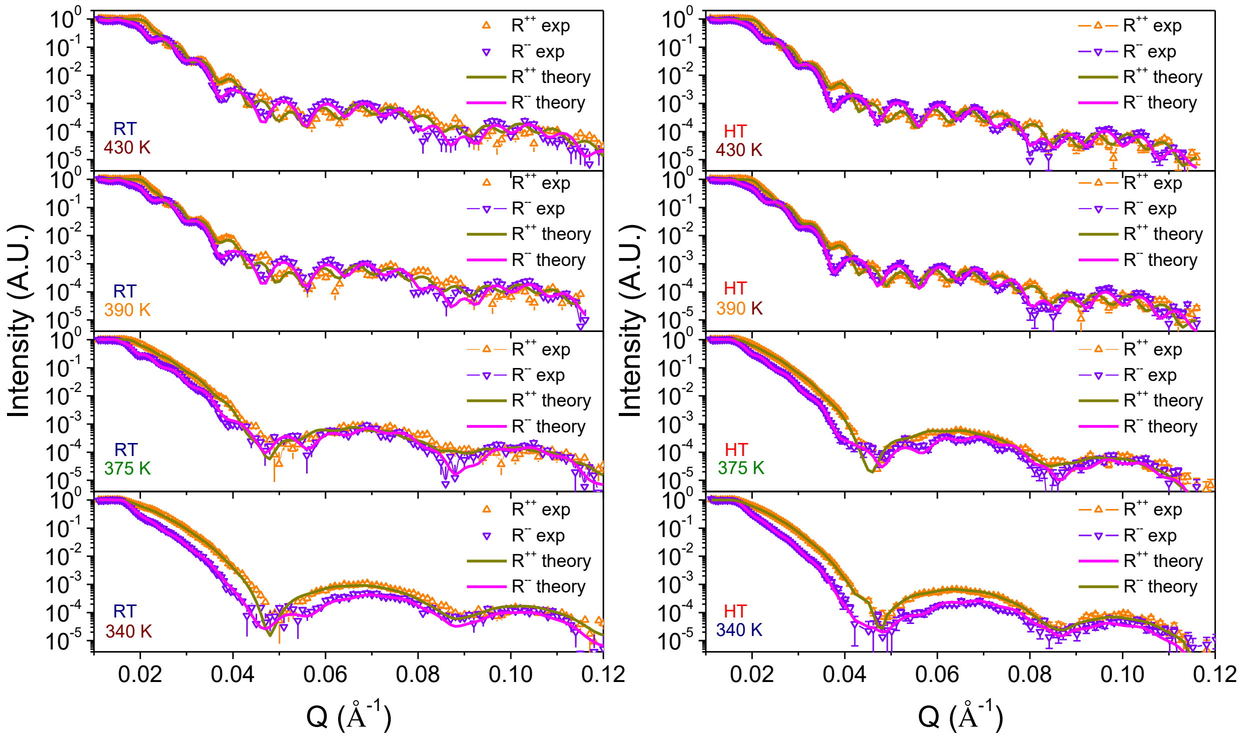

Figure 88. PNR measurements for the RT and HT samples, at various temperatures.

In order to isolate the contributions due solely to the magnetic properties of the bilayer, the Spin Asymmetry (SA) defined as $\frac{R^{++}-R^{--}}{(R^{++}+R^{--})}$ is displayed along with the theoretical values of the best fit model in Figure 89. The details of the model used to fit the data will be discussed momentarily. Briefly, it is clear that the modeling is able to capture most of the features in both the RT and HT samples, particularly for lower values of Q ($Q < 0.05$). At higher Q, the lower intensity of the signal leads to higher uncertainty in the measurement. In addition, many simplifying assumptions made in the model such as a constant magnetic SLD per bin begin to break down at higher Q values. The scans above the phase transition, at 430 K and 390 K, show clear oscillations associated with the FM phase of the FeRh. AT 375 K, in both the RT and HT samples, the oscillations begin to reduce in intensity, as the samples transition through the MSPT. At 375 K, we begin to see some divergence between the modeling and the data, likely due to the difficulty in capturing the details of inhomogeneous, partially transitioned FeRh film with a simple 3 slab model. 375 K also shows a slight difference between the RT and HT sample signals, likely due to the sensitivity of the transition to temperature. Slight differences in temperature of the stage and T_c between the samples as seen in the magnetometry data means one sample will be in a slightly different portion of the transition than the other. At 340 K, the model is again able to capture most of the features in the signal, and there is strong agreement between the RT and HT samples.

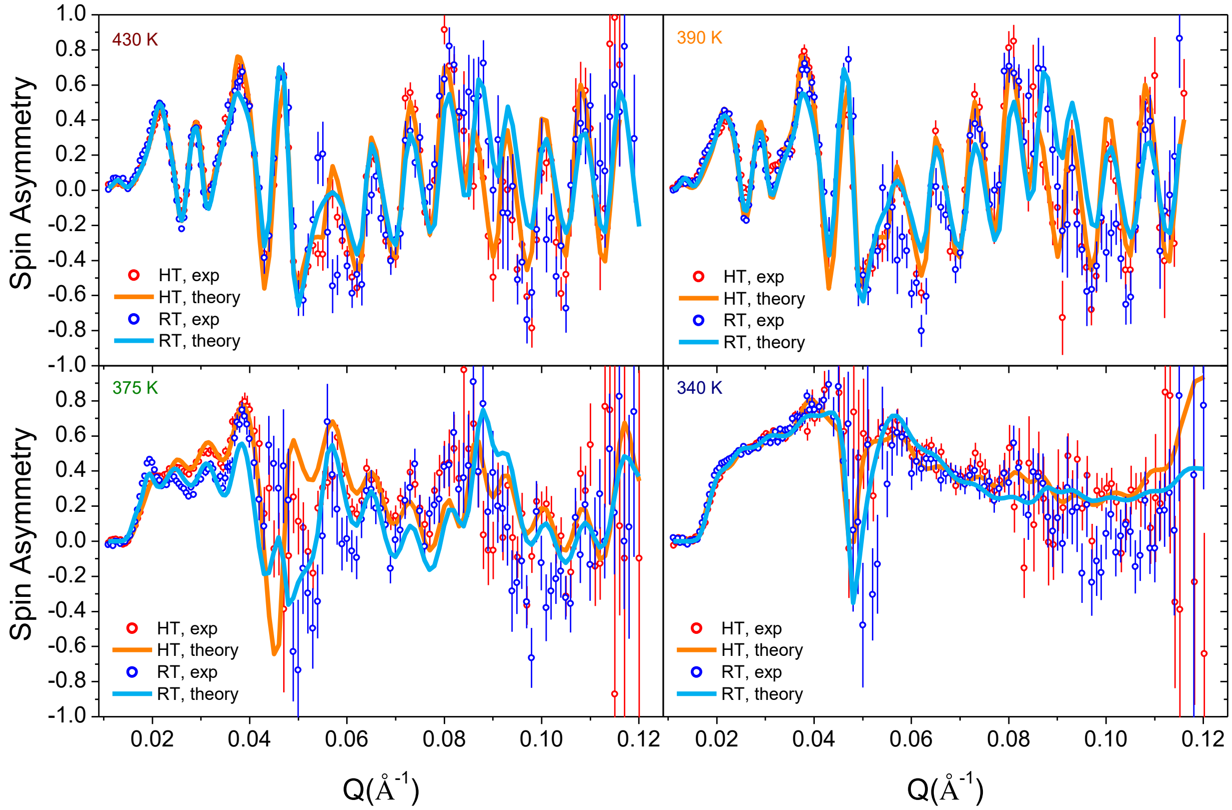

Figure 89. Spin Asymmetry in ‘spin up’ and ‘spin down’ PNR measurements for RT and HT MgO/FeRh/Ni/W thin films.

We now turn our attention to finding a model that best fits the PNR data, produced using the reductus and Refl1D software packages. The raw data was first corrected for background via background subtraction, polarization efficiencies of the incident neutron beam, and the finite footprint of the beam. After performing these corrections in reductus, the resulting data was imported to the Refl1D package. The details for the fitting algorithms used by Refl1D is described in detail in Chapter 2. The XRR data shown previously was used in as the initial starting approximate chemical profile. Since XRR is only sensitive to the nuclear composition of the sample with no confounding magnetic interactions, it provides a convenient starting point. When refining the various fits, the RT and HT profiles are allowed to vary separately from each other. However, the nuclear SLD per sample for each temperature is co-refined to a common SLD profile. Enforcing this constraint ensures a physically plausible result, since the chemical composition and therefore nuclear SLD should not change at different temperatures for the same sample. It also greatly helps in disentangling the nuclear and magnetic contributions to reflectivity since the magnetic contribution of the FeRh is temperature dependent, in contrast to the nuclear component.

In order to identify the best model, two algorithms of the Refl1D package were utilized. First the DREAM algorithm was applied to the regressions for approximately 1000 steps, dependent on the number of free parameters. The efficiency of the DREAM algorithm allows us to sample a large parameter space and identify promising regions for a best fit. Once a likely region is identified, the Nelder-Mead algorithm is applied in order to find a minimum. While robust, the Nelder-Mead algorithm is known to converge slowly and can get stuck in local minima, therefore the combination of the two fitting algorithms allow for a robust search for a best fit model. Of course, optimization algorithms can never guarantee a true global minimum. This problem is particularly acute with methods such as PNR which can be highly degenerate with different models providing similar output. But the convergence to a local minimum along with intuition and common-sense constraints give confidence that the model is reasonable. The corresponding best fit model for the nuclear SLD is presented in Figure 90 and the magnetic contribution in Figure 91. Any errors reported for refined parameters extracted from the fits (such as thicknesses or magnetizations) are taken using a 95% confidence interval calculated by the DREAM algorithm. In the Monte Carlo based DREAM algorithm, this corresponds to the range where 95% of the hops are accepted for a parameter.

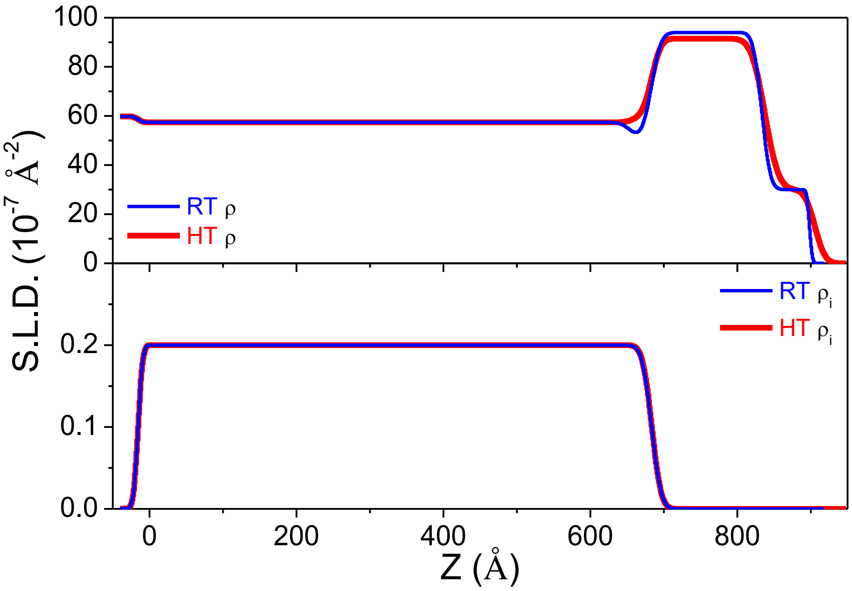

Figure 90. Nuclear SLD depth profiles for the RT and HT sample. (a) the real part of the nuclear SLD. (b) the imaginary part of the nuclear SLD.

In Figure 90, we present the nuclear SLD profile as a function of depth for our RT and HT MgO/FeRh/Ni/W films. The RT film is shown in blue, and the HT in red. The thickness of the HT data has been enhanced to reveal regions when the profiles directly overlap. Because of the constraint during the co-refinement, these nuclear profiles for the HT and RT samples are identical for each measurement temperature and we don't distinguish between the 430 K – 340 K profiles. On the top of Figure 90 is the real part of the nuclear SLD, and on the bottom the imaginary part, in order to handle the large variation in magnitude between the two. Beginning with the real part of the SLD, we see a result that looks extremely similar to the XRR profile. This is expected since both measurement techniques are sensitive to the chemical structure of the films. The profile begins with the MgO substrate at a nominal −50 Å depth, which then meets the FeRh film. The interface between the MgO: FeRh is relatively sharp, and smoothly transitions from the MgO to the FeRh. The interfacial FeRh does not vary from the bulk values despite being allowed to, in contrast to many previous PNR measurements on MgO/FeRh films.

In previous works, this was attributed to diffusion of the Fe into the MgO substrate. Most of those works used a higher deposition temperature, 600 °C as opposed to our 300 °C, which might encourage more interfacial diffusion during the deposition. The high annealing temperature 800 °C does not seem to encourage this diffusion as much as the deposition temperature. Other authors have found that Rh-rich sputtering can help suppress the interfacial layer as well. Continuing through the film, the bulk FeRh in both the RT and HT samples are in agreement. At the FeRh: Ni interface a large difference between the two films is realized, with the RT film showing the same dip in the interfacial FeRh as in the XRR measurements, with the HT instead showing a smooth change from FeRh bulk values to bulk Ni values. The HT interface is considerably rougher than the RT sample, at 14.3 Å vs. 9.11 Å. The bulk Ni corresponds well to a uniform Ni value. The slight elevation in the RT Ni density can be attributed to the fact that the orientation stabilized by the HT sample has a higher in-plane areal density (and therefore lower out-of-plane density), but the difference is slight. At the Ni: W interface we again see a fairly large difference, with the RT sample showing a rather sharp interface and the HT showing a thicker smoothly varying interfacial layer. The same trend is seen at the W: air interface. We note that the W bulk shows a SLD that matches well that for metallic W, indicating that the capping layer successfully protected the sample from oxidation. Any oxidation of the W layer, which typically reverts to stable WO_3 at ambient conditions, would show prominently in the nuclear SLD. For the RT sample, we find a refined thickness of 65.0 ± 0.3 Å and a SLD of $3.10 \pm 0.02 \times 10^{-6}$ Å^{-2}. For the HT, a thickness of 67.8 ± 0.3 Å and $3.02 \pm 0.02 \times 10^{-6}$ Å^{-2}. These SLDs are in good agreement with the theoretical value for metallic W, and the 3% difference between RT and HT samples is well within error.

The bottom of Figure 90 shows an essentially negligible imaginary portion of the nuclear SLD, at three orders of magnitude smaller than the real part of the SLD. It's mainly the FeRh bulk which contributes to this dissipative portion of the reflectivity signal. We next turn our attention to the magnetic contribution to the SLD shown below in Figure 91.

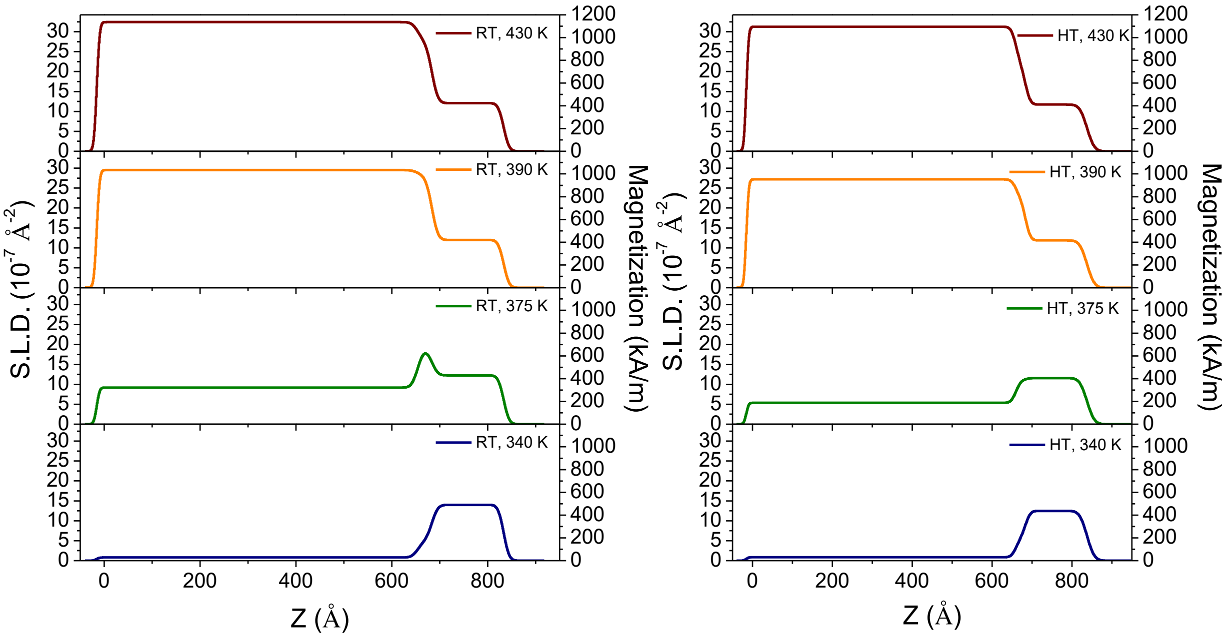

Figure 91. Magnetic S.L.D. and magnetization extracted from PNR model best-fits for various temperatures, for both RT and HT samples. 430 K is shown in dark red, 390 K in orange, 375 K in green, and 340 K in navy blue.

In Figure 91, we plot the magnetic portion of the SLD for both the RT and HT samples at each temperature. The RT sample is shown to the left, and the HT to the right of the figure for direct comparison. Because the magnetic SLD is directly proportional to the magnetization after a scaling factor, the SLD is shown on the left axis, with the corresponding magnetization on the right axis for each plot. For each temperature, we maintain the same axis scaling to allow for easy comparison. The relevant features are easily distinguishable without needing to change scale.

Starting at 430 K, we see very similar profiles between the RT and HT samples. The sample begins with a sharp interface between the nonmagnetic MgO substrate to FM FeRh, with the interfacial FeRh agreeing with the bulk values. The bulk FeRh shows good agreement with the expected magnetization for FeRh, at 1136 $\frac{\text{kA}}{\text{m}}$ in the RT sample, and 1095 $\frac{\text{kA}}{\text{m}}$ in the HT sample. The larger magnetization in the RT sample relative to the HT sample is similar to that seen in the magnetometry data, although a much smaller difference. Unsurprisingly, the two samples show different interfacial magnetism at the FeRh: Ni interface. The HT sample shows a smooth decrease from the bulk FeRh to Ni magnetizations, whereas the RT has something like a kink that is localized closer to the FeRh side of the interface. Initially the slope is lower than in the HT sample, but after the kink shows roughly the same slope as in the HT sample. The Ni layer in both samples is uniform, with magnetizations of 423.5 $\frac{\text{kA}}{\text{m}}$ and 410.9 $\frac{\text{kA}}{\text{m}}$ in the RT and HT. These values are typical for thin film Ni at these temperatures. At the Ni: W interface, we see the same interfacial behavior seen before, with the RT sample showing a sharper interface, and the HT a broader interface. Both vary smoothly from the FM Ni to nonmagnetic W. At 390 K, we see largely the same behavior, except with the FeRh having a slightly lower magnetization at the onset of the transition.

At 375 K, which corresponds to being partially through the FeRh transition, we see a greatly reduced bulk FeRh magnetization in both samples. The bulk FeRh magnetization is now lower than Ni, at 321.8 $\frac{\text{kA}}{\text{m}}$ in the RT sample and 187.9 $\frac{\text{kA}}{\text{m}}$ in the HT sample. The difference between the two samples, as discussed with the magnetometry, is likely due to slight differences in the applied temperature and stoichiometry between the two samples. Therefore, the HT sample is slightly farther through the phase transition as compared to the RT sample at a nominal

375 K. The sensitivity during the sharp transition means even minor differences in the local temperature are noticeable. Specular PNR allows for depth dependent measurements, but any variation in the x-y directions will be averaged out. Therefore, specular PNR is unable to discriminate whether this nominally bulk magnetization has variation in the plane of the film, such as those due to grains or magnetic domains. Previous work using other techniques such as XMCD which are sensitive to in-plane variations in the magnetization show that the FeRh transition follows a nucleation type behavior. The FeRh: Ni interface at 375 K shows rather different behavior as compared to the previous temperatures. Here the interfacial FM phase is prominent in the RT sample, and present although more subtle in the HT sample. The potential origin of this interfacial FM phase will be discussed further in 6.7, which leads to a local decrease of T_c. The fact that this interfacial FM phase is due to a modified T_c rather than forming a different compound can be understood by noting that the interface still experiences the full FeRh transition, with a comparable magnetization to bulk FeRh at 430 K, and nearly fully suppressed as an AF at 340 K. An enhanced view of the HT interface that shows its remanent FM phase more clearly will be shown shortly in Figure 95 and Figure 96. The PNR fitting consistently requires this interfacial FM phase in order to match the spin asymmetry data, indicating it's not an artifact of a particular model but rather an important feature of the magnetic profile in the samples. As just mentioned for in-plane nucleation, it's been demonstrated that the phase transition often nucleates from defects such as interfaces. This interfacial FM phase in both samples is ≅ 3 nm in depth. Past this interface, both samples converge to a uniform bulk Ni layer. At the Ni: W interface a smooth transition is seen, again with the HT interface taking place over a longer distance.

The final measurement was taken at 340 K, which corresponds to being fully below the FeRh MSPT. The FeRh is fully transitioned to its nominally AF state, and the signal is close to 0. On the length scales used by the PNR probe, an AF is essentially 'nonmagnetic' since the alternating spins will average to zero. There is a slight remanent moment in both samples of ≅ $30 \ \frac{\mathrm{kA}}{\mathrm{m}}$, which can be attributed to some slight disorder or off-stoichiometry in the system. The temperature is low enough that the interfacial FM is largely suppressed despite its reduced T_c. Both samples smoothly move to the Ni bulk value at the FeRh: Ni interface. The Ni layer shows similar uniform bulk Ni magnetizations as seen at previous temperatures. The Ni: W behavior is the same as at other temperatures, with the HT having a broader interface.

This concludes the temperature dependent PNR measurements across the FeRh MSPT. The overall picture is roughly what one expects for an FeRh/Ni bilayer as a function of temperature and agrees well with the magnetometry. As we decrease the temperature, the FeRh layer in both samples traverses it's MSPT, going from FM at higher temperatures, to partially transitioned, to finally fully AF. The Ni layer stays FM throughout the measurement, as we're well below its Curie temperature. The interface between the RT and HT samples can be seen to be quite different, both chemically and magnetically. This can be expected to be tied to the FeRh MSPT, and the surface the Ni will see during deposition. Because of both the general importance of the interface in FM bilayer structures and particularly in the case of the FeRh MSPT coupling which is interfacial, the details of the interface are a critical parameter for understanding FeRh/Ni films. The depth dependence of PNR as a technique allows us to confirm that the different magnetic properties seen between RT and HT samples are not simply due to altering the bulk of the sensitive FeRh during the Ni deposition process as well as confirm the continued high quality of the FeRh layer in both samples. The temperature dependent PNR in particular allows us to separate the magnetic and chemical contributions to the PNR signal due to the unique FeRh AF to FM transition with increasing temperature. This is useful both in gaining a better understanding of the dynamics of the FeRh/Ni system as a whole, but as we will see in the next sections, a useful constraint for magnetic field dependent PNR that will be correlated to the magnetic properties of the film.

6.6 Magnetic Switching Event in HT FeRh/Ni Bilayers

During the investigation of the magnetic properties in these bilayers and the discussion of Figure 86, it was noted that the HT sample doesn't simply have a higher coercivity hysteresis loop, but the cause of this hysteresis is the switching event that occurs at a $\cong 25$ mT applied switching field. This so-called 'double switching' is often a hallmark in bilayers composed of 2 FMs, where the two layers are sufficiently decoupled such that one-layer switches at a lower applied field than the other. In principle, it can be possible to tell which layer switches first based on the change in the net magnetization. However, in this particular system, the two switching events are roughly proportional to each other, making it impossible to distinguish the dynamics based on bulk magnetometry.

In order to clarify the details of this switching event, PNR again becomes a good option due to its depth dependence which allows for distinguishing the magnetization of each layer. As with previous measurements, the procedure was designed to mimic the bulk magnetometry measurement as closely as possible. First, the sample is heated to 450 K, to fully induce the FeRh MSPT. A 0.7 T field is applied in-plane, saturating the sample, and then reduced to 100 mT. The temperature was then reduced to the measurement temperature, 350 K. After temperature stabilization, a PNR scan is collected, with the applied 100 mT field. The applied magnetic field is then swept to −0.7 T, large enough to fully saturate the sample in the opposite direction. The field is then increased back to +25 mT, which is near but above the switching field seen in the magnetometry data. A second PNR scan is collected. This data was then analyzed in the reductus and Ref1D software packages. As before, the nuclear profiles of these two measurements are co-refined, enforcing a common chemical structure which is expected since it's the same sample. The raw reflectivity measurements are shown in Figure 92, along with the best model fits. The error bars shown correspond to 1σ.

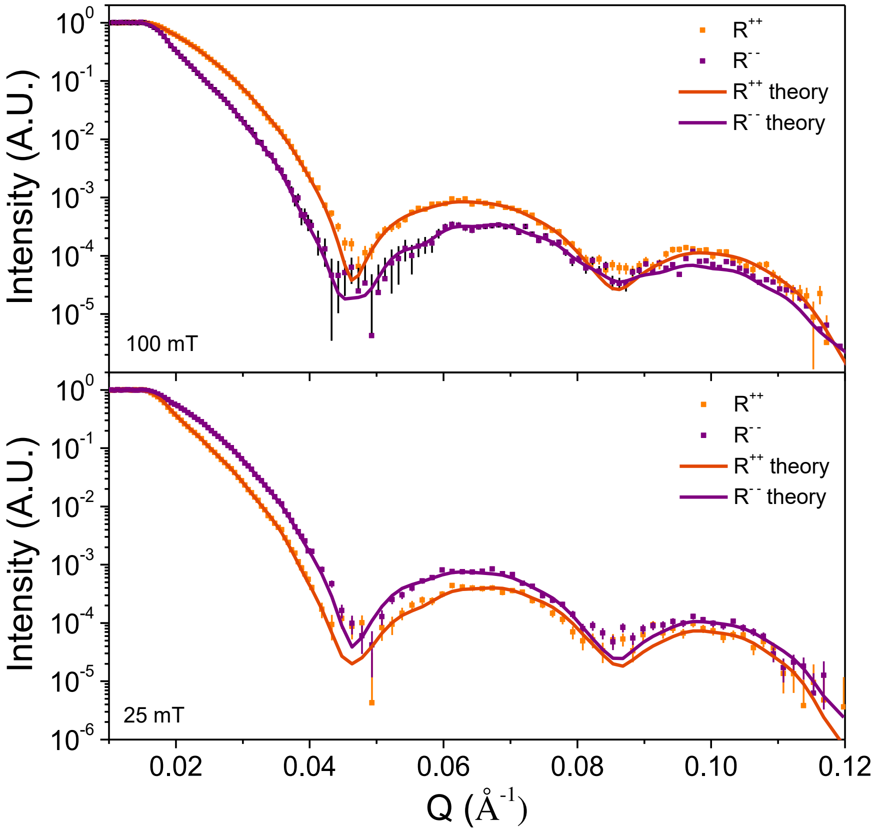

Figure 92. PNR measurements (points) and best fits (lines) for the HT sample at 350 K (a) under +100 mT applied field and (b) under +25 mT applied field (after cycling to -700 mT).

As before, the main takeaway from the raw intensity measurements is how well the model fits the data. In this specific case, it is also worthwhile to point out that the R^{++} and R^{--} signals have inverted when going from 100 mT to 25 mT. This inversion is what one would expect if the film magnetization has reversed to the nominally $'-'$ direction during the hysteresis cycling, but the +25 mT was not sufficient to cause it to reorient back to the $'+'$ direction. An even clearer indication is seen in the spin asymmetry plotted in Figure 93.

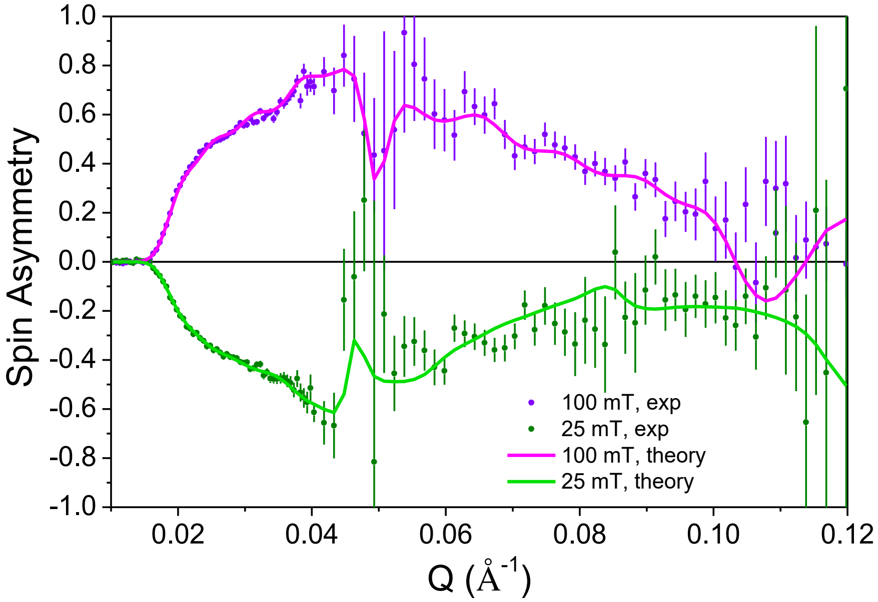

Figure 93. Spin asymmetry data (points) and best fits (lines) for the HT sample at 350 K (a) under +100 mT applied field and (b) under +25 mT applied field (after cycling to -700 mT).

By plotting the SA, we can once again isolate the purely magnetic contributions, and the contrast between the two measurements becomes even more starker, as they essentially mirror themselves about $\text{SA} = 0$. $\text{SA} = 0$ would correspond to a nonmagnetic material, as there wouldn't be any reflectivity contrast for the spin-up vs. spin-down neutrons. This mirroring of the SA signal is an indication that a magnetic feature in the FeRh/Ni bilayer has switched sign, and that the feature is a dominant part of the signal to induce such a complete mirroring. The nuclear and magnetic SLD's extracted from the best fit model corresponding to the theoretical matching of the data are presented in Figure 94 and Figure 95 respectively.

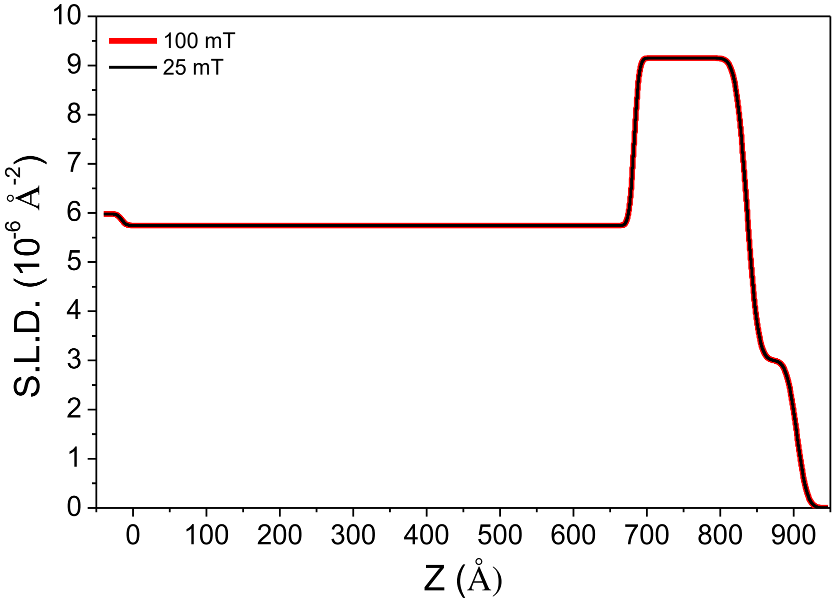

Figure 94. Nuclear depth profiles for the HT sample at 350 K under +100 mT applied field and under +25 mT applied field (after cycling to -700 mT).

As previously, the two nuclear profiles were co-refined, to enforce a common chemical composition, since the measurement was performed on the same sample. Notably, we see a nearly identical nuclear SLD profile as compared to the previous XRR and PNR measurements for the HT sample, despite not explicitly constraining the fit. The nuclear SLD profile from the temperature dependent measurements for the HT sample from the previous section were used as the initial starting configuration.

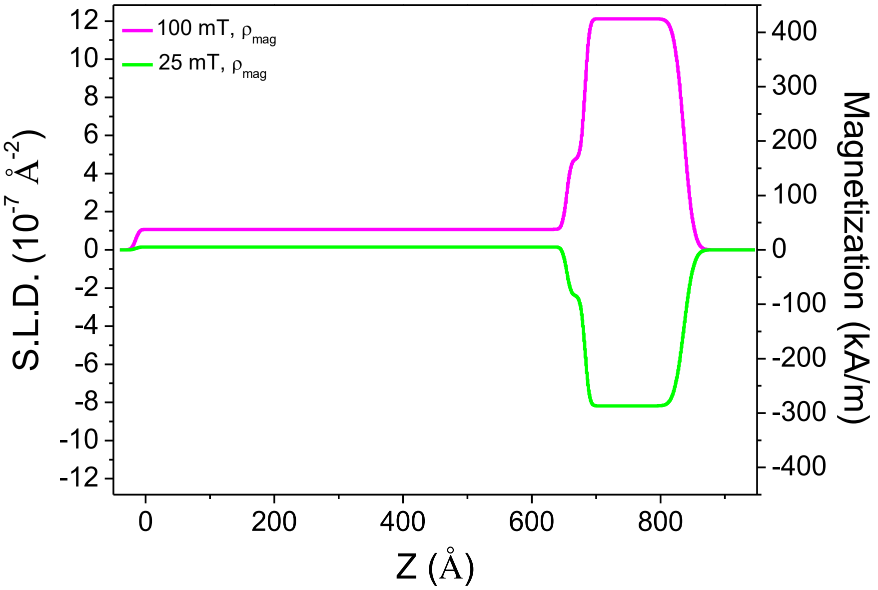

Figure 95. Magnetic depth profiles for the HT sample at 350 K under +100 mT applied field and under +25 mT applied field (after cycling to -700 mT).

Beginning with the +100 mT measurement shown in purple, we see essentially the same results as the 340 K measurement presented earlier. There is a rather sharp interface at the MgO: FeRh interface, with the interfacial FeRh matching the bulk. The bulk FeRh itself has a nonzero remanent moment, despite being nominally well below T_c for the sample. At the FeRh: Ni interface, a region of interfacial FeRh shows an enhanced magnetization relative to the bulk. Again, there is a uniform Ni layer, followed by a relatively smooth transition to the W cap. For the +100 mT measurement, all the magnetic layers align with the field, as expected after being saturated in the positive direction. Turning to the +25 mT measurement shown in green, a rather different profile is seen. The FeRh bulk signal is significantly reduced and close to 0, but definitively positive, as can be seen in Figure 96. The PNR modeling returns a value of 4.1 $\frac{\mathrm{kA}}{\mathrm{m}}$, with values ranging from +0.3 to + 10.7 $\frac{\mathrm{kA}}{\mathrm{m}}$ within the 95% confidence interval of the DREAM algorithm. Despite the small signal, the greater thickness of the FeRh relative to the Ni layer allows it to contribute meaningfully to the overall magnetic signal. The difference in magnitude between the +100 mT and +25 mT magnetization is likely at least partially attributable to how an applied field can stabilize the FM phase, rather than pure magnetization rotation. The interfacial FeRh and Ni layers show a negative SLD, indicating that they're anti-aligned with the applied field. For a +25 mT field, this means the +25 mT is not enough to rotate the Ni magnetization, indicating that the bulk FeRh has flipped first in an applied field. We can therefore definitively conclude that it is the FeRh that causes the first step seen in the two-step hysteresis loop, and the enhanced coercivity is thus due to the Ni layer. In order to further confirm this interpretation, the FeRh magnetization was flipped in the model, but it does not produce the large mirroring change in the SA trend, which is governed by the Ni.

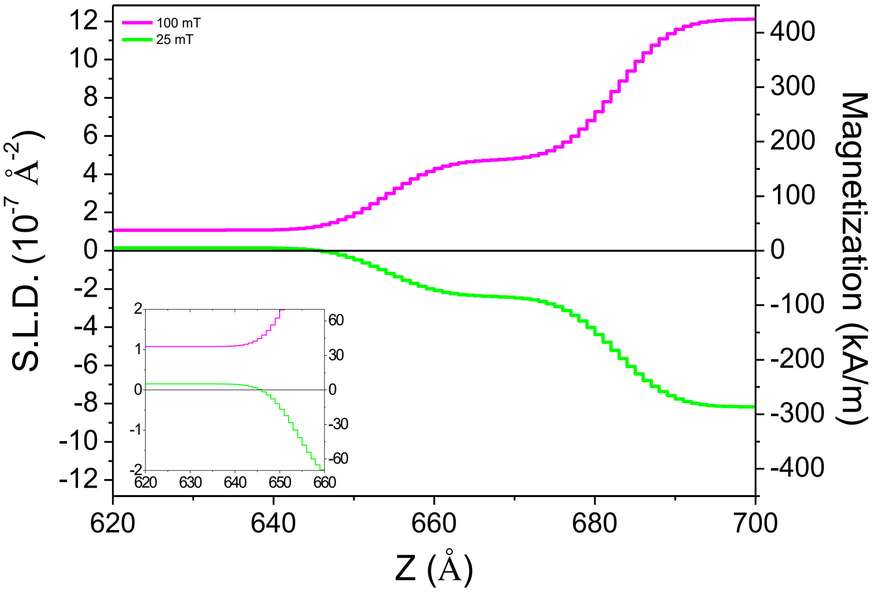

Figure 96. Magnetic depth profiles for the HT sample at 350 K under +100 mT applied field and under +25 mT applied field (after cycling to -700 mT). Enhanced view of Figure 95. (Inset) further scaling to show a non-zero positive moment in the +25 mT curve.

6.7 Interfacial FM phase in FeRh thin films

A focus of intense interest in previous work in FeRh thin films has been the remanent FM signal seen even when the sample is nominally fully transitioned into the AF state. This previous work has shown that that this remanent FM phase can form at either the substrate/FeRh interface or the FeRh/capping layer in a FeRh thin films sample. The exact origin of this interfacial FM phase is unclear, and a number of mechanisms have been proposed. It has been variously interpreted as diffusion,[331] strain effect,[183,185,332,333] a Rh-rich surface layer,[334] or a more general symmetry breaking.[335] The FeRh MSPT's sensitivity to various conditions makes it difficult to definitively isolate a single cause. While not the main focus of this work, the deposition conditions here allow us to approach the question from a different angle as compared to previous work and provide some insight to the mechanism behind the interfacial FM FeRh.

From the model fits, both the RT and HT samples show a remarkably similar $\cong 2.9$ nm interfacial FM layer, which suggests that they are caused by a similar mechanism. One potential mechanism is diffusion, as T_c in FeRh systems can be reduced via doping by Ni, or by being Rh-rich.[191,192,336] Therefore, diffusion of Ni into the FeRh, or conversely, Fe into the Ni layer, are potential mechanisms for this interfacial FM effect. Even doping on the order of 1% or less of either Ni or Rh can radically shift T_c without large changes in the magnetization. In the RT sample, XRR and PNR results showed a clear dip in the nuclear SLD profile at the interface. This dip is incompatible with Ni diffusing into the FeRh or a Rh rich layer left if the Fe diffused into the Ni, and intuitively one can expect a low mobility for atoms during a RT deposition. This dip is not seen in the HT sample, which instead shows a smooth gradient from the bulk FeRh to bulk Ni SLD values. Intuitively, the higher deposition temperature would promote higher atomic mobility. Due to their placement on the periodic table, atomic Fe and Ni both have very similar cross sections for both XRR and PNR techniques, making it impossible to distinguish interdiffusion on the order of 1%. So, while it is hard to pin down the details of the HT sample, the RT results exclude diffusion as a likely mechanism for the interfacial FM. If the dip in the RT nuclear SLD is instead attributed to a native oxide layer rather than a low density Ni layer, this would also not account for the interfacial FM region as FeRh samples capped with a native oxide do not show interfacial FeRh.[331] As with the diffusion mechanism, the HT sample does not show this dip in SLD. Therefore, this oxide layer can also be excluded as a mechanism for the interfacial FM phase. With the similarity between the interfacial FM phase in the RT and HT samples, it seems unlikely for diffusion or native oxide layer to be potential causes. The other major proposed mechanism is strain, which seems more in line with the results presented here.

As will be discussed in more detail in Section 6.8, the strain state at the interface is rather complex. There is a large mismatch between the FeRh/Ni lattices, leading to a large ($> 10\%$) strain, and subsequently misfit dislocations can be expected within the first nm or so. Above this critical thickness, there will be a nontrivial depth dependence of the strain as the film attempts to relax. It seems plausible that both samples have large strains and attempt to relax to the extent possible for their varying interface and texture. Unfortunately, the techniques used in this work don't allow us to directly distinguish such a strained layer directly, and the depth dependence of such a relaxed layer is impossible to predict a priori. But such a mechanism would explain the similar thickness of the interfacial layer, as well as the differences in stabilization of the interfacial FM phase.

6.8 Estimation of Magnetoelastic Strain Anisotropy

In order to gain some understanding of the potential mechanism causing the difference between the RT and HT coercivity, a direct estimate of strain anisotropy field can be made. This is particularly insightful in light of the different Ni orientations as confirmed by XRD, since different Ni orientations will have different magnetocrystalline contributions as well as potentially differences in how they interact to the same applied strain. We begin by writing down all the potential contributions to the free energy[301]

$$\mathrm{E_{tot}} = \mathrm{E_{zeeman}} + \mathrm{E_{demag}} + \mathrm{E_{exchange}} + \mathrm{E_{MC}} + \mathrm{E_{ME}} \tag{5.1}$$

Here, $\mathrm{E_{tot}}$ represents the total free energy, and from left to right on the RHS, contributions come from the Zeeman interaction with an applied field, the demagnetization field of the sample, the exchange interaction between neighboring spins, a magnetocrystalline term, and a magnetoelastic term. The first three terms, which do not depend directly on strain or crystal orientation to a very good approximation, can be condensed into a single term as $\mathrm{E_0}$, which is the energy required to saturate the magnetization along some direction with zero applied strain.[337,338] The free energy becomes

$$\mathrm{E_{tot}} = \mathrm{E_0} + \mathrm{E_{MC}} + \mathrm{E_{ME}} \tag{5.2}$$

$\mathrm{E_{tot}}$ and $\mathrm{E_0}$ can be approximately related to the magnetic field required for saturation as

$$\mathrm{E_{tot}} = \frac{1}{2}\mathrm{H_a M_S} \quad , \quad \mathrm{E_0} = \frac{1}{2}\mathrm{H_0 M_S} \tag{5.3}$$

Where $\mathrm{M_S}$ is the saturation magnetization, $\mathrm{H_0}$ is the field required to saturate the magnetization for an unstrained film, and $\mathrm{H_a}$ is the anisotropy field along the hard axis direction. We now turn our eye to the magnetocrystalline energy $\mathrm{E_{MC}}$, which in general can be expanded in terms of the direction cosines α_i as[223,339]

$$E_{MC}(\vec{m}) = b_0(H_M) + \sum_{i,j} b_{ij}(H_M)\alpha_i\alpha_j + \sum_{i,j,k,l} b_{ijkl}(H_M)\alpha_i\alpha_j\alpha_k\alpha_l \qquad 5.4$$

Where H_M is the magnitude of the applied field along the direction of the magnetization, $\vec{m}$. The coefficients $b_0, b_{i,j}, b_{i,j,k,l}$ will be defined momentarily, when we recast this into the more familiar form. In the above expression, only terms even in $\vec{m}$ need be retained, in order to obey time reversal symmetry. For a system with cubic symmetry, the magnetocrystalline energy can be represented to lowest order in the direction cosines α_i as

$$E_{MC} = K_1(\alpha_1^2 + \alpha_2^2 + \alpha_3^2) + K_2(\alpha_1^2\alpha_2^2\alpha_3^2) \qquad 5.5$$

Where the K_i are the typical anisotropy constants. For Ni, $K_1 = -5480 \frac{J}{m^3}$ and $K_2 = -2.47 \frac{J}{m^3}$.[339] Higher orders in the expansion can be neglected, as the series is quickly convergent. For example, K_3 is already an order of magnitude smaller than K_1,K_2. Because we're only concerned with differences in energy, the constant term (0^{th} order) has been neglected. For the RT sample, which is oriented with the (001) out-of-plane, this yields the well-known differences in anisotropy energy for different magnetization orientations, $E_{mc}^{110} - E_{mc}^{100} = \frac{K_1}{4} = -1370 \frac{J}{m^3}$, $E_{mc}^{111} - E_{mc}^{100} = \frac{K_1}{3} + \frac{K_2}{27} = -1920 \frac{J}{m^3}$, etc. Here, the hkl superscript represents the direction of the magnetization in the crystal frame. A similar calculation can be made for the HT sample, with an appropriate transformation from the lab frame to the crystal frame and vice versa.[340] The appropriate 3x3 rotation matrix $\bar{a}$ to transform from the lab frame to the crystal frame is

$$\bar{a} = \begin{bmatrix} 1 & 0 & 0 \\ 0 & \frac{1}{\sqrt{2}} & \frac{1}{\sqrt{2}} \\ 0 & \frac{-1}{\sqrt{2}} & \frac{1}{\sqrt{2}} \end{bmatrix} \qquad 5.6$$

$\bar{\text{a}}$ thus transforms us from a frame where the (001) is in the +z direction, to one with the (022) of the crystal along the +z direction. Transforming back from the crystal frame to the lab frame can be accomplished by applying the inverse (transpose) of $\bar{\text{a}}$, $\bar{\text{a}}^{\text{T}}$. One useful case is the energy difference $\text{E}_{\text{mc}}^{\sqrt{2}11} - \text{E}_{\text{mc}}^{100} = -2817\frac{\text{J}}{\text{m}^3}$. These coordinates would correspond to rotating the magnetization from the 100 to the 110, or an in-plane rotation of the magnetization in the lab frame while the Ni film is oriented such that the (011) is in the (001) or out-of-plane direction in the lab frame. We can estimate the effective fields H_{eff} from

$$\text{E}_{\text{MC}} = \frac{1}{2}\text{H}_{\text{eff}}\text{M}_{\text{S}} \qquad 5.7$$

Which yields roughly $\text{H}_{\text{eff}} \cong 5.7$ mT for the RT sample, and $\text{H}_{\text{eff}} \cong 11.7$ mT for the HT. While these effective fields aren't trivial, it's immediately clear that the difference in magnetocrystalline anisotropy alone can only contribute roughly a 6 mT difference in effective field or $\cong 30\%$ of the observed effect.

We now turn our eyes to the magnetoelastic contribution to the free energy E_{ME}. In order to quantitatively calculate a value for E_{ME}, a measure of the strain or stress applied to the Ni layer is required. One way to obtain a bulk measurement of the stress is via XRD, as in Figure 81. Application of Bragg's Law $2\text{d}\sin(\theta) = \lambda$, when solved for the lattice spacing d of a desired lattice plane, can be compared to bulk values of unstrained Ni. The strain in the out-of-plane direction is defined to be

$$\epsilon_{\text{zz}} = \frac{\text{d}_{\text{film}} - \text{d}_{\text{bulk}}}{\text{d}_{\text{bulk}}} \qquad 5.8$$

Beginning with the RT sample and a lattice parameter $\text{a} = 3.5238$ Å for unstrained fcc Ni, the XRD reveals a compressive strain $\epsilon_{\text{zz}} = -0.24\%$. From this, we can obtain the values for in-plane strain by minimizing the elastic and magnetoelastic free energies simultaneously. The elastic free energy, is given in Einstein notation by[223,339,340]

$$E_{el} = \frac{1}{2} c_{ijkl} \epsilon_{ij} \epsilon_{kl} \tag{5.9}$$

Where c_{ijkl} is a stiffness matrix, subject to cubic symmetry

$$c_{ij} = \begin{matrix} c_{11} & c_{12} & c_{12} & 0 & 0 & 0 \\ c_{12} & c_{11} & c_{12} & 0 & 0 & 0 \\ c_{12} & c_{12} & c_{11} & 0 & 0 & 0 \\ 0 & 0 & 0 & c_{44} & 0 & 0 \\ 0 & 0 & 0 & 0 & c_{44} & 0 \\ 0 & 0 & 0 & 0 & 0 & c_{44} \end{matrix} \tag{5.10}$$

c_{ij} are the stiffness constants of Ni. $c_{11} = 2.5 \times 10^{11} \frac{J}{m^3}$, $c_{12} = 1.6 \times 10^{11} \frac{J}{m^3}$, $c_{44} = 1.185 \times 10^{11} \frac{J}{m^3}$. The ϵ_{ij} are the symmetric strain tensors. The elastic free energy, simplified, is (in Voigt notation)

$$E_{EL} = \frac{1}{2} c_{11} (\epsilon_1^2 + \epsilon_2^2 + \epsilon_3^2) + \frac{1}{2} c_{44} (\epsilon_4^2 + \epsilon_5^2 + \epsilon_6^2) + c_{12} (\epsilon_1 \epsilon_2 + \epsilon_2 \epsilon_3 + \epsilon_1 \epsilon_3) \tag{5.11}$$

We now turn to the magnetoelastic free energy, which can be written for a cubic crystal as

$$E_{ME} = B_1 (\alpha_1^2 \epsilon_1 + \alpha_2^2 \epsilon_2 + \alpha_3^2 \epsilon_3) + B_2 (\alpha_1 \alpha_2 \epsilon_6 + \alpha_2 \alpha_3 \epsilon_4 + \alpha_1 \alpha_3 \epsilon_5) \tag{5.12}$$

Where B_i are magnetoelastic coupling coefficients. For Ni, $B_1 = 6.2 \times 10^6 \frac{J}{m^3}$ and $B_1 = 9 \times 10^6 \frac{J}{m^3}$. Minimizing the sum $E_{EL} + E_{ME}$ with respect to ϵ_3, assuming negligible shear strains, i.e. $\epsilon_4 = \epsilon_5 = \epsilon_6 = 0$, and allowing the out-of-plane strain free to relax (or stress $\sigma_z = 0$) yields

$$\frac{\mathrm{E_{EL}} + \mathrm{E_{ME}}}{\partial \epsilon_3} = c_{11}\epsilon_3 + c_{12}(\epsilon_1 + \epsilon_2) + \mathrm{B}_1\alpha_3^2 = 0 \qquad 5.13$$

Or

$$\epsilon_3 = -\frac{\mathrm{B}_1\alpha_3^2 + c_{12}(\epsilon_1 + \epsilon_2)}{c_{11}} \qquad 5.14$$

Thus, minimizing both terms leads to a minor ($O(10^{-5})$) correction to the result obtained if we had simply minimized the elastic energy

$$\epsilon_3^{\mathrm{uncorrected}} = \frac{-c_{12}}{c_{11}}(\epsilon_2 + \epsilon_1) = \frac{-\nu}{1-\nu}(\epsilon_2 + \epsilon_1) \qquad 5.15$$

Where ν is Poisson's Ratio, which for Ni $\nu \cong 0.33$. For the FeRh structural change, both in-plane strains will be equal by symmetry and we obtain strains $\epsilon_1 = \epsilon_2 = 0.25$ %. Despite the only minor correction to ϵ_3, there is a large effect to the free energy. Substituting our expression for ϵ_3 into the expressions for $\mathrm{E_{ME}}$ and $\mathrm{E_{EL}}$ yields

$$\mathrm{E_{EL+ME}} = -\left[\frac{\mathrm{B}_1 c_{12}(\epsilon_1 + \epsilon_2)}{c_{11}} + \mathrm{B}_1\epsilon_1\right]\alpha_3^2 - \frac{\mathrm{B}_1^2\alpha_3^4}{2c_{11}} + \mathrm{B}_1\alpha_2^2(\epsilon_2 - \epsilon_1) \qquad 5.16$$

A similar result ($\mathrm{E_{EL+ME}} = \mathrm{B}_1\alpha_2^2(\epsilon_1 - \epsilon_2)$) is obtained if we had used $\epsilon_3^{\mathrm{uncorrected}}$. In order to compare to our magnetic results, we're interested in the in-plane contributions, so taking $\alpha_3 = 0$, we're left with

$$\mathrm{E_{EL+ME}} = \mathrm{B}_1\alpha_2^2(\epsilon_2 - \epsilon_1) \qquad 5.17$$

Which if the in-plane strains are equal as expected for the FeRh transition implies that there is no in-plane magnetoelastic anisotropy. Therefore, in the RT samples there is no effect for in-plane magnetizations due to the magnetoelastic effects, despite a rather large measured strain.

There is however a large out of plane anisotropy (effective fields $\cong 1.2 - 1.47$ T for the uncorrected and corrected ϵ_3's respectively).

We now need to make the analogous calculation for the HT sample. A first step is to estimate ϵ_{zz} from XRD using Eq 5.8, which reveals an out-of-plane compression $\epsilon_{zz} = -0.004575\%$. The next step is to apply Eq's 5.11 and 5.12, but with the appropriate coordinate transformations. The α_i's can be transformed as discussed previously. The strain is a tensor quantity and can be transformed via $\epsilon' = \bar{a}^T \epsilon \bar{a}$, where ϵ' is the strain in the crystal reference frame, and $\bar{a}$ the same rotation matrix as previously.[340] Again, we take the shear strains in the lab frame to be $\epsilon_4 = \epsilon_5 = \epsilon_6 = 0$. This yields a strain in the crystal coordinates

$$\epsilon' = \begin{bmatrix} \epsilon_1 & 0 & 0 \\ 0 & \frac{1}{2}(\epsilon_2 + \epsilon_3) & \frac{1}{2}(\epsilon_2 - \epsilon_3) \\ 0 & \frac{1}{2}(\epsilon_2 - \epsilon_3) & \frac{1}{2}(\epsilon_2 + \epsilon_3) \end{bmatrix}$$

ϵ' can be directly inserted into Eq's 5.11 and 5.12. Minimizing the energy with respect to ϵ_3 yields an expression in terms of the in-plane strains ϵ_1 and ϵ_2

$$\epsilon_3 = \frac{-(B_1\alpha_3^2 + 2B_1\alpha_3\alpha_2 + B_1\alpha_2^2)}{c_{11} + c_{12} + 2c_{44}} + \frac{(-c_{11} - c_{12} + 2c_{44})\epsilon_1 - c_{12}\epsilon_2}{c_{11} + c_{12} + 2c_{44}}$$

Again, the corrections due to the magnetoelastic coupling are negligibly small, of $O(10^{-5})$, but the free energy will be considerably more complicated. The in-plane strains can be estimated $\epsilon_1 = \epsilon_2 = 0.0046\%$. The free energy is

$$E_{ME} = \frac{(-B_1^2\alpha_1^4 + 4B_1B_2\alpha_1^2\alpha_3\alpha_2 - 4B_2^2\alpha_3^2\alpha_2^2)}{4(c_{11} + c_{12} + 2c_{44})} + \frac{(2B_1^2\alpha_1^2 - 4B_1B_2\alpha_3\alpha_2 - 8B_1c_{44}\epsilon_1\alpha_1^2)}{4(c_{11} + c_{12} + 2c_{44})}$$

$$+ \frac{(4B_1\epsilon_2c_{12}\alpha_1^2)}{4(c_{11} + c_{12} + 2c_{44})} + B_1\epsilon_2\alpha_1^2$$

Where we've kept terms to first order in the strain, and higher order terms in the direction cosines. It is immediately obvious that this version of the free energy is quite different from the $E_{EL+ME} = B_1(\epsilon_1 - \epsilon_2)$ term earlier, although the dominant terms are $O(B_i\epsilon_i)$ for reasonable strains. Again, it is fruitful to consider $E_{ME}^{\sqrt{2}11} - E_{ME}^{100} = -412\,\frac{J}{m^3}$, which yields an effective field $H_{eff} \cong 1.8$ mT. While a nontrivial effect, it's still an order of magnitude too small to explain the observed difference between the RT and HT samples.

While the above analysis would seem indicate that direct magnetoelastic anisotropy is likely not the cause of the difference between RT and HT FeRh/Ni bilayers, the above analysis comes with a number of limitations and caveats. Foremost is that these energy calculations only capture direct magnetoelastic anisotropy and cannot account for other magnetoelastic effects such as domain wall pinning at boundaries. There are also significant instrumental limitations, even with regards to the direct magnetoelastic anisotropy estimation. While XRD is a valid technique to extract ϵ_3, full residual strain analysis often requires a rather precise alignment process. In this work, we attempt to correct for slight alignment differences in the sample by correcting the MgO XRD peaks to their theoretical values. However residual strain analysis often requires multiple system specific measurements to reduce the systematic error, and simply correcting to the MgO is insufficient. In particular, the problem is that for a strained film, the Bragg Condition will in general only be satisfied for some subset of grains with the proper hkl, giving a biased sampling to the specular measurement. This can be rectified but requires off axis measurements that were outside the scope of the requested time allotted for the experiment. This uncertainty in 2θ and thus ϵ_3 can be roughly quantified by performing the same calculation for the FeRh (001) peaks. The measurements show $\epsilon_3 = 0.23\%$ for the RT sample and $\epsilon_3 = 0.398\%$ for the HT sample. While these values are roughly what is expected ($\epsilon_3 = 0.33\%$) and has been measured for FeRh on MgO substrate, there is still a significant variation both between the RT and HT, and between our values compared to literature values. It is not clear why there should be any variation between the RT and HT samples, so this difference likely points rather to the imprecision of the probe. The FeRh SPT is expected to cause a strain of $\cong 0.3\%$, so error on the order of $\cong 0.1\%$ would be more than enough to skew any estimations. It is thus worthwhile to note that the limiting factor in our estimation of the magnetoelastic energy in the HT film is inherently limited by the strain value $\epsilon_{zz} = -0.004575\%$, which essentially corresponds to a seemingly relaxed film, and is two orders of magnitude smaller than the FeRh SPT strain value. Repeating the above calculation for an expected $\epsilon_{zz} = -0.3\%$ from the FeRh SPT shows that even a partial transfer of only $10\% - 15\%$ of the FeRh SPT would be allow sufficiently large effective fields to explain the difference between the RT and HT samples. Even with stress relaxation at grain boundaries, this is a reasonable expected strain transfer. It is also well within the expected error from the probe.

The above discussion is further complicated by the fact that Ni does not have an epitaxial relation to the FeRh lattice for the 001 and 011 orientations seen in the RT and HT samples respectively. Both suffer large lattice mismatches, $> 10\%$. In cases where the lattice mismatch is poor, it has been observed that the first few monolayers will follow the epitaxial relationship, and after some critical thickness $\mathrm{d_c}$ will form misfit dislocations to relieve the incredibly large strain.

Above this critical thickness, the films will develop some nontrivial depth dependent strain that isn't easily predicted a priori. The critical thickness can be estimated as

$$d_c = \frac{a_{exp}}{2f_0}$$

Where a_{exp} is the experimentally measured lattice parameter, and f_0 the lattice mismatch. An estimate of d_c for both samples yields $d_c \cong 1$ nm. Therefore, we can expect the Ni layer to have misfit dislocations throughout the film. In Fe films grown on W substrate, which correspond to an approximately 10% lattice mismatch, it was found that the first 1.2 monolayers of Fe matched the W substrate, and subsequent Fe layers were nearly relaxed.[340] These Fe ultrathin films saw heavily modified magnetic properties due to these two different layers interacting, but they were limited to only 10 ML in total thickness. This comparison would seem to compare favorably to our toy model of Ni depositing relaxed on FeRh, and being strained due to the FeRh SPT.

We conclude that the strain of the FeRh SPT is a plausible mechanism for the difference between RT and HT samples, but further measurements are needed in order to pin down the exact structural relationship at the interface. A technique such as temperature dependent TEM would shed additional light to the strain dynamics at the FeRh/Ni interface. Other potential magnetoelastic mechanisms include domain wall pinning on stress defects such as grain boundaries or misfit dislocations. Magnetic coupling to the remanent interfacial FM FeRh phase or the AF phase are also plausible mechanisms.

6.9 Conclusions

In this chapter, we show a method for growing high quality FeRh films on MgO substrate via magnetron sputtering. The deposition and annealing temperatures allow for significant control in tuning the film quality in order to optimize the FeRh MSPT. The film's structural(chemical) and magnetic quality was confirmed via XRD, AFM, and VSM. Once the film quality was confirmed, depositing another FM material onto the FeRh above and below its T_c enables the MSPT to directly modify the magnetic properties of the FeRh/FM bilayer. In particular, this is likely driven partially by magnetoelastic effects, rather than simple magnetic coupling. Samples with Ni deposited below T_c display a low coercivity at low temperature due to their relaxation after their RT deposition, a spike in the coercivity during the transition due to phase coexistence, and then a low but modified coercivity of the combined FM FeRh and Ni. In contrast, samples with the Ni deposited above T_c show a 18.4 mT (179%) higher coercivity at low temperature, likely due to the strain state induced by the FeRh SPT after the Ni deposits relaxed at HT. Across the FeRh transition, it also exhibits a spike in the coercivity, and above T_c a low coercivity similar to that seen in the RT sample, driven by the FM FeRh phase. XRR, PNR and VSM show that the samples are essentially identical in the bulk but vary at the interface, as well as what orientation of Ni is energetically favorable. These interfacial differences can be expected to play a critical role due to the fact that the FeRh/Ni strain interaction is solely an interfacial effect. We also confirmed that these effects are broadly reproducible between samples.

After establishing that the deposition above or below T_c can influence the magnetic properties in our bilayers, we also have a novel route to weigh in on the controversy of the mechanism behind interfacial FM seen in FeRh bilayers. The similar interfacial FM seen in both RT and HT samples points towards a common mechanism. The structural differences between the RT and HT samples seems to indicate that strain is a more likely mechanism for interfacial FM FeRh phase, rather than diffusion.

We then attempt to estimate the theoretical contribution of magnetoelastic anisotropy, as well as the contribution of different magnetocrystalline energies due to stabilization of different Ni orientations in the RT and HT samples. Magnetocrystalline anisotropy from the Ni (002) texture seen in the RT sample as compared to the Ni (022) in the HT sample can only at most account for 30% of the difference measured. Magnetoelastic calculations show that while the FeRh SPT can theoretically account for the coercivity difference between RT and HT samples, the measured strains are too small. This calculation comes with the caveat that the strain measurement is relatively imprecise, limiting the inference that can be drawn from the calculation. Other mechanisms such as domain wall pinning in strain defects such as misfit dislocations, or some type of magnetic coupling are also plausible contributions.

Chapter 7. Summary and Outlook

In summary, this work sought to explore the magnetic properties of magnetic heterostructures consisting of a phase transition material and ferromagnet (FM). Towards that effort, we presented on magnetic bilayers utilizing two canonical phase transition materials, VO_2/Ni and FeRh/Ni. In the VO_2/Ni system, prior work had shown that strain at the interface allowed for the Ni magnetic properties to couple to the VO_2 structural phase transition (SPT) via magnetoelastic coupling.[296] In this work, the first goal was to explore this magnetoelastic coupling by tuning the underlying VO_2, which was accomplished by tuning of the interface, choice of substrate, and growth parameters. The second goal was to extend this concept to a new system in FeRh/Ni, which would allow for magnetic coupling to compete with the structural coupling of an SPT. Adding this additional degree of freedom is a natural synthesis of the prior work on VO_2/Ni and the work by Thiele et al. exploring the magnetic coupling in FeRh/FePt across the FeRh magnetostructural phase transition (MSPT).[199]

Due to the sensitive nature of these phase transition materials Chapter 3 focused exclusively on tuning VO_2 film morphology. While there is an extensive literature on growth conditions, the sensitivity of VO_2 and choice of synthesis techniques leads to a rich parameter space with very different film properties. The literature is further fragmented with studies interested in different VO_2 properties such as the optical properties or the temperature coefficient of resistance rather than the morphology and quality of the SPT. Explicitly using temperature and O_2 flow rate to explore the T vs O_2 phase diagram suitable for high quality VO_2 is relatively underexplored. By varying deposition temperature and O_2 flow rate inversely, we show that one can achieve a high degree of control over the film morphology while simultaneously maintaining all or most of the 4 orders of magnitude VO_2 metal to insulator transition (MIT). The choice of substrate allowed another parameter in tuning the VO_2 MIT features and morphological properties due to the varying epitaxial relationship between VO_2 and the substrate. In cases of deposition temperatures of 625 K or higher, films reproducibly showed a full 5 orders of magnitude MIT rather than the more standard 4 orders seen in most thin films.

After optimizing the VO_2 layer, VO_2/Ni bilayers were fabricated to explore the effect of the VO_2 SPT in VO_2/Ni bilayers. The films were deposited using magnetron sputtering and structurally characterized via atomic force microscopy (AFM) and X-ray Diffraction (XRD). The bilayers show changes in the coercivity and magnetization as functions of temperature at the critical temperature (T_c) of the VO_2 due to inverse magnetostrictive effects. The first set of samples considered were deposited in the 'HT' configuration, with the Ni deposition above the critical temperature of the VO_2 (SPT). These samples all show a coercivity enhancement of around 4.8 mT (37.8%) below the T_c of the underlying VO_2 and a low coercivity above T_c. This coercivity profile corresponds to the Ni being relaxed when the VO_2 is rutile as it was during the initial Ni deposition and becoming strained as the VO_2 crosses the SPT with decreasing temperature. The strain imparted to the Ni at the VO_2:Ni interface is estimated to be around 22 MPa of the 380 MPa VO_2 SPT by comparing this enhanced coercivity relative to the unstrained temperature trend. The choice of substrate can effectively tune this coercivity vs temperature profile by tuning the underlying VO_2 SPT thermal hysteresis width and T_c. Choice of substrate also leads to different Ni morphology, which also influences the coercivity vs temperature profile. Samples on TiO_2 (101) substrate with large uniform Ni grains show a sharp 6.2 mT (73%) coercivity enhancement when the temperature is close to T_c due to the phase coexistence of the underlying VO_2. c-cut and r-cut Al_2O_3 samples with smaller grains show this phase coexistence enhancement reduced or completely suppressed. Magnetization as a function of temperature also shows a sharp increase that begins at T_c with increasing temperature, consistent with an inverse magnetostrictive effect due to compressive stress from the VO_2 SPT.

The Ni deposition temperature can also be used as an additional lever for control of the magnetic properties in VO_2/Ni bilayers. For 'HT' samples Ni was deposited above T_c onto rutile VO_2. By contrast, 'RT' samples had Ni deposited below T_c and therefore onto monoclinic VO_2. RT samples show the opposite magnetic behavior as compared to the HT case, with a low coercivity below T_c and a 0.626 mT (17%) coercivity enhancement above T_c. The Ni is relaxed at low temperature when VO_2 is monoclinic as it was during the initial Ni deposition and becomes strained when the VO_2 transitions to the rutile phase. RT samples also show sharply localized coercivity enhancement close to T_c due to phase coexistence of the VO_2. The magnetization as a function of temperature profile is also reversed, with RT samples showing a sharp decrease at T_c in contrast to the HT samples' increase. As with the HT samples, choice of substrate allows for tunability in the magnetic properties via tuning of the underlying VO_2.

While the HT films show reversibility in their magnetic properties over multiple cycles, RT films displayed irreversible changes in both the coercivity and magnetization as functions of temperature after the first heating across the VO_2 SPT. A similar irreversibility was observed in the R vs. T of bare VO_2 films, with a 27.7% increase in resistance below T_c after the first heating cycle. A plausible cause for both irreversibility in the magnetic properties of the bilayers and resistivity of the bare VO_2 was proposed, that cracks might form to relieve the internal strains of the VO_2 SPT. Cracking across the SPT is commonly seen in VO_2 single crystals and has been previously observed in thin films, although the data is more limited. Attempts to directly image cracking via AFM were unsuccessful, possibly due to instrumental limitations or stress relaxation at grain boundaries. However, theoretical modeling of the VO_2 MIT via a random resistor network model showed that cracks could plausibly cause the changes in the R vs. T properties.

Lastly, the SPT/FM magnetic bilayer concept was extended to a new system, substituting FeRh for the VO_2 layer. FeRh has an SPT in analogy with VO_2, but also introduces magnetic coupling due to the concurrent AF to FM transition of FeRh. Ni was magnetron sputtered on two nearly identical FeRh films in the RT and HT configurations respectively. The quality of the FeRh/Ni bilayers were extensively characterized via XRD, XRR, AFM, and magnetometry. XRD shows that RT films stabilize a (002) out of plane crystal orientation for the Ni, while HT samples suppress the (002) orientation in favor of the (022). As in the VO_2 case, below T_c the RT samples show a low coercivity due to relaxed Ni, with the HT samples showing a 18.4 mT (179%) higher coercivity due to strain imparted by the SPT. This is consistent with Ni being relaxed on the crystal lattice it is deposited on and becoming strained due to the lattice expansion (contraction) with increasing (decreasing) temperature across the SPT. Magnetocrystalline anisotropy energy calculations show that the different Ni orientation see between RT and HT samples can account for at most 30% of the difference in coercivities. Above T_c the FeRh transitions to the FM state, and dominates the bilayer coercive response and magnetization for both RT and HT samples. RT, HT and bare FeRh coercivities all show enhancement localized close to $T_{c,}$ likely due to phase coexistence of the FeRh. Polarized Neutron Reflectivity (PNR) was employed to investigate the structural and magnetic properties of the bilayers with the thickness dependence that was unavailable by magnetometry. The results confirm that the enhanced coercivity is due to the Ni layer, and not remanent FM FeRh phase. In addition, PNR along with XRR results confirm the high quality of the FeRh:Ni interface for both types of samples. Lastly, the PNR results offer a new perspective on the origin of the interfacial FM phase commonly seen in nominally AF FeRh films. Both RT and HT films showed this interfacial 2.9 nm thick FM layer. The similarity in RT and HT interfacial FM layers, constrained by consistency with the scattering length density (SLD) fits from PNR indicate that strain is a more likely mechanism rather than something like diffusion.

Following this work, there are still many open questions. Chapter 3 established that by inversely varying deposition temperature and O_2 flow rate, a high-quality MIT can be maintained while tuning the surface morphology of VO_2. However, it still needs to be established in a systematic way what effect this has on other material properties of VO_2, such as the optical properties. Tuning other deposition parameters such as pressure or substrate biasing in combination with the inverse tuning of T and O_2 flow rate should also be explored further. The so-called “melted” films are particularly interesting, with a firmly established reproducible 5 orders of magnitude MIT, since most works to date have only obtained a 4 orders of magnitude MIT for optimized films. High temperature (> 550 °C) depositions are relatively underexplored due to the desire for low temperature processing for industrial application but might offer superior material properties.

The results of Chapter 4 showed that the magnetic properties of VO_2/Ni bilayers could be tuned by controlling features such as the film morphology or substrate choice. Since the transfer of SPT strain is fundamentally an interfacial effect, nanostructured films or bulk composites that maximize the interface might hold promise for larger coupling or tunability.[27,341,342] The VO_2 SPT is also strongly anisotropic, which was realized in VO_2/Ni films on TiO_2 (101) substrates. Inducing magnetic anisotropy via an SPT strain in magnetic heterostructures should be explored further. Films that are more single crystalline in nature should show a stronger directional dependence.

The investigations into the irreversibility in Chapter 5 left a number of unresolved questions. Foremost, more work needs to be done to understand cracking in VO_2 films beyond simple robustness of the MIT. Commonly, bulk resistivity measurements are the sole confirmation of the robustness of VO_2 films. Additional studies of cracking of VO_2 films across the SPT via techniques such as TEM, in the vein of those performed by Jian et al., would shed light on how potential cracking or stress relaxation methods accommodate the SPT stress.[321] Choice of substrate or deposition conditions would provide the ability to tune film morphology and study the change in response. On the theoretical side, the resistor network model has been well established in capturing the VO_2 MIT. However, while the Preisach model is invaluable in phenomenologically capturing the thermal hysteresis, it would be preferable to capture the thermal hysteresis from first principles. A better understanding of how intergrain interactions lead to hysteresis is needed, particularly if it could be directly correlated to grain morphology or other film properties.

A synthesis of the work in Chapter 6 and the work by Thiele et al. on FeRh/FePt bilayers would be a bilayer using FeRh and a giant magnetostrictive material such as Terfenol-D.[199] In their work, they focused on the exchange coupling between the FeRh and FePt and showed a large coercivity change across the FeRh MSPT. This was justified, since the magnetostrictive coefficient for FePt is similar to Ni, at $\lambda \approx +34 \times 10^{-6}$ and therefore much smaller than the exchange and magnetocrystalline energies.[343] A material like Terfenol-D would maintain the large anisotropy as well as the exchange coupling across the FeRh MSPT. The orders of magnitude larger magnetostrictive coefficient could lead to magnetostrictive effective fields comparable to the magnetocrystalline anisotropy energy, allowing FeRh/Terfenol-D bilayers to leverage both aspects of the FeRh MSPT for applications such as heat assisted magnetic recording (HAMR).

There are a number of investigations that would be of benefit in both VO_2/Ni or FeRh/Ni systems, or SPT/FM bilayers in general. While this dissertation gave a first pass estimate for various magnetoelastic calculations such as the stress anisotropy field using established methods, there is a robust literature in modeling the magnetoelastic effect in a more detailed fashion. Although an exact theoretical framework is still very much in development, established working phenomenological models such as those developed by Jiles-Atherton-Sablik (J-A-S) have been shown to correctly predict a wide range of complex magnetoelastic phenomena including hysteresis loops and the Villari effect.[230] These models can be directly applied to SPT/FM heterostructures. Experimentally, imaging of the FM layer in-plane resolution via techniques such as magnetic force microscopy, XMCD, or neutron scattering would be informative for features such as the domain structure or directly measuring the effects of phase coexistence. While techniques such as PNR have allowed for depth dependent magnetic studies, to date there haven’t been any experiments that able to spatially map the magnetic layer in the lateral directions. Lastly, while VO_2 and FeRh are obvious candidates, there are a wide range of SPT materials to choose from which would offer more tunability in bilayer properties.

References

[1] J. Lauzier, L. Sutton, and J. De La Venta, J. Appl. Phys. **122**, 173902 (2017).

[2] J. Lauzier, L. Sutton, and J. de la Venta, J. Phys. Condens. Matter **30**, 374004 (2018).

[3] R.F. Need, J. Lauzier, L. Sutton, B.J. Kirby, and J. De La Venta, APL Mater. (2019).

[4] K. Liu, S. Lee, S. Yang, O. Delaire, and J. Wu, Mater. Today (2018).

[5] Z. Shao, X. Cao, H. Luo, and P. Jin, NPG Asia Mater. (2018).

[6] L.H. Lewis, C.H. Marrows, and S. Langridge, J. Phys. D. Appl. Phys. **49**, 323002 (2016).

[7] G.H. Jonker and J.H. Van Santen, Physica (1950).

[8] J.G. Bednorz and K.A. Müller, Zeitschrift Für Phys. B Condens. Matter (1986).

[9] J. Valasek, Phys. Rev. (1921).

[10] E. Salje and G. Hoppmann, Mater. Res. Bull. (1976).

[11] E.K.H. Salje, Annu. Rev. Mater. Res. (2012).

[12] D.I. Khomskii, J. Magn. Magn. Mater. **306**, 1 (2006).

[13] E.J.W. VERWEY, Nature **144**, 327 (1939).

[14] F.J. Morin, Phys. Rev. Lett. **3**, 34 (1959).

[15] M. Imada, A. Fujimori, and Y. Tokura, Rev. Mod. Phys. **70**, 1039 (1998).

[16] Pure Appl. Chem. **79**, 1383 (2007).

[17] A.E.B.T.-H. on the P. and C. of R.E. Clark, in *Alloy. Intermet.* (Elsevier, 1979), pp. 231–258.

[18] R. Kainuma, Y. Imano, W. Ito, Y. Sutou, H. Morito, S. Okamoto, O. Kitakami, K. Oikawa, A. Fujita, T. Kanomata, and K. Ishida, Nature **439**, 957 (2006).

[19] Z. Cai, B. Liu, X. Zou, and H.-M. Cheng, Chem. Rev. **118**, 6091 (2018).

[20] P.. Kelly and R.. Arnell, Vacuum **56**, 159 (2000).

[21] B.A. Joyce, Reports Prog. Phys. **48**, 1637 (1985).

[22] H.M. Christen and G. Eres, J. Phys. Condens. Matter **20**, 264005 (2008).

[23] J. Livage, M. Henry, and C. Sanchez, Prog. Solid State Chem. **18**, 259 (1988).

[24] H. Ohno, D. Chiba, F. Matsukura, T. Omiya, E. Abe, T. Dietl, Y. Ohno, and K. Ohtani, Nature **408**, 944 (2000).

[25] W.H. Meiklejohn and C.P. Bean, Phys. Rev. **105**, 904 (1957).

[26] M. Weiler, A. Brandlmaier, S. Geprägs, M. Althammer, M. Opel, C. Bihler, H. Huebl, M.S.

Brandt, R. Gross, and S.T.B. Goennenwein, New J. Phys. **11**, 013021 (2009).

[27] C.A.F. Vaz, J. Phys. Condens. Matter **24**, 333201 (2012).

[28] J.T. Heron, M. Trassin, K. Ashraf, M. Gajek, Q. He, S.Y. Yang, D.E. Nikonov, Y.-H. Chu, S. Salahuddin, and R. Ramesh, Phys. Rev. Lett. **107**, 217202 (2011).

[29] G. Binasch, P. Grünberg, F. Saurenbach, and W. Zinn, Phys. Rev. B **39**, 4828 (1989).

[30] J. Nogués and I.K. Schuller, J. Magn. Magn. Mater. **192**, 203 (1999).

[31] S.S.P. Parkin, N. More, and K.P. Roche, Phys. Rev. Lett. **64**, 2304 (1990).

[32] J. Wang, Annu. Rev. Mater. Res. (2019).

[33] W. Eerenstein, N.D. Mathur, and J.F. Scott, Nature **442**, 759 (2006).

[34] T. Saerbeck, J. de la Venta, S. Wang, J.G. Ramírez, M. Erekhinsky, I. Valmianski, and I.K. Schuller, J. Mater. Res. **29**, 2353 (2014).

[35] J.M. Hu, L.Q. Chen, and C.W. Nan, Adv. Mater. (2016).

[36] T. Taniyama, J. Phys. Condens. Matter (2015).

[37] M. Fiebig, J. Phys. D. Appl. Phys. (2005).

[38] H. Ohno, A. Shen, F. Matsukura, A. Oiwa, A. Endo, S. Katsumoto, and Y. Iye, Appl. Phys. Lett. (1996).

[39] J. Prokop, D.A. Valdaitsev, A. Kukunin, M. Pratzer, G. Schönhense, and H.J. Elmers, Phys. Rev. B **70**, 184423 (2004).

[40] M. Mathews, R. Jansen, G. Rijnders, J.C. Lodder, and D.H.A. Blank, Phys. Rev. B **80**, 64408 (2009).

[41] N.A. Pertsev, A.K. Tagantsev, and N. Setter, Phys. Rev. B **61**, R825 (2000).

[42] J.H. Lee, L. Fang, E. Vlahos, X. Ke, Y.W. Jung, L.F. Kourkoutis, J.-W. Kim, P.J. Ryan, T. Heeg, M. Roeckerath, V. Goian, M. Bernhagen, R. Uecker, P.C. Hammel, K.M. Rabe, S. Kamba, J. Schubert, J.W. Freeland, D.A. Muller, C.J. Fennie, P. Schiffer, V. Gopalan, E. Johnston-Halperin, and D.G. Schlom, Nature **466**, 954 (2010).

[43] G. Srinivasan, Annu. Rev. Mater. Res. **40**, 153 (2010).

[44] D.G. Schlom, L.Q. Chen, C.J. Fennie, V. Gopalan, D.A. Muller, X. Pan, R. Ramesh, and R. Uecker, MRS Bull. (2014).

[45] M.K. Lee, T.K. Nath, C.B. Eom, M.C. Smoak, and F. Tsui, Appl. Phys. Lett. (2000).

[46] W. Eerenstein, M. Wiora, J.L. Prieto, J.F. Scott, and N.D. Mathur, Nat. Mater. (2007).

[47] A. Brandlmaier, S. Geprägs, M. Weiler, A. Boger, M. Opel, H. Huebl, C. Bihler, M.S. Brandt, B. Botters, D. Grundler, R. Gross, and S.T.B. Goennenwein, Phys. Rev. B - Condens. Matter Mater. Phys. **77**, 104445 (2008).

[48] F. Motti, G. Vinai, A. Petrov, B.A. Davidson, B. Gobaut, A. Filippetti, G. Rossi, G.

Panaccione, and P. Torelli, Phys. Rev. B (2018).

[49] T.K. Chung, G.P. Carman, and K.P. Mohanchandra, Appl. Phys. Lett. (2008).

[50] E. De Ranieri, P.E. Roy, D. Fang, E.K. Vehsthedt, A.C. Irvine, D. Heiss, A. Casiraghi, R.P. Campion, B.L. Gallagher, T. Jungwirth, and J. Wunderlich, Nat. Mater. **12**, 808 (2013).

[51] N. Lei, T. Devolder, G. Agnus, P. Aubert, L. Daniel, J. Von Kim, W. Zhao, T. Trypiniotis, R.P. Cowburn, C. Chappert, D. Ravelosona, and P. Lecoeur, Nat. Commun. (2013).

[52] T.A. Ostler, R. Cuadrado, R.W. Chantrell, A.W. Rushforth, and S.A. Cavill, Phys. Rev. Lett. **115**, 67202 (2015).

[53] Q. Li, A. Tan, A. Scholl, A.T. Young, M. Yang, C. Hwang, A.T. N'Diaye, E. Arenholz, J. Li, and Z.Q. Qiu, Appl. Phys. Lett. (2017).

[54] G. Stefanovich, A. Pergament, and D. Stefanovich, J. Phys. Condens. Matter **12**, 8837 (2000).

[55] J.S. Kouvel, J. Appl. Phys. (1966).

[56] Fallot, M., Ann. Phys. **11**, 291 (1938).

[57] H.F. Kay and P. Vousden, London, Edinburgh, Dublin Philos. Mag. J. Sci. **40**, 1019 (1949).

[58] A. Cavalleri, C. Tóth, C.W. Siders, J.A. Squier, F. Ráksi, P. Forget, and J.C. Kieffer, Phys. Rev. Lett. **87**, 237401 (2001).

[59] J.-U. Thiele, M. Buess, and C.H. Back, Appl. Phys. Lett. (2004).

[60] J. Cao, E. Ertekin, V. Srinivasan, W. Fan, S. Huang, H. Zheng, J.W.L. Yim, D.R. Khanal, D.F. Ogletree, J.C. Grossman, and J. Wu, Nat. Nanotechnol. (2009).

[61] I. Suzuki, M. Itoh, and T. Taniyama, Appl. Phys. Lett. **104**, 022401 (2014).

[62] A. Alberca, N.M. Nemes, F.J. Mompean, N. Biskup, A. De Andres, C. Munuera, J. Tornos, C. Leon, A. Hernando, P. Ferrer, G.R. Castro, J. Santamaria, and M. Garcia-Hernandez, Phys. Rev. B - Condens. Matter Mater. Phys. (2011).

[63] H.F. Tian, T.L. Qu, L.B. Luo, J.J. Yang, S.M. Guo, H.Y. Zhang, Y.G. Zhao, and J.Q. Li, Appl. Phys. Lett. (2008).

[64] G. Venkataiah, Y. Shirahata, I. Suzuki, M. Itoh, and T. Taniyama, J. Appl. Phys. (2012).

[65] H. Zheng, J. Wang, S.E. Lofland, Z. Ma, L. Mohaddes-Ardabili, T. Zhao, L. Salamanca-Riba, S.R. Shinde, S.B. Ogale, F. Bai, D. Viehland, Y. Jia, D.G. Schlom, M. Wuttig, A. Roytburd, and R. Ramesh, Science (80-.). (2004).

[66] Y.P. Lee, S.Y. Park, Y.H. Hyun, J.B. Kim, V.G. Prokhorov, V.A. Komashko, and V.L. Svetchnikov, Phys. Rev. B (2006).

[67] M. Ziese, A. Bollero, I. Panagiotopoulos, and N. Moutis, Appl. Phys. Lett. (2006).

[68] G.E. Sterbinsky, B.W. Wessels, J.W. Kim, E. Karapetrova, P.J. Ryan, and D.J. Keavney, Appl. Phys. Lett. (2010).

[69] C.A.F. Vaz, J. Hoffman, A.-B. Posadas, and C.H. Ahn, Appl. Phys. Lett. (2009).

[70] D. Dale, A. Fleet, J.D. Brock, and Y. Suzuki, Appl. Phys. Lett. (2003).

[71] R.O. Cherifi, V. Ivanovskaya, L.C. Phillips, A. Zobelli, I.C. Infante, E. Jacquet, V. Garcia, S. Fusil, P.R. Briddon, N. Guiblin, A. Mougin, A.A. Ünal, F. Kronast, S. Valencia, B. Dkhil, A. Barthélémy, and M. Bibes, Nat. Mater. **13**, 345 (2014).

[72] J. Chen, J. Ma, Y. Zhang, S. Bao, L. Wu, C. Liu, and C.W. Nan, J. Appl. Phys. **121**, (2017).

[73] A. Pergament, G. Stefanovich, and A. Velichko, J. Sel. Top. Nano Electron. Comput. (2014).

[74] A.L. Pergament, G.B. Stefanovich, A.A. Velichko, and S.D. Khanin, Condens. Matter Lead. Edge 1 (2007).

[75] A. Magnéli, Acta Chem. Scand. **2**, 501 (1948).

[76] S. Andersson and L. Jahnberg, Ark. Kemi **21**, 1963 (n.d.).

[77] H.A. Wriedt, Bull. Alloy Phase Diagrams (1989).

[78] S. Kachi, K. Kosuge, and H. Okinaka, J. Solid State Chem. (1973).

[79] J.R. Gannon and R.J.D. Tilley, J. Solid State Chem. (1978).

[80] U. Schwingenschlögl and V. Eyert, Ann. Phys. **13**, 475 (2004).

[81] W. Rüdorff, G. Walter, and J. Stadler, Zeitschrift Für Anorg. Und Allg. Chemie **297**, 1 (1958).

[82] K. Kosuge, T. Takada, and S. Kachi, J. Phys. Soc. Japan **18**, 318 (1963).

[83] C.N. Berglund and H.J. Guggenheim, Phys. Rev. **185**, 1022 (1969).

[84] A.D. Wadsley, Acta Crystallogr. **10**, 261 (1957).

[85] Z. Yang, C. Ko, and S. Ramanathan, Annu. Rev. Mater. Res. (2011).

[86] C.H. Griffiths and H.K. Eastwood, J. Appl. Phys. (1974).

[87] D. Ruzmetov, G. Gopalakrishnan, C. Ko, V. Narayanamurti, and S. Ramanathan, J. Appl. Phys. (2010).

[88] H.T. Kim, B.J. Kim, S. Choi, B.G. Chae, Y.W. Lee, T. Driscoll, M.M. Qazilbash, and D.N. Basov, J. Appl. Phys. (2010).

[89] Y.W. Lee, B.J. Kim, J.W. Lim, S.J. Yun, S. Choi, B.G. Chae, G. Kim, and H.T. Kim, Appl. Phys. Lett. (2008).

[90] B.J. Kim, Y.W. Lee, B.G. Chae, S.J. Yun, S.Y. Oh, H.T. Kim, and Y.S. Lim, Appl. Phys. Lett. (2007).

[91] E. Strelcov, Y. Lilach, and A. Kolmakov, Nano Lett. (2009).

[92] J.M. Baik, M.H. Kim, C. Larson, C.T. Yavuz, G.D. Stucky, A.M. Wodtke, and M. Moskovits, Nano Lett. (2009).

[93] T. Driscoll, H.T. Kim, B.G. Chae, B.J. Kim, Y.W. Lee, N.M. Jokerst, S. Palit, D.R. Smith, M.

Di Ventra, and D.N. Basov, Science (80-.). (2009).

[94] M.J. Dicken, K. Aydin, I.M. Pryce, L.A. Sweatlock, E.M. Boyd, S. Walavalkar, J. Ma, and H.A. Atwater, Opt. Express (2009).

[95] T.C. Chang, X. Cao, S.H. Bao, S.D. Ji, H.J. Luo, and P. Jin, Adv. Manuf. (2018).

[96] G. Gopalakrishnan and S. Ramanathan, J. Mater. Sci. (2011).

[97] J. Mendialdua, R. Casanova A', and Y. Barbaux, *XPS Studies of V205, V6013 , VO 2 and V203* (1995).

[98] L.A. Ladd and W. Paul, Solid State Commun. (1969).

[99] C. Ko and S. Ramanathan, J. Appl. Phys. **104**, 086105 (2008).

[100] R.M. Briggs, I.M. Pryce, and H.A. Atwater, Opt. Express (2010).

[101] C.B. Greenberg, Thin Solid Films (1983).

[102] T. Kikuzuki and M. Lippmaa, Appl. Phys. Lett. (2010).

[103] M. Nakano, K. Shibuya, D. Okuyama, T. Hatano, S. Ono, M. Kawasaki, Y. Iwasa, and Y. Tokura, Nature (2012).

[104] R. Lopez, T.E. Haynes, L.A. Boatner, L.C. Feldman, and R.F. Haglund, Phys. Rev. B - Condens. Matter Mater. Phys. (2002).

[105] J.Y. Suh, R. Lopez, L.C. Feldman, and R.F. Haglund, J. Appl. Phys. (2004).

[106] D. Brassard, S. Fourmaux, M. Jean-Jacques, J.C. Kieffer, and M.A. El Khakani, Appl. Phys. Lett. (2005).

[107] J. Narayan and V.M. Bhosle, J. Appl. Phys. (2006).

[108] H. Wang, J. Jian, W. Zhang, C. Jacob, A. Chen, H. Wang, and J. Huang, Appl. Phys. Lett. (2015).

[109] M. Currie, V.D. Wheeler, B. Downey, N. Nepal, S.B. Qadri, J.A. Wollmershauser, J. Avila, and L. Nyakiti, Opt. Mater. Express (2019).

[110] J. Jeong, N. Aetukuri, T. Graf, T.D. Schladt, M.G. Samant, and S.S.P. Parkin, Science (80-.). **339**, 1402 LP (2013).

[111] M. Nygren and M. Israelsson, Mater. Res. Bull. (1969).

[112] P. Jin and S. Tanemura, Jpn. J. Appl. Phys. (1995).

[113] J.P. Pouget, H. Launois, T.M. Rice, P. Dernier, A. Gossard, G. Villeneuve, and P. Hagenmuller, Phys. Rev. B **10**, 1801 (1974).

[114] D. Kucharczyk and T. Niklewski, J. Appl. Crystallogr. (1979).

[115] G. Andersson, J. Paju, W. Lang, and W. Berndt, Acta Chem. Scand. (2008).

[116] V.M. Goldschmidt, T. Barth, D. Holmsen, G. Lunde, and W. Zachariasen, Skr. Nor.

Videnskaps-Akad. Oslo, Mat.-Nat. Kl. (1926).

[117] H.W. Verleur, A.S. Barker Jr., and C.N. Berglund, Phys. Rev. (1968).

[118] S. Shin, S. Suga, M. Taniguchi, M. Fujisawa, H. Kanzaki, A. Fujimori, H. Daimon, Y. Ueda, K. Kosuge, and S. Kachi, Phys. Rev. B (1990).

[119] P. Baum, D.-S. Yang, and A.H. Zewail, Science (80-.). **318**, 788 LP (2007).

[120] N.F. Mott, Rev. Mod. Phys. **40**, 677 (1968).

[121] T.M. Rice, H. Launois, and J.P. Pouget, Phys. Rev. Lett. (1994).

[122] R.E. Peierls, *Quantum Theory of Solids* (Oxford University Press, Oxford, 2001).

[123] G. Grüner, Rev. Mod. Phys. **60**, 1129 (1988).

[124] D. Paquet and P. Leroux-Hugon, Phys. Rev. B **22**, 5284 (1980).

[125] J. Shi, R. Bruinsma, and A.R. Bishop, Synth. Met. **43**, 3527 (1991).

[126] S. Biermann, A. Poteryaev, A.I. Lichtenstein, and A. Georges, Phys. Rev. Lett. **94**, 26404 (2005).

[127] J.B. Goodenough, Annu. Rev. Mater. Sci. **1**, 101 (1971).

[128] C.J. Hearn, J. Phys. C Solid State Phys. (1972).

[129] N.B. Aetukuri, A.X. Gray, M. Drouard, M. Cossale, L. Gao, A.H. Reid, R. Kukreja, H. Ohldag, C.A. Jenkins, E. Arenholz, K.P. Roche, H.A. Dürr, M.G. Samant, and S.S.P. Parkin, Nat. Phys. (2013).

[130] R.M. Wentzcovitch, W.W. Schulz, and P.B. Allen, Phys. Rev. Lett. **72**, 3389 (1994).

[131] A. Zylbersztejn and N.F. Mott, Phys. Rev. B **11**, 4383 (1975).

[132] J.P. Pouget, H. Launois, J.P. D'Haenens, P. Merenda, and T.M. Rice, Phys. Rev. Lett. (1975).

[133] J.P. D'Haenens, D. Kaplan, and P. Merenda, J. Phys. C Solid State Phys. (1975).

[134] T.J. Huffman, C. Hendriks, E.J. Walter, J. Yoon, H. Ju, R. Smith, G.L. Carr, H. Krakauer, and M.M. Qazilbash, Phys. Rev. B (2017).

[135] V. Eyert, Ann. Der Phys. (2002).

[136] V. Eyert, Phys. Rev. Lett. **107**, 16401 (2011).

[137] S. Xu, X. Shen, K.A. Hallman, R.F. Haglund, and S.T. Pantelides, Phys. Rev. B (2017).

[138] Y. Muraoka, K. Saeki, Y. Yao, T. Wakita, M. Hirai, T. Yokoya, R. Eguchi, and S. Shin, in *J. Electron Spectros. Relat. Phenomena* (2010).

[139] Y. Muraoka, H. Nagao, Y. Yao, T. Wakita, K. Terashima, T. Yokoya, H. Kumigashira, and M. Oshima, Sci. Rep. (2018).

[140] K. Hermann, A. Chakrabarti, A. Haras, M. Witko, and B. Tepper, Phys. Status Solidi Appl. Res. (2001).

[141] K. Miyano, T. Tanaka, Y. Tomioka, and Y. Tokura, Phys. Rev. Lett. (1997).

[142] M.F. Becker, A.B. Buckman, R.M. Walser, T. Lépine, P. Georges, and A. Brun, Appl. Phys. Lett. (1994).

[143] A. Cavalleri, T. Dekorsy, H.H.W. Chong, J.C. Kieffer, and R.W. Schoenlein, Phys. Rev. B - Condens. Matter Mater. Phys. (2004).

[144] H.T. Kim, Y.W. Lee, B.J. Kim, B.G. Chae, S.J. Yun, K.Y. Kang, K.J. Han, K.J. Yee, and Y.S. Lim, Phys. Rev. Lett. (2006).

[145] T. Yao, X. Zhang, Z. Sun, S. Liu, Y. Huang, Y. Xie, C. Wu, X. Yuan, W. Zhang, Z. Wu, G. Pan, F. Hu, L. Wu, Q. Liu, and S. Wei, Phys. Rev. Lett. **105**, 226405 (2010).

[146] M. Nakajima, N. Takubo, Z. Hiroi, Y. Ueda, and T. Suemoto, Appl. Phys. Lett. (2008).

[147] C. Kübler, H. Ehrke, R. Huber, R. Lopez, A. Halabica, R.F. Haglund, and A. Leitenstorfer, Phys. Rev. Lett. (2007).

[148] D. Wegkamp, M. Herzog, L. Xian, M. Gatti, P. Cudazzo, C.L. McGahan, R.E. Marvel, R.F. Haglund, A. Rubio, M. Wolf, and J. Stähler, Phys. Rev. Lett. **113**, 216401 (2014).

[149] V.R. Morrison, R.P. Chatelain, K.L. Tiwari, A. Hendaoui, A. Bruhács, M. Chaker, and B.J. Siwick, Science (80-.). **346**, 445 (2014).

[150] S. Lysenko, A.J. Rua, V. Vikhnin, J. Jimenez, F. Fernandez, and H. Liu, Appl. Surf. Sci. (2006).

[151] M. Hada, K. Okimura, and J. Matsuo, Phys. Rev. B - Condens. Matter Mater. Phys. (2010).

[152] J. Laverock, A.R.H. Preston, D. Newby, K.E. Smith, S. Sallis, L.F.J. Piper, S. Kittiwatanakul, J.W. Lu, S.A. Wolf, M. Leandersson, and T. Balasubramanian, Phys. Rev. B **86**, 195124 (2012).

[153] M. Fallot and R. Hocart, Rev. Sci **77**, 498 (1939).

[154] E.F. Bertaut, A. Delapalme, F. Forrat, G. Roult, F. De Bergevin, and R. Pauthenet, J. Appl. Phys. (1962).

[155] J.S. Kouvel and C.C. Hartelius, J. Appl. Phys. (1962).

[156] F. De Bergevin and L. Muldawer, Comptes Rendus l'Academie Des Sci. **252**, 1347 (1961).

[157] A.I. Zakharov, A.M. Kadomtseva, R.Z. Levitin, and E.G. Ponyatovskii, J. Exp. Theor. Phys. **46**, 1348 (1964).

[158] G. Shirane, C.W. Chen, P.A. Flinn, and R. Nathans, J. Appl. Phys. (1963).

[159] V.L. Moruzzi and P.M. Marcus, Phys. Rev. B (1992).

[160] U. Aschauer, R. Braddell, S.A. Brechbühl, P.M. Derlet, and N.A. Spaldin, Phys. Rev. B **94**, (2016).

[161] L.J. Swartzendruber, Bull. Alloy Phase Diagrams **5**, 456 (1984).

[162] M.J. Richardson, D. Melville, and J.A. Ricodeau, Phys. Lett. A (1973).

[163] D.W. Cooke, F. Hellman, C. Baldasseroni, C. Bordel, S. Moyerman, and E.E. Fullerton, Phys. Rev. Lett. (2012).

[164] J.A. Ricodeau and D. Melville, J. Phys. F Met. Phys. (1972).

[165] C. Kittel, Phys. Rev. (1960).

[166] J.B. McKinnon and E.W. Lee, J. Phys. C Solid State Phys. (1970).

[167] C. Koenig, J. Phys. F Met. Phys. (1982).

[168] J.S. Lee, E. Vescovo, L. Plucinski, C.M. Schneider, and C.C. Kao, Phys. Rev. B - Condens. Matter Mater. Phys. (2010).

[169] A.X. Gray, D.W. Cooke, P. Krüger, C. Bordel, A.M. Kaiser, S. Moyerman, E.E. Fullerton, S. Ueda, Y. Yamashita, A. Gloskovskii, C.M. Schneider, W. Drube, K. Kobayashi, F. Hellman, and C.S. Fadley, Phys. Rev. Lett. (2012).

[170] F. Pressacco, V. Uhlíř, M. Gatti, A. Nicolaou, A. Bendounan, J.A. Arregi, S.K.K. Patel, E.E. Fullerton, D. Krizmancic, and F. Sirotti, Struct. Dyn. (2018).

[171] P. Tu, A.J. Heeger, J.S. Kouvel, and J.B. Comly, J. Appl. Phys. (1969).

[172] M.E. Gruner, E. Hoffmann, and P. Entel, Phys. Rev. B - Condens. Matter Mater. Phys. (2003).

[173] O.N. Mryasov, in *Phase Transitions* (2005).

[174] J. Barker and R.W. Chantrell, Phys. Rev. B - Condens. Matter Mater. Phys. (2015).

[175] G. Ju, J. Hohlfeld, B. Bergman, R.J.M. van de Veerdonk, O.N. Mryasov, J.-Y. Kim, X. Wu, D. Weller, and B. Koopmans, Phys. Rev. Lett. (2004).

[176] B. Bergman, G. Ju, J. Hohlfeld, R.J.M. Van De Veerdonk, J.Y. Kim, X. Wu, D. Weller, and B. Koopmans, Phys. Rev. B - Condens. Matter Mater. Phys. (2006).

[177] I. Radu, C. Stamm, N. Pontius, T. Kachel, P. Ramm, J.U. Thiele, H.A. Dürr, and C.H. Back, Phys. Rev. B - Condens. Matter Mater. Phys. (2010).

[178] C. Stamm, J.U. Thiele, T. Kachel, I. Radu, P. Ramm, M. Kosuth, J. Minár, H. Ebert, H.A. Dürr, W. Eberhardt, and C.H. Back, Phys. Rev. B - Condens. Matter Mater. Phys. (2008).

[179] S.O. Mariager, F. Pressacco, G. Ingold, A. Caviezel, E. Möhr-Vorobeva, P. Beaud, S.L. Johnson, C.J. Milne, E. Mancini, S. Moyerman, E.E. Fullerton, R. Feidenhans'L, C.H. Back, and C. Quitmann, Phys. Rev. Lett. (2012).

[180] F. Quirin, M. Vattilana, U. Shymanovich, A.E. El-Kamhawy, A. Tarasevitch, J. Hohlfeld, D. Von Der Linde, and K. Sokolowski-Tinten, Phys. Rev. B - Condens. Matter Mater. Phys. (2012).

[181] A.A. Ünal, A. Parabas, A. Arora, J. Ehrler, C. Barton, S. Valencia, R. Bali, T. Thomson, F. Yildiz, and F. Kronast, Ultramicroscopy (2017).

[182] J.M. Lommel, J. Appl. Phys. (1966).

[183] Y. Ding, D.A. Arena, J. Dvorak, M. Ali, C.J. Kinane, C.H. Marrows, B.J. Hickey, and L.H.

Lewis, J. Appl. Phys. (2008).

[184] I. Suzuki, T. Koike, M. Itoh, T. Taniyama, and T. Sato, J. Appl. Phys. (2009).

[185] R. Fan, C.J. Kinane, T.R. Charlton, R. Dorner, M. Ali, M.A. De Vries, R.M.D. Brydson, C.H. Marrows, B.J. Hickey, D.A. Arena, B.K. Tanner, G. Nisbet, and S. Langridge, Phys. Rev. B - Condens. Matter Mater. Phys. (2010).

[186] S. Maat, J.U. Thiele, and E.E. Fullerton, Phys. Rev. B - Condens. Matter Mater. Phys. **72**, (2005).

[187] V. Uhlíř, J.A. Arregi, and E.E. Fullerton, Nat. Commun. (2016).

[188] R.C. Wayne, Phys. Rev. **170**, 523 (1968).

[189] J. Van Driel, R. Coehoorn, G.J. Strijkers, E. Brück, and F.R. De Boer, J. Appl. Phys. (1999).

[190] G.C. Han, J.J. Qiu, Q.J. Yap, P. Luo, T. Kanbe, T. Shige, D.E. Laughlin, and J.G. Zhu, J. Appl. Phys. (2013).

[191] S. Inoue, H.Y.Y. Ko, and T. Suzuki, in *IEEE Trans. Magn.* (2008).

[192] P.H.L. Walter, J. Appl. Phys. (1964).

[193] J.M. Lommel and J.S. Kouvel, J. Appl. Phys. (1967).

[194] J. Cao, N.T. Nam, S. Inoue, H.Y.Y. Ko, N.N. Phuoc, and T. Suzuki, in *J. Appl. Phys.* (2008).

[195] Y. Xie, Q. Zhan, T. Shang, H. Yang, B. Wang, J. Tang, and R.W. Li, AIP Adv. (2017).

[196] S.A. Nikitin, G. Myalikgulyev, A.M. Tishin, M.P. Annaorazov, K.A. Asatryan, and A.L. Tyurin, Phys. Lett. A (1990).

[197] G.C. Han, J.J. Qiu, Q.J. Yap, P. Luo, D.E. Laughlin, J.G. Zhu, T. Kanbe, and T. Shige, in *J. Appl. Phys.* (2013).

[198] Y. Liu, L.C. Phillips, R. Mattana, M. Bibes, A. Barthélémy, and B. Dkhil, Nat. Commun. **7**, (2016).

[199] J.U. Thiele, S. Maat, and E.E. Fullerton, Appl. Phys. Lett. **82**, 2859 (2003).

[200] X. Marti, I. Fina, C. Frontera, J. Liu, P. Wadley, Q. He, R.J. Paull, J.D. Clarkson, J. Kudrnovský, I. Turek, J. Kuneš, D. Yi, J.-H. Chu, C.T. Nelson, L. You, E. Arenholz, S. Salahuddin, J. Fontcuberta, T. Jungwirth, and R. Ramesh, Nat. Mater. **13**, 367 (2014).

[201] E. Mancini, F. Pressacco, M. Haertinger, E.E. Fullerton, T. Suzuki, G. Woltersdorf, and C.H. Back, J. Phys. D. Appl. Phys. (2013).

[202] O.A. Cook, J. Am. Chem. Soc. **69**, 331 (1947).

[203] M.M. Qazilbash, A. Tripathi, A.A. Schafgans, B.-J. Kim, H.-T. Kim, Z. Cai, M. V Holt, J.M. Maser, F. Keilmann, O.G. Shpyrko, and D.N. Basov, Phys. Rev. B **83**, 165108 (2011).

[204] M.M. Qazilbash, M. Brehm, B.-G. Chae, P.-C. Ho, G.O. Andreev, B.-J. Kim, S.J. Yun, A. V Balatsky, M.B. Maple, F. Keilmann, H.-T. Kim, and D.N. Basov, Science (80-.). **318**, 1750

(2007).

[205] J. Laverock, S. Kittiwatanakul, A.A. Zakharov, Y.R. Niu, B. Chen, S.A. Wolf, J.W. Lu, and K.E. Smith, Phys. Rev. Lett. **113**, 216402 (2014).

[206] Y. Ding, C.C. Chen, Q. Zeng, H.S. Kim, M.J. Han, M. Balasubramanian, R. Gordon, F. Li, L. Bai, D. Popov, S.M. Heald, T. Gog, H.K. Mao, and M. Van Veenendaal, Phys. Rev. Lett. (2014).

[207] Y. Yokoyama, M. Usukura, S. Yuasa, Y. Suzuki, H. Miyajima, and T. Katayama, J. Magn. Magn. Mater. (1998).

[208] M. Manekar, C. Mukherjee, and S.B. Roy, EPL (2007).

[209] M. Loving, M.A. De Vries, F. Jimenez-Villacorta, C. Le Graët, X. Liu, R. Fan, S. Langridge, D. Heiman, C.H. Marrows, and L.H. Lewis, J. Appl. Phys. (2012).

[210] C. Baldasseroni, C. Bordel, A.X. Gray, A.M. Kaiser, F. Kronast, J. Herrero-Albillos, C.M. Schneider, C.S. Fadley, and F. Hellman, Appl. Phys. Lett. (2012).

[211] C. Baldasseroni, C. Bordel, C. Antonakos, A. Scholl, K.H. Stone, J.B. Kortright, and F. Hellman, J. Phys. Condens. Matter (2015).

[212] D.J. Keavney, Y. Choi, M. V Holt, V. Uhlíř, D. Arena, E.E. Fullerton, P.J. Ryan, and J.-W. Kim, Sci. Rep. **8**, 1778 (2018).

[213] P.J. Cote and L. V. Meisel, Phys. Rev. Lett. (1991).

[214] E. Puppin, Phys. Rev. Lett. (2000).

[215] T.J. Huffman, D.J. Lahneman, S.L. Wang, T. Slusar, B.J. Kim, H.T. Kim, and M.M. Qazilbash, Phys. Rev. B (2018).

[216] S. Wang, J.G. Ramírez, and I.K. Schuller, Phys. Rev. B - Condens. Matter Mater. Phys. **92**, 085150 (2015).

[217] M.A. De Vries, M. Loving, M. McLaren, R.M.D. Brydson, X. Liu, S. Langridge, L.H. Lewis, and C.H. Marrows, Appl. Phys. Lett. (2014).

[218] A. Sharoni, J.G. Ramírez, and I.K. Schuller, Phys. Rev. Lett. **101**, 026404 (2008).

[219] G. Engdahl, *Handbook of Giant Magnetostrictive Materials* (2000).

[220] B.D. Cullity and C.D. Graham, *Introduction to Magnetic Materials (2nd Edition)* (John Wiley and Sons, Hoboken, New Jersey, 2008).

[221] R. Becker and W. Döring, *Ferromagnetismus* (Verlag Julius Springer, Berlin, 1939).

[222] E.R. Callen and H.B. Callen, Phys. Rev. **129**, 578 (1963).

[223] P. Bruno, *Physical Origins and Theoretical Models of Magnetic Anisotropy* (Forschungszentrum Julich, Julich, 1993).

[224] F. Preisach, Zeitschrift Für Phys. (1935).

[225] D.L. Atherton and J.R. Beattie, IEEE Trans. Magn. (1990).

[226] A. Aharoni, in *Phys. B Condens. Matter* (2001).

[227] I.D. Mayergoyz, *Mathematical Models of Hysteresis and Their Applications* (2003).

[228] D.C. Jiles and D.L. Atherton, J. Appl. Phys. (1984).

[229] D.C. Jiles and D.L. Atherton, J. Magn. Magn. Mater. (1986).

[230] M.J. Sablik, IEEE Trans. Magn. (1997).

[231] D.C. Jiles, J. Phys. D. Appl. Phys. (1995).

[232] M.. Sablik and D.C. Jiles, IEEE Trans. Magn. (1993).

[233] A. Ramesh, D.C. Jiles, and J.M. Roderick, IEEE Trans. Magn. (1996).

[234] M.J. Sablik, B. Augustyniak, and M. Chmielewski, J. Appl. Phys. (1999).

[235] C.S. Schneider, P.Y. Cannell, and K.T. Watts, IEEE Trans. Magn. (1992).

[236] R. Venkataraman and P.S. Krishnaprasad, in *Proc. 37th IEEE Conf. Decis. Control (Cat. No.98CH36171)* (1998), pp. 2443–2448 vol.3.

[237] S.E. Zirka, Y.I. Moroz, R.G. Harrison, and K. Chwastek, J. Appl. Phys. (2012).

[238] C.C.H. Lo, E. Kinser, and D.C. Jiles, in *J. Appl. Phys.* (2003).

[239] S. Koide and H. Takei, J. Phys. Soc. Japan (1967).

[240] E.N. Fuls, D.H. Hensler, and A.R. Ross, Appl. Phys. Lett. (1967).

[241] M. Borek, F. Qian, V. Nagabushnam, and R.K. Singh, Appl. Phys. Lett. (1993).

[242] K.G. West, J. Lu, J. Yu, D. Kirkwood, W. Chen, Y. Pei, J. Claassen, and S.A. Wolf, J. Vac. Sci. Technol. A Vacuum, Surfaces, Film. (2008).

[243] F.C. Case, J. Vac. Sci. Technol. A **8**, 1395 (1990).

[244] M. Sambi, G. Sangiovanni, G. Granozzi, and F. Parmigiani, Phys. Rev. B - Condens. Matter Mater. Phys. (1997).

[245] D. Ruzmetov, K.T. Zawilski, V. Narayanamurti, and S. Ramanathan, J. Appl. Phys. (2007).

[246] L.D. Landau and E.M. Lifshitz, in *Electrodyn. Contin. Media (Second Ed.*, edited by L.D. LANDAU and E.M. LIFSHITZ, Second Edi (Pergamon, Amsterdam, 1984), pp. 439–451.

[247]*X-Ray and Neuron Reflectivity: Principles and Applications* (2007).

[248] M. Birkholz, *Thin Film Analysis by X-Ray Scattering* (2006).

[249] Bruker, Https://Www.Bruker.Com/Products/x-Ray-Diffraction-and-Elemental-Analysis/x-Ray-Diffraction/D8-Discover-Family.Html (2019).

[250] M. Björck and G. Andersson, J. Appl. Crystallogr. (2007).

[251] A. Nelson, J. Appl. Crystallogr. (2006).

[252] P.A. Kienzle, J. Krycka, N. Patel, and I. Sahin, Refl1D (Version 0.7.9a2) [Computer Software]. Coll. Park. MD Univ. Maryland. Retrieved Novemb. 30, 2016. Available from Http//Reflectometry.Org/Danse (2011).

[253] S.K. Sinha, E.B. Sirota, S. Garoff, and H.B. Stanley, Phys. Rev. B (1988).

[254] D.K.G. De Boer, Phys. Rev. B (1994).

[255] G. Binning, H. Rohrer, C. Gerber, and E. Weibel, Phys. Rev. Lett. (1982).

[256] G. Binnig, C.F. Quate, and C. Gerber, Phys. Rev. Lett. **56**, 930 (1986).

[257] I. Horcas, R. Fernández, J.M. Gómez-Rodríguez, J. Colchero, J. Gómez-Herrero, and A.M. Baro, Rev. Sci. Instrum. (2007).

[258] D. Nečas and P. Klapetek, Cent. Eur. J. Phys. **10**, 181 (2012).

[259] Sears V.F, *Neutron Optics*, 1st ed. (Oxford University Press, 1989).

[260] X.L. Zhou and S.H. Chen, Phys. Rep. (1995).

[261] C.F. Majkrzak, K. V. O'Donovan, and N.F. Berk, in *Neutron Scatt. from Magn. Mater.* (2006).

[262] F. Mezei, Phys. B+C (1986).

[263] J.A. Vrugt, C.J.F. Ter Braak, C.G.H. Diks, B.A. Robinson, J.M. Hyman, and D. Higdon, Int. J. Nonlinear Sci. Numer. Simul. (2009).

[264] W.H. Press, S.A. Teukolsky, W.T. Vetterling, and B.P. Flannery, *Numerical Recipes 3rd Edition: The Art of Scientific Computing*, 3rd ed. (Cambridge University Press, New York, NY, USA, 2007).

[265] B.B. Maranville, A. Green, and P.A. Kienzle, (2017).

[266] B. Maranville, W. Ratcliff, and P. Kienzle, J. Appl. Crystallogr. (2018).

[267] B.J. Kirby, P.A. Kienzle, B.B. Maranville, N.F. Berk, J. Krycka, F. Heinrich, and C.F. Majkrzak, Curr. Opin. Colloid Interface Sci. **17**, 44 (2012).

[268] J. Cui, D. Da, and W. Jiang, Appl. Surf. Sci. (1998).

[269] S. Chen, H. Ma, S. Wang, N. Shen, J. Xiao, H. Zhou, X. Zhao, Y. Li, and X. Yi, Thin Solid Films (2006).

[270] D. Ruzmetov, S.D. Senanayake, V. Narayanamurti, and S. Ramanathan, Phys. Rev. B - Condens. Matter Mater. Phys. (2008).

[271] B.D. Gauntt, E.C. Dickey, and M.W. Horn, J. Mater. Res. (2009).

[272] Y. Cui and S. Ramanathan, J. Vac. Sci. Technol. A Vacuum, Surfaces, Film. (2011).

[273] Y.Y. Luo, L.Q. Zhu, Y.X. Zhang, S.S. Pan, S.C. Xu, M. Liu, and G.H. Li, J. Appl. Phys. (2013).

[274] M. Jiang, X. Cao, S. Bao, H. Zhou, and P. Jin, Thin Solid Films (2014).

[275] X. Ma, X. Liu, H. Li, A. Zhang, and M. Huang, Appl. Phys. A Mater. Sci. Process. (2017).

[276] A. Razavi, T. Hughes, J. Antinovitch, and J. Hoffman, J. Vac. Sci. Technol. A Vacuum, Surfaces, Film. (1989).

[277] T. Christmann, B. Felde, W. Niessner, D. Schalch, and A. Scharmann, Thin Solid Films (1996).

[278] Y. Zhao, C. Chen, X. Pan, Y. Zhu, M. Holtz, A. Bernussi, and Z. Fan, J. Appl. Phys. (2013).

[279] D.P. Zhang, M.D. Zhu, Y. Liu, K. Yang, G.X. Liang, Z.H. Zheng, X.M. Cai, and P. Fan, J. Alloys Compd. (2016).

[280] E. Kusano, J.A. Theil, and J.A. Thornton, J. Vac. Sci. Technol. A Vacuum, Surfaces, Film. (1988).

[281] R.O. Dillon, K. Le, and N. Ianno, in *Thin Solid Films* (2001).

[282] S. Wang, Inhomogenous Phase Transition of Vanadium Oxide on Mesoscopic Scale, PhD thesis, UC San Diego, 2014.

[283] Y. Choi, Y. Jung, and H. Kim, Thin Solid Films (2016).

[284] R.E. Marvel, R.R. Harl, V. Craciun, B.R. Rogers, and R.F. Haglund, Acta Mater. (2015).

[285] J. Nag and R.F. Haglund, J. Phys. Condens. Matter (2008).

[286] J.H. Claassen, J.W. Lu, K.G. West, and S.A. Wolf, Appl. Phys. Lett. **96**, 132102 (2010).

[287] D.H. Kim and H.S. Kwok, Appl. Phys. Lett. (1994).

[288] B.J. Kim, Y.W. Lee, S. Choi, B.G. Chae, and H.T. Kim, J. Korean Phys. Soc. (2007).

[289] A.M. Makarevich, I.I. Sadykov, D.I. Sharovarov, V.A. Amelichev, A.A. Adamenkov, D.M. Tsymbarenko, A. V. Plokhih, M.N. Esaulkov, P.M. Solyankin, and A.R. Kaul, J. Mater. Chem. C (2015).

[290] J.A. Venables, G.D.T. Spiller, and M. Hanbucken, Reports Prog. Phys. (1984).

[291] D.L. Smith, *Thin-Film Deposition : Principles and Practice* (McGraw-Hill, New York, N.Y., 1995).

[292] M.A. Herman, *Epitaxy : Physical Principles and Technical Implementation* (Springer, Berlin ;, 2004).

[293] J.A. Thornton, J. Vac. Sci. Technol. A Vacuum, Surfaces, Film. (1986).

[294] I. Petrov, P.B. Barna, L. Hultman, and J.E. Greene, J. Vac. Sci. Technol. A Vacuum, Surfaces, Film. (2003).

[295] C. V. Thompson, Annu. Rev. Mater. Res. (2012).

[296] J. de la Venta, S. Wang, J.G. Ramirez, and I.K. Schuller, Appl. Phys. Lett. **102**, 122404 (2013).

[297] J. de la Venta, S. Wang, T. Saerbeck, J.G. Ramírez, I. Valmianski, and I.K. Schuller, Appl.

Phys. Lett. **104**, 62410 (2014).

[298] M. Sharma, J. Gazquez, M. Varela, J. Schmitt, and C. Leighton, Phys. Rev. B **84**, 24417 (2011).

[299] J.G. Ramirez, T. Saerbeck, S. Wang, J. Trastoy, M. Malnou, J. Lesueur, J.-P. Crocombette, J.E. Villegas, and I.K. Schuller, Phys. Rev. B **91**, 205123 (2015).

[300] B. Viswanath, C. Ko, and S. Ramanathan, Scr. Mater. **64**, 490 (2011).

[301] R.C. O'Handley, *Modern Magnetic Materials : Principles and Applications* (Wiley, New York, 1999).

[302] A.S. Barker, H.W. Verleur, and H.J. Guggenheim, Phys. Rev. Lett. **17**, 1286 (1966).

[303] I. Balberg and W.R. Roach, in *Proc. Int. Conf. Conduct. Low Mobil. Mater.* (Taylor & Francis, London, 1971), p. 77.

[304] P.B. Allen, R.M. Wentzcovitch, W.W. Schulz, and P.C. Canfield, Phys. Rev. B (1993).

[305] T. Mitsuishi, Jpn. J. Appl. Phys. **6**, 1060 (1967).

[306] A.I. Ivon, V.R. Kolbunov, and I.M. Chernenko, J. Eur. Ceram. Soc. **19**, 1883 (1999).

[307] B. Fisher and L. Patlagan, Materials (Basel). **10**, 554 (2017).

[308] J.B. MacChesney, J.F. Potter, and H.J. Guggenheim, J. Electrochem. Soc. (1968).

[309] W.R. Roach and I. Balberg, Solid State Commun. **9**, 551 (1971).

[310] G. Guzman, F. Beteille, R. Morineau, and J. Livage, J. Mater. Chem. **6**, 505 (1996).

[311] K. Nagashima, T. Yanagida, H. Tanaka, and T. Kawai, Phys. Rev. B **74**, 172106 (2006).

[312] E. Abreu, M. Liu, J. Lu, K.G. West, S. Kittiwatanakul, W. Yin, S.A. Wolf, and R.D. Averitt, New J. Phys. **14**, 1 (2012).

[313] V. Balakrishnan, C. Ko, and S. Ramanathan, J. Mater. Res. **27**, 1476 (2012).

[314] K. Kawatani, T. Kanki, and H. Tanaka, Phys. Rev. B - Condens. Matter Mater. Phys. **90**, 054203 (2014).

[315] A. Sohn, T. Kanki, H. Tanaka, and D.W. Kim, Appl. Phys. Lett. **107**, 171603 (2015).

[316] T. Yajima, Y. Ninomiya, T. Nishimura, and A. Toriumi, Phys. Rev. B - Condens. Matter Mater. Phys. **91**, 205102 (2015).

[317] H. Paik, J.A. Moyer, T. Spila, J.W. Tashman, J.A. Mundy, E. Freeman, N. Shukla, J.M. Lapano, R. Engel-Herbert, W. Zander, J. Schubert, D.A. Muller, S. Datta, P. Schiffer, and D.G. Schlom, Appl. Phys. Lett. **107**, 163101 (2015).

[318] D. Lee, J. Lee, K. Song, F. Xue, S.Y. Choi, Y. Ma, J. Podkaminer, D. Liu, S.C. Liu, B. Chung, W. Fan, S.J. Cho, W. Zhou, J. Lee, L.Q. Chen, S.H. Oh, Z. Ma, and C.B. Eom, Nano Lett. (2017).

[319] Y. Sharma, M. V. Holt, N. Laanait, X. Gao, I.N. Ivanov, L. Collins, C. Sohn, Z. Liao, E.

Skoropata, S. V. Kalinin, N. Balke, G. Eres, T.Z. Ward, and H.N. Lee, APL Mater. (2019).

[320] K. Shibuya, M. Kawasaki, and Y. Tokura, Appl. Phys. Lett. **96**, 022102 (2010).

[321] J. Jian, A. Chen, Y. Chen, X. Zhang, and H. Wang, Appl. Phys. Lett. **111**, 153102 (2017).

[322] M. Taya, *Electronic Composites* (Cambridge University Press, Cambridge, 2005).

[323] L. Almeida, G.S. Deep, A. Nogueira-Lima, and H. Neff, Opt. Eng. (2002).

[324] J. Rozen, R. Lopez, R.F. Haglund, and L.C. Feldman, Appl. Phys. Lett. **88**, 081902 (2006).

[325] A. Shekhawat, S. Papanikolaou, S. Zapperi, and J.P. Sethna, Phys. Rev. Lett. (2011).

[326] I.D. Mayergoyz, J. Appl. Phys. (1985).

[327] L.A.L. De Almeida, G.S. Deep, A.M. Nogueira Lima, H.F. Neff, and R.C.S. Freire, in *IEEE Trans. Instrum. Meas.* (2001).

[328] J.G. Ramírez, A. Sharoni, Y. Dubi, M.E. Gómez, and I.K. Schuller, Phys. Rev. B - Condens. Matter Mater. Phys. (2009).

[329] I. Suzuki, Y. Hamasaki, M. Itoh, and T. Taniyama, Appl. Phys. Lett. (2014).

[330] H. Ohldag, A. Scholl, F. Nolting, S. Anders, F.U. Hillebrecht, and J. Stöhr, Phys. Rev. Lett. (2001).

[331] C. Baldasseroni, G.K. Pálsson, C. Bordel, S. Valencia, A.A. Unal, F. Kronast, S. Nemsak, C.S. Fadley, J.A. Borchers, B.B. Maranville, and F. Hellman, J. Appl. Phys. (2014).

[332] J.W. Kim, P.J. Ryan, Y. Ding, L.H. Lewis, M. Ali, C.J. Kinane, B.J. Hickey, C.H. Marrows, and D.A. Arena, Appl. Phys. Lett. (2009).

[333] M.G. Loving, R. Barua, C. Le Graët, C.J. Kinane, D. Heiman, S. Langridge, C.H. Marrows, and L.H. Lewis, J. Phys. D. Appl. Phys. **51**, 24003 (2017).

[334] F. Pressacco, V. Uhlíř, M. Gatti, A. Bendounan, E.E. Fullerton, and F. Sirotti, Sci. Rep. (2016).

[335] C.J. Kinane, M. Loving, M.A. De Vries, R. Fan, T.R. Charlton, J.S. Claydon, D.A. Arena, F. Maccherozzi, S.S. Dhesi, D. Heiman, C.H. Marrows, L.H. Lewis, and S. Langridge, New J. Phys. (2014).

[336] R. Barua, F. Jiménez-Villacorta, and L.H. Lewis, Appl. Phys. Lett. (2013).

[337] J. Cui, J.L. Hockel, P.K. Nordeen, D.M. Pisani, C.Y. Liang, G.P. Carman, and C.S. Lynch, Appl. Phys. Lett. (2013).

[338] Y. Tan, K. Liang, Z. Mei, P. Zhou, Y. Liu, Y. Qi, Z. Ma, and T. Zhang, Ceram. Int. (2018).

[339] C. Kittel, Rev. Mod. Phys. **21**, 541 (1949).

[340] D. Sander, Reports Prog. Phys. **62**, 809 (1999).

[341] C. Urban, A. Quesada, T. Saerbeck, M.A. Garcia, M.A. De La Rubia, I. Valmianski, J.F. Fernández, and I.K. Schuller, Appl. Phys. Lett. (2016).

[342] L. Sutton, J. Lauzier, and J. De La Venta, J. Appl. Phys. (2018).

[343] F.E. Spada, F.T. Parker, C.L. Platt, and J.K. Howard, J. Appl. Phys. (2003).

Appendices

Appendix A (Resistor Network Code)

In this section, we present the code used for the resistor grid model presented in Ch. 3. The current implementation is a Matlab script file, with several function calls. The function calls are provided below. Originally written in Matlab2016b. It requires the sparse matric package. The majority of the code (on a per line basis) is updating the conductance matrix, which requires many special case checks, implemented for computational speed not readability. As a reminder to the reader, grids larger than roughly 100 by 100 grains are memory intensive.

```
%%%%%%%%%%%%%%%%%%%%%%%%%%%%%%%%%%%%%%%%%%%%%%%%%%%%%%%%%%%%%%%%
close all
format long


%initializes size of grid, starting temp, ending temp, and
stepsize
X=100;
Y=100;
T_start=295;
T_end=385;
T_stepsize=10;

%alpha sets the decay for the semiconducting state e^(alpha/kt)
alpha=2775;
%initalizes the grains, conductance matrix etc
[R_metal,R_ins,R_break,X,Y,G,I,iter,sigmasq,Tc_avg,temp,node_col
,switch_col,Tc_grid,R_eq_vec,solvertime1,Tc_grid_break]=Resistor
Initializer2(X,Y,T_start,T_end,T_stepsize,alpha);

%initializes the voltage vector
R_eq_vec2=R_eq_vec;
V=zeros(X*Y+1,1);
V=sparse(V);
```

```
updatetime=0;
fullstart=tic;
%steps through each temperature
for temp_step=1:iter

    temp=temp+T_stepsize

    %function that switches a grain between states
    [node_col,switch_col]=switcher(
node_col,switch_col,X,Y,R_ins,R_metal,R_break,temp,Tc_grid,Tc_gr
id_break,alpha);

    %apply the e^(alpha/kt) semiconducting correction
    for iiii=1:Y
        for jjjj=1:X
            if ((node_col(jjjj+X*(iiii-1),1) > R_metal) &
(node_col(jjjj+X*(iiii-1),1)<R_break)) & (temp>(T_start-
2*T_stepsize))

                node_col(jjjj+X*(iiii-1),1) = R_ins.*
exp(alpha/temp)./exp(alpha/300);
            end
        end
    end

    %after grains switched for new temp, update conductance
matrix
    updatestart=tic;
    G=firstrow(G,X,Y,node_col,switch_col);
    G=middle(G,X,Y,node_col,switch_col);
    G=lastrow(G,X,Y,node_col,switch_col);
    updatetime=toc(updatestart)

    %solve the linear algebra problem
    tic;
    V=G \ I;
    toc;

    %save solution. 585 is a scale factor, to match metallic
state value.
    %can be absorbed into R values
    R_eq_vec(temp_step,1)=(V(1,1))*585;
```

```
end


%reset switch record for cooling branch
for iii=1:Y
    for jjj=1:X
        if node_col(jjj+X*(iii-1),1)<R_break
            switch_col(jjj+X*(iii-1),1)=0;
        end
    end
end

%make sure 'broken' grains dont unswitch
for i=1:X
    for j=1:Y
        if Tc_grid_break(i,j)~=500
            Tc_grid(i,j)=500;
        end
    end
end

%reshuffle the RNG
rng('shuffle','twister');
%hysteresis width
hysteresis= 5.8;
%reformat with new TC's
Tc_grid = sigmasq.*randn(X,Y)+ Tc_avg-hysteresis;

for temp_step=1:iter
    %same as heating temperature steps, but for cooling
    temp=temp-T_stepsize

    [node_col,switch_col]=switchercool(
node_col,switch_col,X,Y,R_ins,R_metal,R_break,temp,Tc_grid,Tc_gr
id_break,alpha);



    updatestart=tic;
    G=firstrow(G,X,Y,node_col,switch_col);
    G=middle(G,X,Y,node_col,switch_col);
    G=lastrow(G,X,Y,node_col,switch_col);
    updatetime=toc(updatestart);

    V=G \ I;

    R_eq_vec2(iter-temp_step+1,1)=(V(1,1))*585;
```

```
    R_eq_vec2(iter-temp_step+1,1);
end

fullend=toc(fullstart);

solvertime1;

%plots the R vs. T for both heating and cooling
tempaxis=[T_start+T_stepsize:T_stepsize:T_end]';
R_eq_vec2fix=R_eq_vec2.*0;
for ijk=2:iter
    R_eq_vec2fix(ijk-1,1)=R_eq_vec2(ijk,1);
end


semilogy(tempaxis,R_eq_vec,'r.');
hold on
semilogy(tempaxis,R_eq_vec2fix,'b.');

plotter=zeros(iter,3);
plotter(:,1)=tempaxis;
plotter(:,2)=R_eq_vec;
plotter(:,3)=R_eq_vec2fix;


hold off
%%%%%%%%%%%%%%%%%%%%%%%%%%%%%%%%%%%%%%%%%%%%%%%%%%%%%%%%%%%%%%%%

%%%%%%%%%%%%%%%%%%%%%%%%%%%%%%%%%%%%%%%%%%%%%%%%%%%%%%%%%%%%%%%%
function [
R_metal,R_ins,R_break,X,Y,G,I,iter,sigmasq,Tc_avg,temp,node_col,
switch_col,Tc_grid,R_eq_vec,solvertime1,Tc_grid_break ] =
ResistorInitializer(X,Y,T_start,T_end,T_stepsize,alpha)
%Initializes everything, sets parameter values like resistance
etc
R_metal= (0.1);
R_ins= 881268.41/585; %exact values fit to data
R_break=1e13; %arbitrary, but not too large to make matrix
singular



G=Gbuild8(X,Y,R_metal,R_ins);

I= sparse(X*Y+1,1);
V4=I;
I(1,1)= (1);
```

```
%intializes RNG
rng('shuffle','twister');

%sets Tc, spread in TC for diff grains etc
iter=(T_end-T_start)/(T_stepsize);
sigmasq = 8;%8;
Tc_avg = 333.35;%332.75;%333.75;%333.25;
temp=T_start-T_stepsize;


%records resistance for grains
node_col=R_ins.* ones(X*Y,1);








switch_col=int8(zeros(X*Y,1));
%records TC for grains
Tc_grid = sigmasq.*randn(X,Y)+ Tc_avg;



R_eq_vec=zeros(iter,1);


solvertime1=0;

%how many grains should break. a is the % allowed to break
break_grid=zeros(X,Y);

for i=1:X
    for j=1:Y
        a=rand();
        if a <= 0.0625;
            break_grid(i,j)=1;
        end
    end
end

%grains have same spread as TC to break
Tc_grid_break=sigmasq.*randn(X,Y)+ Tc_avg;
Tc_grid_break=break_grid .* Tc_grid_break;
```

```
for i=1:X
    for j=1:Y
        if Tc_grid_break(i,j)==0
            Tc_grid_break(i,j)=500;
        end
    end
end



temp=T_start-T_stepsize;

end
%%%%%%%%%%%%%%%%%%%%%%%%%%%%%%%%%%%%%%%%%%%%%%%%%%%%%%%%%%%%%%%%


%%%%%%%%%%%%%%%%%%%%%%%%%%%%%%%%%%%%%%%%%%%%%%%%%%%%%%%%%%%%%%%%
function [ node_col,switch_col] = switcher(
node_col,switch_col,X,Y,R_ins,R_metal,R_break,temp,Tc_grid,Tc_gr
id_break,alpha)
%switches grains from semiconducting to metallic if >Tc. also
breaks chosen
%grains

for ii=1:Y
    for jj=1:X
        if (node_col(jj+X*(ii-1),1) < (R_ins *
exp(alpha/temp)./exp(alpha/300)+0.1) || node_col(jj+X*(ii-1),1)
> (R_ins* exp(alpha/temp)./exp(alpha/300)-0.1))
            if temp > Tc_grid(jj,ii) &
(Tc_grid_break(jj,ii)==500)
                node_col(jj+X*(ii-1),1)=R_metal;
                switch_col(jj+X*(ii-1),1)=1;
            end
            if (temp > Tc_grid(jj,ii)) &
(Tc_grid_break(jj,ii)<500)
                node_col(jj+X*(ii-1),1)=R_break;
                switch_col(jj+X*(ii-1),1)=1;
            end
        end
    end
end

end
%%%%%%%%%%%%%%%%%%%%%%%%%%%%%%%%%%%%%%%%%%%%%%%%%%%%%%%%%%%%%%%%
```

```
%%%%%%%%%%%%%%%%%%%%%%%%%%%%%%%%%%%%%%%%%%%%%%%%%%%%%%%%%%%%%%%%
function [ a ] = g( node_col,x,y )
%definition of conductance between 2 grains. simply to clean up
code

a=((node_col(x,1)+node_col(y,1))/2 );

end
%%%%%%%%%%%%%%%%%%%%%%%%%%%%%%%%%%%%%%%%%%%%%%%%%%%%%%%%%%%%%%%%

%%%%%%%%%%%%%%%%%%%%%%%%%%%%%%%%%%%%%%%%%%%%%%%%%%%%%%%%%%%%%%%%
function [ G ] = firstrow( G,X,Y,node_col,switch_col )
%updates first row of conductance matrix. special cases for
edges (has to go out to next
%nearest neighbors)

for n=1:X


    if (n>1) && (n<X)

        G(n+1,n+1)=1./g(node_col,n,n-
1)+1./g(node_col,n,n+1)+1./g(node_col,n,n+X)+2./node_col(n,1);

        if (n > 2) && (n < (X-1) )
            G(n,n)=1./g(node_col,n-1,n-2)+1./g(node_col,n-
1,n)+1./g(node_col,n-1,n+X-1)+2./node_col(n-1,1);

G(n+2,n+2)=1./g(node_col,n+1,n)+1./g(node_col,n+1,n+2)+1./g(node
_col,n+1,n+X+1)+2./node_col(n+1,1);
            G(n+1+X,n+1+X)=1./g(node_col,n+X,n-
1+X)+1./g(node_col,n+X,n+X+1)+1./g(node_col,n+X,n)+1./g(node_col
,n+X,n+X+X);
        else
            if n==2
                G(n,n)=1./g(node_col,n-1,n)+1./g(node_col,n-
1,n+X-1)+2./node_col(n-1,1);

G(n+2,n+2)=1./g(node_col,n+1,n)+1./g(node_col,n+1,n+2)+1./g(node
_col,n+1,n+X+1)+2./node_col(n+1,1);
                G(n+1+X,n+1+X)=1./g(node_col,n+X,n-
1+X)+1./g(node_col,n+X,n+1+X)+1./g(node_col,n+X,n)+1./g(node_col
,n+X,n+X+X);
            end
            if n==(X-1)
```

```
G(n+2,n+2)=1./g(node_col,n+1,n)+1./g(node_col,n+1,n+X+1)+2./node
_col(n+1,1);
        G(n,n)=1./g(node_col,n-1,n-2)+1./g(node_col,n-
1,n)+1./g(node_col,n-1,n+X-1)+2./node_col(n-1,1);
        G(n+1+X,n+1+X)=1./g(node_col,n+X,n-
1+X)+1./g(node_col,n+X,n+X+1)+1./g(node_col,n+X,n)+1./g(node_col
,n+X,n+X+X);
      end

    end



    G(n+1,n+2)=-1./g(node_col,n,n+1);
    G(n+2,n+1)=-1./g(node_col,n+1,n);
    G(n,n+1)=-1./g(node_col,n-1,n);
    G(n+1,n)=-1./g(node_col,n,n-1);

    G(n+1+X,n+1)=-1./g(node_col,n+X,n);
    G(n+1,n+1+X)=-1./g(node_col,n,n+X);
    G(1,n+1)=-2./node_col(n,1);
    G(n+1,1)=G(1,n+1);

  else
    if n==1

G(n+1,n+1)=1./g(node_col,n,n+1)+1./g(node_col,n,n+X)+2./node_col
(n,1);



G(n+2,n+2)=1./g(node_col,n+1,n)+1./g(node_col,n+1,n+X+1)+1./g(no
de_col,n+1,n+2)+2./node_col(n+1,1);

G(n+1+X,n+1+X)=1./g(node_col,n+X,n+1+X)+1./g(node_col,n+X,n)+1./
g(node_col,n+X,n+X+X);

      G(1,n+1)=-2./node_col(n,1);
      G(n+1,1)=G(1,n+1);

      G(n+1,n+2)=-1./g(node_col,n,n+1);
      G(n+2,n+1)=-1./g(node_col,n+1,n);
      G(n+1+X,n+1)=-1./g(node_col,n+X,n);
      G(n+1,n+1+X)=-1./g(node_col,n,n+X);

    end
```

```
        if n==(X)
            G(n+1,n+1)=1./g(node_col,n,n-
1)+1./g(node_col,n,n+X)+2./node_col(n,1);

            G(n,n)=1./g(node_col,n-1,n-2)+1./g(node_col,n-
1,n)+1./g(node_col,n-1,n+X-1)+2./node_col(n-1,1);
            G(n+1+X,n+1+X)=1./g(node_col,n+X,n-
1+X)+1./g(node_col,n+X,n)+1./g(node_col,n+X,n+X+X);



            G(1,n+1)=-2./node_col(n,1);
            G(n+1,1)=G(1,n+1);

            G(n+1,n+2)=0;
            G(n+2,n+1)=0;
            G(n+1,n)=-1./g(node_col,n,n-1);
            G(n,n+1)=-1./g(node_col,n-1,n);

            G(n+1+X,n+1)=-1./g(node_col,n+X,n);
            G(n+1,n+1+X)=-1./g(node_col,n,n+X);
        end

    end






    junkvar=0;
    for k=2:X+1
        junkvar=junkvar+G(k,1);

    end
    G(1,1)=-junkvar;





    switch_col(n,1)=2;
end
end
%%%%%%%%%%%%%%%%%%%%%%%%%%%%%%%%%%%%%%%%%%%%%%%%%%%%%%%%%%%%%%%%


%%%%%%%%%%%%%%%%%%%%%%%%%%%%%%%%%%%%%%%%%%%%%%%%%%%%%%%%%%%%%%%%
function [ G ] = lastrow( G,X,Y,node_col,switch_col )
```

```
%updates last row of conductance matrix. special cases for edges
(has to go out to next
%nearest neighbors)
for n=X*Y-X+1:X*Y





    if n > (X*Y-X+1) && (n < (X*Y))

        G(n+1,n+1)=1./g(node_col,n,n-
1)+1./g(node_col,n,n+1)+1./g(node_col,n,n-X)+2./node_col(n,1);

        if (n> (X*Y-X+2)) && (n < (X*Y-1))
            G(n,n)=1./g(node_col,n-1,n-2)+1./g(node_col,n-
1,n)+1./g(node_col,n-1,n-X-1)+2./node_col(n-1,1);

G(n+2,n+2)=1./g(node_col,n+1,n)+1./g(node_col,n+1,n+2)+1./g(node
_col,n+1,n-X+1)+2./node_col(n+1,1);
            G(n+1-X,n+1-X)=1./g(node_col,n-X,n-1-
X)+1./g(node_col,n-X,n+1-X)+1./g(node_col,n-
X,n)+1./g(node_col,n-X,n-X-X);

            G(n+1,n+2)=-1./g(node_col,n,n+1);
            G(n+2,n+1)=-1./g(node_col,n+1,n);
            G(n,n+1)=-1./g(node_col,n-1,n);
            G(n+1,n)=-1./g(node_col,n-1,n);
            G(n+1-X,n+1)=-1./g(node_col,n-X,n);
            G(n+1,n+1-X)=-1./g(node_col,n,n-X);

        else
            if n == (X*Y-X+2)
                G(n,n)=1./g(node_col,n-1,n)+1./g(node_col,n-1,n-
X-1)+2./node_col(n-1,1);

G(n+2,n+2)=1./g(node_col,n+1,n)+1./g(node_col,n+1,n+2)+1./g(node
_col,n+1,n-X+1)+2./node_col(n+1,1);
                G(n+1-X,n+1-X)=1./g(node_col,n-X,n-1-
X)+1./g(node_col,n-X,n-X+1)+1./g(node_col,n-
X,n)+1./g(node_col,n-X,n-X-X);

                G(n,n+1)=-1./g(node_col,n-1,n);
                G(n+1,n)=-1./g(node_col,n,n-1);

                G(n+2,n+1)=-1./g(node_col,n+1,n);
                G(n+1,n+2)=-1./g(node_col,n,n+1);
```

```
                G(n+1-X,n+1)=-1./g(node_col,n-X,n);
                G(n+1,n+1-X)=-1./g(node_col,n,n-X);


            end

            if n == (X*Y-1)

G(n+2,n+2)=1./g(node_col,n+1,n)+1./g(node_col,n+1,n-
X+1)+2./node_col(n+1,1);
                G(n,n)=1./g(node_col,n-1,n-2)+1./g(node_col,n-
1,n)+1./g(node_col,n-1,n-X-1)+2./node_col(n-1,1);
                G(n+1-X,n+1-X)=1./g(node_col,n-X,n-1-
X)+1./g(node_col,n-X,n-X+1)+1./g(node_col,n-
X,n)+1./g(node_col,n-X,n-X-X);
                G(n+1-X,n+1)=-1./g(node_col,n,n+1);


                G(n,n+1)=-1./g(node_col,n-1,n);
                G(n+1,n)=-1./g(node_col,n-1,n);
                G(n+2,n+1)=-1./g(node_col,n+1,n);
                G(n+1,n+2)=-1./g(node_col,n,n+1);

                G(n+1-X,n+1)=-1./g(node_col,n-X,n);
                G(n+1,n+1-X)=-1./g(node_col,n,n-X);


            end
        end
    else
        if n == (X*Y-X+1)

            G(n+1,n+1)=1./g(node_col,n,n+1)+1./g(node_col,n,n-
X)+2./node_col(n,1);


G(n+2,n+2)=1./g(node_col,n+1,n)+1./g(node_col,n+1,n+2)+1./g(node
_col,n+1,n-X+1)+2./node_col(n+1,1);
            G(n+1-X,n+1-X)=1./g(node_col,n-X,n+1-
X)+1./g(node_col,n-X,n)+1./g(node_col,n-X,n-X-X);

            G(n+1,n+2)=-1./g(node_col,n,n+1);
            G(n+2,n+1)=-1./g(node_col,n+1,n);

            G(n+1-X,n+1)=-1./g(node_col,n-X,n);
            G(n+1,n+1-X)=-1./g(node_col,n,n-X);
```

```
            G(n,n+1)=0;
            G(n+1,n)=0;



        end

        if n== (X*Y)

            G(n+1,n+1)=1./g(node_col,n,n-1)+1./g(node_col,n,n-
X)+2./node_col(n,1);

            G(n,n)=1./g(node_col,n-1,n-2)+1./g(node_col,n-
1,n)+1./g(node_col,n-1,n-X-1)+2./node_col(n-1,1);
            G(n+1-X,n+1-X)=1./g(node_col,n-X,n-1-
X)+1./g(node_col,n-X,n)+1./g(node_col,n-X,n-X-X);



            G(n+1-X,n+1)=-1./g(node_col,n-X,n);
            G(n+1,n+1-X)=-1./g(node_col,n,n-X);

            G(n,n+1)=-1./g(node_col,n-1,n);
            G(n+1,n)=-1./g(node_col,n,n-1);


        end
    end






    switch_col(n,1)=2;
end
end
%%%%%%%%%%%%%%%%%%%%%%%%%%%%%%%%%%%%%%%%%%%%%%%%%%%%%%%%%%%%%%%%


%%%%%%%%%%%%%%%%%%%%%%%%%%%%%%%%%%%%%%%%%%%%%%%%%%%%%%%%%%%%%%%%
function [ G ] = middle( G,X,Y,node_col,switch_col )
%updates conductance matrix. at least 2 away from any edge (has
to go out to next
%nearest neighbors)

for n=X+1:X*Y-X
    if (mod(n,X)~= 1) && (mod(n,X)~= 0)
```

```
        G(n+1,n+1)=1./g(node_col,n,n-
1)+1./g(node_col,n,n+1)+1./g(node_col,n,n-
X)+1./g(node_col,n,n+X);

        if (mod(n,X)>2) && (mod(n,X) < (X-1))

G(n+2,n+2)=1./g(node_col,n+1,n)+1./g(node_col,n+1,n+2)+1./g(node
_col,n+1,n-X+1)+1./g(node_col,n+1,n+X+1);
            G(n,n)=1./g(node_col,n-1,n-2)+1./g(node_col,n-
1,n)+1./g(node_col,n-1,n-X-1)+1./g(node_col,n-1,n+X-1);


            if (n > (2*X+2)) && (n < (X*Y-2*X-1))
                G(n+1+X,n+1+X)=1./g(node_col,n+X,n-
1+X)+1./g(node_col,n+X,n)+1./g(node_col,n+X,n+X+1)+1./g(node_col
,n+X,n+X+X);
                G(n+1-X,n+1-X)=1./g(node_col,n-X,n-1-
X)+1./g(node_col,n-X,n)+1./g(node_col,n-X,n+1-
X)+1./g(node_col,n-X,n-X-X);

                G(n,n+1)=-1./g(node_col,n-1,n);
                G(n+1,n)=-1./g(node_col,n,n-1);


                G(n+1,n+2)=-1./g(node_col,n,n+1);
                G(n+2,n+1)=-1./g(node_col,n+1,n);

                G(n+1+X,n+1)=-1./g(node_col,n+X,n);
                G(n+1,n+1+X)=-1./g(node_col,n,n+X);
                G(n+1-X,n+1)=-1./g(node_col,n-X,n);
                G(n+1,n+1-X)=-1./g(node_col,n,n-X);
            else
                if (n > (X+1)) && (n < (2*X-1))
                    G(n+1+X,n+1+X)=1./g(node_col,n+X,n-
1+X)+1./g(node_col,n+X,n)+1./g(node_col,n+X,n+X+1)+1./g(node_col
,n+X,n+X+X);
                    G(n+1-X,n+1-X)=1./g(node_col,n-X,n-1-
X)+1./g(node_col,n-X,n)+1./g(node_col,n-X,n+1-X)+2./node_col(n-
X,1);

                    G(n,n+1)=-1./g(node_col,n-1,n);
                    G(n+1,n)=-1./g(node_col,n,n-1);

                    G(n+1,n+2)=-1./g(node_col,n,n+1);
                    G(n+2,n+1)=-1./g(node_col,n+1,n);

                    G(n+1+X,n+1)=-1./g(node_col,n+X,n);
```

```
                    G(n+1,n+1+X)=-1./g(node_col,n,n+X);
                    G(n+1-X,n+1)=-1./g(node_col,n-X,n);
                    G(n+1,n+1-X)=-1./g(node_col,n,n-X);
                end
                if (n > (X*Y-2*X+2)) && (n < (X*Y-X-1))
                    G(n+1+X,n+1+X)=1./g(node_col,n+X,n-
1+X)+1./g(node_col,n+X,n)+1./g(node_col,n+X,n+X+1)+2./node_col(n
+X,1);
                    G(n+1-X,n+1-X)=1./g(node_col,n-X,n-1-
X)+1./g(node_col,n-X,n)+1./g(node_col,n-X,n+1-
X)+1./g(node_col,n-X,n-X-X);

                    G(n,n+1)=-1./g(node_col,n-1,n);
                    G(n+1,n)=-1./g(node_col,n,n-1);

                    G(n+1,n+2)=-1./g(node_col,n,n+1);
                    G(n+2,n+1)=-1./g(node_col,n+1,n);

                    G(n+1+X,n+1)=-1./g(node_col,n+X,n);
                    G(n+1,n+1+X)=-1./g(node_col,n,n+X);
                    G(n+1-X,n+1)=-1./g(node_col,n-X,n);
                    G(n+1,n+1-X)=-1./g(node_col,n,n-X);
                end
            end
        else
            if mod(n,X)==2

G(n+2,n+2)=1./g(node_col,n+1,n)+1./g(node_col,n+1,n+2)+1./g(node
_col,n+1,n-X+1)+1./g(node_col,n+1,n+X+1);
                G(n,n)=1./g(node_col,n-1,n)+1./g(node_col,n-1,n-
X-1)+1./g(node_col,n-1,n+X-1);


                if (n > (X+2)) && (n < (X*Y-2*X+2))
                    G(n+1+X,n+1+X)=1./g(node_col,n+X,n-
1+X)+1./g(node_col,n+X,n)+1./g(node_col,n+X,n+X+1)+1./g(node_col
,n+X,n+X+X);
                    G(n+1-X,n+1-X)=1./g(node_col,n-X,n-1-
X)+1./g(node_col,n-X,n)+1./g(node_col,n-X,n+1-
X)+1./g(node_col,n-X,n-X-X);

                    G(n,n+1)=-1./g(node_col,n-1,n);
                    G(n+1,n)=-1./g(node_col,n,n-1);

                    G(n+1,n+2)=-1./g(node_col,n,n+1);
                    G(n+2,n+1)=-1./g(node_col,n+1,n);
```

```
                    G(n+1+X,n+1)=-1./g(node_col,n+X,n);
                    G(n+1,n+1+X)=-1./g(node_col,n,n+X);
                    G(n+1-X,n+1)=-1./g(node_col,n-X,n);
                    G(n+1,n+1-X)=-1./g(node_col,n,n-X);
                else
                    if n==(X+2)
                        G(n+1+X,n+1+X)=1./g(node_col,n+X,n-
1+X)+1./g(node_col,n+X,n)+1./g(node_col,n+X,n+X+1)+1./g(node_col
,n+X,n+X+X);
                        G(n+1-X,n+1-X)=1./g(node_col,n-X,n-1-
X)+1./g(node_col,n-X,n)+1./g(node_col,n-X,n+1-X)+2./node_col(n-
X,1);

                        G(n,n+1)=-1./g(node_col,n-1,n);
                        G(n+1,n)=-1./g(node_col,n,n-1);

                        G(n+1,n+2)=-1./g(node_col,n,n+1);
                        G(n+2,n+1)=-1./g(node_col,n+1,n);

                        G(n+1+X,n+1)=-1./g(node_col,n+X,n);
                        G(n+1,n+1+X)=-1./g(node_col,n,n+X);
                        G(n+1-X,n+1)=-1./g(node_col,n-X,n);
                        G(n+1,n+1-X)=-1./g(node_col,n,n-X);
                    end
                    if n==(X*Y-2*X+2)
                        G(n+1+X,n+1+X)=1./g(node_col,n+X,n-
1+X)+1./g(node_col,n+X,n)+1./g(node_col,n+X,n+X+1)++2./node_col(
n+X,1);
                        G(n+1-X,n+1-X)=1./g(node_col,n-X,n-1-
X)+1./g(node_col,n-X,n)+1./g(node_col,n-X,n+1-
X)+1./g(node_col,n-X,n-X-X);

                        G(n,n+1)=-1./g(node_col,n-1,n);
                        G(n+1,n)=-1./g(node_col,n,n-1);

                        G(n+1,n+2)=-1./g(node_col,n,n+1);
                        G(n+2,n+1)=-1./g(node_col,n+1,n);

                        G(n+1+X,n+1)=-1./g(node_col,n+X,n);
                        G(n+1,n+1+X)=-1./g(node_col,n,n+X);
                        G(n+1-X,n+1)=-1./g(node_col,n-X,n);
                        G(n+1,n+1-X)=-1./g(node_col,n,n-X);
                    end
                end

            end
```

```
            if mod(n,X)==(X-1) && n > (X-1)

G(n+2,n+2)=1./g(node_col,n+1,n)+1./g(node_col,n+1,n+1-
X)+1./g(node_col,n+1,n+X+1);
                G(n,n)=1./g(node_col,n-1,n-2)+1./g(node_col,n-
1,n)+1./g(node_col,n-1,n-X-1)+1./g(node_col,n-1,n+X-1);


                if (n > (2*X)) && (n < (X*Y-X-1))
                    G(n+1+X,n+1+X)=1./g(node_col,n+X,n-
1+X)+1./g(node_col,n+X,n)+1./g(node_col,n+X,n+X+1)+1./g(node_col
,n+X,n+X+X);
                    G(n+1-X,n+1-X)=1./g(node_col,n-X,n-1-
X)+1./g(node_col,n-X,n)+1./g(node_col,n-X,n+1-
X)+1./g(node_col,n-X,n-X-X);

                    G(n,n+1)=-1./g(node_col,n-1,n);
                    G(n+1,n)=-1./g(node_col,n,n-1);

                    G(n+1,n+2)=-1./g(node_col,n,n+1);
                    G(n+2,n+1)=-1./g(node_col,n+1,n);

                    G(n+1+X,n+1)=-1./g(node_col,n+X,n);
                    G(n+1,n+1+X)=-1./g(node_col,n,n+X);
                    G(n+1-X,n+1)=-1./g(node_col,n-X,n);
                    G(n+1,n+1-X)=-1./g(node_col,n,n-X);
                else
                    if n==(2*X-1)
                        G(n+1+X,n+1+X)=1./g(node_col,n+X,n-
1+X)+1./g(node_col,n+X,n)+1./g(node_col,n+X,n+X+1)+1./g(node_col
,n+X,n+X+X);
                        G(n+1-X,n+1-X)=1./g(node_col,n-X,n-1-
X)+1./g(node_col,n-X,n)+1./g(node_col,n-X,n+1-X)+2./node_col(n-
X,1);

                        G(n,n+1)=-1./g(node_col,n-1,n);
                        G(n+1,n)=-1./g(node_col,n,n-1);

                        G(n+1,n+2)=-1./g(node_col,n,n+1);
                        G(n+2,n+1)=-1./g(node_col,n+1,n);

                        G(n+1+X,n+1)=-1./g(node_col,n+X,n);
                        G(n+1,n+1+X)=-1./g(node_col,n,n+X);
                        G(n+1-X,n+1)=-1./g(node_col,n-X,n);
                        G(n+1,n+1-X)=-1./g(node_col,n,n-X);
                    end
```

```
                    if n==(X*Y-X)

                        G(n+1+X,n+1+X)=1./g(node_col,n+X,n-
1+X)+1./g(node_col,n+X,n)+1./g(node_col,n+X,n+X+1)++2./node_col(
n+X,1);
                        G(n+1-X,n+1-X)=1./g(node_col,n-X,n-1-
X)+1./g(node_col,n-X,n)+1./g(node_col,n-X,n+1-
X)+1./g(node_col,n-X,n-X-X);

                        G(n,n+1)=-1./g(node_col,n-1,n);
                        G(n+1,n)=-1./g(node_col,n,n-1);

                        G(n+1,n+2)=-1./g(node_col,n,n+1);
                        G(n+2,n+1)=-1./g(node_col,n+1,n);

                        G(n+1+X,n+1)=-1./g(node_col,n+X,n);
                        G(n+1,n+1+X)=-1./g(node_col,n,n+X);
                        G(n+1-X,n+1)=-1./g(node_col,n-X,n);
                        G(n+1,n+1-X)=-1./g(node_col,n,n-X);
                    end
                end

            end
        end
    else
        if mod(n,X)==1
            G(n+1,n+1)=1./g(node_col,n,n+1)+1./g(node_col,n,n-
X)+1./g(node_col,n,n+X);

G(n+2,n+2)=1./g(node_col,n+1,n)+1./g(node_col,n+1,n+2)+1./g(node
_col,n+1,n-X+1)+1./g(node_col,n+1,n+X+1);

            if n < (X*Y-2*X+1)

G(n+1+X,n+1+X)=1./g(node_col,n+X,n+X+1)+1./g(node_col,n+X,n)+1./
g(node_col,n+X,n+X+X);
                if n > (X+1)
                    G(n+1-X,n+1-X)=1./g(node_col,n-X,n+1-
X)+1./g(node_col,n-X,n)+1./g(node_col,n-X,n-X-X);

                    G(n+1,n+2)=-1./g(node_col,n,n+1);
                    G(n+2,n+1)=-1./g(node_col,n+1,n);

                    G(n+1+X,n+1)=-1./g(node_col,n+X,n);
                    G(n+1,n+1+X)=-1./g(node_col,n,n+X);
                    G(n+1-X,n+1)=-1./g(node_col,n-X,n);
                    G(n+1,n+1-X)=-1./g(node_col,n,n-X);
```

```
          G(n,n+1)=0;
          G(n+1,n)=0;
        else
          if n == (X+1)
            G(n+1-X,n+1-X)=1./g(node_col,n-X,n+1-
X)+1./g(node_col,n-X,n)+2./node_col(n-X,1);

            G(n+1,n+2)=-1./g(node_col,n,n+1);
            G(n+2,n+1)=-1./g(node_col,n+1,n);

            G(n+1+X,n+1)=-1./g(node_col,n+X,n);
            G(n+1,n+1+X)=-1./g(node_col,n,n+X);
            G(n+1-X,n+1)=-1./g(node_col,n-X,n);
            G(n+1,n+1-X)=-1./g(node_col,n,n-X);
            G(n,n+1)=0;
            G(n+1,n)=0;
          end
        end
      else
        if n == (X*Y-2*X+1)

G(n+1+X,n+1+X)=1./g(node_col,n+X,n+X+1)+1./g(node_col,n+X,n)+2./
node_col(n+X,1);
          G(n+1-X,n+1-X)=1./g(node_col,n-X,n+1-
X)+1./g(node_col,n-X,n)+1./g(node_col,n-X,n-X-X);

          G(n+1,n+2)=-1./g(node_col,n,n+1);
          G(n+2,n+1)=-1./g(node_col,n+1,n);

          G(n+1+X,n+1)=-1./g(node_col,n+X,n);
          G(n+1,n+1+X)=-1./g(node_col,n,n+X);
          G(n+1-X,n+1)=-1./g(node_col,n-X,n);
          G(n+1,n+1-X)=-1./g(node_col,n,n-X);
          G(n,n+1)=0;
          G(n+1,n)=0;
        end
      end



    end

    if mod(n,X)== 0
      G(n+1,n+1)=1./g(node_col,n,n-1)+1./g(node_col,n,n-
X)+1./g(node_col,n,n+X);
      G(n,n)=1./g(node_col,n-1,n-2)+1./g(node_col,n-
1,n)+1./g(node_col,n-1,n-1-X)+1./g(node_col,n-1,n-1+X);
```

```
            if n <(X*Y-2*X+1)
                G(n+1+X,n+1+X)=1./g(node_col,n+X,n-
1+X)+1./g(node_col,n+X,n)+1./g(node_col,n+X,n+X+X);

                if n> (2*X)
                    G(n+1-X,n+1-X)=1./g(node_col,n-X,n-1-
X)+1./g(node_col,n-X,n-X-X)+1./g(node_col,n-X,n);

                    G(n,n+1)=-1./g(node_col,n-1,n);
                    G(n+1,n)=-1./g(node_col,n,n-1);

                    G(n+1,n+2)=0;
                    G(n+2,n+1)=0;


                    G(n+1-X,n+1)=-1./g(node_col,n-X,n);
                    G(n+1,n+1-X)=-1./g(node_col,n,n-X);
                    G(n+1+X,n+1)=-1./g(node_col,n+X,n);
                    G(n+1,n+1+X)=-1./g(node_col,n,n+X);
                else
                    if n == (2*X)
                        G(n+1-X,n+1-X)=1./g(node_col,n-X,n-1-
X)+1./g(node_col,n-X,n)+2./node_col(n-X,1);

                        G(n,n+1)=-1./g(node_col,n-1,n);
                        G(n+1,n)=-1./g(node_col,n,n-1);

                        G(n+1,n+2)=0;
                        G(n+2,n+1)=0;


                        G(n+1-X,n+1)=-1./g(node_col,n-X,n);
                        G(n+1,n+1-X)=-1./g(node_col,n,n-X);
                        G(n+1+X,n+1)=-1./g(node_col,n+X,n);
                        G(n+1,n+1+X)=-1./g(node_col,n,n+X);
                    end
                end

            else
                if n == (X*Y-X)
                    G(n+1+X,n+1+X)=1./g(node_col,n+X,n-
1+X)+1./g(node_col,n+X,n)+2./node_col(n+X,1);
                    G(n+1-X,n+1-X)=1./g(node_col,n-X,n-1-
X)+1./g(node_col,n-X,n-X-X)+1./g(node_col,n-X,n);

                    G(n,n+1)=-1./g(node_col,n-1,n);
```

```
                    G(n+1,n)=-1./g(node_col,n,n-1);

                    G(n+1,n+2)=0;
                    G(n+2,n+1)=0;


                    G(n+1-X,n+1)=-1./g(node_col,n-X,n);
                    G(n+1,n+1-X)=-1./g(node_col,n,n-X);
                    G(n+1+X,n+1)=-1./g(node_col,n+X,n);
                    G(n+1,n+1+X)=-1./g(node_col,n,n+X);
                end
            end


        end
    end






    switch_col(n,1)=2;
end
end


%%%%%%%%%%%%%%%%%%%%%%%%%%%%%%%%%%%%%%%%%%%%%%%%%%%%%%%%%%%%%%%%


%%%%%%%%%%%%%%%%%%%%%%%%%%%%%%%%%%%%%%%%%%%%%%%%%%%%%%%%%%%%%%%%
function [ node_col,switch_col ] = switcher(
node_col,switch_col,X,Y,R_ins,R_metal,R_break,temp,Tc_grid,Tc_gr
id_break,alpha )
%%switches grains from metallic to semiconducting if <Tc. also
breaks chosen
%grains

for ii=1:Y
    for jj=1:X
        if (node_col(jj+X*(ii-1),1) < (R_ins *
exp(alpha/temp)./exp(alpha/300)+0.00001) || node_col(jj+X*(ii-
1),1) > (R_ins* exp(alpha/temp)./exp(alpha/300)-0.00001))&
(node_col(jj+X*(ii-1),1)~=R_break)
            if temp < Tc_grid(jj,ii)
                node_col(jj+X*(ii-1),1)=R_ins*
exp(alpha/temp)./exp(alpha/300);
                switch_col(jj+X*(ii-1),1)=1;
            end
```

```
        end
    end
end

end
%%%%%%%%%%%%%%%%%%%%%%%%%%%%%%%%%%%%%%%%%%%%%%%%%%%%%%%%%%%%%%%%
```

Appendix B (Sputtering Deposition Procedure)

In this appendix, we provide the detailed procedure used during the sputtering of both the VO_2/Ni and FeRh/Ni bilayers. The same procedure was used for each material, with any differences noted. The substrate holder is rotated at 40 rotations/min throughout the process in order to improve deposition uniformity. The procedure is as follows:

(1) The temperature is ramped by set point to the deposition temperature. Its first set to 200 °C, then increased to 400 °C in steps of 50 °C. From there, it's continually incremented in steps of 25 °C to the desired deposition temperature. At each set point, the system is allowed to settle at the set temperature before continuing the ramp. Once the deposition temperature is reached, the sample is allowed to thermally equilibrate for 15 minutes. This process corresponds to an approximate heating rate of 15-17 °C/min.

(2) Concurrent with the thermal equilibration step in (1), a presputter is performed to prepare the target for deposition. With the shutter of the sputtering gun closed, the target is first presputtered for 5 minutes in a pure Ar atmosphere at 50 W and 4 mTorr pressure.

(3) For the reactive VO_2 sputter, a second presputter is performed for 10 minutes under the operating conditions in order to prepare a stable and uniform plasma for the deposition.

(4) The actual sputter is performed with power applied to the target. Details on the conditions (temperature, gas partial pressures, length of sputter, etc.) will be given below.

(5) The sample is returned to room temperature in a procedure analogous to (1), except all temperature steps are 25 °C. It is worth noting that the system does not have an active cooling system, so the rate is significantly slower than the initial heating process, leading to an approximate rate of 13 °C/min. Gas flow, partial pressures, and total pressure are all maintained at the deposition conditions during the cooling until the sample is below 200 °C. Below 200 °C, the chamber is evacuated back to vacuum, and the sample is removed when the temperature is below 40 °C.

(6) In the case of FeRh, an in-situ anneal is required. Immediately after deposition, the temperature is raised as in step (1) to the annealing temperature. The anneal is done under the same Ar flow and pressure as in the deposition.

(7) If this is the final layer, a capping layer of 3-5 nm of Al is applied in-situ after the sample has cooled below 40 °C. The Al gun is operated at 4 mTorr Ar, 50 W in a DC magnetron setup. If Ni is to be deposited, the sample is removed from the chamber to atmosphere and reintroduced, following the above procedure.

Appendix C (XRD/XRR Procedure)

Here, we provide the procedure used to collect XRD scans on a Bruker D-8 Series-I diffractometer. The same procedure was used for XRR scans, with minor modifications as discussed below, in order to optimize the measurement results.

(1) The source is set to 40 V and 40 mA and allowed to warm up for approximately 10 minutes to allow for thermal equilibrium.

(2) The sample is mounted to the sample stage, placed approximately at the center of the beam.

(3) A scan is performed along z-axis, and the sample is set a value half between where the scan begins showing a maximum and a minimum signal. This corresponds to the surface of the film being at the halfway point in the beam profile. The source and detector both contain slits with widths of 0.1 mm. A copper foil is used to attenuate the beam appropriately.

(4) Next, a scan is performed along the x-axis, and the sample is placed at the minimum of the signal. This corresponds to the sample profile being directly in the beam, and hence the maximum reduction in signal.

(5) Step 2 is repeated, with a scan rate of 1 second per step, and step size 0.005 mm.

(6) The slits are changed to a 0.2 mm slit on the source, and a 0.2 mm followed (in the sense of source to detector) by a 0.6 mm slit.

(7) A 'rocking curve' scan (ω scan) is performed. This is equivalent to decoupling $\theta/2\theta$ in a small range and adjusting θ. The sample is rocked, typically on an expected substrate peak such as the (1-102) peak for r-cut sapphire at 25.68°. A step size of 0.005° and collection time 1 second per step is adequate. By picking the peak, this accounts for any small shifts between the theoretical $\theta/2\theta$ match. A typical discrepancy is 0.2°.

(8) Optionally, other alignment may be performed while the sample is at the rocking curve angles. The first is a y-axis scan, to maximize the signal by maximizing the surface area of the sample in the beam. The other is a χ scan, which tilts the sample stage in a rotation around the y-axis.

(9) A $\theta/2\theta$ scan is performed for the desired range, with a step size of 0.2° and 0.5 s collection time per step. The same 0.2/0.2/0.6 mm slit set up as in 6 is maintained.

For XRR, some minor adjustments are made to the above procedure. To begin, the preference is to mount the sample without the glass slide. While in principle it does not matter, in practice it makes the alignment significantly easier, and there is no signal from the Al backplate to worry about. The XRR procedure follows that given for XRD up until step 5. Step 5 is performed, but is done 3 times, and the results averaged, for a finer average. Steps 4-6 are often iterated to improve the alignment. Then a rocking curve is performed with the 0.1 mm/0.1 mm slits, at some low angle below the critical angle, typically $0 - 0.5°$. A χ scan can optionally be performed. Then the actual scan is taken for the desired range, typically $0.2 - 5°$, or until the Kiessig fringes are sufficiently hidden by background noise. One major difference from the XRD procedure is the wide range of intensities that need to be accommodated. In order to do so, the slit size (ranging from 0.05 mm to 0.2 mm), Soller slits, copper foil, and knife edge are adjusted manually. The detector used works best for counts per second (CPS) below 50,000, but above 10,000. In addition, the detector behavior is linear below 50,000 CPS. When possible, this range was utilized. Thus, a full scan is done in pieces, and later stitched together and artificially renormalized to the first scan using Bruker's proprietary EVA software. Each scan segment is averaged over at least 3 runs to improve signal to noise ratios. Each scan uses a 0.005° step size, 1 second collection time.

Appendix D (VSM Magnetometry Procedure)

In this section, we provide the detailed procedure for both M vs. T and M vs. H measurements respectively. For the M vs. T, the procedure is as follows:

(1) The sample is mounted onto the carbon fiber rod, as described above.

(2) The sample rode is then inserted through the top of the VSM motor until the magnet seal engages. No sample shield is used during this process.

(3) The chamber is then pumped down to low vacuum (~33 Torr). If the VSM Oven option (described below) is used, the system is pumped down to high vacuum (~0.1 mTorr).

(4) The coils are then run through a demagnetization process, wherein the field is ramped to 2 T, and then oscillated back down to 0 T. This helps to reduce any remanent magnetization in the pickup coils.

(5) The sample is then centered by applying a 100 mT field and looking for a peak in voltage while the sample is moved through the coils. For the VO_2/Ni samples, this is done at room temperature, using the FM Ni signal. For the FeRh/Ni samples, the samples are heated above T_c and either the FM FeRh in bare FeRh or the combined signal of FM FeRh and Ni is used to center the sample. Often a sample hysteresis loop is taken to verify the sample is correctly mounted.

(6) If the cooling branch is run first, the temperature is ramped at 5 K/min to a temperature sufficiently above T_c to fully transition the film, and a 1 T field is applied to saturate the magnetization. The temperature is stabilized for approximately 10 minutes, and then the field is reduced to the measurement field 100-250 mT.

(7) The temperature is then decreased by 1 K/min continuously to room temperature or slightly below, to ensure the SPT material has fully transitioned. The magnetization of the sample is recorded at 1 Hz intervals.

(8) The temperature is then increased at 1 K/min back to the starting temperature while recording the magnetization, again at 1 Hz.

The procedure for M vs. H is similar:

(1) The sample is mounted onto the carbon fiber rod, as described above.

(2) The sample rode is then inserted through the top of the VSM motor until the magnet seal engages. No sample shield is used during this process.

(3) The chamber is then pumped down to low vacuum (~mTorr). If the VSM Oven option (described below) is used, the system is pumped down to high vacuum ().

(4) The coils are then run through a demagnetization process, wherein the field is ramped to 2 T, and then oscillated back down to 0 T. This helps to reduce any remanent magnetization in the pickup coils.

(5) The sample is then centered by applying a 100 mT field and looking for a peak in voltage while the sample is moved through the coils. For the VO_2/Ni samples, this is done at room temperature, using the FM Ni signal. For the FeRh/Ni samples, the samples are heated above T_c and either the FM FeRh in bare FeRh or the combined signal of FM FeRh and Ni is used to center the sample.

(6) If the cooling branch is run first, the temperature is ramped at 5 K/min to a temperature sufficiently above T_c to fully transition the film, and a 1 T field is applied to saturate the magnetization. The temperature is stabilized for approximately 10minutes, and then the field is reduced to 100-250 mT, corresponding to the smallest field needed to complete a full closed hysteresis loop. The temperature is then reduced to the first measurement temperature at 1 K/min and allowed to stabilize for 5 minutes. The applied magnetic field is swept through a full hysteresis loop at this temperature. The sample is then

automatically re-centered, before proceeding to the next temperature where this process is repeated.

(7) Once the cooling branch is complete, after the last measurement temperature, the temperature is increased to the first heating measurement temperature at 1 K/min, and the temperature is allowed to stabilize for 5 minutes. The applied magnetic field is swept through a full hysteresis loop at this temperature. The sample is then automatically re-centered, before proceeding to the next temperature where this process is repeated.

Note that steps 5 and 6 are interchangeable. Whether the heating or cooling branch is done first is picked for convenience corresponding to what temperature the centering is done at and has no impact on the measurement. For VO_2, this means that the heating is first, followed by the cooling branch. Whereas for FeRh, the cooling branch is followed by the heating branch. The exception is when virgin samples are needed to study the effects of the first thermal cycling, which will be indicated and discussed in the results sections when necessary. If both M vs. H and M vs. T characteristics are measured for the same sample, often they are done sequentially. Steps 1-4 will be performed, then the M vs. H procedure, followed by steps 5-7 of the M vs. T procedure. Again, this has no effect on the measurement, except when studying the effects of the first thermal cycle. One comment needs to be made with respect to steps 5-6 in the M vs. H procedure. It was found that there was a roughly 0.5 K temperature drift away from the set point at the start of the hysteresis loop, regardless of the time allowed for the temperature to stabilize. However, during the active measurement of the loop, the QD system fixes this discrepancy. The VO_2/Ni films were relatively insensitive to this phenomenon, however for the FeRh and FeRh/Ni samples, often 2-3 loops were run consecutively when near T_c, in order to get a proper hysteresis loop. More details will be given in future sections, but it is believed that this artifact of the system did not meaningfully affect the results shown.

Appendix E (SQUID Magnetometry Procedure)

In this section, we provide the detailed procedure for both M vs. T and M vs. H measurements respectively. The procedure for a M vs. T measurement in the SQUID is as follows:

(1) The sample is mounted onto the sample rod, as described above.

(2) The sample rod is then inserted into a glass sleeve, which acts as an intermediate Load-Lock system. The glass sleeve is purged and pumped down three times.

(3) The valve to the sample chamber is opened, and the rod can be inserted into the lip seal. Once it is lowered into the chamber, a Swagelock clamp is tightened onto the top of the rod.

(4) Optionally, a demagnetization process can be performed, but it is slow and uses a large amount of helium, so is only done when necessary. The magnet is ramped to 1 T (maximum for the magnet), and then oscillates back to 0 T in order to reduce any magnetization of the pickup coils. The magnet also has a full reset option that corresponds to allowing portions of the magnet to go normal but uses too much helium to be used in the standard procedure.

(5) The centering process is started. For FeRh based samples, this is done at 400 K and 100 mT applied field. The temperature is ramped at 5 K/min, and the sample is allowed to

stabilize for 10 min. Again, a peak in voltage appears as the sample is moved through the pickup coils.

(6) The sample is saturated at 1 T. The field is then ramped down to 100 mT in No Overshoot mode, which compensates for the inherent relaxation of the superconducting magnet.

(7) The cooling branch is begun, reducing the temperature at 1 K/min with a steady 100 mT applied field. Data is collected in approximately 1 second intervals, limited by the linear motor.

Once the cooling branch is complete, the heating branch is done by increasing the temperature at 1 K/min, again in the same 100 mT field. Data is collected in approximately 1 second intervals, limited by the linear motor.

Appendix F (AFM Procedure)

In this appendix, we provide the procedure used for AFM measurements. The procedure is given below:

(1) If necessary, load the tip into a Bruker designed chip carrier. The tips used in this work were either pre-mounted to a ceramic chip carrier via adhesive, or a Bruker metallic chip carrier utilizing a spring clip. The pre-mounted tips tend to be much more robust and give better images but stopped becoming commercially available during the course of this work.

(2) Once loaded, the chip carrier is mounted onto an AFM probe cartridge. The chip carrier is held down via another spring clip. 3 balls insert into slots in the chip carrier to hold it in place. The cartridge contains the circuity used to excite the cantilever.

(3) The sample is placed onto the sample mount, and then the probe cartridge is inserted.

(4) The laser is aligned onto the tip of the cantilever, with the aid of an optical microscope.

(5) The reflection into the photodetector is optimized for maximum voltage and centered on the array by adjusting mirrors that bounce the signal into the detector. A typical maximum voltage is ~2.5 V, with lateral centering at less than 0.1 V off center

(6) Next, tune to find the resonance peak. Most parameters such as the driving voltage are automated by Bruker software, with the exception of setting the gain (x8) and target tapping signal. We use 3.5 V on the left shoulder of the resonance peak, which is in the 60-70% recommended range of the max signal of 5V.

(7) The tip is then brought to the sample surface. First it is lowered via motor to a safe distance, and then engaged utilizing the feedback system. The distance to the surface is set by another target voltage, roughly 2.0-2.1 V, again roughly 60% of the 3.5 V target voltage. Lower voltages correspond to the tip being closer to the surface and vice versa.

(8) The PID controls are also in this step. PID values of either P=.33, I=0.3, D=0 or P=0.5, I=0.3, D=0 were used. These choices were verified empirically using known stepped silicon calibration grids.

(9) The system is ready to begin scanning. Typical scan settings are 0.1-0.3 Hz scan rate, and either a 5x5 micron grid or a 2x2 micron grid, in both forward and backward scans. The 5x5 scans have 512 lines resolution, and 2x2 256 lines, roughly proportional. A typical scan with these parameters takes roughly 10-30 minutes. We utilize the Height channels, which use the piezo inputs to calculate z heights and comes with some nonlinearity, particularly over large (>10 microns) scan sizes. This can be corrected via software as done in this work, or the Height sensor channel can be used instead.

(10) Once the scan is complete, steps (7), (3), (2) and (1) in reverse order can be used to remove the tip and sample.